

UNIVERSIDADE DO PORTO
FACULDADE DE ENGENHARIA



FEUP

PHD THESIS

**Multi-material joints
for high-speed train structures**

Giuseppe CATALANOTTI

Supervisors:

Prof. Pedro P. CAMANHO
Prof. António T. MARQUES
Dr. Pascal GHYS

November, 2010

To Paola

Abstract

The work presented in this thesis addresses the design and the simulation of hybrid mechanically fastened joints for the railway industry.

The work includes different levels of detail in the simulation of the joints. An experimental campaign is conducted on single and double lap joints with different geometries and materials. As result of the experimental tests, design charts are proposed to assist the engineers during the preliminary definition of a structure.

To simulate in detail the behavior of a bolted joint, a set of three-dimensional failure criteria and a progressive damage model are proposed. It was shown that the previously developed failure criterion for matrix compression works correctly for the embedded lamina only if the *in-situ* parameters are correctly computed. For matrix tension it was shown that previous failure criteria are not consistent.

The progressive damage model uses cohesive softening laws which are determined experimentally measuring the R-curves in the longitudinal direction. A methodology to measure the J-Integral around the crack tip using Digital Image Correlation was proposed. It was shown that for compact-tension test the results are virtually the same as those obtained using data reduction schemes based on Finite Element analyses. For compression, the methodology provides a significant improvement on the determination of the R-curve.

The cost of a 3D FE model in terms of computing time is not suitable for the industry where the results must be obtained quickly. Therefore, a simple 2D FE model, using a 2D version of the failure criteria proposed, is used and is applied to a train subcomponent. A good agreement between the numerical predictions and the experimental results was obtained.

Résumé

Le travail présenté dans cette thèse aborde la conception et la simulation des joints hybrides rivetés et boulonnés pour l'industrie ferroviaire.

Le travail concernant la simulation des joints a été conduit à différents niveaux de détail. Une campagne expérimentale est menée pour les joints simples et doubles avec différentes géométries et matériaux. Comme résultats de tests expérimentaux, des tables de conception sont proposées pour assister les ingénieurs durant la première phase de définition de la structure.

Pour simuler en détail le comportement d'un joint boulonné, une série de critères tridimensionnels d'endommagement et une modélisation de propagation de l'endommagement sont proposées. On a montré que le critère d'endommagement précédemment développé pour la compression de la matrice ne fonctionne proprement pour la couche intérieure au laminé que si les paramètres *in-situ* sont correctement calculés. Pour la traction de la matrice, il a été prouvé que les critères précédemment utilisés ne sont pas cohérents.

Le modèle de propagation de l'endommagement utilise des lois cohésives qui sont déterminées expérimentalement en mesurant les courbes de résistance dans la direction longitudinale. Une méthode qui utilise la corrélation digitale d'images a été proposée pour mesurer l'intégrale J autour de la pointe de la fissure. On a démontré que pour les tests de compact-tension les résultats sont pratiquement équivalents à ceux obtenus en utilisant les méthodes d'analyse basées sur les éléments finis.

Le coût d'un modèle tridimensionnel aux éléments finis en termes de temps de calcul n'est pas approprié pour l'industrie ferroviaire pour laquelle les résultats doivent être obtenus rapidement. En conséquence, il a été proposé un simple modèle 2D qui utilise la version 2D des critères d'endommagement proposés. Une bonne concordance a été trouvée entre les prédictions numériques et les résultats expérimentaux.

Resumo

O trabalho apresentado nesta tese aborda o projecto e simulação de juntas aparafusadas híbridas para a indústria ferroviária.

O trabalho inclui diferentes níveis de detalhe para simulação das juntas. Realizou-se um programa experimental com juntas de sobreposição simples e dupla usando geometrias e materiais diferentes. Como resultado dos ensaios experimentais, foram propostas regras de projecto para a definição preliminar da estrutura.

Para simular em detalhe o comportamento de uma junta aparafusada foi proposto um conjunto de critérios de rotura e um modelo de dano progressivo. Foi demonstrado que o critério de rotura da matriz em compressão desenvolvido previamente só funciona correctamente para uma camada embebida se forem utilizados os parâmetros *in-situ*. Para o caso da tracção da matriz, foi demonstrado que os critérios de rotura desenvolvidos previamente não são consistentes.

O modelo de dano progressivo usa leis de dano coesivas que são determinadas experimentalmente através das curvas de resistência na direcção longitudinal. Foi proposta a metodologia de Correlação Digital de Imagem para calcular o integral-J na vizinhança da extremidade da fissura. Foi demonstrado que para o ensaio de *compact-tension* os resultados são semelhantes aos obtidos através de análises em métodos de elementos finitos. Para compressão, a referida metodologia resulta num melhoramento significativo na determinação da curva de resistência.

O elevado custo computacional de um modelo de Elementos Finitos 3D torna-os inviáveis para utilização pela indústria, uma vez que normalmente pretende-se obter resultados rapidamente. Assim, foi implementado um modelo 2D de Elementos Finitos para projecto de um subcomponente de um comboio, usando a versão 2D do critério de rotura proposto. Foi obtido um resultado numérico próximo dos resultados experimentais.

Contents

Abstract	iii
Acronyms	xxi
List of Symbols	xxiii
Greek Letters	xxvii
Acknowledgments	xxix
1 Introduction	1
2 Literature Review	3
2.1 Experimental Analysis	3
2.1.1 Failure Modes	3
2.1.2 Influence of the geometry	5
2.1.3 Influence of the fiber orientation	6
2.1.4 Influence of lateral constraint	6
2.1.5 Influence of the stacking sequence	7
2.1.6 Influence of the fastener type	8
2.1.7 Influence of metallic inserts	8
2.1.8 Hybrid laminates	9
2.1.9 Multi fastener joints	10
2.1.10 Stress distribution	10
2.1.11 Fatigue	11
2.2 Stress analysis	11
2.2.1 Classical methods of stress analysis	11
2.2.2 Numerical methods of stress analysis	12
2.2.3 Strength prediction methods	15
2.2.4 Combined methods	16
2.2.5 Progressive damage models	17
2.2.6 Application to multi-fastener joints	19
2.3 Relaxation in composite joints	20
2.3.1 Experimental studies	20

2.3.2	FE analyses	21
2.4	Effects of environmental conditions	23
2.5	State of art in the railway industry	24
2.5.1	Comparison of different technologies	25
2.5.2	Connections in railway industry	25
3	Experimental Work	29
3.1	Materials used	29
3.1.1	Metals	29
3.1.2	Composites	30
3.2	Strain gauges	32
3.2.1	Selection of strain gauges	32
3.2.2	Surface preparation	33
3.2.3	Strain gauge bonding	33
3.3	Test Plan and Taguchi method	34
3.3.1	Definition of the geometry	34
3.3.2	Samples denomination	36
3.4	Specimen preparation	38
3.4.1	Hole Drilling	38
3.4.2	Bolts, characteristics and installation	38
3.5	Tests	40
3.5.1	Calculation and Report	40
3.5.2	Three Point Bending Test	41
3.5.3	Double-lap Bolted Joint	42
3.5.4	Single-lap Bolted Joint	61
3.5.5	Pull-Trough Test	94
3.6	Conclusions	101
4	CT-CC experimental tests	103
4.1	DIC technique	103
4.1.1	Introduction	103
4.1.2	Crack detection algorithm	105
4.1.3	J-Integral computation	109
4.2	Experimental Work	115
4.2.1	Experimental Setup	115
4.2.2	Experimental results	118
5	3D Numerical Model	127
5.1	Matrix Failure Criteria for 3D stress states	127
5.1.1	Failure criteria for matrix compression	129
5.1.2	Failure Criteria for Matrix Tension	133
5.2	Fiber Failure Criteria for 3D stress states	147
5.2.1	Fiber tension failure ($\sigma_{11} > 0$)	147

5.2.2	Fiber kinking failure ($\sigma_{11} \leq 0$)	147
5.3	Verification Problems	155
5.3.1	Example 1: Relationship between Y_C^{is} , η_L and S_L^{is}	155
5.3.2	Example 2: σ_{22} - τ_{12} failure envelopes	157
5.3.3	Example 3: Compression of thick lamina	158
5.3.4	Example 4: σ_{11} - σ_{22} failure envelopes	159
5.3.5	Example 5: σ_{11} - τ_{12} failure envelopes	160
5.3.6	Example 6: Influence of hydrostatic pressure	161
5.3.7	Conclusions	163
5.4	Damage Model	163
5.4.1	Complementary free energy and damage operators	163
5.4.2	Damage activation functions	165
5.4.3	Damage evolution	165
5.4.4	Dissipation	166
5.4.5	Damage evolution laws	167
5.4.6	Computational Model	167
6	Numerical Results	169
6.1	FE model	171
6.1.1	Python scripts	171
6.1.2	Details of the models	171
6.2	Comparison between FEM and experiments	175
6.2.1	Bearing	175
6.2.2	Net-Tension	178
6.2.3	Shear-Out	180
6.3	Conclusions	182
7	2D Numerical Model	183
7.1	Introduction	183
7.2	Experimental Analysis	183
7.2.1	Subcomponent Design	183
7.2.2	Experimental Setup	184
7.2.3	Experimental Results	185
7.3	Quick Design Tool and Analysis Results	187
7.3.1	Generalities	187
7.3.2	Industrial application	190
8	Conclusions and future work	193
8.1	Conclusions	193
8.2	Future work	195
A	Crack detection algorithm	211
B	J-Integral algorithm	215

C Parametric Model for J-Integral calculation	219
D 2D Model for Industrial Application	227

List of Figures

2.1	Geometry of the specimen.	3
2.2	Bearing test failure modes for ASTM D 5961/D 5961M-05.	4
2.3	Definition of planes, θ and α	4
2.4	Variation of bearing strength of (0/ \pm 45) laminates.	5
2.5	Effect of lateral constraint on bearing strength.	7
2.6	Inserts' geometry.	9
2.7	Bolts installed in rows and lines.	10
2.8	Stress distributions around a pin-loaded hole for several coefficients of friction.	12
2.9	Effects of clearance.	13
2.10	Effects of w/d and e/d on stress concentration factor.	14
2.11	Definition of characteristic lengths.	16
2.12	Characteristic curve.	17
2.13	Bearing-by-pass diagram for damage onset strength.	20
2.14	Stiffness as a function of temperature for a typical polymer matrix material.	24
2.15	Main connections in a carbody shell.	27
2.16	Main connections in a carbody shell: details.	27
3.1	True-stress true-strain curve for metals used	30
3.2	Strain gage installation	33
3.3	Specimens' geometry	36
3.4	Specimens after the installation of the strain gauges	38
3.5	Unbrako bolts	39
3.6	Three point bending test	42
3.7	Equipment set-up for DBJ test	43
3.8	Load vs. displacement for E-1-I specimens	44
3.9	Force vs. strain for E-1-1 specimen	44
3.10	E-1-3 specimen after loading	44
3.11	Load vs. displacement for E-2-I specimens	45
3.12	Load vs. strain for E-2-1 specimen	45
3.13	E-2-3 specimen after loading	45
3.14	Load vs. displacement for E-3-I specimens	46

3.15	Load vs. strain for E-3-1 specimen	46
3.16	E-3-3 specimen after loading	46
3.17	Load vs. displacement for E-4-I specimens	47
3.18	Load vs. strain for E-4-1 specimen	47
3.19	E-4-3 specimen after loading	47
3.20	Load vs. displacement for V-1-I specimens	48
3.21	Load vs. strain for V-1-1 specimen	48
3.22	V-1-2 specimen after loading	48
3.23	Load vs. displacement for V-2-I specimens	49
3.24	Load vs. strain for V-2-1 specimen	49
3.25	V-2-3 specimen after loading	49
3.26	Load vs. displacement for V-3-I specimens	50
3.27	Load vs. strain for V-3-1 specimen	50
3.28	V-3-2 specimen after loading	50
3.29	Load vs. displacement for V-4-I specimens	51
3.30	Load vs. strain for V-4-1 specimen	51
3.31	V-4-1 specimen after loading	51
3.32	Load vs. displacement for P-1-I specimens	52
3.33	Load vs. strain for P-1-1 specimen	52
3.34	P-1-1 specimen after loading	52
3.35	Load vs. displacement for P-2-I specimens	53
3.36	Load vs. strain for P-2-1 specimen	53
3.37	P-2-2 specimen after loading	53
3.38	Load vs. displacement for P-3-I specimens	54
3.39	Load vs. strain for P-3-1 specimen	54
3.40	P-3-3 specimen after loading	54
3.41	Load vs. displacement for P-4-I specimens	55
3.42	Load vs. strain for P-4-1 specimen	55
3.43	P-4-3 specimen after loading	55
3.44	Correct calculation of bearing strain	57
3.45	Bearing stress vs. bearing strain for E-4-I specimens	58
3.46	Bearing stress vs. bearing strain for P-4-I specimens	59
3.47	Bearing stress vs. bearing strain for V-4-I specimens	59
3.48	Comparison of results for specimens #1 (DBJ)	60
3.49	Comparison of results for specimens #2 (DBJ)	60
3.50	Comparison of results for specimens #3 (DBJ)	61
3.51	Comparison of results for specimens #4 (DBJ)	61
3.52	Equipment set-up for SBJ test	62
3.53	Load vs. displacement for P-A-1-I specimens	63
3.54	Load vs. strain for P-A-1-1 specimen	63
3.55	P-A-1-2 specimen after loading	63
3.56	Load vs. displacement for P-A-2-I specimens	64
3.57	Load vs. strain for P-A-2-1 specimen	64

3.58	P-A-2-2 specimen after loading	64
3.59	Load vs. displacement for P-A-3-I specimens	65
3.60	Load vs. strain for P-A-3-1 specimen	65
3.61	P-A-3-3 specimen after loading	65
3.62	Load vs. displacement for P-A-4-I specimens	66
3.63	Load vs. strain for P-A-4-1 specimen	66
3.64	P-A-4-2 specimen after loading	66
3.65	Load vs. displacement for P-S-1-I specimens	67
3.66	Load vs. strain for P-S-1-1 specimen	67
3.67	P-S-1-2 specimen after loading	67
3.68	Load vs. displacement for P-S-2-I specimens	68
3.69	Load vs. strain for P-S-2-1 specimen	68
3.70	P-S-2-2 specimen after loading	68
3.71	Load vs. displacement for P-S-3-I specimens	69
3.72	Load vs. strain for P-S-3-1 specimen	69
3.73	P-S-3-2 specimen after loading	69
3.74	Load vs. displacement for P-S-4-I specimens	70
3.75	Load vs. strain for P-S-4-1 specimen	70
3.76	P-S-4-2 specimen after loading	70
3.77	Load vs. displacement for V-A-1-I specimens	71
3.78	Load vs. strain for V-A-1-1 specimen	71
3.79	V-A-1-3 specimen after loading	71
3.80	Load vs. displacement for V-A-2-I specimens	72
3.81	Load vs. strain for V-A-2-1 specimen	72
3.82	V-A-2-1 specimen after loading	72
3.83	Load vs. displacement for V-A-3-I specimens	73
3.84	Load vs. strain for V-A-3-1 specimen	73
3.85	V-A-3-3 specimen after loading	73
3.86	Load vs. displacement for V-A-4-I specimens	74
3.87	Load vs. strain for V-A-4-1 specimen	74
3.88	V-A-4-2 specimen after loading	74
3.89	Load vs. displacement for V-S-1-I specimens	75
3.90	Load vs. strain for V-S-1-1 specimen	75
3.91	V-S-1-2 specimen after loading	75
3.92	Load vs. displacement for V-S-2-I specimens	76
3.93	Load vs. strain for V-S-2-1 specimen	76
3.94	V-S-2-2 specimen after loading	76
3.95	Load vs. displacement for V-S-3-I specimens	77
3.96	Load vs. strain for V-S-3-1 specimen	77
3.97	V-S-3-3 specimen after loading	77
3.98	Load vs. displacement for V-S-4-I specimens	78
3.99	Load vs. strain for V-S-4-1 specimen	78
3.100	V-S-4-3 specimen after loading	78

3.101	Load vs. displacement for V-P-1-I specimens	79
3.102	Load vs. strain for V-P-1-1 specimen	79
3.103	V-P-1-I specimens after loading	79
3.104	Load vs. displacement for V-P-2-I specimens	80
3.105	Load vs. strain for V-P-2-1 specimen	80
3.106	V-P-2-1 specimen after loading	80
3.107	Load vs. displacement for V-P-3-I specimens	81
3.108	Load vs. strain for V-P-3-1 specimen	81
3.109	V-P-3-2 specimen after loading	81
3.110	Load vs. displacement for V-P-4-I specimens	82
3.111	Load vs. strain for V-P-4-1 specimen	82
3.112	V-P-4-1 specimen after loading	82
3.113	Bearing correction for SBJ	83
3.114	Bearing stress vs. bearing strain for P-A-4-I specimens	83
3.115	Bearing stress vs. bearing strain for P-S-4-I specimens	84
3.116	Bearing stress vs. bearing strain for V-A-4-I specimens	84
3.117	Bearing stress vs. bearing strain for V-S-4-I specimens	85
3.118	Bearing stress vs. bearing strain for V-P-4-I specimens	85
3.119	Load case of a bolted joint	86
3.120	Load vs. displacement for V-P-4-I specimens	86
3.121	Aluminium-vinylester connection after being loaded	86
3.122	Comparison of results for SBJ	87
3.123	Strength for SBJ specimens	88
3.124	DBJ Glass-Epoxy design chart	90
3.125	DBJ Glass-Vinylester design chart	90
3.126	DBJ Glass-Phenolic design chart	91
3.127	SBJ Glass-Vinylester/Aluminum design chart	91
3.128	SBJ Glass-Vinylester/Steel design chart	92
3.129	SBJ Glass-Phenolic/Aluminum design chart	92
3.130	SBJ Glass-Phenolic/Steel design chart	93
3.131	SBJ Glass-Vinylester/Glass-Phenolic design chart	93
3.132	Equipment set-up for PT test	94
3.133	Pull-trough test; load vs. displacement for GF-epoxy specimens	96
3.134	Pull-trough test; load vs. displacement for GF-phenolic specimens	98
3.135	Pull-trough test; load vs. displacement for GF-vinylester specimens	100
3.136	Pull-trough specimens after loading	100
3.137	Comparison of PT tests failure loads	101
4.1	Initial and deformed pattern	105
4.2	Points M and N before and after crack propagation	106
4.3	Different position of the discontinuity respect to the pattern	107
4.4	Relation between the crack length and time for different values of α	108
4.5	KT function	109

4.6	Contour for the calculation of the J-Integral in 2D case	110
4.7	Contour for the calculation of J-integral in 3D case	111
4.8	Contour in presence of a cohesive zone	112
4.9	Contour used in Matlab algorithm	114
4.10	Main window of Matlab software developed	115
4.11	Geometry of CT-CC specimens	116
4.12	Equipment set-up during CT-CC tests	117
4.13	FEM model of CT/CC specimen	119
4.14	J-Integral for CT/CC specimens: numerical values and fitting functions.	120
4.15	Load-displacement in a CT-C-I test specimen	120
4.16	R-curves extracted from a CT-C-I specimen using FEM and DIC	121
4.17	R-curves extracted from all CT-C specimens using DIC, and corresponding mean R-curve. Each symbol corresponds to one CT test	121
4.18	Load-displacement in a CC-C-I test specimen	122
4.19	R-curves extracted from a CC specimen using FEM and DIC	123
4.20	CC-G-I specimen during the loading	124
4.21	Softening law used in the progressive damage model.	125
5.1	Components of traction on the fracture plane	128
5.2	FMC as a function of α for IM-78552 ($\sigma_{22} = -Y_C^{is}$)	131
5.3	FMC as a function of α ($\tau_{12} = S_L^{is}$)	132
5.4	FMC as a function of α ($\tau_{23} = Y_T^{is}$)	132
5.5	FMT as a function of α for different k ($\sigma_{22} = -Y_T^{is}$)	134
5.6	FMT as a function of α for IM7/8552 (quadratic criterion)	135
5.7	Puck criterion: FMT as a function of α for IM7/8552 ($\sigma_{22} = Y_T^{is}$)	138
5.8	FMT as a function of α ($\sigma_{22} = Y_T^{is}$)	140
5.9	FMT as a function of α ($\sigma_{33} = Y_T^{is}$)	141
5.10	FMT as a function of α ($\tau_{23} = Y_T^{is}$)	142
5.11	FMT as a function of α ($\tau_{12} = S_L^{is}$)	142
5.12	FMT as a function of α ($\tau_{13} = S_L^{is}$)	143
5.13	Shear stresses as a function of σ_{22}	144
5.14	τ_{12} as a function of σ_{22} for several value of the transverse stress σ_{33}	145
5.15	σ_{33} as a function of σ_{22} for different values of τ_{12}	146
5.16	σ_{33} as a function of σ_{22} for different values of τ_{13}	146
5.17	σ_{33} as a function of σ_{22} for different values of τ_{23}	147
5.18	Fiber kinking, coordinate systems	148
5.19	Stresses in the misalignment frame (2D)	150
5.20	σ_{11} - σ_{22} failure envelope for IM7/8552 carbon	153
5.21	σ_{11} - σ_{22} failure envelope for different values of transverse stress σ_{33} for IM7/8552 carbon	154
5.22	σ_{11} - τ_{12} failure envelope for IM7/8552 carbon	155

5.23	σ_{11} - τ_{12} failure envelope for different values of transverse stress σ_{33} for IM7/8552 carbon	156
5.24	τ_{12} as a function of σ_{22} for different materials and correspondent values of Y_C^{is} , η_L and S_L^{is}	157
5.25	σ_{22} - τ_{12} failure envelopes for different material	158
5.26	Off-axis compression test of IM7/8552 carbon lamina	159
5.27	σ_{11} - σ_{22} failure envelope for E-Glass/MY750 epoxy lamina	160
5.28	σ_{11} - τ_{12} failure envelope for T300/914C lamina	161
5.29	Compressive strength as function of the hydrostatic pressure	162
5.30	Shear strength as function of the hydrostatic pressure	162
6.1	FE models	170
6.2	Isometric view of DBJ model	172
6.3	Isometric view of DBJ model, detail	173
6.4	DBJ model, mesh	173
6.5	DBJ model, loading configuration	174
6.6	Bearing stress as function of the corrected displacement	176
6.7	Contour plots of the damage index of the fiber in function of the bearing stress for the bearing specimen	177
6.8	Bearing specimen after loading	177
6.9	Tensile stress as function of the corrected displacement	178
6.10	Tension specimen after loading	178
6.11	Contour plots of the damage index of the fiber in function of the bearing stress for the tension specimen	179
6.12	Shear stress as function of the corrected displacement	180
6.13	Shear specimen after loading	180
6.14	Contour plots of the damage index of the fiber in function of the bearing stress for the shear specimen	181
7.1	Design of the sub-component	184
7.2	Loading configuration	184
7.3	Equipment setup	185
7.4	V-P-4-1 specimen after loading	185
7.5	Load - displacement curve	186
7.6	Failure modes of the multi-material sub-component	186
7.7	Superposition of load cases	188
7.8	Coupled node and contour nodes considered for the submodelling.	189
7.9	Loads and pressure applied to the sub-model	189
7.10	FE model of the prototype	191
7.11	Contour plot of the Failure Index around the hole for the submodel	191
7.12	Failure Indexes as function of the applied load	192

List of Tables

3.1	Mechanical properties of metals used	30
3.2	Material properties of GF-epoxy UD laminate	31
3.3	Orientation pattern for GF-vinylester / phenolic composite	31
3.4	Mechanical properties of GF-vinylester and phenolic UD laminate	32
3.5	Strain gages technical data	33
3.6	2 ³ Factorial Design	34
3.7	Experimental plan	36
3.8	Bolts' mechanical properties and geometry	39
3.9	Washers' geometrical parameters	40
3.10	Elastic modulus of the specimens tested	42
3.11	Maximum load for E-1-I specimens	44
3.12	Maximum load for E-2-I specimens	45
3.13	Maximum load for E-3-I specimens	46
3.14	Maximum load for E-4-I specimens	47
3.15	Maximum load for V-1-I specimens	48
3.16	Maximum load for V-2-I specimens	49
3.17	Maximum load for V-3-I specimens	50
3.18	Maximum load for V-4-I specimens	51
3.19	Maximum load for P-1-I specimens	52
3.20	Maximum load for P-2-I specimens	53
3.21	Maximum load for P-3-I specimens	54
3.22	Maximum load for P-4-I specimens	55
3.23	Maximum load for DBJ specimens	56
3.24	Thickness of bearing specimens	58
3.25	Bearing response for E-4-I specimens	58
3.26	Bearing response for P-4-I specimens	59
3.27	Bearing response for V-4-I specimens	59
3.28	Maximum load for P-A-1-I specimens	63
3.29	Maximum load for P-A-2-I specimens	64
3.30	Maximum load for P-A-3-I specimens	65
3.31	Maximum load for P-A-4-I specimens	66
3.32	Maximum load for P-S-1-I specimens	67
3.33	Maximum load for P-S-2-I specimens	68

3.34	Maximum load for P-S-3-I specimens	69
3.35	Maximum load for P-S-4-I specimens	70
3.36	Maximum load for V-A-1-I specimens	71
3.37	Maximum load for V-A-2-I specimens	72
3.38	Maximum load for V-A-3-I specimens	73
3.39	Maximum load for V-A-4-I specimens	74
3.40	Maximum load for V-S-1-I specimens	75
3.41	Maximum load for V-S-2-I specimens	76
3.42	Maximum load for V-S-3-I specimens	77
3.43	Maximum load for V-S-4-I specimens	78
3.44	Maximum load for V-P-1-I specimens	79
3.45	Maximum load for V-P-2-I specimens	80
3.46	Maximum load for V-P-3-I specimens	81
3.47	Maximum load for V-P-4-I specimens	82
3.48	Bearing response for P-A-4-I specimens	83
3.49	Bearing response for P-S-4-I specimens	84
3.50	Bearing response for V-A-4-I specimens	84
3.51	Bearing response for V-S-4-I specimens	85
3.52	Bearing response for V-P-4-I specimens	85
3.53	GF-E specimens' dimensions	95
3.54	Pull-trough test, results for PT-E-6-I specimens	96
3.55	Pull-trough test, results for PT-E-10-I specimens	96
3.56	GF-P specimens' dimensions	97
3.57	Pull-trough test, results for PT-P-6-I specimens	97
3.58	Pull-trough test, results for PT-P-10-I specimens	98
3.59	GF-V specimens' dimensions	99
3.60	Pull-trough test, results for PT-V-6-I specimens	99
3.61	Pull-trough test, results for PT-V-10-I specimens	99
4.1	Parameters used in the ARAMIS-GOM software	118
4.2	Parameters for the J-integral fitting (thickness $h = 4\text{mm}$)	119
5.1	Mechanical properties of IM7/8552	144
5.2	Material properties of investigated composites	156
5.3	Material properties of investigated composites	157
5.4	Material properties of IM78552	158
5.5	Material properties of E-Glass/MY750 epoxy	159
5.6	Material properties of T300/914C	160
6.1	Nominal dimensions of the bolted joints tested.	169
6.2	First-peak load (N)	182
7.1	UD mechanical properties	184

Acronyms

2D Two-Dimensional.

3D Three-Dimensional.

AFNOR Association française de Normalisation.

ASTM American Society for Testing and Materials.

BE Bearing.

CC Compact Compression.

CFRP Carbon Fiber Reinforced Plastics.

CI Confidence interval.

CL Cleavage.

CT Compact Tension.

CV Coefficient of variation.

DBJ Double bolted joint.

SBJ Single bolted joint.

DIC Digital Image Correlation.

EADS European Aeronautic Defence and Space Company.

FNLBS First Non-Linearity Bearing Strength.

GFRP Glass Fiber Reinforced Plastics.

IPBS Initial Peak Bearing Strength.

LVDT Linear variable differential transformer.

NT Net-Tension.

OBS Offset Bearing Strength.

PT Pull trough test.

SO Shear-Out.

STDV Standard deviation.

List of Symbols

a, b, c variables in Two-Levels Factorial Design (Taguchi Method).

c_f conversion factor (DIC).

\mathbf{d} displacement of each pixel (DIC).

d hole diameter of a mechanically fastened joint.

d_{min} minimum diameter of the screw.

e edge distance of a mechanically fastened joint.

e_A, e_B, e_C main effects in Two-Levels Factorial Design (Taguchi Method).

e_{AB}, e_{AC}, e_{BC} two-factors effects in Two-Levels Factorial Design (Taguchi Method).

f discrete function of the gray level at each pixel (DIC).

f_{ub} bolt ultimate tensile strength.

h specimen thickness.

n normal at the fracture plane.

n_1, n_2 direction cosines.

n_j cubic spline interpolation functions (DIC).

t specimen thickness (bolted joint).

t_n traction vector on the fracture plane.

\mathbf{u} unknown displacements (DIC).

$\{u\}$ displacement vector.

w specimen width.

x coordinate of the pixel (DIC).

A_b gross section area of the bolt.

A, B, C main factors in Two-Levels Factorial Design (Taguchi Method).

A_s tensile stress area of the bolt.

C coefficient of correlation (DIC).

E Young's modulus.

F_i pretension force.

FI_F failure index for fiber tension.

FI_s bolt failure index for shear.

FI_{st} bolt failure index for combined presence of tension and shear.

FI_t bolt failure index for tension.

FK failure index for fiber kinking.

FMC failure index for matrix compression.

FMT failure index for matrix tension.

J J-Integral.

J_{COH} J-Integral calculated on the cohesive zone.

J_{EXT} J-Integral calculated on the external path.

J_{TIP} J-Integral calculated on the crack tip.

K factor used in pretension torque calculation under standard conditions, discrete function (DIC).

\bar{K} average value of K function (DIC).

K_{sb} shear stress concentration factor.

K_T threshold function (DIC).

K_{tb} tensile stress concentration factor.

L support span in three-point bending test.

M surface of reference pattern (DIC).

$[\mathbf{M}]$ matrix of cubic spline interpolation functions (DIC).

P load.

P_{bp} by-pass load.

P_p load reacted at the hole.

P_u load.

S_b bearing stress.

S_{bp} by-pass stress.

S_L longitudinal shear strength.

S_T transversal shear strength.

T pre-tension torque.

$\{T\}$ traction vector.

W strain energy density.

X_C longitudinal compressive strength.

X_T longitudinal tensile strength.

Y_C transverse compressive strength.

Y_T transverse tensile strength.

Greek Letters

α angle of fracture plane.

α_T threshold value (DIC).

β shear factor.

β_b ratio between bearing stress and by-pass stress.

δ displacement of the testing machine.

δ_{LVDT} displacement of the LVDT.

ε strain.

ε_R strain at rupture.

$\{\varepsilon\}$ strain vector.

η_L slope in the σ_N - τ_L diagram.

η_T slope in the σ_N - τ_T diagram.

ν Poisson's ratio.

ω angle between the shear stress τ_T and τ .

ρ density.

σ stress.

σ_i^{br} bearing stress.

σ_{ii} direct component of the stress tensor.

σ_N component of the traction normal to the fracture plane.

σ_{rr} radial stress.

$|\sigma|$ stress tensor.

$\sigma_{\theta\theta}$ hoop stress.

$\{\sigma\}$ stress vector.

σ_{xy} shear stress.

σ_y yield stress.

τ_{ij} shear component of the stress tensor.

τ_L component of the traction of the fracture plane in L direction.

τ_T component of the traction of the fracture plane in T direction.

Γ contour for the calculation of J Integral in 2D.

Ω contour for the calculation of J Integral in 3D.

Acknowledgments

The author would acknowledge his supervisors, prof. Pedro P. Camanho and prof. Antonio T. Marques from FEUP, and Mr. Pascal Ghys from Alstom Transport for their constant guidance, advice, understanding and support during the last three years.

The financial support of the European Commission under Contract No. MRTN-CT-2005-019198 is acknowledged. In particular the author would acknowledge dr. Roberto Palacin, coordinator of the Momentum project and all the other people involved.

The author would acknowledge dr. Giuseppe Pitarresi and dr. Davide Tumino from University of Palermo for their encouragement and interest shown in his work.

The author would acknowledge all the people that he met and that worked with him during his Phd and in particular Dr. Albert Turon, Emili González, Hannes Koerber, Dr. Jose Xavier, prof. Francisco Pires and dr. Carlos Dávila. Collaborations and discussions with them were always productive and useful.

The author would acknowledge Julien Sillani and his fantastic family for their friendship, helpfulness and to have made his experience in France delightful.

Finally the author would acknowledge his family. Their love and continuous encouragement was the most important thing he has had every day.

Chapter 1

Introduction

Composite materials are widely used in the industry because of their superior specific characteristics. They are light and stiff, and composite structures are easy to manufacture and assemble.

Nowadays, however, the use of composites as main load-carrying structures is often limited to the aerospace and automotive industries. While it is possible to find in the railway industry some examples of the use of composites as main load-carrying structures, this is limited to a few cases or to particular applications. In the railway industry, composites are limited to non structural parts (cab, skirts, interiors, etc.). This is justified by the fact that the use of composite requires a know-how that the railway industry does not currently have, and for this reason metals are preferred.

However, the use of composites is a vital issue for the railway industry. In fact, their advantages are numerous, namely:

- the reduction of the weight and, consequently, of the energy necessary for the railway transportation;
- the reduction of the cost of manufacturing: if a correct design is performed it is possible to obtain a simplification of the parts that form a structure and, consequently, a reduction of the time and of the costs required for the assembly of the final structure;
- the reduction of the recurring costs, because composite structures require generally less maintenance when compared with metallic structures.

Comparing the different design solutions of the main structure of a train, namely, the use of only metals, the use of only composites, the use of metals and composites (hybrid solution), it is possible to shown [1] that for a train structure the hybrid solution yields the lowest manufacturing cost. Similarly to other composite structures, one of the main design drivers in hybrid structures is the calculation of the

strength and the behavior of the hybrid joints. In fact, the prediction of the stiffness of hybrid structures is straightforward, and the main challenge in the design of such of structures is the prediction of failure, which typically occurs at stress concentrations, such as bolted joints.

Therefore, the main objectives of this work are to investigate the mechanical response of mechanically fastened joints in composite materials and to define design methods for such joints with different levels of refinement, ranging from full three-dimensional Finite Element models to simple analysis models that can provide a solution in a short amount of time.

The thesis is organized as follows.

Chapter 2 presents a literature review on composite bolted joints including both experimental investigations and analysis models.

In Chapter 3, an experimental campaign conducted on bolted joints with different geometries and materials (or material combinations) is presented. These results may form an integral part of the design process.

Chapter 4 presents a new methodology to obtain the material properties that are required for the numerical simulation of fracture of composite joints.

In Chapter 5, a three-dimensional (3D) numerical model to predict failure of composite material is proposed. The numerical model includes, new, fully three-dimensional failure criteria and the associated damage model that represent the propagation of the different failure mechanism.

In Chapter 6, the proposed progressive damage model is used to predict different failure modes in composite bolted joints. The numerical results are compared with experimental data previously obtained.

The computational cost of a three-dimensional analysis is not suitable for an industrial use, where results must be obtained in a short account of time. For this reason, in Chapter 7 a two-dimensional numerical model is used to compute the onset of the damage. The two-dimensional numerical model implement locally a two-dimensional version of the failure criteria presented in Chapter 5. Finally, a real industrial case is studied. A prototype was manufactured and tested and the corresponding experimental results are compared with the numerical predictions.

Chapter 2

Literature Review

2.1 Experimental Analysis

The experimental research on composite bolted joints typically consists in the determination of the geometric and material parameters that affect the joint strength. Generally, two procedures are followed:

- the joint is tested until its final failure varying the parameter under study;
- the stress distribution in the vicinity of the hole is investigated.

2.1.1 Failure Modes

Figure 2.1 shows the classical geometry of the specimen and the geometrical parameters that influence its behavior:

- the width of the specimen (w);
- the end distance (e);
- the diameter of the hole (d);
- the thickness of the specimen (t).

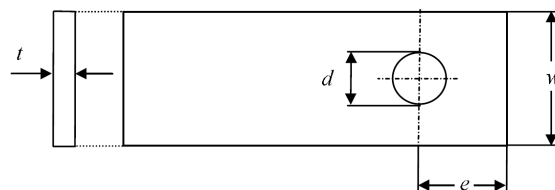


Figure 2.1: Geometry of the specimen [2].

The ASTM D 5961/D 5961 M-05 [3] norm reports five common in plane failure modes:

- the lateral or net-tension failure mode;
- the shear-out failure mode;
- the bearing failure mode;
- the tear-out failure mode;
- the cleavage failure mode.

The pull-trough failure mode is an out-of-plane failure mode that must be also considered. All these failure modes identified in ASTM D 5961/D 5961M-05 [3] are shown in Figure 2.2. The joints may also fail in a combination of different failure modes.

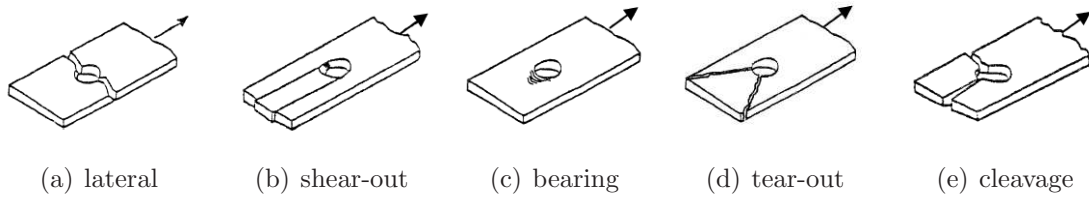


Figure 2.2: Bearing test failure modes for ASTM D 5961/D 5961M-05 [3].

If the tear-out and the cleavage failure modes are considered particular cases of the shear-out failure mode, then the principal in plane failure modes are the net-tension, the shear-out and the bearing planes. These planes are represented in Figure 2.3. The circumferential coordinate direction, θ , and the fibre orientation angle, α are also represented.

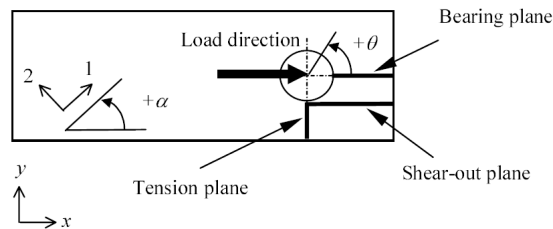


Figure 2.3: Definition of planes, θ and α [2].

The definitions of these planes allow the definition of the following ultimate stress:

- the ultimate bearing strength

$$\sigma_{b(u)} = \frac{P_u}{dt} \quad (2.1)$$

- the ultimate tensile strength

$$\sigma_{n(u)} = \frac{P_u}{(w-d)t} \quad (2.2)$$

- the ultimate shear strength

$$\sigma_{xy(u)} = \frac{P_u}{2et} \quad (2.3)$$

where P_u is the peak (failure) load, w the width, e the end distance, d the hole diameter and t the specimen thickness (see Figure 2.1).

2.1.2 Influence of the geometry

The importance of width (w), end-distance (e), bolt diameter (d) and laminates thickness (t) was highlighted by several authors [4–9]. Hart-Smith [4] highlighted the importance of the d/w ratio on the joint failure modes. When the diameter is large compared with the width of the specimen net-tension failure modes occurs. The critical value of the d/w ratio that defines the change in the failure modes from net-tension to bearing depends on the material and on the lay-up used. Kretsis and Matthews [5] showed that the transition from bearing to net-tension reduces the load capacity of the joint as showed in Figure 2.4(a). The authors identified a similar trend in the shear-out and bearing failure modes when e/w ratio varies, as shown in Figure 2.4(b).

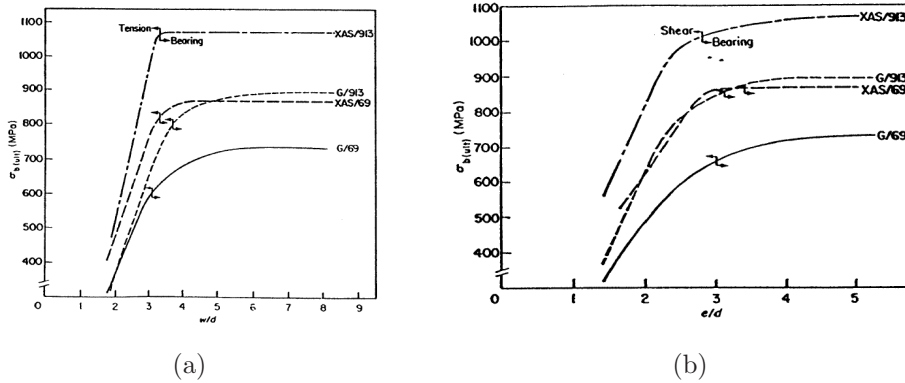


Figure 2.4: Variation of bearing strength of (0/±45) laminates [5].

Collings [6] investigated CFRP specimens with different lay-ups and hole-sizes. The author showed that the critical values of w/d and e/d depend on the lay-up

used. The author highlighted that no thickness effects on the bearing strength are noticed if a clamping pressure of 22MPa is applied on the washer.

Hart-Smith [4, 7] showed that when the ratio d/w decreases the joint structural efficient increases until an optimum value. Moreover, the author demonstrated that when the load is larger than a critical value delamination occurs near the edge of the hole and this reduces the value of the stress concentration factor. Hart-Smith [4, 7] considered that a small value of the e/d ratio increases the tensile stress concentration factor. He suggested, then, the use a minimum end distance equal to $3d$.

Hodgkinson *et al.* [9] tested several types of joints in Kevlar fibre-reinforced plastics (KFRP). Like in CFRP and GFRP, small values of e/d ratio caused shear-out failures, large values resulted in tensile failures.

2.1.3 Influence of the fiber orientation

Collings [6] tested CFRP laminates with $[0/\pm\alpha]_S$ lay-up. He observed that for these laminates the bearing strength was dependent on the ratio between 0° plies and $\pm\alpha^\circ$ plies and, that the effect of these plies was dependent on the type of failure.

Collings [10] studied CFRP balanced laminates with $[0/\pm45]_S$ and $[90/\pm45]_S$ lay-ups. It was observed that the presence of $\pm45^\circ$ plies increases the bearing strength of the laminate until these plies are approximately 75% of the total laminate thickness.

Kretsis and Matthews [5] showed that lay-up influences the strength and failure mode of GFRP joints and that the critical values of w/d and e/d depend on the lay-up used.

Hart-Smith [4, 7] showed that for laminates rich in 0° and lacking of 90° or with 50% of 0° plies and 50% of $\pm45^\circ$ plies, shear-out failure mode occurs. The author demonstrated that bearing strength is maximum for quasi-isotropic laminates.

2.1.4 Influence of lateral constraint

Collings [6] showed that the bearing strength of CFRP joints increases when clamping pressure increases until a maximum of 22MPa. At higher clamping pressures, negligible improvements are noticed. Obviously, clamping pressure has to be limited to avoid failure in the clamped region.

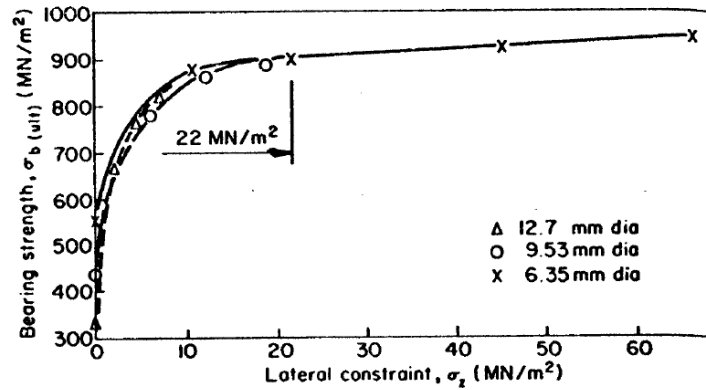


Figure 2.5: Effect of lateral constraint on bearing strength [6].

Kretsis and Matthews [5] also demonstrated the beneficial effect of lateral pressure on GFRP joints. They explained that the clamping pressure reduces the propagation of the cracks that develop under the washer.

Matthews *et al.* [7] considered that the joint strength depends on the through-thickness restraint offered by the fastener. For these reasons a pin loaded specimen gives the lowest bearing strength while bolted joints gives the highest bearing strength.

Hart-Smith [4, 7] concluded that the clamped area has a significant influence on the joint strength. The author noticed that inner laps gives higher values of the bearing strength with respect to the other laps. This occurs because the inner lap is better constrained and because the clamped area is larger.

2.1.5 Influence of the stacking sequence

Quinn and Matthews [11] noticed that the joint strength depends on the stacking sequence used: the through-thickness direct and shear stresses at the hole edge depends on the stacking sequence and these influence the joint strength. Placing 90° plies at the surface of the laminate produces a compressive through thickness direct stress that inhibits the delamination and that increases the joint strength.

Collings [6] also showed that interlaminar shear stress can produce delamination at the hole edge and reduce the joint strength. Large variations in fiber orientation angles in consecutive plies are responsible for higher shear stress, and this fact reduces the strength of the joint.

2.1.6 Influence of the fastener type

Different choices can be made when composite materials have to be joined. Fastener typically used are screws, rivets and bolts. However the correct choice of the fastener is a function of the particular application. Moreover, all fasteners used for metallic joints cannot be used with composites. For this reason it is possible to find very specialized fasteners for particular applications.

Collings [12] noticed that self-tapping screws are easy to install but reduce the joint efficiency. A solution is to use helicoil metallic inserts to avoid thread stripping.

Hart-Smith [4] show that the use of countersunk fasteners reduce the efficiency of the joint if compared with bolts.

Cole *et al.* [13] highlighted that galvanic corrosion is one of the biggest problem if wrong material are chosen. The authors presented a compatibility chart showing that titanium (and its alloys) is the best choice for CFRP laminates. To reduce the damage during the installation Cole *et al.* [13] suggested to use fasteners with larger countersunk angles and enlarged footprints.

2.1.7 Influence of metallic inserts

Several authors [14–17] proposed the use of bonded metallic insert to prevent the damage of the hole due to repeated installations or due to the high stress that occurs at the hole edge.

Nilsson [15] compared the strengths of bolted joints in the presence and in the absence of metallic inserts. The authors highlighted that the introduction of the insert reduces the ratios d/w and d/e and this changes the failure mode of the joint. The use of metallic inserts can then either increase or decrease the bearing strength of the joint.

Mirabella [16] performed experimental tests on single-lap CFRP laminates with different insert's configurations: the single and double straight, the top-hat and the top-hat with tapered ends (See Figure 2.6).

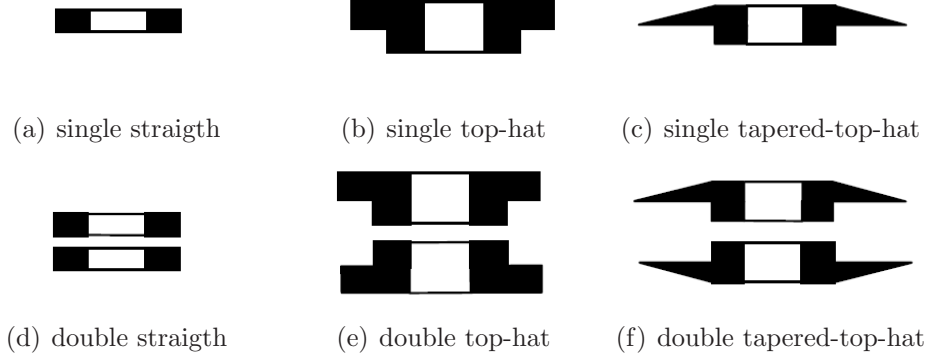


Figure 2.6: Inserts' geometry [16].

It was shown that strength and failure mode depends on the material and on the type of the insert used. Moreover, when compared with the specimens without insert, the use of the insert may change the failure mode and the strength of the joints.

2.1.8 Hybrid laminates

The use of carbon-glass hybrid laminates in mechanically fastened joints has been investigated by several authors [4, 18, 19].

Hart-Smith [4] showed that the inclusion of glass fibre softening strips near the loaded hole improved the net-tension strength of carbon fibre-reinforced laminates.

Matthews *et al.* [18] investigated hybrid carbon/glass laminates with different lay-ups. It was shown that the trend of the strength versus the w/d and e/d ratios is similar to that one exhibited by homogeneous laminates. The maximum strength is achieved when w/d and e/d are greater than 4. For high values of e/d and w/d (bearing failure mode) the full carbon laminate shows the highest values of the strength. For small value of w/d , net-tension failure mode occurs and the hybrid laminate exhibit an higher value of the strength when compared with the full carbon joint. This result was confirmed by Hart-Smith [4].

Oh *et al.* [19] investigated the effects of clamping pressure and stacking sequence on hybrid joints. It was shown that the bearing strength increases with increasing clamping pressures up to 71MPa. It was found also that $[0C/\pm 45G/\pm 45C/90C]_S$ (C:carbon; G:glass) laminates exhibit the higher value of the bearing strength when $\pm 45^\circ G$ plies were located between the $90^\circ C$ and $\pm 45^\circ C$ plies.

2.1.9 Multi fastener joints

In practical applications, several fasteners are used to connect composite laminates. For sufficiently large pitches, the interaction with other bolts is negligible and it is possible to estimate the strength and the failure mode of the joint using single-fastener joint data [6]. If small pitches are used interaction may occur and the strength of the multi-fastener joint is lower than that estimated using single-fastener joint data [8].

Godwin *et al.* [20] tested multi-bolts joints in GFRP. Lines (parallel to the load) and rows (perpendicular to the load) of bolts were considered. It was found that if the pitch is higher than 6 diameters bearing failure occurs.

When the pitch is equal to 2.5 diameters and the end-distance is 5 diameter the strength is maximized. Net-tension failure (catastrophic) occurs and this corresponds to an increase of 17% of the joint efficiency.

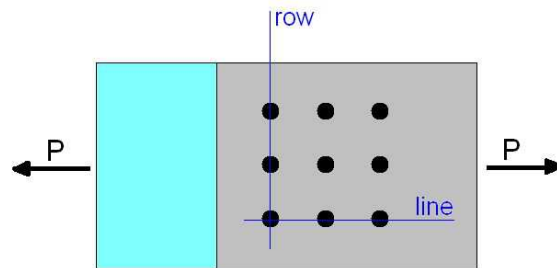


Figure 2.7: Bolts installed in rows and lines.

Hart-Smith [4,7] highlighted that the improvements in efficiency of multi-fasteners joints is negligible with respect to single-fastener joints. To increase the strength of the joint above the maximum strength of a single-fastener joint, the bearing stress of the multi-fastener joint should be reduced and this is possible only if large p_i/d are used. The author concluded that using more bolts in line increases negligibly the strength of the joint (two bolt increase the strength of about 10%, eight or ten bolts 25%) and that the strongest joint has only one row of bolts. In practical applications, multirow joints are used for stability in compression.

2.1.10 Stress distribution

A few experimental studies have also been made in order to determine experimentally the stress distribution near a loaded hole.

Hyer and Liu [21] used the photoelastic technique in transparent glass-epoxy plates. The radial and hoop stresses around the hole, the shear stresses in the

shear-out section, the net-section tensile stresses and the compressive stresses in the bearing plane were found.

Using the photoelastic technique, Prabhakaran [22] studied the effect of e on the stress distribution in a pin-loaded hole. GFRP specimens with e/d equal to 2, 4 and 6 were considered. It was found that the highest shear stress near the hole occurs in the specimen with the smallest end distance as previously indicated in the work of other authors [4, 5].

2.1.11 Fatigue

Many authors considered that a joint designed for a static test satisfies the fatigue design. Hart-Smith [7] showed that composite bolted joints do not show any damage under fatigue load. On the contrary, if interference fits are used, the residual stress may slightly increase due to the relief of stress concentration at the hole edge caused by sub-critical damage. If clearance fits are used, fretting fatigue damage may occur at the bolt-composite contact surface.

Collings [12] showed that after a fatigue test the hole show an elongation that could up to 5% of the hole diameter. The author suggested to use the maximum elongation as a criterion of bolted joints under fatigue load.

Crews [23] also tested CFRP bearing joints after water absorption. It was shown that water can reduce fatigue life up to 40%. The author concluded that care should be taken when designing bolted joints for wet environments.

Smith and Pascoe [24] and Herrington and Sabbaghian [25] showed that increasing the clamping pressure results in an increase of the fatigue life and in a reduction of the hole elongation.

2.2 Stress analysis

An accurate stress analysis is required for the prediction of the joint strength. Both classical and numerical methods of stress analysis are present in the literature.

2.2.1 Classical methods of stress analysis

T. de Jong [26] obtained the stress distribution around the hole of a pinned frictionless joint. The analysis was based on the complex function method proposed by Muskhelishvili [27] and his adaptation to orthotropic materials proposed by Lekhnitskii [28]. The authors considered unidirectional, quasi-isotropic and $[0_s/\pm 45]_s$ CFRP laminates with different geometries ($w/d = 2.5, 5, \infty$). The author showed

that the stress distribution at the hole boundary is highly dependent on the lay-up and geometry used.

Zhang and Ueng [29] proposed a way to calculate the direct and the shear stress using Lekhnitskii's [28] method. Considering infinite dimensions, the stress distributions were found for several lay-ups. Figure 2.8 shows the stress distributions at the hole boundary of a $[0_4/\pm 45]_s$ laminate. It was highlighted that these stress distributions were dependent on the lay-up and on the coefficient of friction.

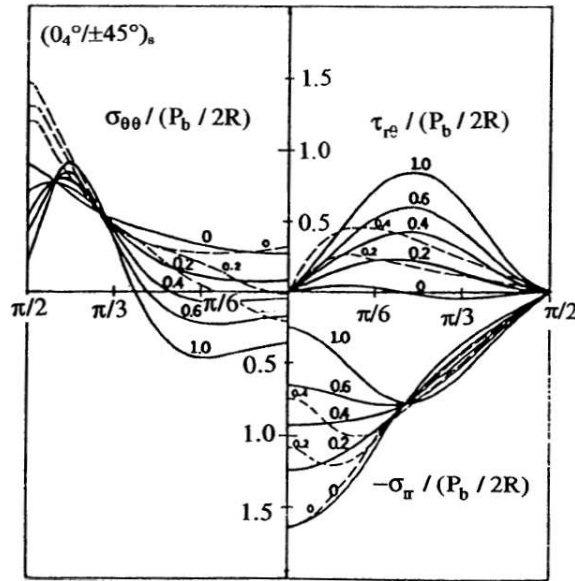


Figure 2.8: Stress distributions around a pin-loaded hole in a $[0_4/\pm 45]_s$ laminate for several coefficients of friction [29].

2.2.2 Numerical methods of stress analysis

2.2.2.1 Two-dimensional models

Several authors [30–38] developed 2D models to find the stress distribution around the hole of a loaded laminate. Since these models usually assumed a plane stress state and used the classical lamination theory [39], they cannot account for the effects of stacking sequence or clamping pressure. The contact angle ϕ of the pin with the hole boundary was sometimes considered constant [30], or, more realistically, varying non-linearly with the load [31–38, 40].

Naik and Crews [31] studied the effect of clearance in a frictionless pinned laminate. As expected, the contact angle varies with the clearance as shown in Figure 2.9(a) where c_d is the diametral clearance. It can be concluded that increasing the clearance decreases the contact angle. Figure 2.9(b) reports, for a bearing stress of 475 MPa, the distributions of radial and hoop stresses.

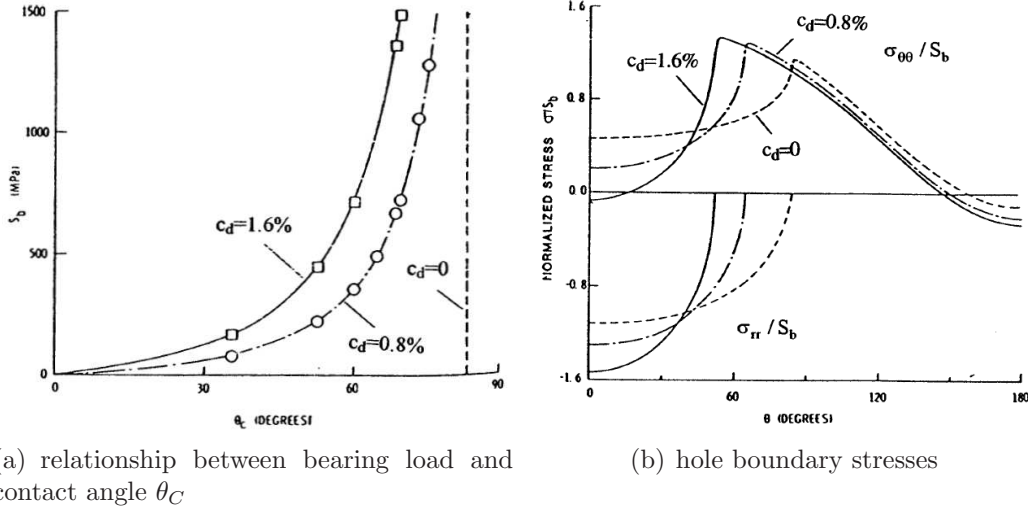


Figure 2.9: Effects of clearance [31].

Crews *et al.* [34] considered six lay-ups $[0/\pm 45/90]_s$, $[0]$, $[90]$, $[0/90]_s$, $[\pm 45]_s$ and $[0/\pm 45]_s$, assumed a frictionless contact and no clearance. The distributions of the hoop stress, $\sigma_{\theta\theta}$, the radial stress, σ_{rr} , and the shear stress, σ_{xy} , were found. As these stress are related with tension, bearing and shear-out failure respectively, the tensile stress concentration factor K_{tb} and the shear stress concentration factor K_{sb} , were defined:

$$K_{tb} = \frac{(\sigma_{\theta\theta})_{Max}}{S_b} \quad (2.4)$$

$$K_{sb} = \frac{(\sigma_{xy})_{Max}}{S_b} \quad (2.5)$$

where S_b is the bearing stress. Figure 2.10(a) shows that, for a constant value of end distance, K_{tb} increases with decreasing w/d while Figures 2.10(b)-2.10(c), show that both K_{tb} and K_{sb} increase with decreasing e/d .

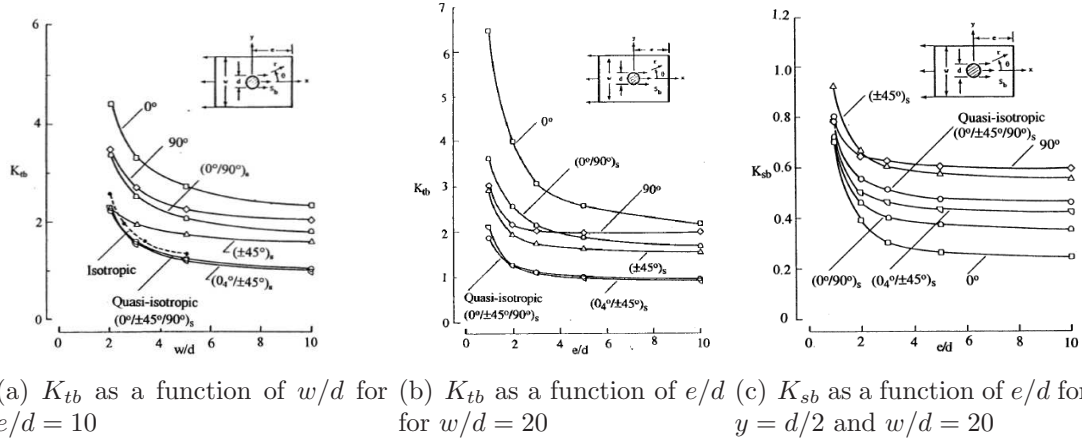


Figure 2.10: Effects of w/d and e/d on stress concentration factor [34].

2.2.2.2 Three-dimensional models

Unfortunately, simple 2D analysis cannot take into account for the through-thickness effects that have an important effect on the joint strength. In order to have better predictions on joints strength, 3D model have developed by several authors [40–47]. The use of three-dimensional models allows to study the influence of the friction, geometry, clearance and through-thickness effect; unfortunately they are computationally expensive and require a severe modeling effort.

2.2.2.3 Multi-fastener joints

The numerical investigations of stress distributions in multi-fastener joints found in the literature were based on two-dimensional finite element models. Both lines [48] (parallel to the load) or rows [49–51] (perpendicular to the load) of fasteners have been considered.

Naik and Crews [51] investigated the stress distribution of a frictionless multi-row pinned joint [51] using an inverse technique previously developed [31]. The coefficient β_b was defined as:

$$\beta_b = \frac{S_b}{S_{bp}} \quad (2.6)$$

where S_b and S_{bp} are the bearing stress and the by-pass stress respectively and are defined as:

$$S_b = \frac{P_b}{dt} \quad (2.7)$$

$$S_{bp} = \frac{P_{bp}}{(w-d)t} \quad (2.8)$$

where P_b and P_{bp} are respectively the load reacted at the hole and the by-pass load. It was highlighted that, for a constant bearing stress, β_b has a substantial influence on the contact angle and peak stress at the hole boundary: when β_b decreases the contact angle ϕ increases. If a tensile by-pass load is applied, increasing S_{bp} the hoop stress significantly increases and its peak is located near the contact region. If a compressive by-pass load is applied, increasing $|S_{np}|$ the peak value of the hoop stress becomes compressive.

2.2.3 Strength prediction methods

The joint strength depends on the definition of the failure: the maximum load supported by the joint, the maximum elongation of the hole [52], the first peak, the first non linearity in the load vs. displacement plot [3] and the load at which crack onset occurs [53].

2.2.3.1 Failure Theories

Several authors [54–57] used the peak local stress on the boundary and a failure theory to predict the laminate strength.

Waszczak and Cruse [54] defined a criterion using the peak stress, the peak strain and the distortional energy. Hart-Smith [4] noticed that the use of these failure theories gives a conservative prediction because the real value of stress at the hole boundary is lower than the elastic one. This is due to the *hole size effect* (the strength decreases for larger holes). As noticed by Crews [58] and Whitney and Nuismer [59], small holes are interested by high stresses in small regions. The localized damage reduces the stresses and redistribute the load. This effect is less pronounced for large holes.

2.2.3.2 Two-parameter methods

The parameters considered by these methods are the unnotched tensile strength and a characteristic dimension. Two methods are used: the point stress and the average stress method that compare the strength of the unnotched material with the direct stress and the average stress respectively.

Agarwal [60] proposed to modify the average stress criterion. In case of tension failure the stress (normal to the applied load) is averaged over a distance a_{0t} along the lines AB as shown in Figure 2.11.

Tension failure occurs when the averaged stress over a distance a_{0t} (assumed equal to 0.229 cm) along AB , $A'B'$ and $A''B''$ reached the laminate tensile strength in the direction tangent to the point A , A' , A'' respectively. The same procedure was used to predict bearing failure (the average stress was calculated over a_{0c} , assumed

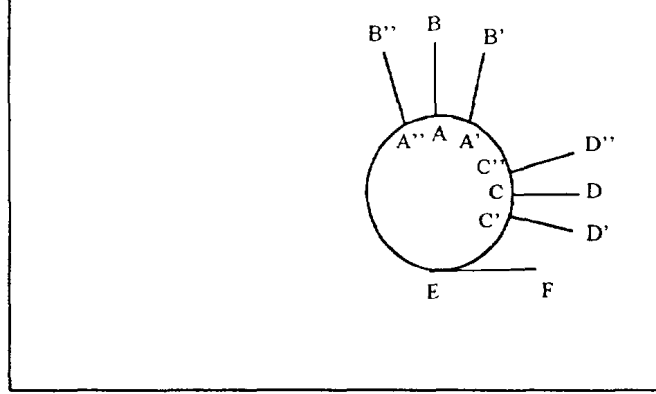


Figure 2.11: Definition of characteristic lengths [60].

equal to 0.622 cm) along CD , $C'D'$ and $C''D''$ and shear-out failure (average shear stress along EF assuming a_{0s} equal to 1.143 cm). It was concluded that the accuracy of the method depends on the laminate lay-up.

Wilson and Pipes [61] proposed a point stress criterion to study the influence of e/d and w/d on the shear-out strength. The stress distribution on the shear plane was obtained using a FE model. The characteristic distance was assumed:

$$d_{0s} = \frac{1}{c^*} \left(\frac{R}{R_0} \right)^{m^*} \quad (2.9)$$

where R is the hole radius, R_0 a reference radius and c^* and m^* two parameters experimentally obtained.

For a $[45/0/-45/0_2/-45/0/45/0_2/90]_s$ laminate, good agreement was found between predicted shear-out strength and experimental results obtained for three fastener sizes.

2.2.4 Combined methods

Combined methods use a combination of a characteristic distance [59] and a failure theory and were used by several authors [62–67].

Chang *et al.* [62] used the Yamada-Sun [68] failure criterion together with a proposed characteristic curve in a 2D FE model.

The Yamada-Sun [68] failure criterion is expressed as:

$$\left(\frac{\sigma_{11}}{X} \right)^2 + \left(\frac{\sigma_{12}}{S_c} \right)^2 = e_f^2 \quad (2.10)$$

where σ_{11} and σ_{12} are respectively the longitudinal and shear stress in a ply, X is the ply longitudinal strength and S_c the ply shear strength measured from a cross-ply laminate. Failure occurs when $e_f \geq 1$. The characteristic curve represented in Figure 2.12 was defined as:

$$r_c(\theta) = \frac{d}{2} + d_{0t} + (d_{0c} + d_{0t}) \cos \theta \quad (2.11)$$

d_{0t} and d_{0c} are the characteristic dimensions for tension and compression, respectively. Both parameters were obtained experimentally.

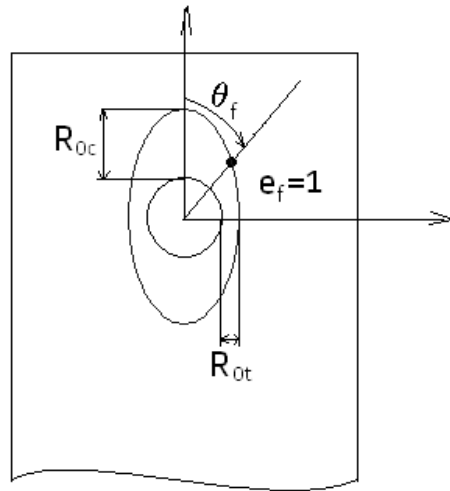


Figure 2.12: Characteristic curve [62].

Chang *et al.* [67] used a previous work [62] to account for the non-linear shear stress-shear strain relation in the Yamada-Sun [68] criterion. Hahn and Tsai [69] formula was used:

$$\gamma_{xy} = \left(\frac{1}{G_{xy}} \right) \sigma_{xy} + \alpha_1 \sigma_{xy}^3 \quad (2.12)$$

where α_1 is an empirical constant. It was shown that for cross-ply and angle-ply laminates predictions agreed well with experimental data.

2.2.5 Progressive damage models

Progressive damage models try to simulate damage initiation and growth using degradation models that are function of the type of damage predicted [70–89].

The progressive damage model developed by Chang and Chang [70] is able to predict tensile and shear-out failures of notched laminates [71]. Four different damage mechanisms were considered: matrix cracking, fibre-matrix shearing, fibre fracture and matrix compressive failure. Matrix cracking was predicted using the Yamada-Sun failure criterion [68]:

$$\left(\frac{\sigma_{22}}{Y}\right)^2 + \frac{\frac{\sigma_{12}^2}{2G_{12}} + \frac{3\alpha_1\sigma_{12}^4}{4}}{\frac{S_c^2}{2G_{12}} + \frac{3\alpha_1 S_c^4}{4}} = e_f^2 \quad (2.13)$$

where Y is the transverse tensile strength of a ply. When at one position in any of the plies in a laminate e_f is equal to or greater than 1, matrix cracking is assumed to occur in that position and layer. Both fibre-matrix shearing failure and fibre fracture were predicted using the Yamada-Sun [68] criterion:

$$\left(\frac{\sigma_{11}}{X}\right)^2 + \frac{\frac{\sigma_{12}^2}{2G_{12}} + \frac{3\alpha_1\sigma_{12}^4}{4}}{\frac{S_c^2}{2G_{12}} + \frac{3\alpha_1 S_c^4}{4}} = e_f^2 \quad (2.14)$$

where X is the longitudinal tensile strength of a ply. Matrix compressive failure was predicted using the Hashin failure criterion [90]:

$$\left[\left(\frac{Y_c}{2S_c}\right)^2 - 1\right] \frac{\sigma_{22}}{Y_c} + \left(\frac{\sigma_{22}}{2S_c}\right)^2 + \frac{\frac{\sigma_{12}^2}{2G_{12}} + \frac{3\alpha_1\sigma_{12}^4}{4}}{\frac{S_c^2}{2G_{12}} + \frac{3\alpha_1 S_c^4}{4}} = e_f^2 \quad (2.15)$$

The material properties are modified when damage occurs, and this depends upon the failure mechanisms. When matrix failure occurs is assumed that $E_{22}, \nu_{21} = 0$. If fiber failure occurs $E_{22}, \nu_{21} = 0$ and the longitudinal modulus E_{11} and the shear modulus G_{12} vary following a Weibull distribution:

$$\frac{E_{11}^d}{E_{11}} = \exp \left[- \left(\frac{A}{\delta_f^2} \right)^{\beta_1^*} \right] \quad (2.16)$$

$$\frac{G_{12}^d}{G_{12}} = \exp \left[- \left(\frac{A}{\delta_f^2} \right)^{\beta_1^*} \right] \quad (2.17)$$

where E_{11}^d and G_{12}^d are the reduced moduli, δ_f is the fibre failure interaction zone [91], A is the damage zone predicted by the failure criterion and β_1^* is the shape of the Weibull distribution for the property degradation. Once damage propagated across the laminate, total failure was assumed to occur. It was shown that for a large number of laminate configurations and geometries the error was less than 20%. In other work [74,75], the effect of matrix cracking on the elastic properties was modeled

taking into account the analysis of cracked lamina and not assuming simply that $E_{22}, \nu_{21} = 0$.

Lessard and Shokrieh [84] used 2D linear and non-linear models to predict the strength of pin-loaded holes. Matrix tensile and compressive failure, fibre-matrix shearing and fibre tensile failure were considered and predicted using the Hashin [90] failure criterion:

$$\left(\frac{\sigma_{11}}{X_c}\right)^2 > 1, \quad \sigma_{11} < 0 \quad (2.18)$$

where X_c is the longitudinal compressive strength. Once again, when matrix failure occurs it is assumed that E_{22}, ν_{21} become equal to zero while if fibre-matrix shearing occurs is assumed that $\nu_{12}, \nu_{21}, G_{12}$ are zero. In case of fiber failure all elastic parameters are assumed to be equal to 0. It was shown that for several combinations of e/d and w/d the model was able to predict the strength and the failure modes of a $[0/\pm 45/90]_s$ CFRP laminate. The non-linear model was based on Chang and Lessard [72] work, and resulted in an improved prediction of the bearing failure load.

Chen *et al.* [41] proposed a 3D model capable of predicting delamination onset based on the Ye [92] delamination criterion. The criterion takes the form:

$$\left(\frac{\bar{\sigma}_{33}}{Z_{33}}\right)^2 + \left(\frac{\bar{\sigma}_{31}}{Z_{31}}\right)^2 + \left(\frac{\bar{\sigma}_{23}}{Z_{23}}\right)^2 \geq 1, \quad \bar{\sigma}_{33} > 0 \quad (2.19)$$

$$\left(\frac{\bar{\sigma}_{31}}{Z_{31}}\right)^2 + \left(\frac{\bar{\sigma}_{23}}{Z_{23}}\right)^2 \geq 1, \quad \bar{\sigma}_{33} \leq 0 \quad (2.20)$$

For $[0_6/90_6]_s$ and $[90_6/0_6]_s$ laminates it was concluded that increasing friction decreased the delamination onset region at the bearing plane, but enlarged the delamination onset region along the other zones of contact. Different delamination onset regions were obtained for different lay-ups.

2.2.6 Application to multi-fastener joints

Many authors used the strength prediction methods previously described to predict the strength of multi-holes joints [93–95].

Naik and Crews [56, 57] studied the effects of the bearing stress and of bypass stress ratio, β (see equations (2.6-2.8)) on a single fastener of a multi-fastener joint. The bearing-by-pass diagram for a $[0/45/90/-45]_{2s}$ CFRP laminate is shown in Figure 2.13.

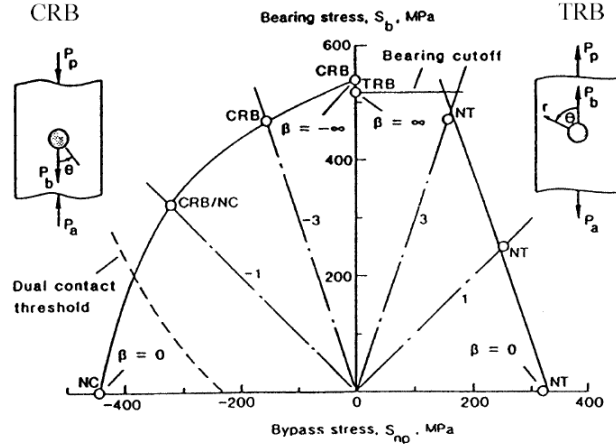


Figure 2.13: Bearing-by-pass diagram for damage onset strength [56].

where \circ represents measured bearing stress S_b and by-pass stress S_{np} values at which damage occurs and NT, TRB, NC, CRB indicate the failure mode: net-section tension, tension reacted bearing, net-section compression and compression reacted bearing respectively. The authors highlighted that for by-pass loading ($\beta_b = 0$) the specimens failed soon after damage onset, while for bearing loading ($\beta_b = \pm\infty$) the specimens failed at a higher load respect to the damage onset load.

2.3 Relaxation in composite joints

The viscoelastic behavior of composites has to be considered during the design of a joint, especially for severe environmental conditions. In fact, creep and relaxation effects are amplified if high temperatures or moisture are present. Viscoelastic effects mainly influence the matrix-dominated properties: for a composite joint, relaxation modifies the value of the preload, and therefore the capacity to support a given load.

2.3.1 Experimental studies

Shivakumar and Crews [96, 97] investigated the clamp-up relaxation in T300/5208 laminates. Three environment's temperature were investigated: the room-temperature dry (RTD), the room-temperature ambient (RTA, specific humidity SH=0.46%), the elevated temperature (66°C) dry (ETD). A torque of 5.65 Nm was applied to double-shear bolted joints and the specimens were kept at the chosen environment conditions for 100 days. Specimens showed a relaxation of 12% for RTD and EDT and of 14% for RTA conditions.

Horn and Schmitt [98, 99] studied the effect of fastener type and torque on clamping relaxation of carbon-fiber single-bolted joint. Titanium bolts were installed with torques of 6.8 and 11.3 Nm. It was shown that after 1000 hours all the specimens

showed a relaxation between 3.8% and 19.3%. To investigate the effect of the bolt's relaxation on the bearing strength, the joints were tested before and after ageing: it was shown that the influence of relaxation on the bearing strength is negligible.

Thoppul *et al.* [100] performed a comprehensive study on the effects of various bolt pre-loads, viscoelasticity and external applied static and dynamic loads on bolt load relaxation in carbon/epoxy bolted joints. Four levels of preload were selected: 4200 N, 5050 N, 6700 N and 7850 N that correspond to 12.5%, 15%, 20% and 23.5% of the maximum tensile load. The joint were tested in a 3-point bending test to study the combined effect of shear and bending. After applying an initial preload to the composite bolted joint, the bolt load was monitored for a period of 30 h for the following cases:

- bolt preload in the absence of external beam load;
- bolt preload plus a static applied load of 250 N at the beam midspan;
- bolt preload plus a dynamic load of 250 N amplitude and frequencies of 1 Hz and 5 Hz at the beam midspan.

It was shown that, depending on the external load, in 30 hours the relaxation is 1.25-4.25%. It was also shown that increasing the preload decreases the relaxation and it is concluded that a sufficiently high preload should be provided. Comparing the bolt relaxation in steel and in composite joint it is possible to conclude that only 1/3 of the relaxation in composite joints is justified by the viscoelastic behavior of the resin while the remaining 2/3 of the relaxation is due to other mechanisms (tread slip, plasticity, external load).

2.3.2 FE analyses

To develop numerical models able to simulate the viscoelastic behavior of composite joints several authors [96,97,100,101] used the data presented by Kibler and Carter [102] and by Beckwith [103] respectively for epoxy 5208 and for Shell 58-68 epoxy at 75°F (24°C). The lamina properties are calculated from micro-mechanical equations assuming that:

- the fibers have a linear elastic behavior;
- the composite is orthotropic and transversely isotropic;
- the matrix has a linear-viscoelastic behavior that can be described by a power law:

$$D(t) = D_0 + D_1 t^n \quad (2.21)$$

where

- $D(t)$ is the time dependent isotropic creep compliance of the matrix;

- D_0 is the initial elastic compliance of matrix;
 - D_1 is the creep coefficient of the matrix;
 - t is the time;
 - n is a dimensionless creep exponent.
- the matrix obeys hygrothermal shift factor rules for time-temperature/moisture superposition;
 - the viscoelastic response depends only on the time computed since the application of the load;
 - the effective time-dependent compliance, $D(t)$, for the polymer matrix resin is often represented by the empirical power law equation for creep compliance [102].

To account for effects of temperature and moisture by using hygrothermal shift factors, a_{TH} , equation (2.21) can be written as [104]:

$$D(t) = D_0 + D_1 \left(\frac{t}{a_{TH}} \right)^n \quad (2.22)$$

A time-dependent matrix modulus, $E_m(t)$, can be estimated as [102]:

$$E_m(t) \approx \left(\frac{1}{D(t)} \right) \quad (2.23)$$

The viscoelastic properties of the lamina can be estimated using elastic fiber properties and time-dependent viscoelastic resin properties [105].

Using this procedure, Shivakumar and Crews [96] investigated the effects of viscoelasticity, temperature and moisture on the clamping load of T300/5208 laminates using a 2D FE model. Relaxation of bolt load was predicted for three steady state temperatures (23°C, 66°C and 121°C), for four moisture levels (0%, 0.5%, 1% and 1.5%) and for 1 day, 1 month, 1 year, 20 year exposure durations. The results showed a 8% reduction in bolt load at RTD (23°C and 0% moisture) conditions for the 1 day period and relaxation of 31% for the 20 year duration. It was highlighted that increasing temperature and moisture levels increases the relaxation rate. Moreover it was found that the relaxation due to environmental conditions are additive to the viscoelastic effects. A simple equation was proposed to calculate the time-dependent bolt clamp-up force/preload, F_t :

$$F_t = \frac{F_0}{1 + F_1 t^n} \quad (2.24)$$

where F_1 and n are empirical constants obtained fitting the FE results for RTD case and F_0 represents the initial value of the preload. If it should take into account the effect of the moisture the equation (2.24) should be modified introducing the shift-factor a_{TH} as:

$$F_t = \frac{F_0}{1 + F_1(t/a_{TH})^n} \quad (2.25)$$

Equations (2.24)-(2.25) can be used to determine the relaxation only in the case of steady state temperature and moisture conditions.

Shivakumar and Crews [97] extended their previous work to transient temperature and moisture conditions using a small increment time method. A general equation to calculate bolt load relaxation was proposed:

$$F_t = \sum_{i=1}^N \frac{\Delta F_{0i}}{1 + F_1 \left(\sum_{j=1}^N \frac{t_{j+1} - t_j}{(a_{TH})_j} \right)^n} \quad (2.26)$$

where:

- ΔF_{0i} is the elastic clamp-up increment for the i th time interval;
- $(a_{TH})_j$ is the shift-factor at j^{th} time interval;
- N is the total interval number.

Recently, 3D joint models have been used to predict the effect of viscoelasticity. Gibson [105] used an approximate quasi-static approach to evaluate the bolt relaxation. In this approach, the quasi-elastic solutions were approximated by a series of elastic solutions corresponding to different elastic properties at different times, while the stresses were assumed to be constant during each time increment.

Thoppul *et al.* [101] compared the relaxation predictions made from an ABAQUS [106] viscoelastic solution with those from the quasi-elastic approach for an unreinforced isotropic epoxy beam. The bolt preload relaxation was predicted for different static and dynamic loads using both viscoelastic and quasi-elastic approaches. Relaxation of about 4.75% in the bolt preload was predicted for a period of 50 h, and the difference between viscoelastic and quasi-elastic predictions was shown to be less than 2%.

2.4 Effects of environmental conditions

As previously described the *thermal* and *hygroscopic effects* have a significant influence on the behavior of polymer-matrix materials.

Hygrothermal changes of the environment influence the composite behavior mainly in two ways [105]:

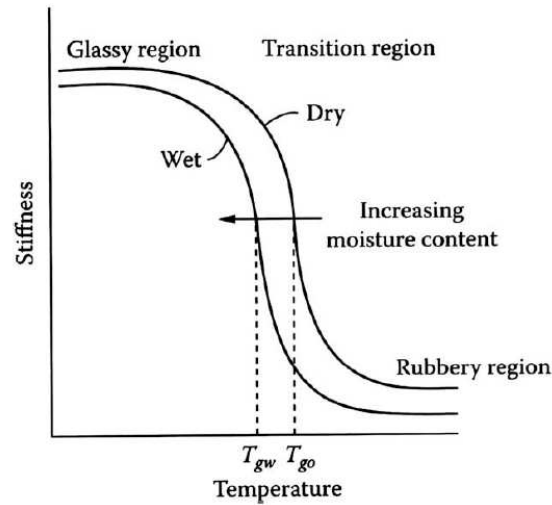


Figure 2.14: Stiffness as a function of temperature for a typical polymer matrix material [105].

- when the temperature increases and becomes higher than the glass-transition temperature, T_g , the polymer becomes softer and cannot be used in structural applications. Figure 2.14 shows this effect. The glass-transition temperature in *dry* conditions is indicated as T_{g0} , while, when the material is fully wet M_m , the *wet* glass transition temperature is denoted by T_{gw} ;
- increase or decrease temperature or moisture cause differential residual hygrothermal stresses and strains.

Therefore, environmental conditions may influence the failure and the strength of both bolted [107–116] or pinned [117–120] composite joints and for these reasons these effects have to be taken into account.

2.5 State of art in the railway industry

Currently, the use of composites is often limited to the aerospace and automotive industries. While it is possible to find in the railway industry some examples of the use of composites, their use is limited to non structural parts (cab, skirts, interiors, etc..). Composites are limited to high-speed trains (secondary structures) and are absent in other kind of trains, such as tramway and metro. This results from the fact that the use of composite requires a know-how that the railways industry does not currently have, and for this reason metals are preferred.

However the use of composites is a vital issue for the railway industry. In fact, their advantages are numerous:

- it allows to reduce the weight and consequently the energy necessary for the transportation;

- it reduces the cost of manufacturing: if the design is correctly performed (integration of functions) a structure manufactured in composites requires less parts and consequently less time to be assembled or disassembled.
- it reduces the recurring costs because composite structures require less maintenance than metal structures.

2.5.1 Comparison of different technologies

In the railway industry, the principal issue related with the use of composites is to find the way to substitute an original structure (that generally is manufactured in aluminum or steel) with another one, manufactured in composites, that gives the same or better performances. Obviously, the new technical solution can only be accepted if a gain in mass and in cost is obtained. Therefore if the *composite* version of a structure does not ensure these gains in mass and in cost, the solution cannot be accepted. Consequently, it is important to make a comparison between different technologies to evaluate that one that gives the best performance in reduction of weight and cost. Three different carbody-shell can be compared [1]:

- the carbody-shell manufactured completely in aluminum (aluminum carbody-shell, standard);
- the carbody-shell manufactured completely in composites (composite carbody-shell);
- the carbody-shell manufactured using steel and composites (hybrid carbody-shell).

It was shown that the hybrid solution gives the best performances [1]. It can be estimated that an hybrid carbody shell leads to a gain in mass of about 12-24% and a gain in cost of about 20%. Improved performance could be reached by developing enhanced design methods.

2.5.2 Connections in railway industry

Given that a hybrid carbody shell assures the best performance for the next generation of train designs, the most difficult task concerns the design of joints between dissimilar materials (metals and composites). The section of a carbody shell and the main connections are shown in Figure 2.15:

- the connection between the main frame and the floor, A1;
- the connection between the carbody shell and the top floor, A2 (in case of a double deck carbody shell);
- the connection between the main frame and the carbody shell, B;

- the connection between the carbody shell and the roof, C.

Figure 2.16 shows the details of these connections. Figure 2.16(a) shows the current connection between the floor and the main frame. The roof is manufactured in aluminum and is riveted or bolted to the main frame (manufactured in steel). In the future, the floor would be manufactured using glass fiber reinforced composites. Figure 2.16(b) shows the connection of the top floor of a double deck with the carbody shell. Currently, the floor is an aluminum profile, but it could be manufactured using a sandwich structure. Figure 2.16(c) represents the connection between the main frame and the carbody shell. This connection has to be made using two different materials. In fact, the internal panel cannot be toxic, while the external panel must have a good fire resistance [121]. For this reason, the internal panel can be manufactured in phenolic resin, while the external panel can be manufactured in vinylester resin. Figure 2.16(d) shows the connection between the carbody-shell and the roof. Identical considerations as above can be done for the selection of the materials of external and internal panel. The roof could be manufactured in vinylester resins or in epoxy to have better impact performance.

It is possible to find an analogy between the structural connections of Figure 2.15 and the simple connections like single or double lap joint.

To understand how all these materials behave, an experimental campaign is conducted and it is presented in Chapter 3. Different parameters are considered in the experimental work:

- geometrical parameters like e , w , d ;
- the different of material used (steel-glass fiber,etc...)

The experimental results will be used to obtain design charts that can be used to estimate in a easy and quick way the strength of a bolted joint.

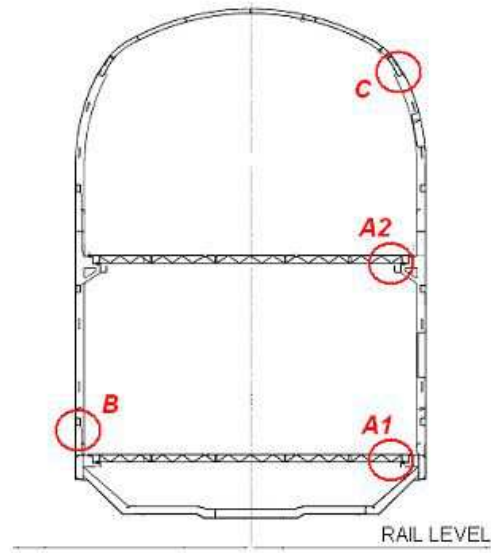


Figure 2.15: Main connections in a carbody shell.

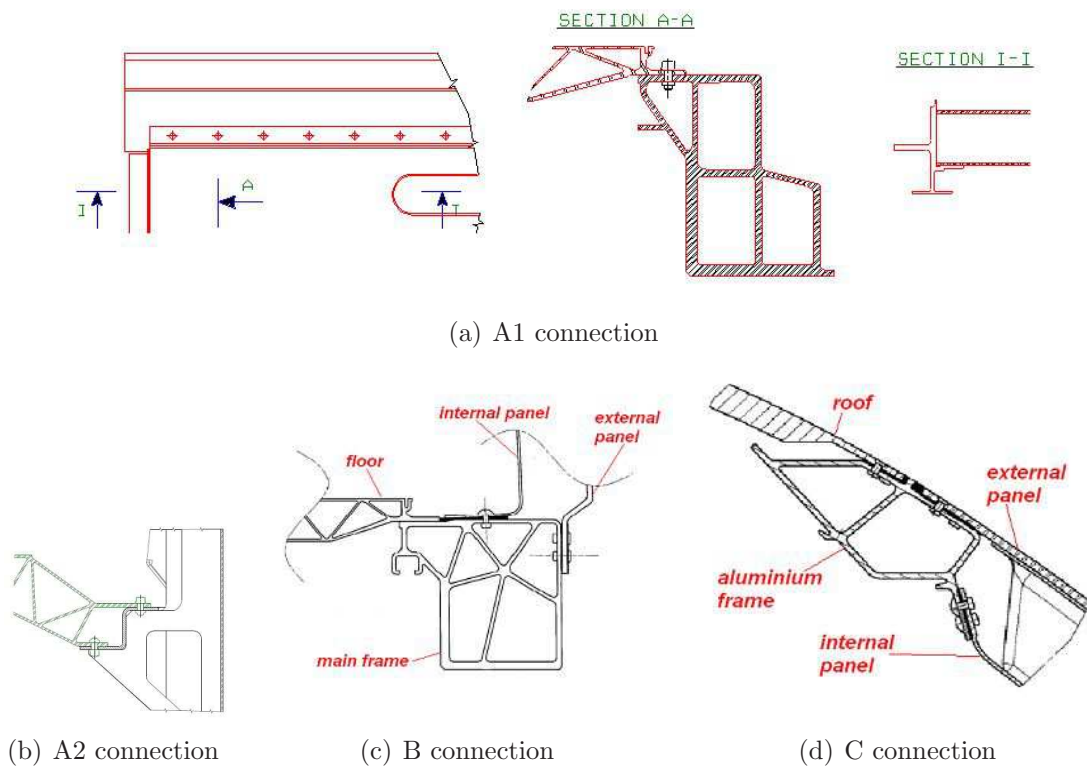


Figure 2.16: Main connections in a carbody shell: details.

Chapter 3

Experimental Work

This chapter describes the experimental work done performed on bolted joints with different materials and joint configurations. The experiments aim to characterize the behavior of the joint when the geometric parameters (w , e , d) vary, and to compare different composite materials for multi-material bolted joints. In the previous chapter (see Section 2.5.2) the typical joints that are used in railway applications were described, and it was shown how it is possible to find an analogy between a structural connection and a simple test configuration. It was found that it is possible to obtain relevant information on the strength of the joint if two types of tests are performed:

- the test for evaluating the bearing response of the composite;
- the test for measuring the fastener pull-through resistance of the laminate.

The first test was performed using two different joint configurations: the double-lap joint and the single lap-joint. Also, the three point bending test was performed to evaluate the flexural properties of the laminates. The materials used to manufacture the joints are metals and composites that are commonly used in the railway industry.

3.1 Materials used

3.1.1 Metals

The metals used are:

- steel S500MC;
- aluminum 6082 T6.

Both materials are intensively used in the manufacture of trains. The mechanical properties of these materials, reported in Table 3.1, were obtained from the European

norms [122, 123]. Figure 3.1 shows the true-stress/true-strain curve of the materials used.

Table 3.1: Mechanical properties of metals used

material	E (MPa)	ν	σ_y (MPa)	ρ (kg/m ³)	hardening law
S500MC	210000	0.3	500	7850	$\sigma = 800\varepsilon^{0.745}$ [124]
6082 T6	70000	0.34	260	2700	$\sigma = 460\varepsilon^{0.11}$

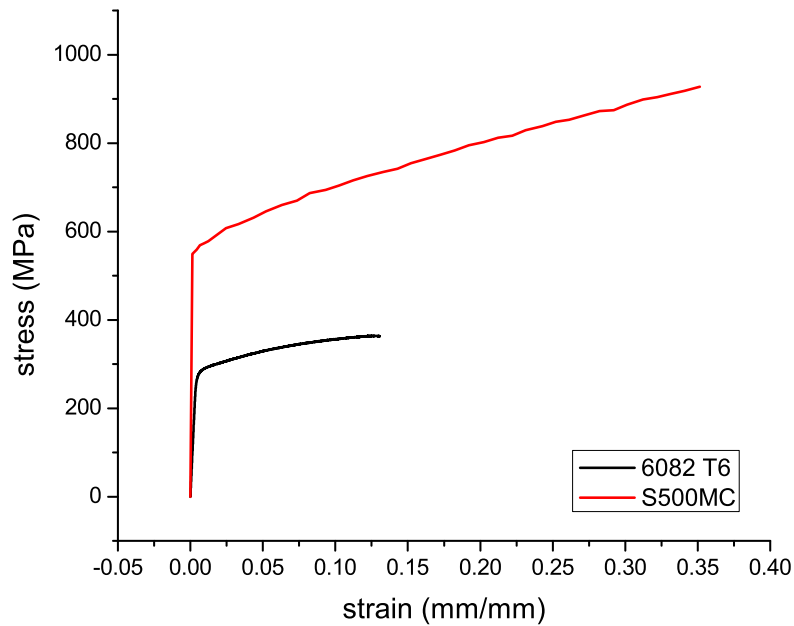


Figure 3.1: True-stress true-strain curve for metals used

3.1.2 Composites

The composites used are:

- Fiber Glass-epoxy composite¹;
- Fiber Glass-vinylester composite²;
- Fiber Glass-phenolic composite²

The glass-fiber(GF)-epoxy panel was manufactured using Hexply®M9/M10 preregs with a ply orientation pattern of $[\pm 45/90/\pm 45/0/\pm 45]_S$. The 0-90 plies have an initial thickness (thickness of the prepreg before lamination and curing) of 0.8 mm,

¹Manufactured by Ecole des Mines de Douai

²Manufactured by Composites Aquitaine, EADS group

and the $\pm 45^\circ$ plies have a thickness of 0.6 mm. After curing, the nominal thickness of each ply is 0.5 mm and 0.4 mm for the 0-90 plies and for the $\pm 45^\circ$ plies respectively. The characteristics of the unidirectional lamina of the GF-epoxy composite are given by the supplier (Hexcel Composites) and are reported in Table 3.2.

The other laminates (i.e. GF-vinylester, GF-phenolic) were manufactured using the technique of resin infusion and they have the quasi-isotropic lay-up reported in Table 3.3. The mechanical properties of these laminates were measured by Composites Aquitaine and are reported in Table 3.4. The material was tested after a heat ageing treatment according to the AFNOR norm [125].

Table 3.2: Material properties of GF-epoxy UD laminate

E (GPa)	3.2
X_T (MPa)	85
ε_R (%)	3.75

Table 3.3: Orientation pattern for GF-vinylester / phenolic composite

ply	type of product	name	supplier
14	$\pm 45^\circ - 610 \text{ g/m}^2$	EBX 600	SELCOM
13	$90^\circ - 600 \text{ g/m}^2$	roving UD 600 CHOMARAT	GAZECHIM
12	$\pm 45^\circ - 610 \text{ g/m}^2$	EBX 600	SELCOM
11	$90^\circ - 600 \text{ g/m}^2$	roving UD 600 CHOMARAT	GAZECHIM
10	$\pm 45^\circ - 610 \text{ g/m}^2$	EBX 600	SELCOM
9	$0^\circ - 1246 \text{ g/m}^2$	UNIE 1200	SELCOM
8	$\pm 45^\circ - 610 \text{ g/m}^2$	EBX 600	SELCOM
7	$\pm 45^\circ - 610 \text{ g/m}^2$	EBX 600	SELCOM
6	$0^\circ - 1246 \text{ g/m}^2$	UNIE 1200	SELCOM
5	$\pm 45^\circ - 610 \text{ g/m}^2$	EBX 600	SELCOM
4	$90^\circ - 600 \text{ g/m}^2$	roving UD 600 CHOMARAT	GAZECHIM
3	$\pm 45^\circ - 610 \text{ g/m}^2$	EBX 600	SELCOM
2	$\pm 90^\circ - 600 \text{ g/m}^2$	roving UD 600 CHOMARAT	GAZECHIM
1	$\pm 45^\circ - 610 \text{ g/m}^2$	EBX 600	SELCOM
	isoftalic poliester gelcoat	GCI S90000 VM10 SAF 1	POLYPROCESS

Table 3.4: Mechanical properties of GF-vinylester and phenolic UD laminate

materials	GF-vinylester ^a	GF-phenolic ^b
E_1 (MPa)	42830	35200
$E_2 = E_3$ (MPa)	1530	3000
ν_{12}	0.35	0.35
$\nu_{13} = \nu_{23}$	0.3	0.3
G_{12} (MPa)	2800	3400
$G_{13} = G_{23}$ (MPa)	2800	3400
X_T (MPa)	350	355
$Y_T = Z_T$ (MPa)	35	35
X_C (MPa)	300	300
$Y_C = Z_C$ (MPa)	30	30
S_T (MPa)	10	19
S_L (MPa)	22	14
ρ (kg/m ³)	1863	1900

^a Heat ageing @ 90°C for 24 hours^b Heat ageing @ 80°C for 24 hours

3.2 Strain gauges

3.2.1 Selection of strain gauges

The strain gauges used in this work are of the type C2A-13-125LW-350 (see Table 3.5). These general purpose strain gages are produced by Vishay Micro-Measurements. These strain gauges were chosen due to the following reasons:

- Their 350 Ω resistance, associated with a high voltage supply, promotes a better hysteresis effect and the zero load stability;
- The strain gauges already incorporate electrical wiring allowing the remaining electrical cables to be welded without damaging the composite material;
- The grid size is approximately ten times bigger than the fibre diameter, allowing the characterization of the composite material;
- The strain gauges are compensated for aluminum. Taking into account that the tests will be performed at constant temperature, the effect of small temperature variations was neglected.

The strain gauges were connected to the data acquisition system, *Spider 80*, in quarter-bridge using the three wires technique. To collect the data the software *Catman 3.0* was used.

Table 3.5: Strain gages technical data

Grid resistance (Ω)	$350 \pm 0.6\%$
Temp. Comp. of gage factor ($\%/100^\circ\text{C}$)	$+1.3 \pm 0.2$
Gage factor @ 24°C	$2.130 \pm 0.5\%$
Transverse sensitivity	$(0.3 \pm 0.2)\%$

3.2.2 Surface preparation

Surface preparation is of crucial importance in strain gauging, because it influences the quality of the adhesion between the test specimen and the strain gauge. The surface preparation will be performed as follows:

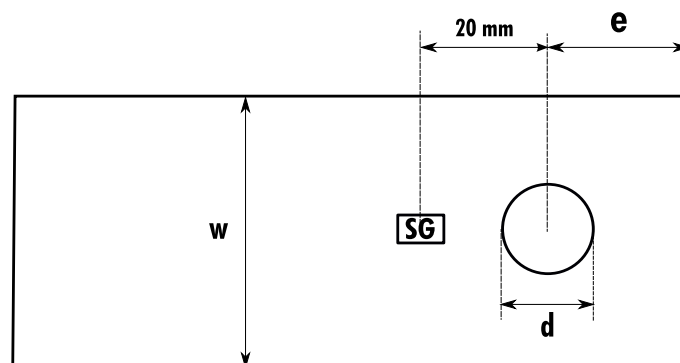
- Surface degreasing using HBM-RMS1 cleaning solution (acetone and isopropanol);
- Manually abrasion of the specimen surface with sandpaper n° 400;
- Degreasing using HBM-RMS1 to assure a total removal of all the possible dust and grease that may remain on the specimen surface.

3.2.3 Strain gauge bonding

After the cleaning process, and to complete the strain gauging process, it was necessary to execute the steps described beneath:

- Orientation guidelines were drawn upon the specimen surface to aid the correct alignment of the strain gauge;
- The strain gauge was finally glued using MBOND 200, which is a cyanoacrylate adhesive.

After these steps, the specimens were ready to be soldered to the data acquisition system wires. The strain gages were installed according to the representation shown in Figure 3.2.

**Figure 3.2:** Strain gage installation

3.3 Test Plan and Taguchi method

3.3.1 Definition of the geometry

It was shown in the previous chapter that the behavior of the specimens (strength and type of damage) depends on three parameters that are the diameter of the hole, the edge-distance and the width of the specimen. It was shown how the width and the edge distance influences the failure of the joint (2.1.2). In fact, when the ratio w/d is approximately smaller than 3, the specimen exhibits a net-tension failure while if w/d is larger the specimens exhibit a bearing failure. In the same way, the ratio e/d influences the failure of the specimen; if e/d is smaller than 4 the specimens exhibit shear-out failure while, if e/d is bigger, bearing occurs ³. As showed by Camanho *et al.* [126] the diameter has also an influence on the behavior of the specimen because it influences the characteristics dimensions in tension and in compression. Therefore, it is necessary to study the influence of these three parameters in the mechanical response of the joints manufactured using the material selected. For this purpose, the Taguchi method [127] may be used. If only two levels for each variable are considered the use of a Two-Level Full Factorial Design requires $2^3 = 8$ runs for each material combination. In Table 3.6 the 2^3 factorial design (plus and minus signs are the two levels for each factor, a , b , c are the three variables and A , B , C are the effects of each variable) is reported. For 8 combinations using 3 specimens per test the total number of tests is equal to $23 \times 8 \times 3 = 128$.

Table 3.6: 2^3 Factorial Design

Variable combination	Factorial Effect							
	I	A	B	C	AB	AC	BC	ABC
a	+	+	-	-	-	-	+	+
b	+	-	+	-	-	+	-	+
c	+	-	-	+	+	-	-	+
abc	+	+	+	+	+	+	+	+
ab	+	+	+	-	+	-	-	-
ac	+	+	-	+	-	+	-	-
bc	+	-	+	+	-	-	+	-
(1)	+	-	-	-	+	+	+	-

However, it is reasonable to assume that certain high-order interactions are negligible and to obtain information on the main effects and low order interactions only a fraction of the complete factorial experiment plan is required [128, 129]. It can be

³These consideration are rigorous for carbon-fiber composites but they can be generalized for different types of composites

assumed, for example, that only half of the full-factorial design that corresponds to the above part of Table 3.6 is executed. In this case, using the linear combination of the observations to estimate the main effects A, B and C it is possible to write:

$$e_A = \frac{1}{2}(a - b - c + abc) \quad (3.1)$$

$$e_B = \frac{1}{2}(-a + b - c + abc) \quad (3.2)$$

$$e_C = \frac{1}{2}(-a - b + c + abc) \quad (3.3)$$

and the two factors iteration can be written as:

$$e_{BC} = \frac{1}{2}(a - b - c + abc) \quad (3.4)$$

$$e_{AC} = \frac{1}{2}(-a + b - c + abc) \quad (3.5)$$

$$e_{AB} = \frac{1}{2}(-a - b + c + abc) \quad (3.6)$$

Thus the following relations can be written: $e_A = e_{BC}$, $e_B = e_{AC}$, $e_C = e_{AB}$; consequently it is impossible to differentiate, for example, between the A and BC . In fact when A , B and C are estimated using equations (3.1)-(3.3), the values of $A + BC$, $B + AC$ and $C + AB$ are really estimated. However if the two-levels interactions can be neglected also the error in evaluating principal effects can be neglected.

In the case under investigation here, there are three parameters d , e/d and w/d and so the two-levels interactions for these parameters are $(d; e/d)$, $(d; w/d)$ and $(w/d; e/d)$. The interaction between $(d; e/d)$ can be neglected; in fact it is known that the resistance and the behavior of the joint (shear-out or bearing) depends only on e/d parameter and so there are not interactions. In the same way, there are no interactions between $(d; w/d)$; in this case the resistance and the behavior of the joint (net-tension and bearing) depends only on the w/d parameter. Also the interaction $(w/d; e/d)$ can be neglected. Suppose, for example, that a joint has a w/d lower than 3. In this case if the other parameter, e/d , is equal to 5 or 10 the behavior of the joint does not change because it is a net-tension joint⁴. The same thing happens in a joint that has, for example, the e/d parameter lower than 3; changing the other parameter the behavior of the joint does not change and it will be always a shear-out specimen.

After these considerations, the experimental plan for the tests is designed. For each variable it is necessary to decide two levels, $()_+$ and $()_-$:

$$d_- = 6 \text{ mm} \quad d_+ = 10 \text{ mm} \quad (3.7)$$

⁴Rigorously if the parameter e/d became smaller than 3 the specimen could show a mixed behavior (net-tension / shear-out / cleavage). However, generally, at least one parameters larger than the critical value that differentiates between shear-out / net-tension and bearing behavior.

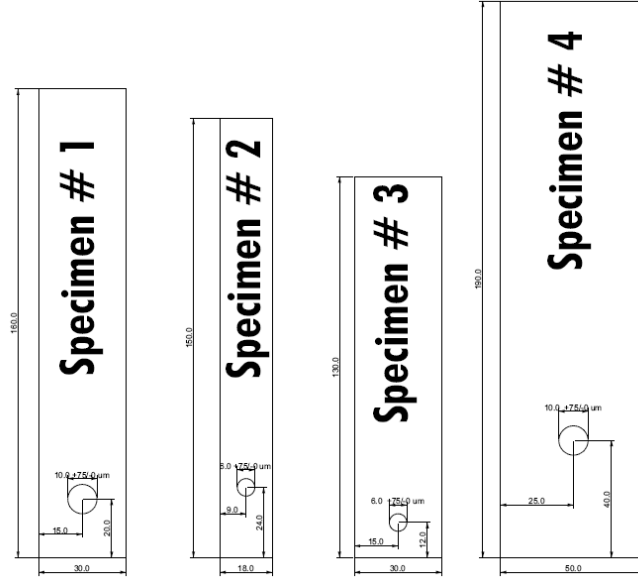


Figure 3.3: Specimens' geometry

$$(e/d)_- = 2 \quad (e/d)_+ = 4 \quad (3.8)$$

$$(w/d)_- = 3 \quad (w/d)_+ = 5 \quad (3.9)$$

The experimental plan is shown in Table 3.7.

Table 3.7: Experimental plan

run	D	w/D	e/D
1	10	3	2
2	6	5	2
3	6	3	4
4	10	5	4

3.3.2 Samples denomination

The specimens are identified in terms of the materials, the geometry and the type of the test. Three specimens were used for each type of test.

3.3.2.1 Three-point bending test (3PB)

The denomination of the specimen is the following:

C-M-I

where M is the material used and I is the index that identify the number of the sample:

- M=E (GF-epoxy), V (GF-vinylester), P (GF-phenolic);
- I=1,2,3

3.3.2.2 Double-lap bolted joint (DBJ)

The denomination of the specimen is the following:

$$M-J-I$$

where M is the material used, J is the index that identifies the geometry and I is the index that identifies the number of the sample. For our case we have:

- M=E (GF-epoxy), V (GF-vinylester), P (GF-phenolic);
- J=1,2,3,4;
- I=1,2,3

3.3.2.3 Single-lap bolted joint (SBJ)

For SBJ specimens there are two different materials and so the denomination of the specimen is the following:

$$M1-M2-J-I$$

where M1 and M2 are the material used, J and I have the same meaning and the same values that for BDJ:

- M1=S (steel), A (aluminum), V (GF-vinylester);
- M2=E (GF-epoxy), V, P (GF-phenolic);

3.3.2.4 Pull-Trough test (PT)

For PT specimens the following denomination was used:

$$PT-M-d-I$$

where M is the material, d is the diameter (in millimeter) of the hole and I is the number of the sample. M and I take the same values that were used in the denomination of DBJ specimen. The d parameter takes the values d=6, 10.

3.4 Specimen preparation

The laminates were cut using a wet cutting tile saw according to the dimensions specified in ASTM norms [3,130]. The dimensions of the specimen (shown in Figure 3.2) were respected with a tolerance of 0.1 mm. The specimens were afterwards drilled and the strain gages were installed as explained in Section 3.2. Figure 3.4 shows the specimens after the installation of the strain gages. Metal tabs (in aluminum) are bonded on the specimen and, at the end, bolts are inserted and preloaded (see Section 3.4.2).

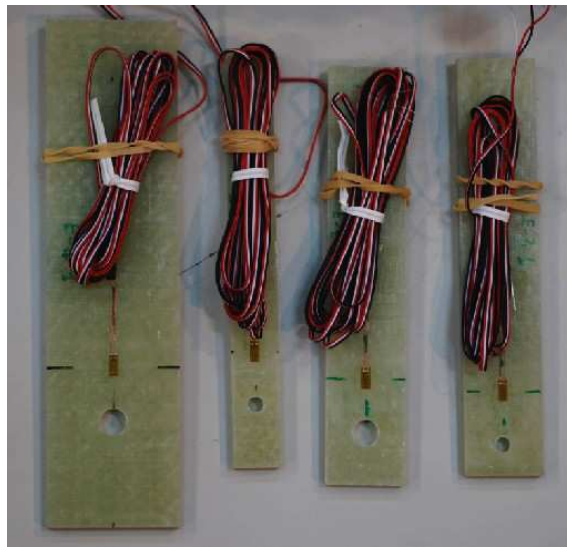


Figure 3.4: Specimens after the installation of the strain gauges

3.4.1 Hole Drilling

The method for the hole generation consists in drilling the laminate, which is supported by sacrificial frontal and backing plates.

Considering that 2 specimens are drilled in each operation, hard metal drills with a tip angle of 140, for hole generations only, were used. The drills are manufactured by SGS Tool Company and are compliant with the DIN338 standard. The commercial reference of the drills is DIN 338 - Standard Length Drills.

All holes were machined to achieve the tolerance of $-0/ + 70 \mu\text{m}$ used in the aerospace applications as reported in [126].

3.4.2 Bolts, characteristics and installation

To avoid plastic deformation at the bolts, high-strength bolts were chosen. The bolts selected are manufactured by UNBRAKO and they have the following characteristics:

- Treads: ANSI B1.13M, ISO 261
- Property class: 12.9-ISO 898/1
- Material: ASTM A574M, DIN ENISO 4762-alloy steel
- Hardness: Rc 38-43
- Tensile Stress: 1300 MPa
- Yield Stress 1170 MPa

Figure 3.5 shows the bolt's geometry and Table 3.8 shows the geometric parameters of the bolt selected. The bolts were installed using the general purpose washers having the dimensions shown in Table 3.9.

The pre-load applied to the bolt was defined imposing a 22MPa pressure to the washer. Therefore the values of pretension torque was calculated using:

$$T = K F_i d_{min} \quad (3.10)$$

where K is a factor that in standard conditions is equal to 0.2, F_i is the force applied to the screw and d_{min} is the minimum diameter of the screw. Using equation (3.10) the torques are $T_{d=10} = 10$ N/m and $T_{d=6} = 2$ N/m.

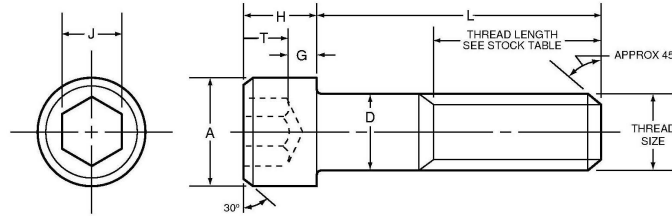


Figure 3.5: Unbrako bolts

Table 3.8: Bolts' mechanical properties and geometry

D^c	pitch	A^a	D^a	H^a	J^c	G^b	T^b	L^c	Strength ^b
	(mm)	(mm)	(mm)	(mm)	(mm)	(mm)	(mm)	(mm)	(kN)
M6	1.0	10.0	6.0	6.0	5.0	2.3	3.0	35.0	26.1
M10	1.5	16.0	10.0	10.0	8.0	4.0	5.0	50.0	75.4

^a maximum value

^b minimum value

^c nominal value

Table 3.9: Washers' geometrical parameters

d_{nom} (mm)	d_{int} (mm)	d_{ext} (mm)	h_{nom} (mm)
6	7.5	11.8	1.4
10	10.6	19.6	1.9

3.5 Tests

3.5.1 Calculation and Report

3.5.1.1 Statistics

For each series of tests and for each property measured the average value \bar{x} , the standard deviation STDV (s_{n-1}), the coefficient of variation CV and the confidence interval IC at 95% are calculated using the following equations:

$$\bar{x} = \frac{\sum_{i=1}^n x_i}{n} \quad (3.11)$$

$$s_{n-1} = \sqrt{\sum_{i=1}^n x_i^2 - n\bar{x}^2} \quad (3.12)$$

$$CV = 100 \times s_{n-1}/\bar{x} \quad (3.13)$$

$$IC = t_{(n-1;2.5\%)} \frac{s_{n-1}}{\sqrt{n}} \quad (3.14)$$

where:

- x_i is the measured or derived property;
- n is the number of the specimens
- $t_{(n-1;2.5\%)}$ is the value of the t distribution for a symmetrical 95% confidence interval.

3.5.1.2 Unities of measure

All measured or derived properties, if it is not otherwise specified, are expressed using the following unities of measure:

- displacement in mm
- load in N

- strain in m/m
- stress in MPa

3.5.2 Three Point Bending Test

The 3PB test was performed for two reasons: the first one is to compare the characteristics of the materials without and with heat ageing. The material tested was not aged as explained in section 3.1.2. Therefore, it is necessary to verify if the characteristics of the material are the same as those reported in Table 3.4.

The second reason is that the value of the Young modulus of the laminate can be calculated from the 3PB test. This information will be used for the calculation of the bearing response of the laminate (Section 3.5.3.3).

The tests were performed in INEGI using the INSTRON 4208 testing machine. The testing machine was equipped with a load cell of 100kN.

The experimental set-up is shown in Figure 3.6(a). During the test the temperature was $t = 23^\circ\text{C}$ and under the relative humidity of $h = 50\%$.

To calculate the elastic moduli the following formula was used [130]:

$$E_x^L = \frac{PL^3}{4wh^3\delta} \quad (3.15)$$

where δ is the displacement measured by the testing machine, L is the support-span, P is the load, w and h are width and thickness of the specimens⁵.

The results are reported in Table 3.10. Figure 3.6(b) shows the load-displacement curve obtained for different materials during the 3PB test.

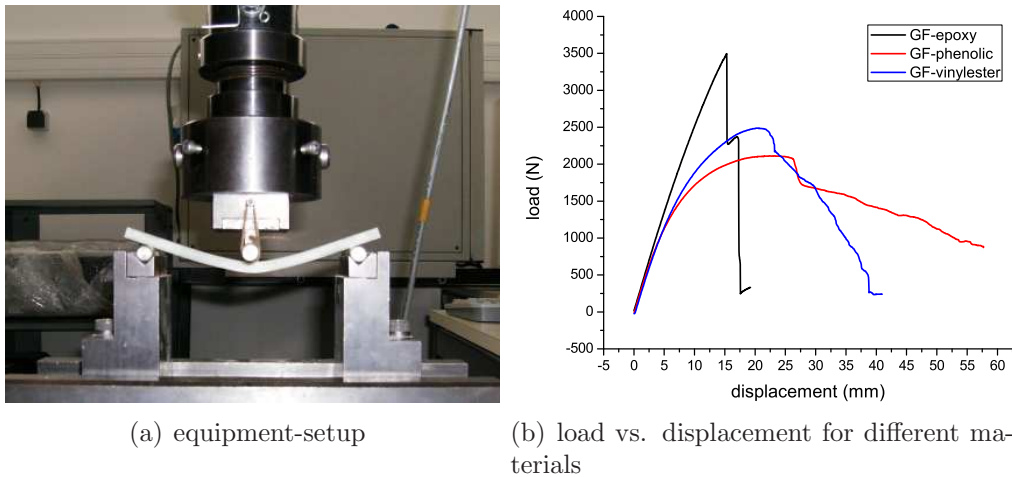
⁵Rigorously the elastic modulus calculated by equation (3.15) is not the real modulus of the material but the apparent modulus. In [130], in fact, the effects of the shear stresses are neglected. If the effect of the shear is taken into account the displacement in the middle of the specimen can be written as:

$$E_x^L = \frac{PL^3}{4wh^3\delta} + \frac{3PL}{8whG} = \frac{PL^3}{4wh^3\delta} (1 + \beta) \quad (3.16)$$

Therefore equation (3.15) neglects β . However for an high value of the span this approximation is valid.

Table 3.10: Elastic modulus of the specimens tested

specimen	E (MPa)	specimen	E (MPa)	specimen	E (MPa)
C-E-1	19861	C-P-1	17595	C-V-1	17387
C-E-2	17882	C-P-2	17615	C-V-2	16788
C-E-3	19663	C-P-3	18085	C-V-3	14644
Average	19135	Average	17765	Average	16273
STDV	1090	STDV	277	STDV	1442
CV (%)	6	CV (%)	2	CV (%)	9
IC (95%)	2708	IC (95%)	689	IC (95%)	3582

**Figure 3.6:** Three point bending test

3.5.3 Double-lap Bolted Joint

3.5.3.1 Description of the test

This test was done according to the norm ASTM D5961/D5961M-01 [3]. The test was conducted using the MTS-810 testing machine in FEUP's laboratories. Figure 3.7 shows the experimental set-up used: the specimen was clamped with a special fixture defined in the norm, and two LVDTs⁶ were used to obtain the information required to calculate the bearing strain in a more accurate way than that defined in [3] (see Section 3.5.3.3.1). The two LVDTs are also used to measure the eventual misalignment of the specimen.

The testing machine is equipped with a load cell of 100 kN. For each type of configuration of the joint a strain gauge is used. The strain gauges were installed

⁶Linear Variable Differential Transformer.

only in specimen M-J-1 (see Section 3.3.2.2). The speed of the machine in the displacement controlled test was 2 mm/min.

After each test the damaged specimen was examined and the type of failure was identified. The type of failure⁷ was identified for each specimen according to Figure 2.2.

At the end of each test the eventual plastic deformation of the bolt was also verified.

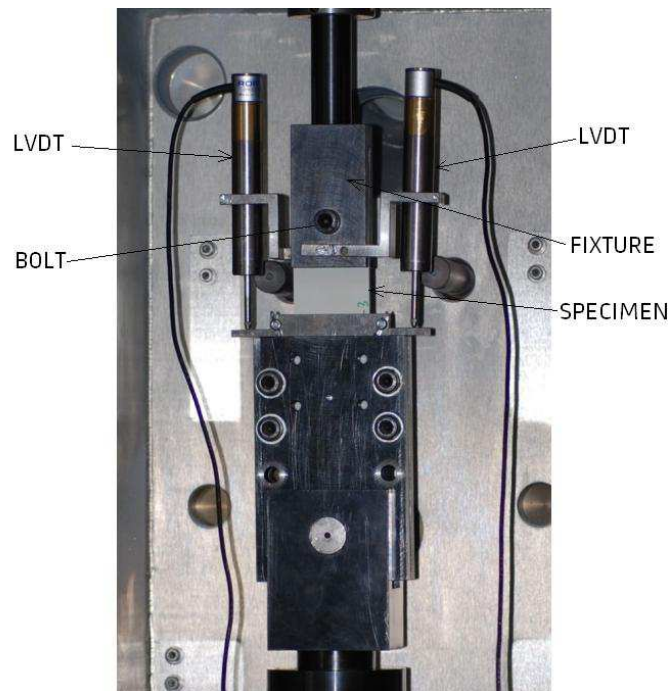


Figure 3.7: Equipment set-up for DBJ test

3.5.3.2 Experimental Data

3.5.3.2.1 Results obtained on specimens E-J-I

3.5.3.2.1.1 Specimens E-1-I Figure 3.8 shows the load displacement curve for the specimens E-1-I. The values of maximum load for each specimen and the statistics are presented in Table 3.11. Figure 3.9 shows the load-strain curve for the specimen E-1-1. Finally, Figure 3.10 shows the damaged zone in the specimen E-1-3. This specimen failed by tear-out and net-tension and showed the presence of delamination.

⁷SO=Shear-Out, NT=Net-Tension, CL=Cleavage, TO=Tear-Out BE=Bearing

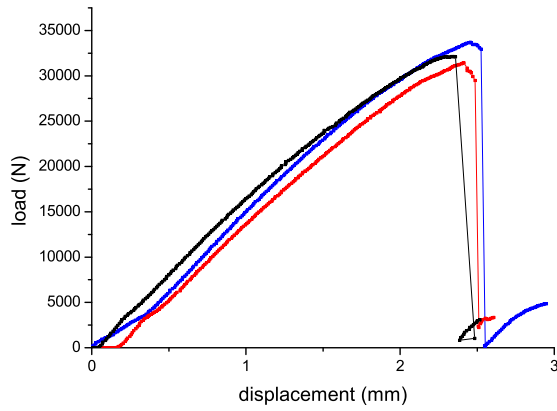


Figure 3.8: Load vs. displacement for E-1-I specimens

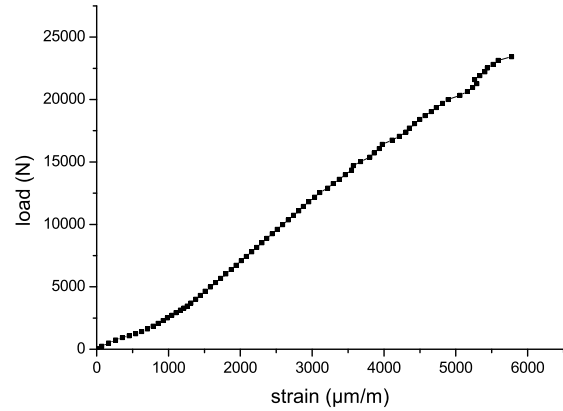


Figure 3.9: Force vs. strain for E-1-1 specimen

Table 3.11: Maximum load for E-1-I specimens

specimen	maximum load
E-1-1	33695 N
E-1-2	32129 N
E-1-3	31408 N
Average	32411N
STDV	1169
CV (%)	4
IC (95%)	2905 N



Figure 3.10: E-1-3 specimen after loading

3.5.3.2.1.2 Specimens E-2-I Figure 3.11 shows the load displacement curve for the specimens E-2-I. The values of maximum load for each specimen and the statistics are presented in Table 3.12. Figure 3.12 shows the load-strain curve for the specimen E-2-1. Finally, Figure 3.13 shows the damaged zone in the specimen E-2- 3. This specimen failed by net-tension and showed the presence of delamination.

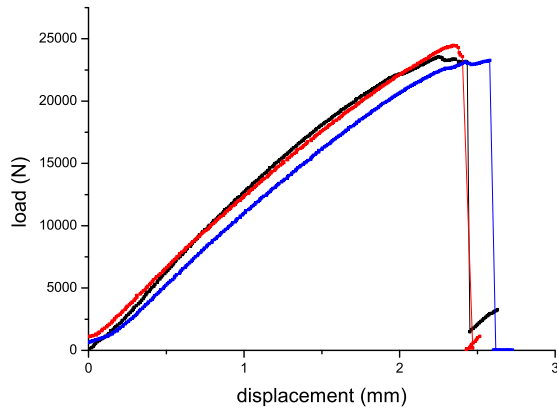


Figure 3.11: Load vs. displacement for E-2-I specimens

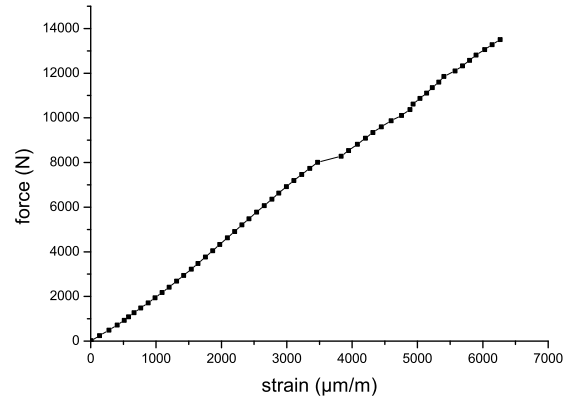


Figure 3.12: Load vs. strain for E-2-1 specimen

Table 3.12: Maximum load for E-2-I specimens

specimen	maximum load
E-2-1	23561 N
E-2-2	23268N
E-2-3	24468 N
Average	23766 N
STDV	626
CV (%)	3
IC (95%)	1554 N



Figure 3.13: E-2-3 specimen after loading

3.5.3.2.1.3 Specimens E-3-I Figure 3.14 shows the load displacement curve for the specimens E-3-I. The values of maximum load for each specimen and the statistics are presented in Table 3.13. Figure 3.15 shows the load-strain curve for the specimen E-3-1. Finally, Figure 3.16 shows the damaged zone in the specimen E-3-3. This specimen failed by tear-out and showed the presence of delamination.

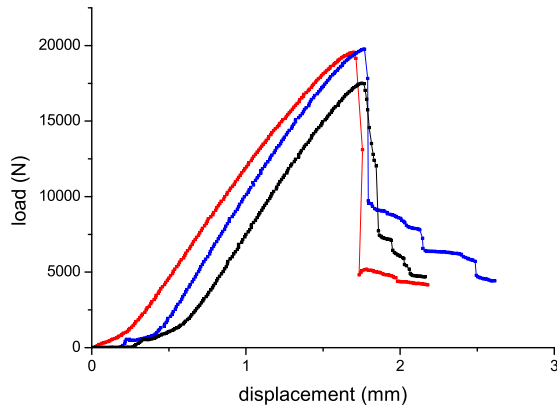


Figure 3.14: Load vs. displacement for E-3-I specimens

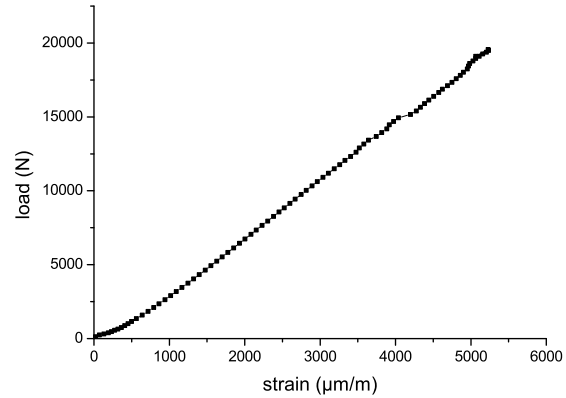


Figure 3.15: Load vs. strain for E-3-1 specimen

Table 3.13: Maximum load for E-3-I specimens

specimen	maximum load
E-3-1	19533 N
E-3-2	17511 N
E-3-3	19760 N
Average	18935 N
STDV	1238
CV (%)	7
IC (95%)	3076 N

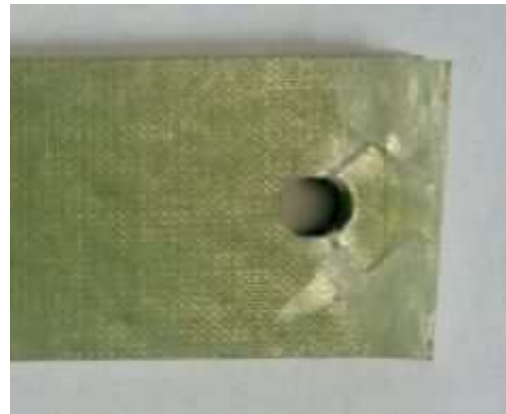


Figure 3.16: E-3-3 specimen after loading

3.5.3.2.1.4 Specimens E-4-I Figure 3.17 shows the load displacement curve for the specimens E-4-I. The values of maximum load for each specimen and the statistics are presented in Table 3.14. Figure 3.18 shows the load-strain curve for the specimen E-4-1.

It should be noted that that the strain measured is not the bearing strain, but the strain in the point where the strain gage is installed. For this reason, when the load reaches the critical value the deformation measured by the strain gage decreases or it remains constant (between $4000\mu\text{m}/\text{m}$ and $6000\mu\text{m}/\text{m}$ after failure occurs).

Finally, Figure 3.19 shows the damaged zone in the specimen E-4-3. This specimen failed by bearing and showed the presence of delamination.

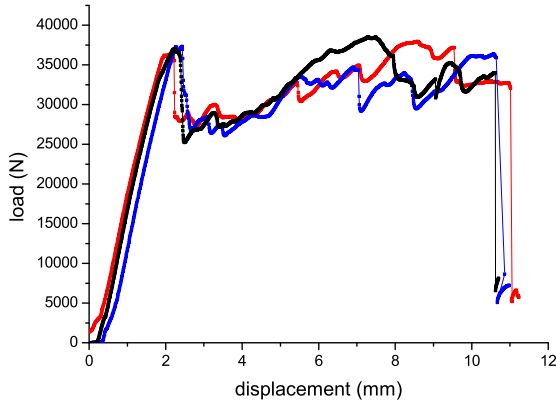


Figure 3.17: Load vs. displacement for E-4-I specimens

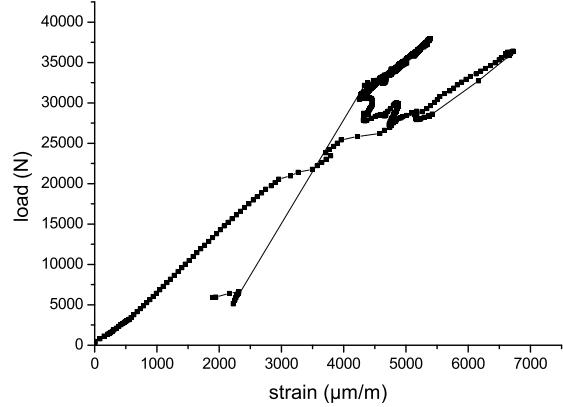


Figure 3.18: Load vs. strain for E-4-1 specimen

Table 3.14: Maximum load for E-4-I specimens

specimen	first load	maximum load
E-4-1	34416 N	37954 N
E-4-2	37037 N	38527 N
E-4-3	37333 N	37333N
Average	36262 N	37938 N
STDV	1606	597
CV (%)	4	2
IC (95%)	3988 N	1483N



Figure 3.19: E-4-3 specimen after loading

3.5.3.2.2 Results obtained on specimens V-J-I

3.5.3.2.2.1 Specimens V-1-I Figure 3.20 shows the load displacement curve for the specimens V-1-I. The values of maximum load for each specimen and the statistics are presented in Table 3.15. Figure 3.21 shows the load-strain curve for the specimen V-1-1. Finally, Figure 3.22 shows the damaged zone in the specimen V-1-2. This specimen failed by shear-out and cleavage and showed the presence of delamination.

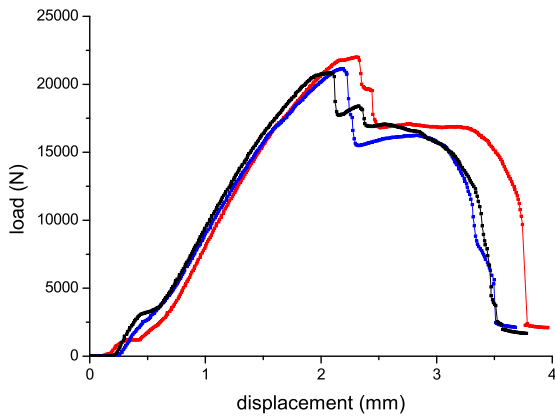


Figure 3.20: Load vs. displacement for V-1-I specimens

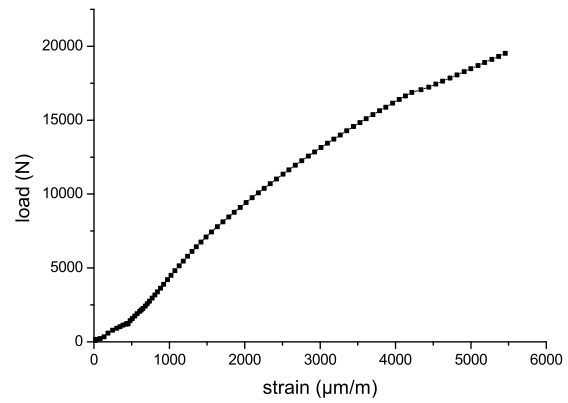


Figure 3.21: Load vs. strain for V-1-1 specimen

Table 3.15: Maximum load for V-1-I specimens

specimen	maximum load
V-1-1	21995N
V-1-2	20843 N
V-1-3	21136 N
Average	21325 N
STDV	599
CV (%)	3
IC (95%)	1487 N



Figure 3.22: V-1-2 specimen after loading

3.5.3.2.2 Specimens V-2-I Figure 3.23 shows the load displacement curve for the specimens V-2-I. The values of maximum load for each specimen and the statistics are presented in Table 3.16. Figure 3.24 shows the load-strain curve for the specimen V-2-1. Finally, Figure 3.25 shows the damaged zone in the specimen V-2-3. This specimen failed by shear-out, bearing and net-tension and showed the presence of delamination.

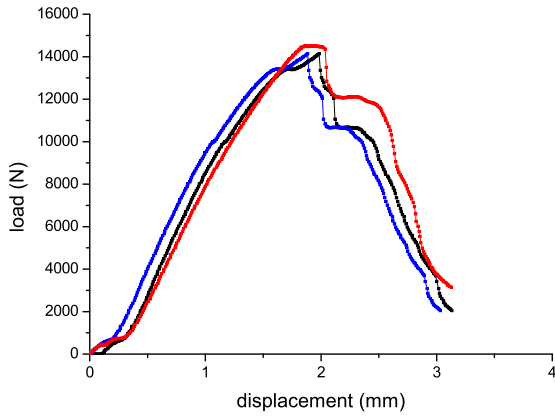


Figure 3.23: Load vs. displacement for V-2-I specimens

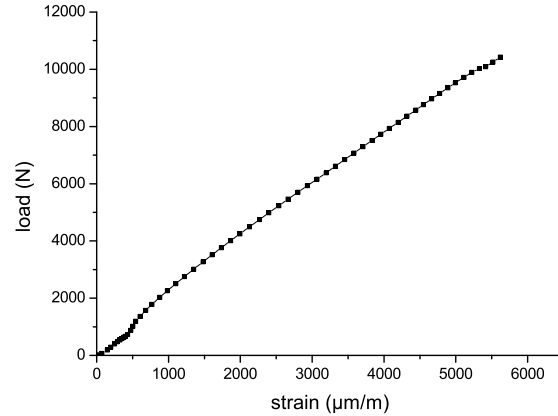


Figure 3.24: Load vs. strain for V-2-1 specimen

Table 3.16: Maximum load for V-2-I specimens

specimen	maximum load
V-2-1	14134 N
V-2-2	14524N
V-2-3	13703N
Average	14120N
STDV	411
CV (%)	3
IC (95%)	1020 N



Figure 3.25: V-2-3 specimen after loading

3.5.3.2.2.3 Specimens V-3-I Figure 3.26 shows the load displacement curve for the specimens V-3-I. The values of maximum load for each specimen and the statistics are presented in Table 3.17. Figure 3.27 shows the load-strain curve for the specimen V-3-1. Finally, Figure 3.28 shows the damaged zone in the specimen V-3-2. This specimen failed by shear-out and cleavage and showed the presence of delamination.

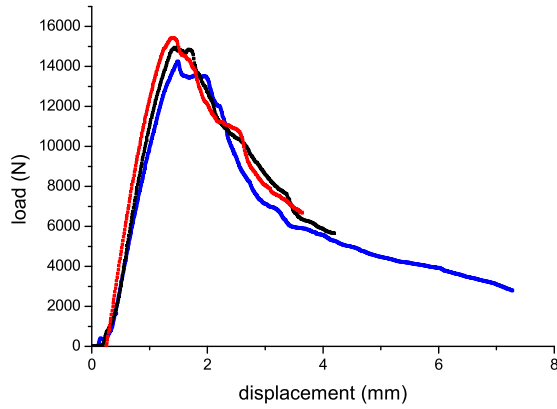


Figure 3.26: Load vs. displacement for V-3-I specimens

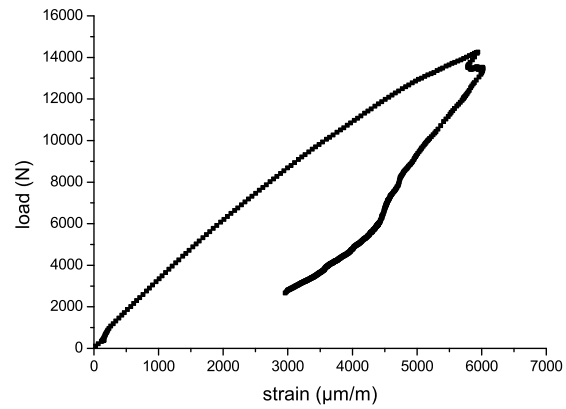


Figure 3.27: Load vs. strain for V-3-1 specimen

Table 3.17: Maximum load for V-3-I specimens

specimen	maximum load
V-3-1	14252 N
V-3-2	15431 N
V-3-3	14945 N
Average	14876 N
STDV	593
CV (%)	4
IC (95%)	1472 N

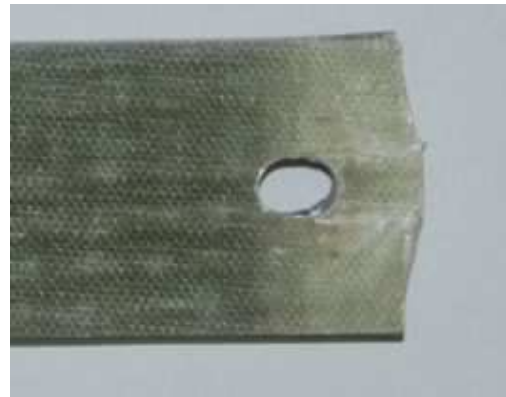


Figure 3.28: V-3-2 specimen after loading

3.5.3.2.2.4 Specimens V-4-I Figure 3.29 shows the load displacement curve for the specimens V-4-I. The values of maximum load for each specimen and the statistics are presented in Table 3.18. Figure 3.30 shows the load-strain curve for the specimen V-4-1. Finally, Figure 3.31 shows the damaged zone in the specimen V-4-1. This specimen failed by bearing and shear-out and showed the presence of delamination.

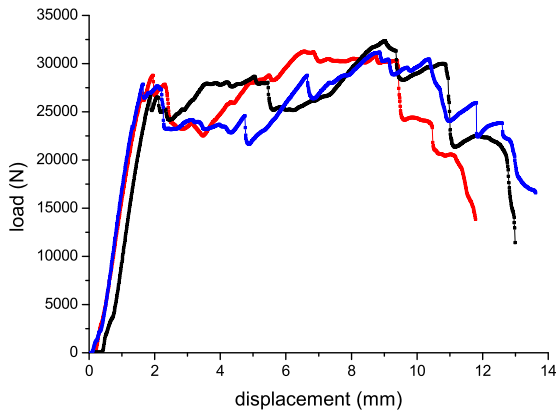


Figure 3.29: Load vs. displacement for V-4-I specimens

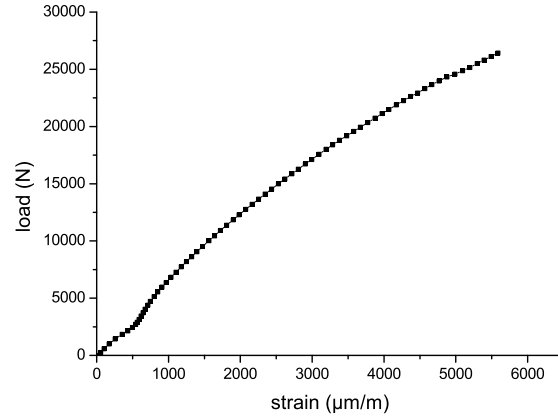


Figure 3.30: Load vs. strain for V-4-1 specimen

Table 3.18: Maximum load for V-4-I specimens

specimen	first load	maximum load
V-4-1	28779 N	31284N
V-4-2	27862 N	31184 N
V-4-3	26748 N	32377N
Average	27796 N	31615N
STDV	1017	662
CV (%)	4	2
IC (95%)	2527 N	1644 N



Figure 3.31: V-4-1 specimen after loading

3.5.3.2.3 Results obtained on specimens P-J-I

3.5.3.2.3.1 Specimens P-1-I Figure 3.32 shows the load displacement curve for the specimens P-1-I. The values of maximum load for each specimen and the statistics are presented in Table 3.19. Figure 3.33 shows the load-strain curve for the specimen P-1-1. Finally, Figure 3.34 shows the damaged zone in the specimen P-1-1. This specimen failed by bearing, shear-out and cleavage and showed the presence of delamination.

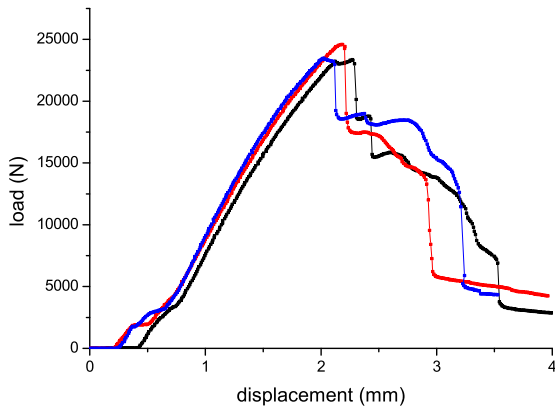


Figure 3.32: Load vs. displacement for P-1-I specimens

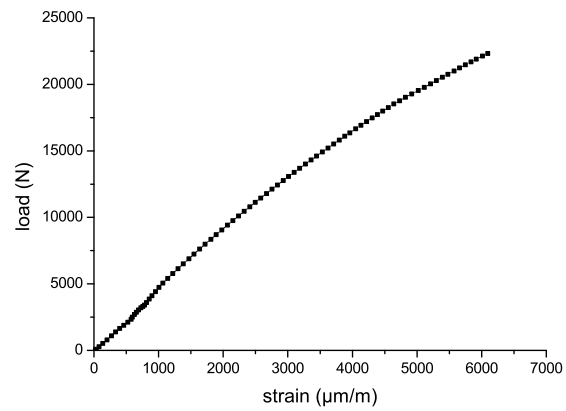


Figure 3.33: Load vs. strain for P-1-1 specimen

Table 3.19: Maximum load for P-1-I specimens

specimen	maximum load
P-1-1	23357 N
P-1-2	23468 N
P-1-3	24592 N
Average	23806 N
STDV	683
CV (%)	3
IC (95%)	1697 N



Figure 3.34: P-1-1 specimen after loading

3.5.3.2.3.2 Specimens P-2-I Figure 3.35 shows the load displacement curve for the specimens P-2-I. The values of maximum load for each specimen and the statistics are presented in Table 3.20. Figure 3.36 shows the load-strain curve for the specimen P-2-1. Finally, Figure 3.37 shows the damaged zone in the specimen P-2-2. This specimen failed by bearing and net tension and showed the presence of delamination.

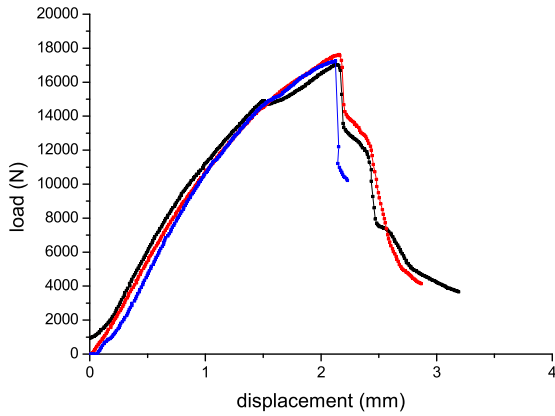


Figure 3.35: Load vs. displacement for P-2-I specimens

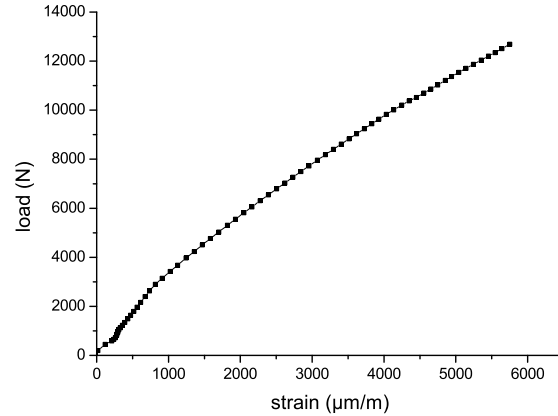


Figure 3.36: Load vs. strain for P-2-1 specimen

Table 3.20: Maximum load for P-2-I specimens

specimen	maximum load
P-2-1	17028 N
P-2-2	17242 N
P-2-3	17618 N
Average	17296 N
STDV	299
CV (%)	2
IC (95%)	742 N



Figure 3.37: P-2-2 specimen after loading

3.5.3.2.3.3 Specimens P-3-I Figure 3.38 shows the load displacement curve for the specimens P-3-I. The values of maximum load for each specimen and the statistics are presented in Table 3.21. Figure 3.39 shows the load-strain curve for the specimen P-3-1. Finally, Figure 3.40 shows the damaged zone in the specimen P-3-3. This specimen failed by bearing and cleavage and showed the presence of delamination.

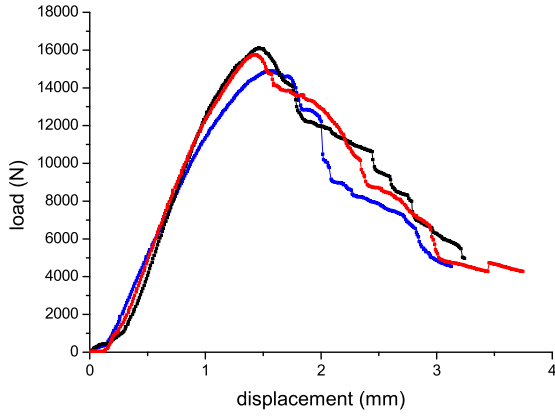


Figure 3.38: Load vs. displacement for P-3-I specimens

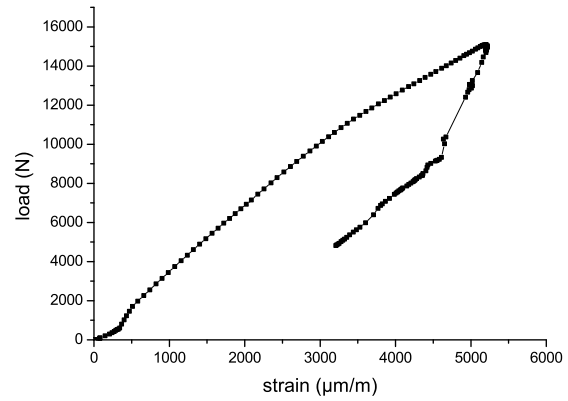


Figure 3.39: Load vs. strain for P-3-1 specimen

Table 3.21: Maximum load for P-3-I specimens

specimen	maximum load
P-3-1	14893 N
P-3-2	15759 N
P-3-3	16114 N
Average	15589 N
STDV	628
CV (%)	4
IC (95%)	1560 N



Figure 3.40: P-3-3 specimen after loading

3.5.3.2.3.4 Specimens P-4-I Figure 3.41 shows the load displacement curve for the specimens P-4-I. The values of maximum load for each specimen and the statistics are presented in Table 3.22. Figure 3.42 shows the load-strain curve for the specimen P-4-1. Finally, Figure 3.43 shows the damaged zone in the specimen P-4-3. This specimen failed by bearing and showed the presence of delamination.

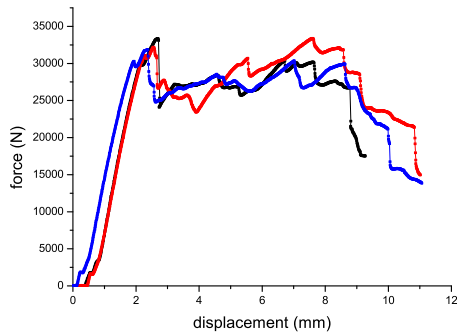


Figure 3.41: Load vs. displacement for P-4-I specimens

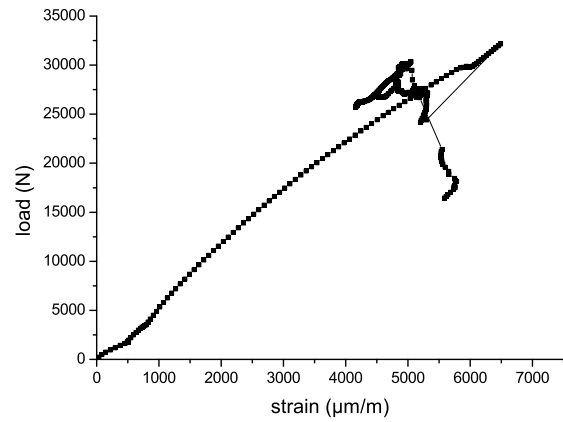


Figure 3.42: Load vs. strain for P-4-1 specimen

Table 3.22: Maximum load for P-4-I specimens

specimen	first load	maximum load
P-4-1	33360	33360
P-4-2	30276	31884
P-4-3	31080	33377
Average	31572	32874
STDV	1600	857
CV (%)	5	3
IC (95%)	3974	2129



Figure 3.43: P-4-3 specimen after loading

3.5.3.2.4 Summary for DBJ specimens Table 3.23 presents the statistics of the maximum load measured for each specimen type. The values obtained are similar for GF-vinylestyer and GF-phenolic specimens, probably for the reason that these two material were be manufactured using the same technique (resin infusion) and because the same lay-up is used.

Table 3.23: Maximum load for DBJ specimens

specimen	Type ^a	Average (N)	STDV	CV (%)	IC @ 95% (N)
E-1-I	TO, NT	32411	1169	4	2905
E-2-I	NT	23766	626	3	1554
E-3-I	TO	18935	1238	7	3076
E-4-I	BE	36262	1606	4	3988
V-1-I	SO, CL	21325	599	3	1487
V-2-I	SO, BE, NT	14120	411	3	1020
V-3-I	SO, CL	14876	593	4	1472
V-4-I	BE, SO	27796	1017	4	2527
P-1-I	BE, SO, CL	23806	683	3	1697
P-2-I	BE, NT	17296	299	2	742
P-3-I	BE, CL	15589	628	4	1560
P-4-I	BE	31572	1600	5	3974

^a SO=Shear-Out, NT=Net-Tension, CL=Cleavage, TO=Tear-Out, BE=Bearing

3.5.3.3 Analysis of bearing response (DBJ)

3.5.3.3.1 Correct calculation of ε_i^{br} To analyze the bearing response of the specimens it is necessary to calculate the value of the bearing stress (σ_i^{br}) and the bearing strain (ε_i^{br}) for each specimen. The value of these properties can be calculated as:

$$\sigma_i^{br} = \frac{P_i}{dh} \quad (3.17)$$

$$\varepsilon_i^{br} = \frac{d_i - d}{d} \quad (3.18)$$

where:

- σ_i^{br} is the bearing stress;
- ε_i^{br} is the bearing strain;
- P_i is the load;
- h is the thickness of the specimen;
- d and d_i are respectively the diameter of the hole before and during the loading.

The suggested expression [3] to evaluate the bearing strain in equation (3.18) is (see Figure 3.44):

$$\varepsilon_i^{br} = \frac{v - v_0}{d} = \frac{\delta_{LVDT}}{d} \quad (3.19)$$

where δ_{LVDT} is the displacement registered by the LVDT. However as showed by Camanho *et al.* [126] equations (3.18) and (3.19) are not completely equivalent. In fact the ASTM norm [3] neglects the deformation of the specimen. The correct equation that consider also the deformation of the specimen is:

$$\varepsilon_i^{br} = \frac{\delta_{LVDT} - \frac{PL_0}{whE_x^L}}{d} \quad (3.20)$$

where E_x^L is the Young modulus in the direction of the load P_i applied to the bolt. Note that the value of E_x^L has not be calculated but measured during the 3PB test.

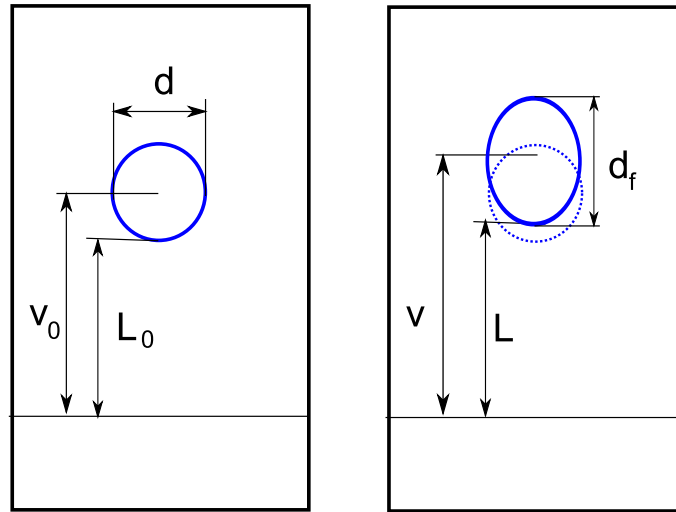


Figure 3.44: Correct calculation of bearing strain

3.5.3.3.2 Effective bearing strain In the following plots of the bearing stress as a function of the bearing strain, the later is not calculated directly using (3.20). Rather, the effective bearing strain is calculated using equation (3.20) applying a correction factor to evaluate the effective origin of the plot.

For this purpose the Bearing Chord Stiffness in the essentially linear part of the bearing stress/bearing strain curve was calculated as $E^{br} = \Delta\sigma^{br}/\Delta\varepsilon^{br}$. The effective origin is found by intersecting the chord stiffness line with the bearing strain axis.

3.5.3.3.3 Derived Properties The properties evaluated after the bearing test are:

- the Offset Bearing Strength at 2%, defined in [3] as the strength calculated as the intersection between the bearing stress-bearing strain curve and the offset of the chord line (offset=2%);

- the Initial Peak Bearing Strength: this is the strength at the initial peak;
- the First Non Linearity Bearing Strength: the strength at the first non-linearity in the curve.

Tables 3.25-3.27 show that these three values are practically the same and this is due to the particular material. It should be noted that the Ultimate Strength (defined as the maximum value of the strength) is not reported; this because the material shows an initial peak and after that the load does not increase but rather remains constant or decreases.

These properties depend also on the thickness of the specimens near the hole that are reported in Table 3.24.

Table 3.24: Thickness of bearing specimens

Specimen	h (mm)	Specimen	h (mm)	Specimen	h (mm)
E-4-1	6.45	P-4-1	6.85	V-4-1	6.65
E-4-2	6.45	P-4-2	6.80	V-4-2	6.50
E-4-3	6.45	P-4-3	6.80	V-4-3	6.80

3.5.3.3.4 Experimental results for bearing specimens

3.5.3.3.4.1 Specimens E-4-I The curves of the bearing stress as a function of the bearing strain are shown in Figure 3.45. Table 3.25 presents the bearing strengths.

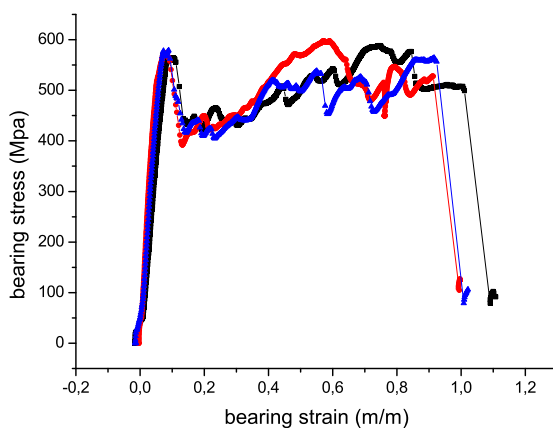


Figure 3.45: Bearing stress vs. bearing strain for E-4-I specimens

Table 3.25: Bearing response for E-4-I specimens

Specimen	OBS ^a 2%	IPBS ^b	FNLBS ^c
E-4-1	562	564	562
E-4-2	566	574	524
E-4-3	567	579	573
Average	565.278	572.556	552.947
STDV	2.544	7.379	25.794
CV (%)	0.450	1.289	4.665
IC (95%)	6.320	18.330	64.077

^a Offset Bearing Strength

^b Initial Peak Bearing Strength

^c First Non-Linearity Bearing Strength

3.5.3.3.4.2 Specimens P-4-I The curves of the bearing stress as a function of the bearing strain are shown in Figure 3.46. Table 3.26 presents the bearing strengths.

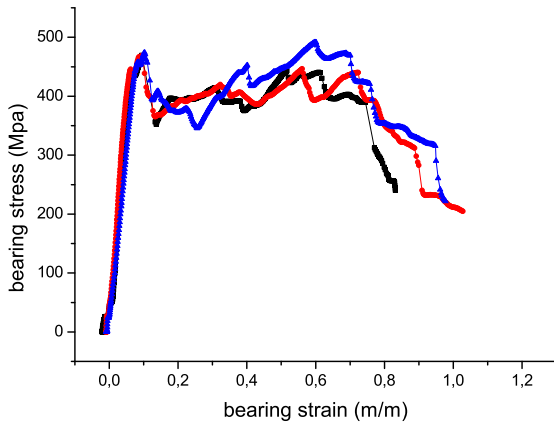


Figure 3.46: Bearing stress vs. bearing strain for P-4-I specimens

Table 3.26: Bearing response for P-4-I specimens

Specimen	OBS ^a 2%	IPBS ^b	FNLBS ^c
P-4-1	441	498	435
P-4-2	436	469	446
P-4-3	463	488	453
Average	446.507	485.010	444.542
STDV	14.656	14.734	9.214
CV (%)	3.282	3.038	2.073
IC (95%)	36.408	36.600	22.890

^a Offset Bearing Strength

^b Initial Peak Bearing Strength

^c First Non-Linearity Bearing Strength

3.5.3.3.4.3 Specimens V-4-I The curves of the bearing stress as a function of the bearing strain are shown in Figure 3.47. Table 3.27 presents the bearing strengths.

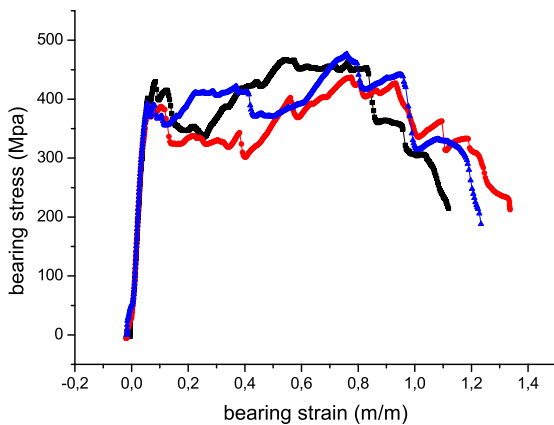


Figure 3.47: Bearing stress vs. bearing strain for V-4-I specimens

Table 3.27: Bearing response for V-4-I specimens

Specimen	OBS ^a 2%	IPBS ^b	FNLBS ^c
V-4-1	398	444	402
V-4-2	389	390	390
V-4-3	370	396	396
Average	385.531	409.918	395.982
STDV	14.062	29.370	6.038
CV (%)	3.647	7.165	1.525
IC (95%)	34.932	72.959	14.999

^a Offset Bearing Strength

^b Initial Peak Bearing Strength

^c First Non-Linearity Bearing Strength

3.5.3.4 Discussion on results for DBJ

In the previous sections, it was shown that specimens with the same geometry but different materials exhibit different failure modes. To compare these results it should

be noted that the laminates tested are all quasi-isotropic but they have different lay-ups and thickness and they were manufactured using different techniques. For these reasons, to compare the results the P/h parameter instead that the load P should be used.

In fact, the different failure modes (net-tension, shear-out, bearing) are related with different stresses defined for each failure mode as the net-tension stress, the shear-out stress and the bearing stress (see equations (2.1-2.3)). These stress are proportional to the P/h ratio and for this reason this parameter it is used to compare the behavior of different laminates.

Figures 3.48-3.51 show the load-displacement curves and the histograms of the $(P/h)_{Max}$ ratio for different specimens. The dashed rectangle in the histogram represents the 95% interval of confidence.

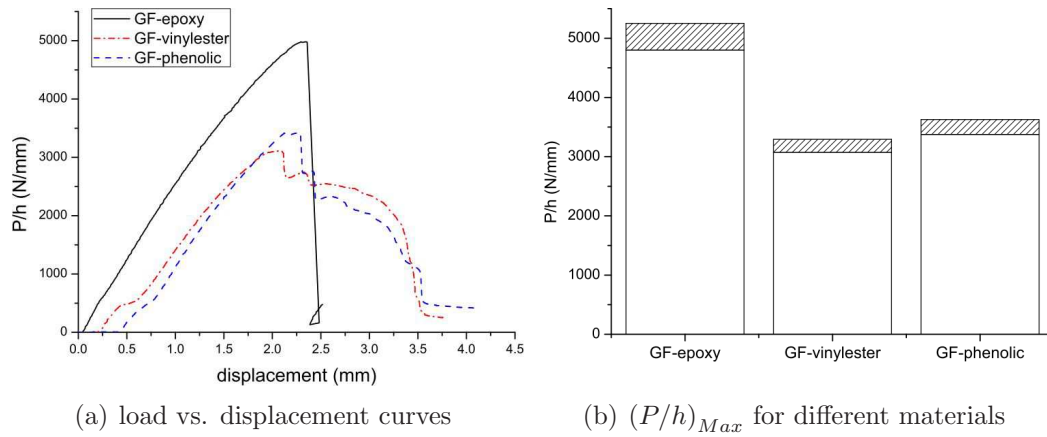


Figure 3.48: Comparison of results for specimens #1 (DBJ)

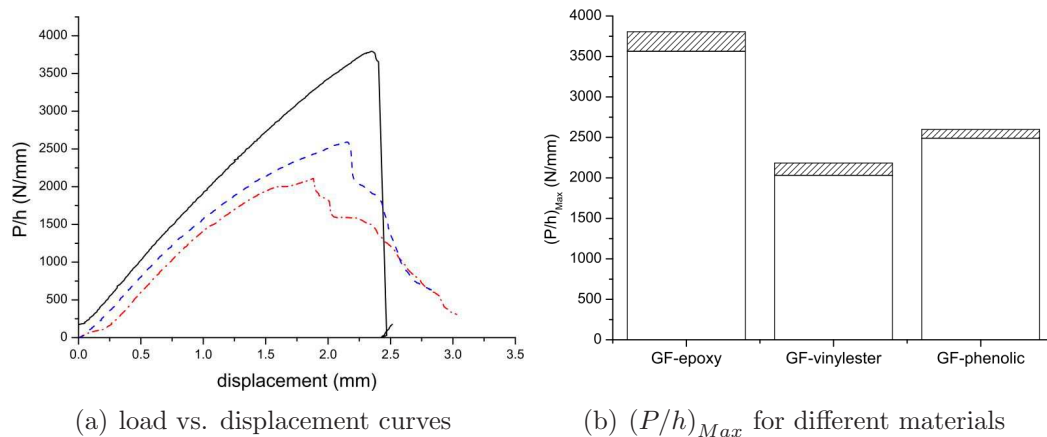


Figure 3.49: Comparison of results for specimens #2 (DBJ)

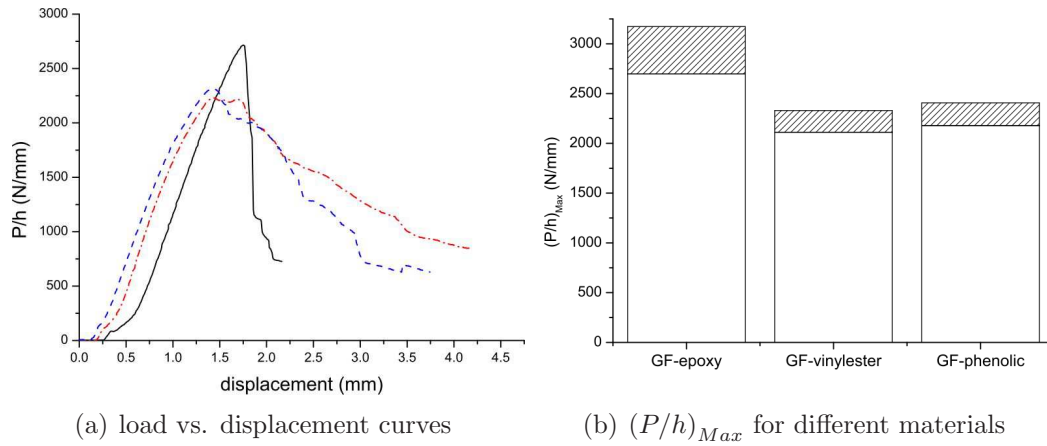


Figure 3.50: Comparison of results for specimens #3 (DBJ)

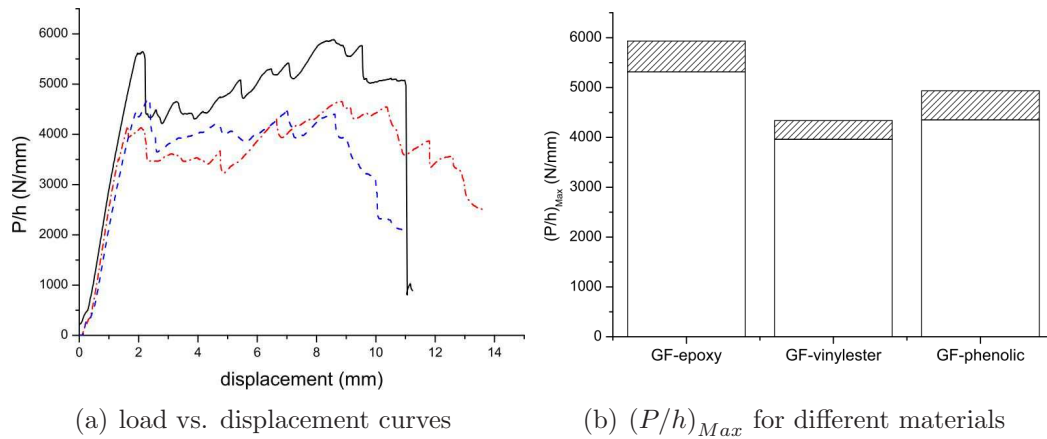


Figure 3.51: Comparison of results for specimens #4 (DBJ)

It is observed that the GF-epoxy specimens exhibit the highest strength. However, these specimens are characterized by a catastrophic failure while the other specimens are characterized by a progressive failure after the peak load.

The specimens manufactured with GF-phenolic and GF-vinylester show the same behavior after the peak load and this is due to the fact that both were manufactured using the vacuum resin infusion technique.

Regarding the strength of the joint, the GF-epoxy specimens show the best performances while the GF-vinylester show the worst.

3.5.4 Single-lap Bolted Joint

3.5.4.1 Description of the test

The test was effectuated according to the norm ASTM D5961/D5961M-01 [3].

The test was conducted using the INSTRON-4208 test machine in the laboratories of INEGI. The experimental set-up used is shown in Figure 3.52 .

The test machine is equipped with a 100kN load cell. For each type of configuration a strain gauge was used. The strain gauges were installed only in the specimens M1-M2-J-1 (see Section 3.3.2.3). The speed of the machine (displacement controlled test) was 2mm/min. The temperature of the room was 23°C and the relative humidity was 50% for all the duration of the tests.

After each test the damaged specimen was examined and the type of failure was identified. It was observed that the bolts did not suffer any plastic deformation.

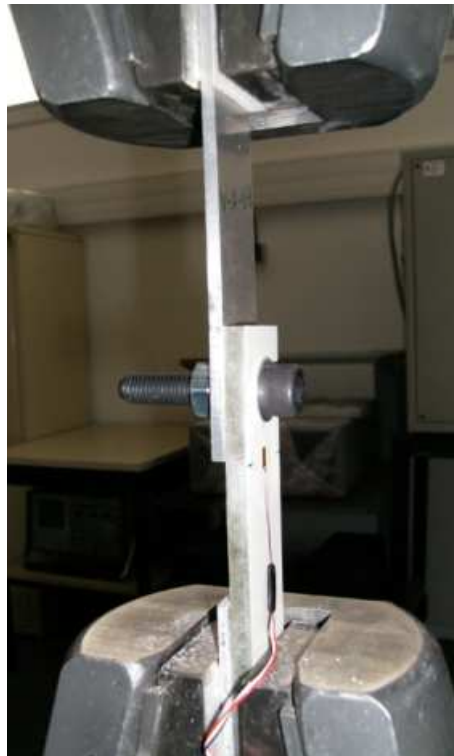


Figure 3.52: Equipment set-up for SBJ test

3.5.4.2 Specimens P-A-J-I

3.5.4.2.1 Specimens P-A-1-I Figure 3.53 shows the force-displacement curve for the specimens P-A-1-I. In Table 3.28 the value of the maximum load for each specimen and the statistics are reported. Figure 3.54 shows the force-strain curve for the specimen P-A-1-1. Figure 3.55 shows the damaged zones in the specimen P-A-1-2.

The composite is damaged and the aluminum deformed plastically, due to the effect of bending moment. Before complete failure, it is possible to note that some interlaminar cracks appear in the composite; these cracks are responsible for the reduction of the stiffness of the specimen. These consideration are valid for all the

specimens tested.

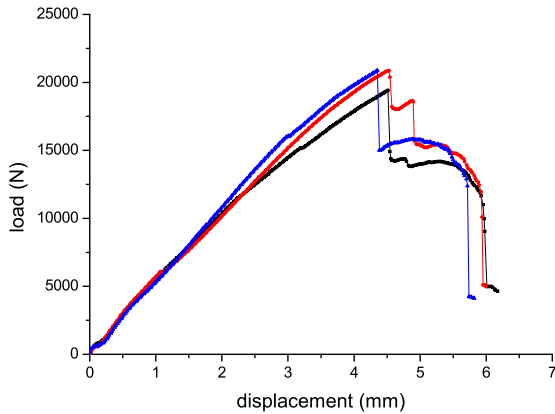


Figure 3.53: Load vs. displacement for P-A-1-I specimens

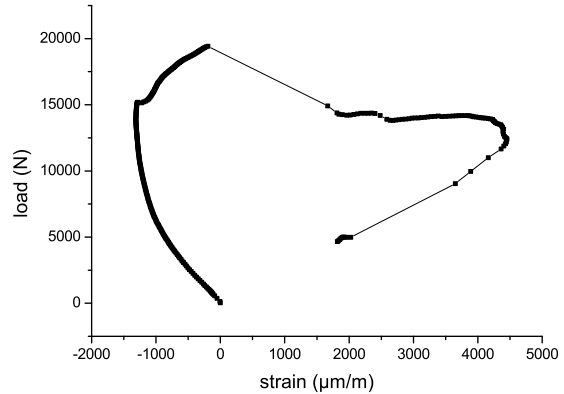


Figure 3.54: Load vs. strain for P-A-1-1 specimen

Table 3.28: Maximum load for P-A-1-I specimens

specimen	maximum load
P-A-1-1	19424
P-A-1-2	20876
P-A-1-3	20884
Average	20395
STDV	841
CV (%)	4
IC (95%)	2088



(a) side view



(b) top view

Figure 3.55: P-A-1-2 specimen after loading

3.5.4.2.2 Specimens P-A-2-I Figure 3.56 shows the force-displacement curve for the specimens P-A-2-I. In Table 3.29 the value of the maximum load for each specimen and the statistics are reported. Figure 3.57 shows the force-strain curve for the specimen P-A-2-1. Figure 3.58 shows the damaged zones in the specimen P-A-2-2.

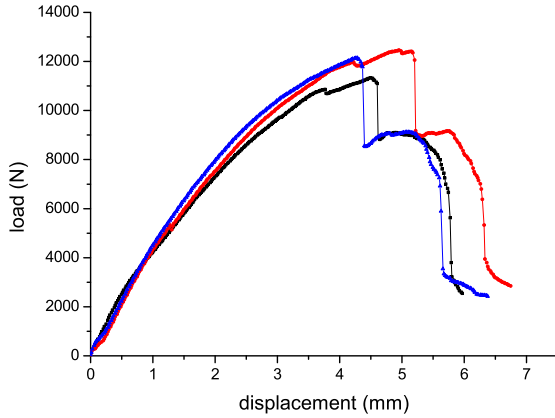


Figure 3.56: Load vs. displacement for P-A-2-I specimens

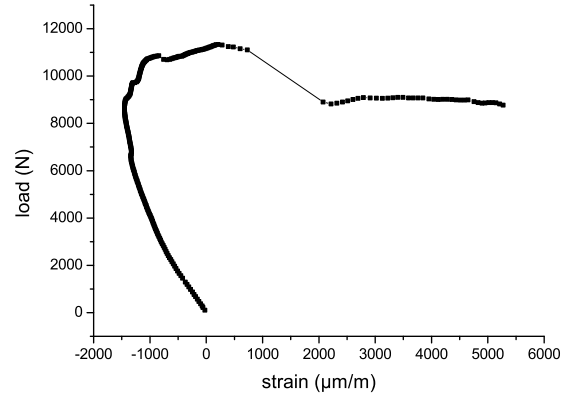


Figure 3.57: Load vs. strain for P-A-2-1 specimen

Table 3.29: Maximum load for P-A-2-I specimens

specimen	maximum load
P-A-2-1	11340
P-A-2-2	12456
P-A-2-3	12148
Average	11981
STDV	576
CV (%)	5
IC (95%)	1432



(a) side view



(b) top view

Figure 3.58: P-A-2-2 specimen after loading

3.5.4.2.3 Specimens P-A-3-I Figure 3.59 shows the force-displacement curve for the specimens P-A-3-I. In Table 3.30 the value of the maximum load for each specimen and the statistics are reported. Figure 3.60 shows the force-strain curve for the specimen P-A-3-1. Figure 3.61 shows the damaged zones in the specimen P-A-3-3.

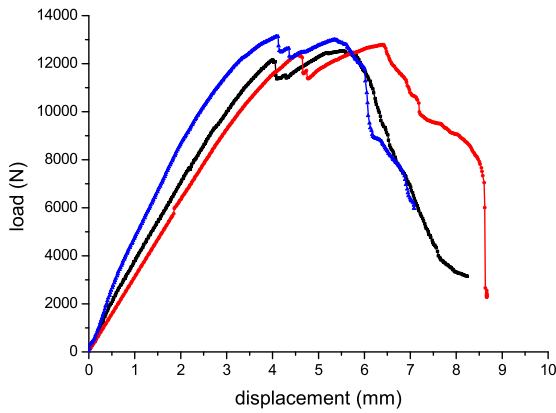


Figure 3.59: Load vs. displacement for P-A-3-I specimens

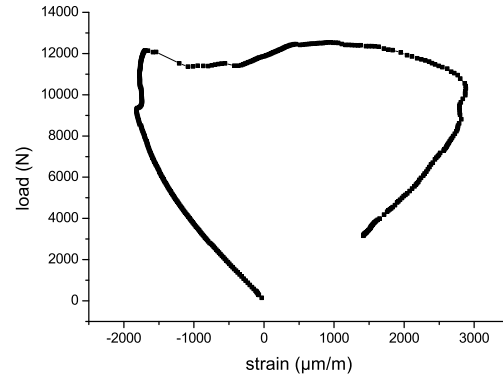


Figure 3.60: Load vs. strain for P-A-3-1 specimen

Table 3.30: Maximum load for P-A-3-I specimens

specimen	maximum load
P-A-3-1	12540
P-A-3-2	12788
P-A-3-3	13132
Average	12820
STDV	297
CV (%)	2
IC (95%)	739



Figure 3.61: P-A-3-3 specimen after loading

3.5.4.2.4 Specimens P-A-4-I Figure 3.62 shows the force-displacement curve for the specimens P-A-4-I. In Table 3.31 the value of the maximum load for each specimen and the statistics are reported. Figure 3.63 shows the force-strain curve for the specimen P-A-4-1. Figure 3.64 shows the damaged zones in the specimen P-A-4-2.

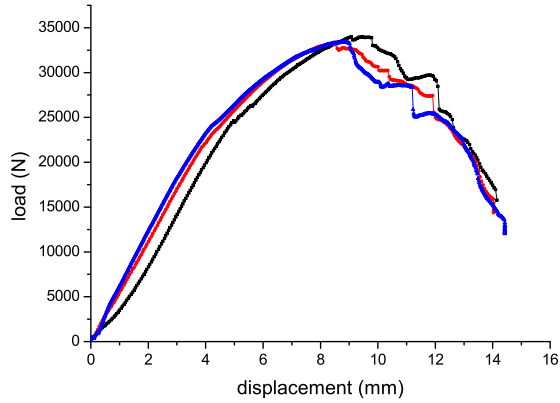


Figure 3.62: Load vs. displacement for P-A-4-I specimens

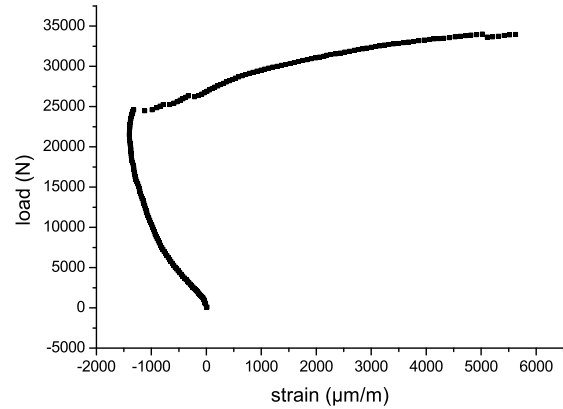


Figure 3.63: Load vs. strain for P-A-4-1 specimen

Table 3.31: Maximum load for P-A-4-I specimens

specimen	maximum load
P-A-4-1	34012
P-A-4-2	33236
P-A-4-3	33404
Average	33551
STDV	408
CV (%)	1
IC (95%)	1014



(a) side view



(b) top view

Figure 3.64: P-A-4-2 specimen after loading

3.5.4.3 Specimens P-S-J-I

3.5.4.3.1 Specimens P-S-1-I Figure 3.65 shows the force-displacement curve for the specimens P-S-1-I. In Table 3.32 the value of the maximum load for each specimen and the statistics are reported. Figure 3.66 shows the force-strain curve for the specimen P-S-1-1. Figure 3.67 shows the damaged zones in the specimen P-S-1-2.

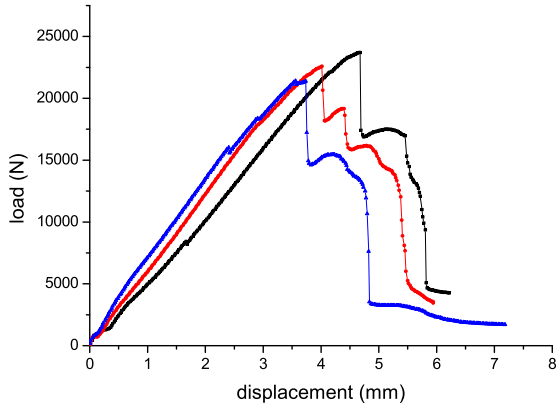


Figure 3.65: Load vs. displacement for P-S-1-I specimens

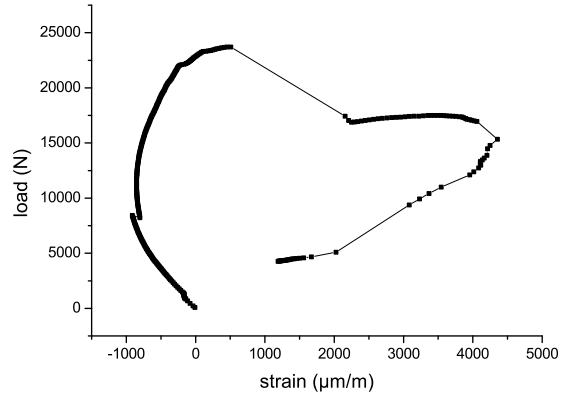


Figure 3.66: Load vs. strain for P-S-1-1 specimen

Table 3.32: Maximum load for P-S-1-I specimens

specimen	maximum load
P-S-1-1	23708
P-S-1-2	22592
P-S-1-3	21412
Average	22571
STDV	1148
CV (%)	5
IC (95%)	2852



(a) side view



(b) top view

Figure 3.67: P-S-1-2 specimen after loading

3.5.4.3.2 Specimens P-S-2-I Figure 3.68 shows the force-displacement curve for the specimens P-S-2-I. In Table 3.33 the value of the maximum load for each specimen and the statistics are reported. Figure 3.69 shows the force-strain curve for the specimen P-S-2-1. Figure 3.70 shows the damaged zones in the specimen P-S-2-2.

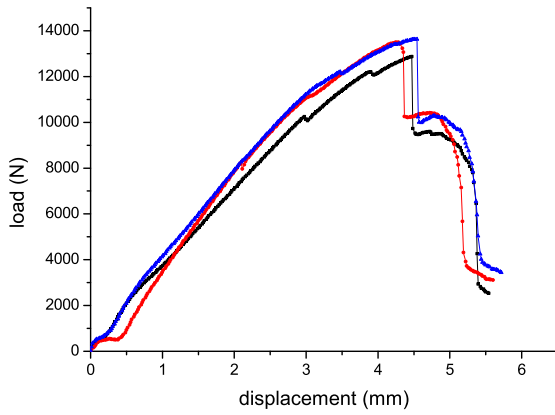


Figure 3.68: Load vs. displacement for P-S-2-I specimens

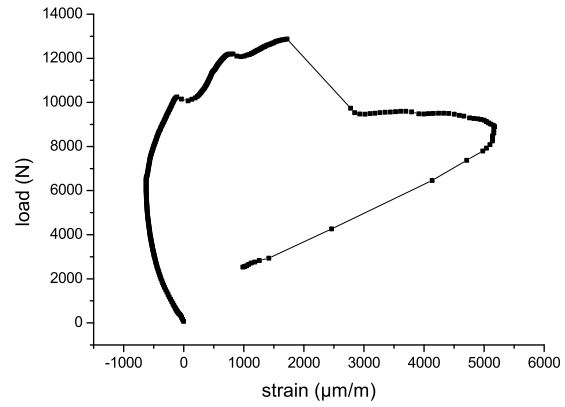


Figure 3.69: Load vs. strain for P-S-2-1 specimen

Table 3.33: Maximum load for P-S-2-I specimens

specimen	maximum load
P-S-2-1	12872
P-S-2-2	13500
P-S-2-3	13632
Average	13335
STDV	406
CV (%)	3
IC (95%)	1009



(a) side view



(b) top view

Figure 3.70: P-S-2-2 specimen after loading

3.5.4.3.3 Specimens P-S-3-I Figure 3.71 shows the force-displacement curve for the specimens P-S-3-I. In Table 3.34 the value of the maximum load for each specimen and the statistics are reported. Figure 3.72 shows the force-strain curve for the specimen P-S-3-1. Figure 3.73 shows the damaged zones in the specimen P-S-3-2.

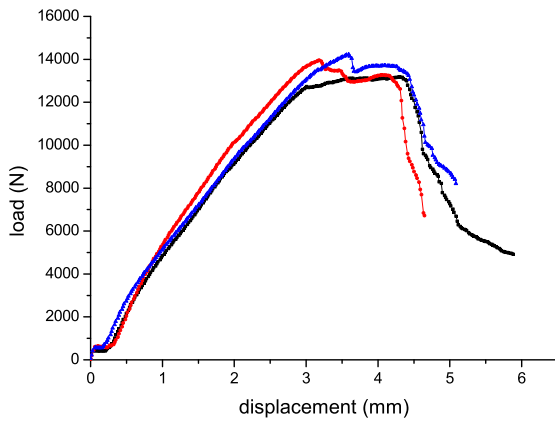


Figure 3.71: Load vs. displacement for P-S-3-I specimens

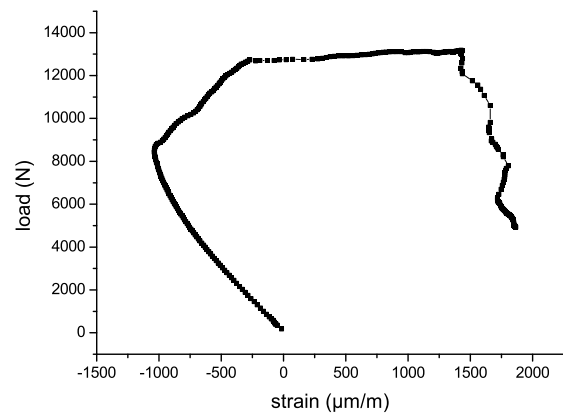


Figure 3.72: Load vs. strain for P-S-3-1 specimen

Table 3.34: Maximum load for P-S-3-I specimens

specimen	maximum load
P-S-3-1	13180
P-S-3-2	13960
P-S-3-3	14232
Average	13791
STDV	546
CV (%)	4
IC (95%)	1356



(a) side view



(b) top view

Figure 3.73: P-S-3-2 specimen after loading

3.5.4.3.4 Specimens P-S-4-I Figure 3.74 shows the force-displacement curve for the specimens P-S-4-I. In Table 3.35 the value of the maximum load for each specimen and the statistics are reported. Figure 3.75 shows the force-strain curve for the specimen P-S-4-1. Figure 3.76 shows the damaged zones in the specimen P-S-4-2.

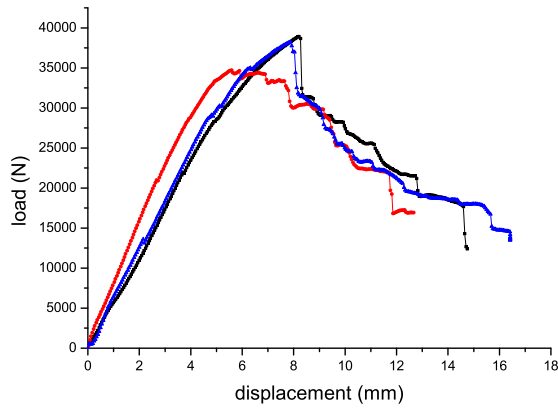


Figure 3.74: Load vs. displacement for P-S-4-I specimens

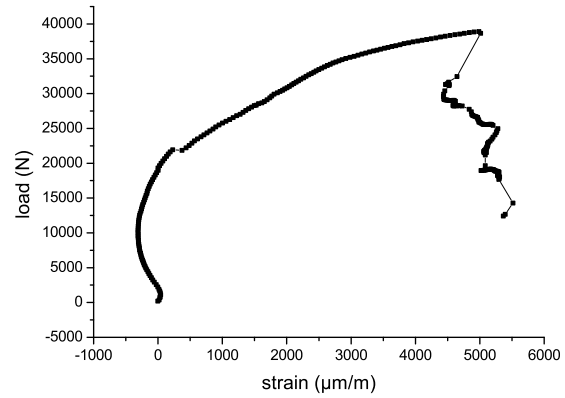


Figure 3.75: Load vs. strain for P-S-4-1 specimen

Table 3.35: Maximum load for P-S-4-I specimens

specimen	maximum load
P-S-4-1	38916
P-S-4-2	34704
P-S-4-3	38220
Average	37280
STDV	2258
CV (%)	6
IC (95%)	5609



(a) side view



(b) top view

Figure 3.76: P-S-4-2 specimen after loading

3.5.4.4 Specimens V-A-J-I

3.5.4.4.1 Specimens V-A-1-I Figure 3.77 shows the force-displacement curve for the specimens V-A-1-I. In Table 3.36 the value of the maximum load for each specimen and the statistics are reported. Figure 3.78 shows the force-strain curve for the specimen V-A-1-1. Figure 3.79 shows the damaged zones in the specimen V-A-1-3.

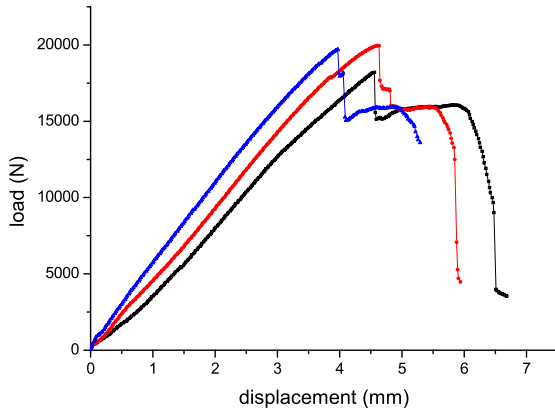


Figure 3.77: Load vs. displacement for V-A-1-I specimens

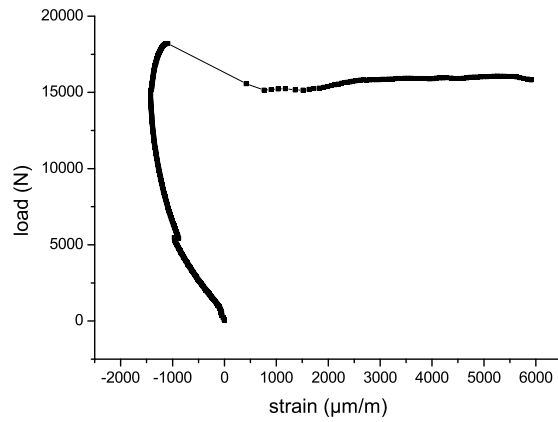


Figure 3.78: Load vs. strain for V-A-1-1 specimen

Table 3.36: Maximum load for V-A-1-I specimens

specimen	maximum load
V-A-1-1	18212
V-A-1-2	19964
V-A-1-3	19708
Average	19295
STDV	946
CV (%)	5
IC (95%)	2351



(a) side view



(b) top view

Figure 3.79: V-A-1-3 specimen after loading

3.5.4.4.2 Specimens V-A-2-I Figure 3.80 shows the force-displacement curve for the specimens V-A-2-I. In Table 3.37 the value of the maximum load for each specimen and the statistics are reported. Figure 3.81 shows the force-strain curve for the specimen V-A-2-1. Figure 3.82 shows the damaged zones in the specimen V-A-2-1.

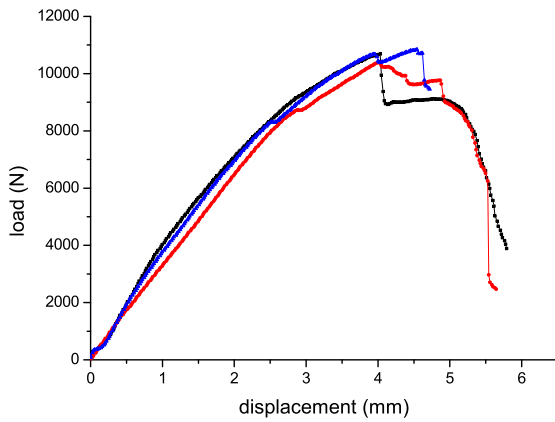


Figure 3.80: Load vs. displacement for V-A-2-I specimens

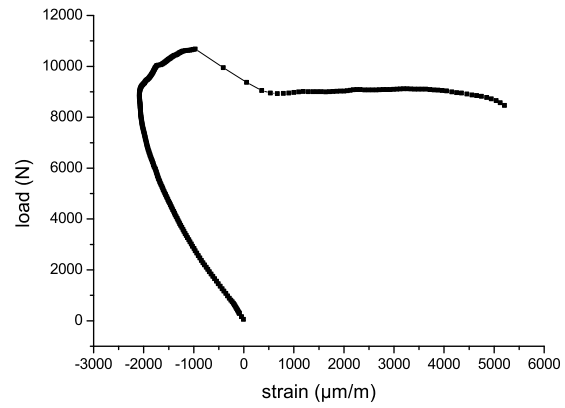


Figure 3.81: Load vs. strain for V-A-2-1 specimen

Table 3.37: Maximum load for V-A-2-I specimens

specimen	maximum load
V-A-2-1	10684
V-A-2-2	10396
V-A-2-3	10840
Average	10640
STDV	225
CV (%)	2
IC (95%)	560



(a) side view



(b) top view

Figure 3.82: V-A-2-1 specimen after loading

3.5.4.4.3 Specimens V-A-3-I Figure 3.83 shows the force-displacement curve for the specimens V-A-3-I. In Table 3.38 the value of the maximum load for each specimen and the statistics are reported. Figure 3.84 shows the force-strain curve for the specimen V-A-3-1. Figure 3.85 shows the damaged zones in the specimen V-A-3-3.

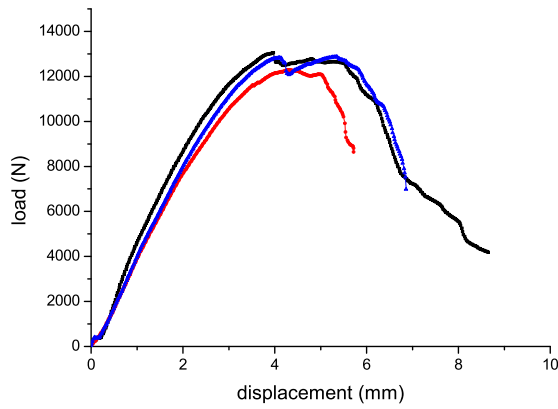


Figure 3.83: Load vs. displacement for V-A-3-I specimens

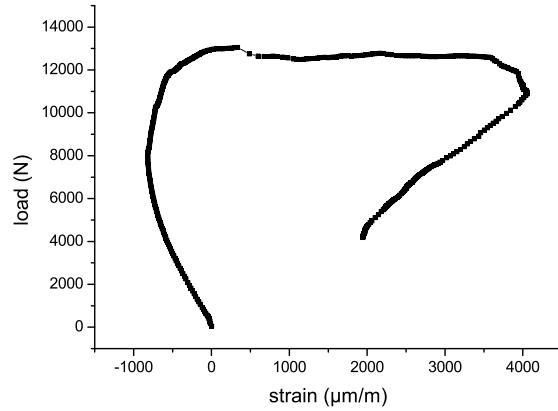


Figure 3.84: Load vs. strain for V-A-3-1 specimen

Table 3.38: Maximum load for V-A-3-I specimens

specimen	maximum load
V-A-3-1	13052
V-A-3-2	12292
V-A-3-3	12872
Average	12739
STDV	397
CV (%)	3
IC (95%)	987



(a) side view



(b) top view

Figure 3.85: V-A-3-3 specimen after loading

3.5.4.4.4 Specimens V-A-4-I Figure 3.86 shows the force-displacement curve for the specimens V-A-4-I. In Table 3.39 the value of the maximum load for each specimen and the statistics are reported. Figure 3.87 shows the force-strain curve for the specimen V-A-4-1. Figure 3.88 shows the damaged zones in the specimen V-A-4-2.

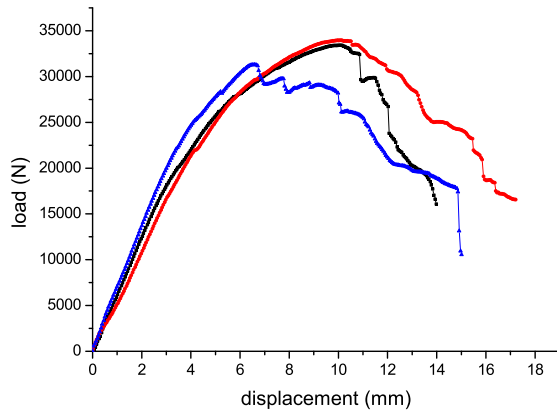


Figure 3.86: Load vs. displacement for V-A-4-I specimens

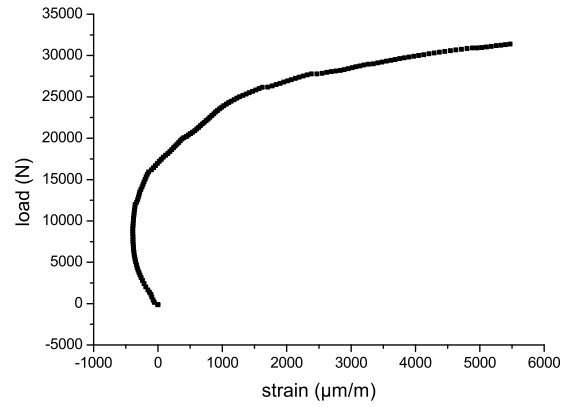


Figure 3.87: Load vs. strain for V-A-4-1 specimen

Table 3.39: Maximum load for V-A-4-I specimens

specimen	maximum load
V-A-4-1	33416
V-A-4-2	33968
V-A-4-3	31320
Average	32901
STDV	1397
CV (%)	4
IC (95%)	3470



(a) side view



(b) top view

Figure 3.88: V-A-4-2 specimen after loading

3.5.4.5 Specimens V-S-J-I

3.5.4.5.1 Specimens V-S-1-I Figure 3.89 shows the force-displacement curve for the specimens V-S-1-I. In Table 3.40 the value of the maximum load for each specimen and the statistics are reported. Figure 3.90 shows the force-strain curve for the specimen V-S-1-1. Figure 3.91 shows the damaged zones in the specimen V-S-1-2.

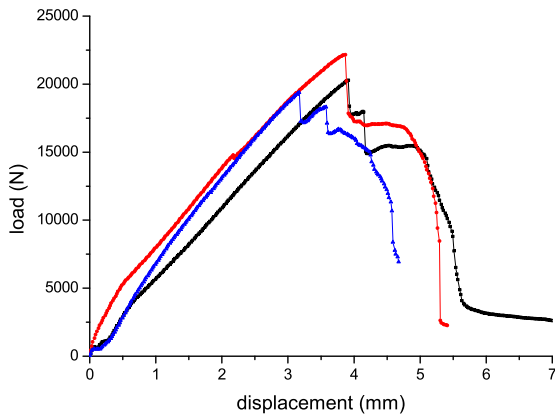


Figure 3.89: Load vs. displacement for V-S-1-I specimens

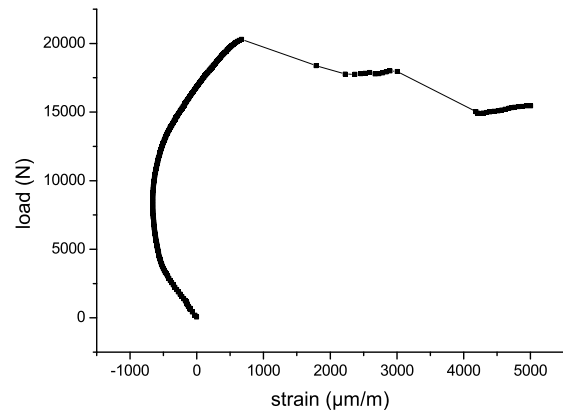


Figure 3.90: Load vs. strain for V-S-1-1 specimen

Table 3.40: Maximum load for V-S-1-I specimens

specimen	maximum load
V-S-1-1	20296
V-S-1-2	22156
V-S-1-3	19384
Average	20612
STDV	1413
CV (%)	7
IC (95%)	3509



(a) side view



(b) top view

Figure 3.91: V-S-1-2 specimen after loading

3.5.4.5.2 Specimens V-S-2-I Figure 3.92 shows the force-displacement curve for the specimens V-S-2-I. In Table 3.41 the value of the maximum load for each specimen and the statistics are reported. Figure 3.93 shows the force-strain curve for the specimen V-S-2-1. Figure 3.94 shows the damaged zones in the specimen V-S-2-2.

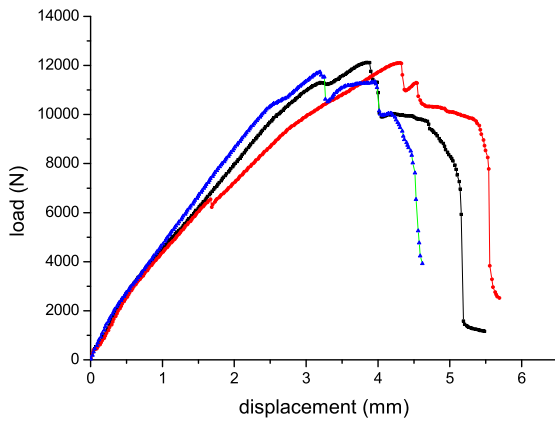


Figure 3.92: Load vs. displacement for V-S-2-I specimens

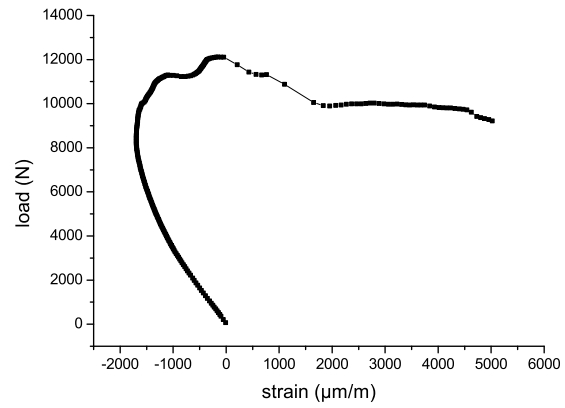


Figure 3.93: Load vs. strain for V-S-2-1 specimen

Table 3.41: Maximum load for V-S-2-I specimens

specimen	maximum load
V-S-2-1	12120
V-S-2-2	12108
V-S-2-3	11732
Average	11987
STDV	221
CV (%)	2
IC (95%)	548



(a) side view



(b) top view

Figure 3.94: V-S-2-2 specimen after loading

3.5.4.5.3 Specimens V-S-3-I Figure 3.95 shows the force-displacement curve for the specimens V-S-3-I. In Table 3.42 the value of the maximum load for each specimen and the statistics are reported. Figure 3.96 shows the force-strain curve for the specimen V-S-3-1. Figure 3.97 shows the damaged zones in the specimen V-S-3-3.

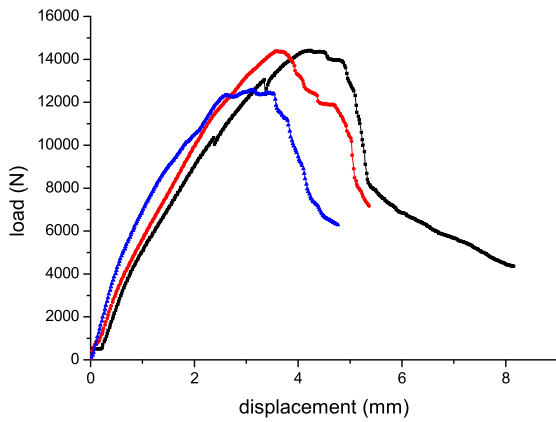


Figure 3.95: Load vs. displacement for V-S-3-I specimens

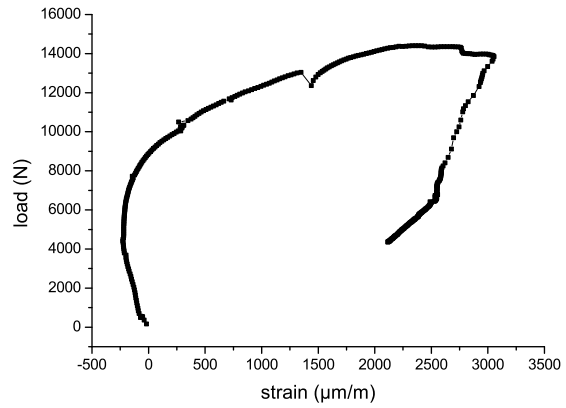


Figure 3.96: Load vs. strain for V-S-3-1 specimen

Table 3.42: Maximum load for V-S-3-I specimens

specimen	maximum load
V-S-3-1	14408
V-S-3-2	14384
V-S-3-3	12568
Average	13787
STDV	1055
CV (%)	8
IC (95%)	2622

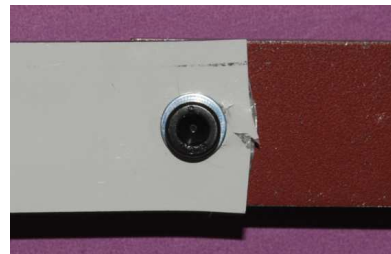


Figure 3.97: V-S-3-3 specimen after loading

3.5.4.5.4 Specimens V-S-4-I Figure 3.98 shows the force-displacement curve for the specimens V-S-4-I. In Table 3.43 the value of the maximum load for each specimen and the statistics are reported. Figure 3.99 shows the force-strain curve for the specimen V-S-4-1. Figure 3.100 shows the damaged zones in the specimen V-S-4-3.

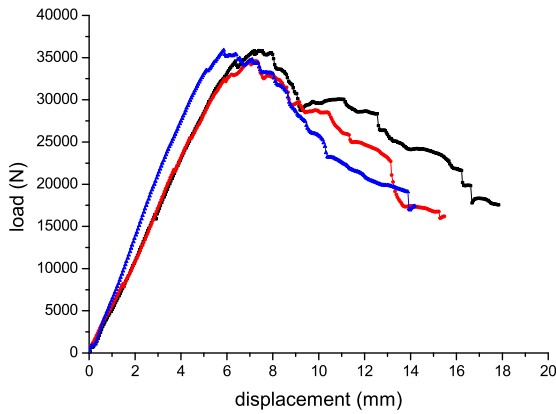


Figure 3.98: Load vs. displacement for V-S-4-I specimens

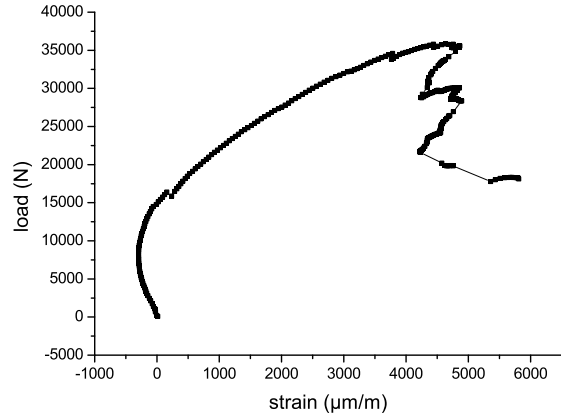


Figure 3.99: Load vs. strain for V-S-4-1 specimen

Table 3.43: Maximum load for V-S-4-I specimens

specimen	maximum load
V-S-4-1	35844
V-S-4-2	34732
V-S-4-3	35876
Average	35484
STDV	651
CV (%)	2
IC (95%)	1618



(a) side view



(b) top view

Figure 3.100: V-S-4-3 specimen after loading

3.5.4.6 Specimens V-P-J-I

3.5.4.6.1 Specimens V-P-1-I Figure 3.101 shows the force-displacement curve for the specimens V-P-1-I. In Table 3.44 the value of the maximum load for each specimen and the statistics are reported. Figure 3.102 shows the force-strain curve for the specimen V-P-1-1. Note that in this case there are two curves: one is the strain detected by the strain gage installed on vinylester, the other is detected by the strain gage installed on phenolic. Figure 3.103 shows the damaged zones in the specimen V-P-1-3 and V-P-1-2 respectively.

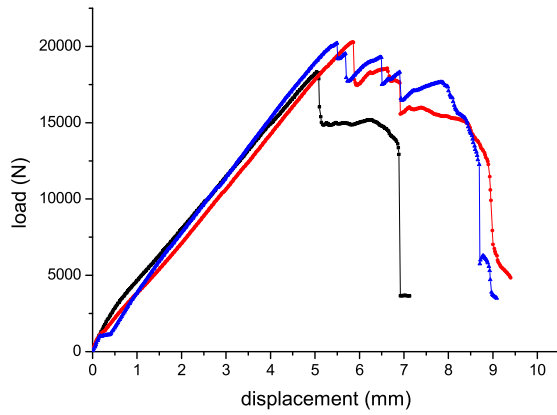


Figure 3.101: Load vs. displacement for V-P-1-I specimens

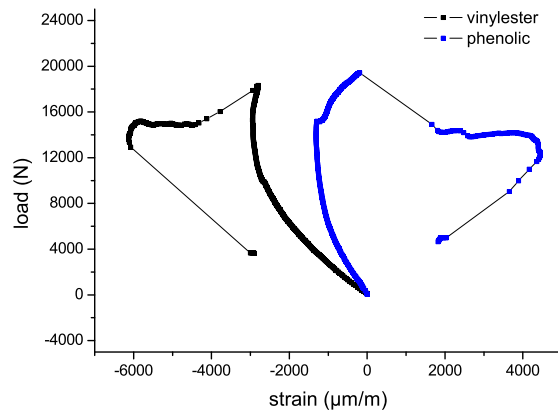


Figure 3.102: Load vs. strain for V-P-1-1 specimen

Table 3.44: Maximum load for V-P-1-I specimens

specimen	maximum load
V-P-1-1	18324
V-P-1-2	20292
V-P-1-3	20204
Average	19607
STDV	1112
CV (%)	6
IC (95%)	2762



(a) V-P-1-3 specimen (side view)



(b) V-P-1-2 specimen (top view)

Figure 3.103: V-P-1-I specimens after loading

3.5.4.6.2 Specimens V-P-2-I Figure 3.104 shows the force-displacement curve for the specimens V-P-2-I. In Table 3.45 the value of the maximum load for each specimen and the statistics are reported. Figure 3.105 shows the force-strain curve for the specimen V-P-2-1. Figure 3.106 shows the damaged zones in the specimen V-P-2-1.

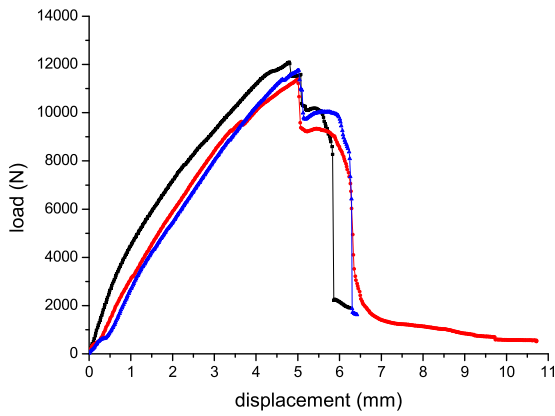


Figure 3.104: Load vs. displacement for V-P-2-I specimens

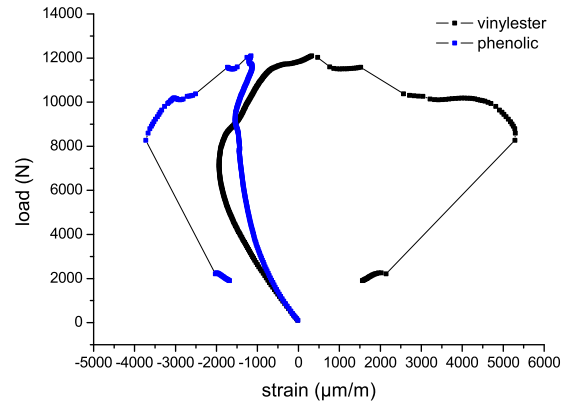


Figure 3.105: Load vs. strain for V-P-2-1 specimen

Table 3.45: Maximum load for V-P-2-I specimens

specimen	maximum load
V-P-2-1	12100
V-P-2-2	11376
V-P-2-3	11752
Average	11743
STDV	362
CV (%)	3
IC (95%)	899



Figure 3.106: V-P-2-1 specimen after loading

3.5.4.6.3 Specimens V-P-3-I Figure 3.107 shows the force-displacement curve for the specimens V-P-3-I. In Table 3.46 the value of the maximum load for each specimen and the statistics are reported. Figure 3.108 shows the force-strain curve for the specimen V-P-3-1. Figure 3.109 shows the damaged zones in the specimen V-P-3-2.

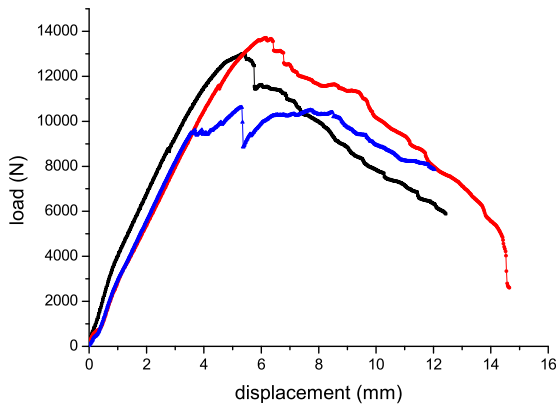


Figure 3.107: Load vs. displacement for V-P-3-I specimens

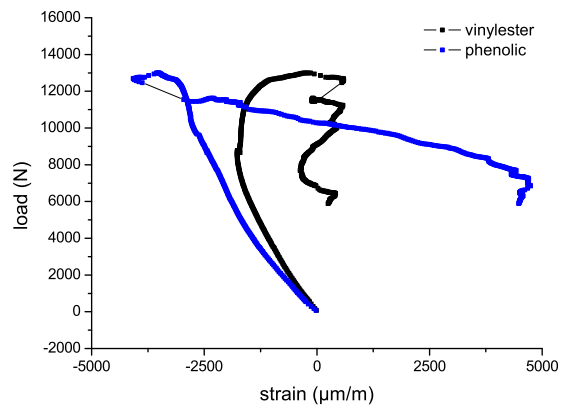


Figure 3.108: Load vs. strain for V-P-3-1 specimen

Table 3.46: Maximum load for V-P-3-I specimens

specimen	maximum load
V-P-3-1	13000
V-P-3-2	13712
V-P-3-3	10616
Average	12443
STDV	1622
CV (%)	13
IC (95%)	4028



(a) side view



(b) top view



(c) bottom view

Figure 3.109: V-P-3-2 specimen after loading

3.5.4.6.4 Specimens V-P-4-I Figure 3.110 shows the force-displacement curve for the specimens V-P-4-I. In Table 3.47 the value of the maximum load for each specimen and the statistics are reported. Figure 3.111 shows the force-strain curve for the specimen V-P-4-1. Figure 3.112 shows the damaged zones in the specimen V-P-4-1.

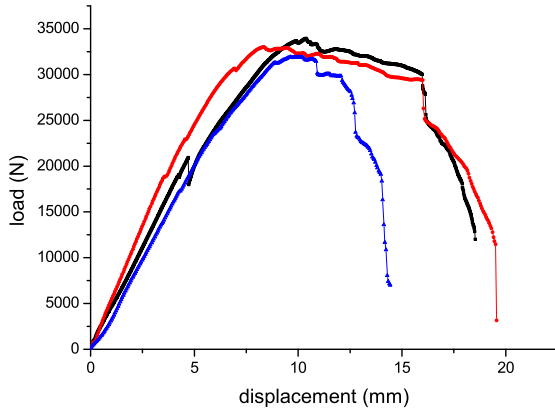


Figure 3.110: Load vs. displacement for V-P-4-I specimens

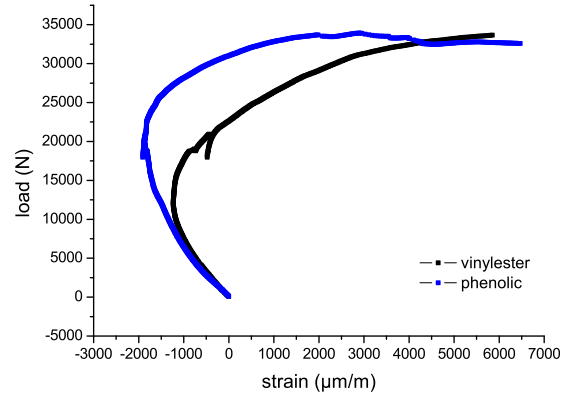


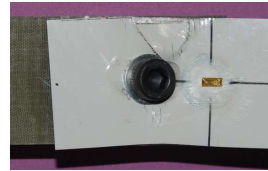
Figure 3.111: Load vs. strain for V-P-4-1 specimen

Table 3.47: Maximum load for V-P-4-I specimens

specimen	maximum load
V-P-4-1	33936
V-P-4-2	33020
V-P-4-3	31916
Average	32957
STDV	1011
CV (%)	3
IC (95%)	2513



(a) side view



(b) top view



(c) bottom view

Figure 3.112: V-P-4-1 specimen after loading

3.5.4.7 Analysis of bearing response (SBJ)

The analysis of bearing response is performed using the same procedure applied in the analysis of the DBJ bearing specimen.

The calculation of the bearing strain is effectuated as described in 3.5.3.3.1. In analogy with equation (3.19) the following formula to evaluate the bearing strain is used:

$$\varepsilon_i^{br} = \frac{\delta_{LVDT} - \frac{PL_0}{whE_{x,M1}^L} - \frac{PL_0}{whE_{x,M2}^L}}{d} \quad (3.21)$$

In this case there are two materials to consider, M1 and M2 (see Figure 3.113). It should be noted that when the second material is a metal as steel the correc-

tion $-PL_0/whE_{x,M2}^L$ can be neglected. However when M2 is aluminum or another composite this correction must be used.

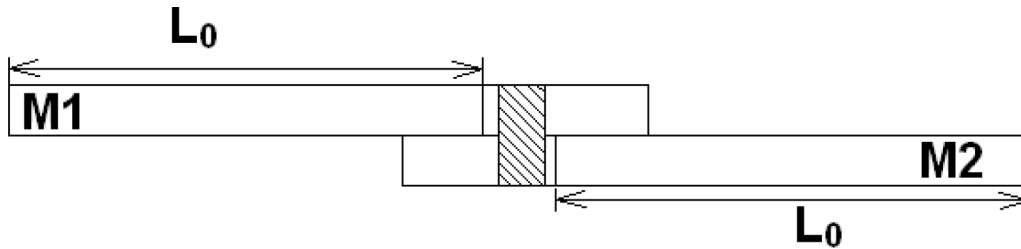


Figure 3.113: Bearing correction for SBJ

3.5.4.7.1 Specimens P-A-4-I Figure 3.114 shows the curves of the bearing stress as a function of the effective bearing strain. Table 3.48 reports the derived properties with statistics. These properties are illustrated in Section 3.5.3.3.3.

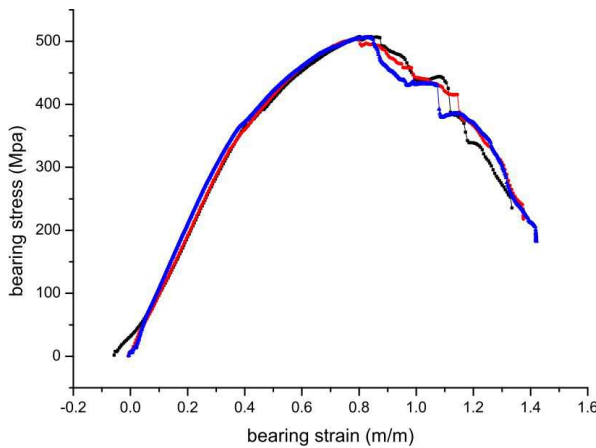


Figure 3.114: Bearing stress vs. bearing strain for P-A-4-I specimens

Table 3.48: Bearing response for P-A-4-I specimens

Specimen	OBS ^a 2%	IPBS ^b	FNLBS ^c
P-S-4-1	419	587	320
P-S-4-2	427	522	310
P-S-4-3	468	570	350
Average	438	560	327
STDV	26.531	33.710	20.817
CV (%)	6.054	6.023	6.372
IC (95%)	65.907	83.739	51.711

^a Offset Bearing Strength

^b Initial Peak Bearing Strength

^c First Non-Linearity Bearing Strength

3.5.4.7.2 Specimens P-S-4-I Figure 3.115 shows the curves of the bearing stress as a function of the effective bearing strain. Table 3.49 reports the derived properties with statistics.

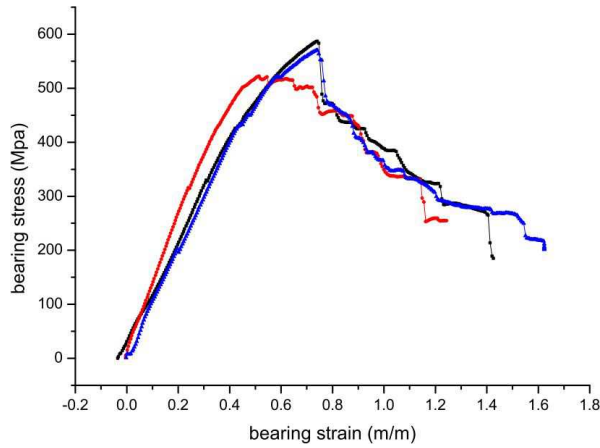


Figure 3.115: Bearing stress vs. bearing strain for P-S-4-I specimens

Table 3.49: Bearing response for P-S-4-I specimens

Specimen	OBS ^a 2%	IPBS ^b	FNLBS ^c
P-S-4-1	419	587	320
P-S-4-2	427	522	310
P-S-4-3	468	570	350
Average	438	560	327
STDV	26.531	33.710	20.817
CV (%)	6.054	6.023	6.372
IC (95%)	65.907	83.739	51.711

^a Offset Bearing Strength

^b Initial Peak Bearing Strength

^c First Non-Linearity Bearing Strength

3.5.4.7.3 Specimens V-A-4-I Figure 3.116 shows the curves of the bearing stress as a function of the effective bearing strain. Table 3.50 reports the derived properties with statistics.

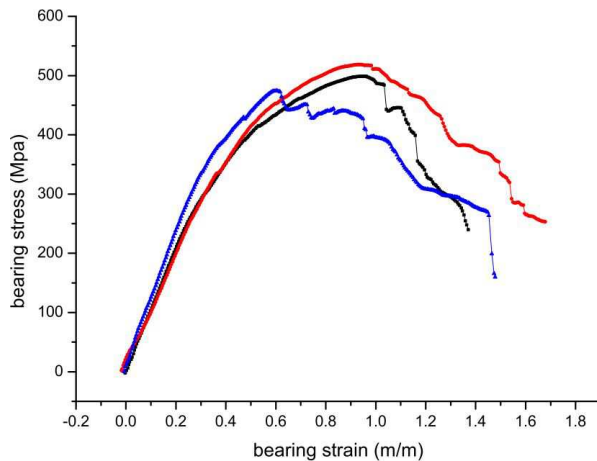


Figure 3.116: Bearing stress vs. bearing strain for V-A-4-I specimens

Table 3.50: Bearing response for V-A-4-I specimens

Specimen	OBS ^a 2%	IPBS ^b	FNLBS ^c
V-A-4-1	290	499	278
V-A-4-2	320	518	259
V-A-4-3	377	474	298
Average	329	497	278
STDV	44.110	22.068	19.502
CV (%)	13.410	4.440	7.007
IC (95%)	109.576	54.820	48.446

^a Offset Bearing Strength

^b Initial Peak Bearing Strength

^c First Non-Linearity Bearing Strength

3.5.4.7.4 Specimens V-S-4-I Figure 3.117 shows the curves of the bearing stress as a function of the effective bearing strain. Table 3.51 reports the derived properties with statistics.

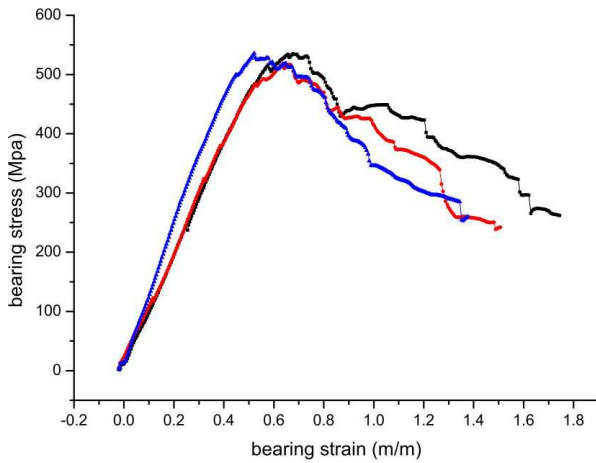


Figure 3.117: Bearing stress vs. bearing strain for V-S-4-I specimens

Table 3.51: Bearing response for V-S-4-I specimens

Specimen	OBS ^a 2%	IPBS ^b	FNLBS ^c
V-S-4-1	497	534	455
V-S-4-2	472	514	420
V-S-4-3	478	535	427
Average	482	527	434
STDV	13.051	11.846	18.520
CV (%)	2.706	2.245	4.267
IC (95%)	32.421	29.428	46.007

^a Offset Bearing Strength

^b Initial Peak Bearing Strength

^c First Non-Linearity Bearing Strength

3.5.4.7.5 Specimens V-P-4-I Figure 3.118 shows the curves of the bearing stress as a function of the effective bearing strain. Table 3.52 reports the derived properties with statistics.

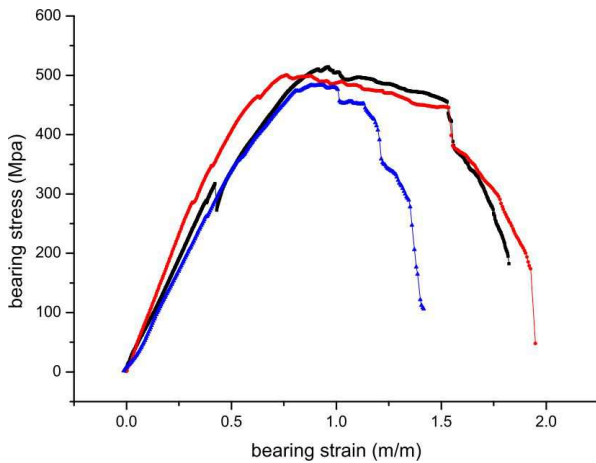


Figure 3.118: Bearing stress vs. bearing strain for V-P-4-I specimens

Table 3.52: Bearing response for V-P-4-I specimens

Specimen	OBS ^a 2%	IPBS ^b	FNLBS ^c
V-P-4-1	330	512	317
V-P-4-2	352	498	322
V-P-4-3	365	483	320
Average	349	498	320
STDV	17.692	14.503	2.517
CV (%)	5.069	2.914	0.787
IC (95%)	43.949	36.027	6.252

^a Offset Bearing Strength

^b Initial Peak Bearing Strength

^c First Non-Linearity Bearing Strength

3.5.4.8 Discussion on results for SBJ

To compare different SBJ specimens the load P is considered and not the P/h ratio because the vinylester and the phenolic laminates have approximately the same thickness.

Figure 3.122 shows the load-displacement curves for different materials combinations. The curve related to the double bolted joint and the curves related to

the single bolted joints are shown for each type of specimen and for each material. Figure 3.123 shows the histograms of the strength for different single-bolted joint. The dashed rectangle represents the confidence interval at 95%.

The DBJ configuration exhibits the highest value of the failure load for all types of specimens, except for the bearing specimen (specimen #4, see Figures 3.122(g)-3.122(h) and Figures 3.123(g)-3.123(h)). Surprisingly, for this type of specimen the failure load of the DBJ is the lowest. This result obtained for multi-material joint is not in agreement to the previous work presented in literature for other material (carbon-epoxy) [126]. However, it may be possible to explain this behavior taking into account that two effects occurs a single bolted joint is loaded:

- the first is that bending effects reduce the contact between the bolt and the surfaces of the hole when increasing the load as described in Figure 3.119. This create a stress concentration on the edge of the hole and reduce the strength of the joint;
- the second is that bending effects change the failure modes from in plane failure mode to in-plane/pull-through failure modes. This increase the load capacity of the specimen.

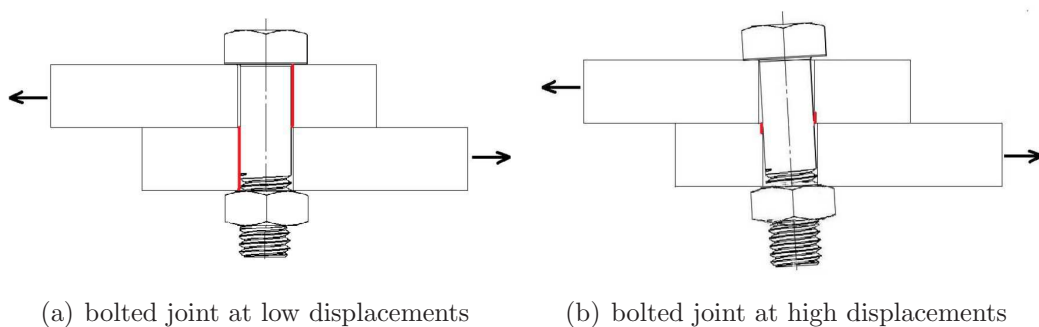


Figure 3.119: Load case of a bolted joint

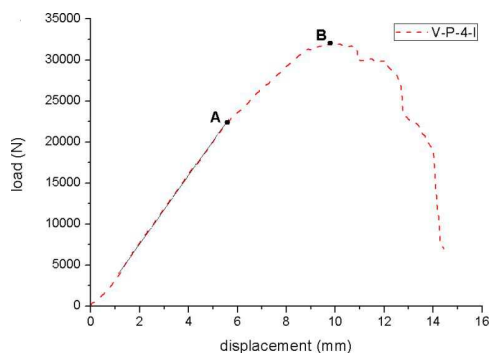


Figure 3.120: Load vs. displacement for V-P-4-I specimens



Figure 3.121: Aluminium-vinylester connection after being loaded

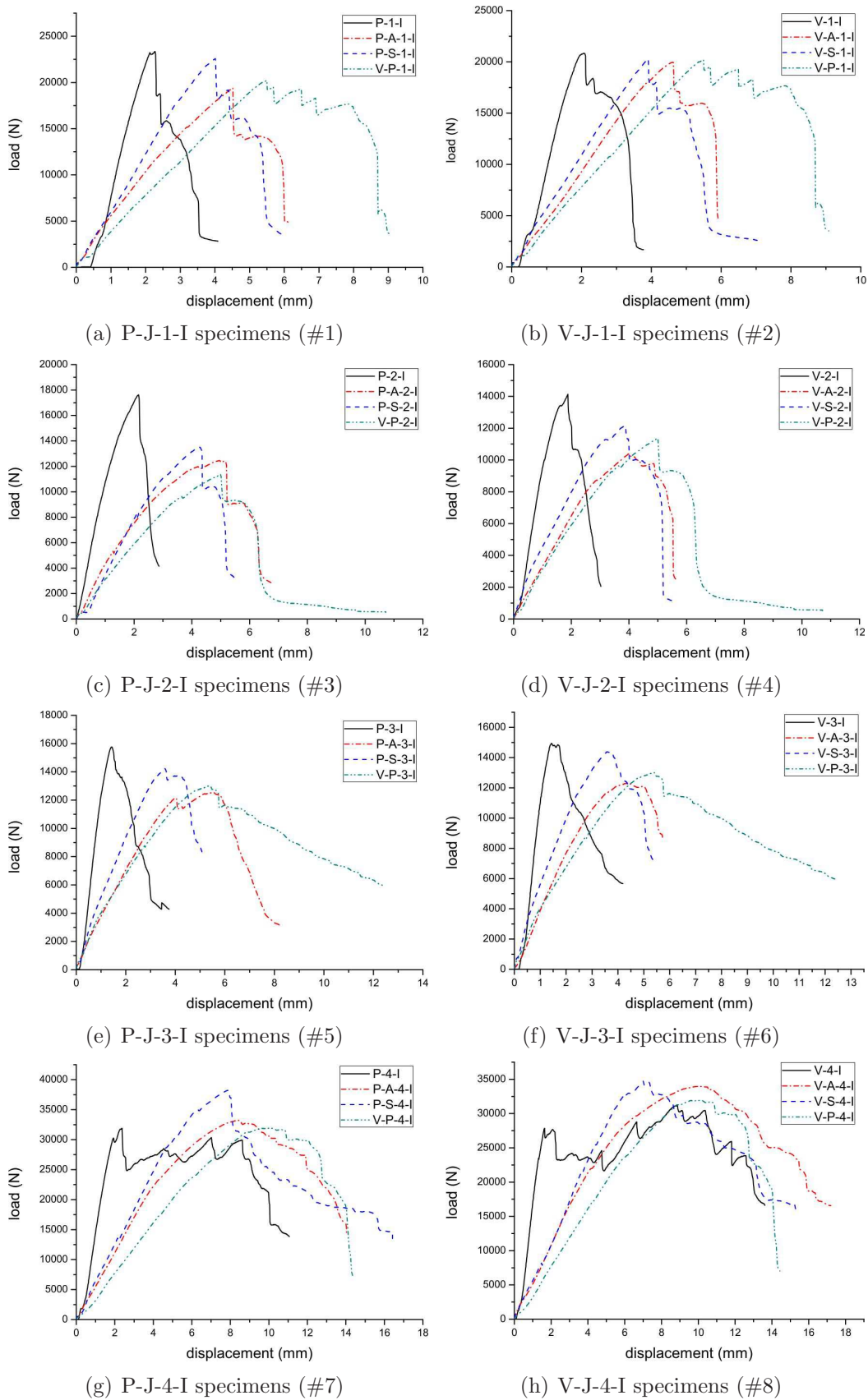


Figure 3.122: Comparison of results for SBJ

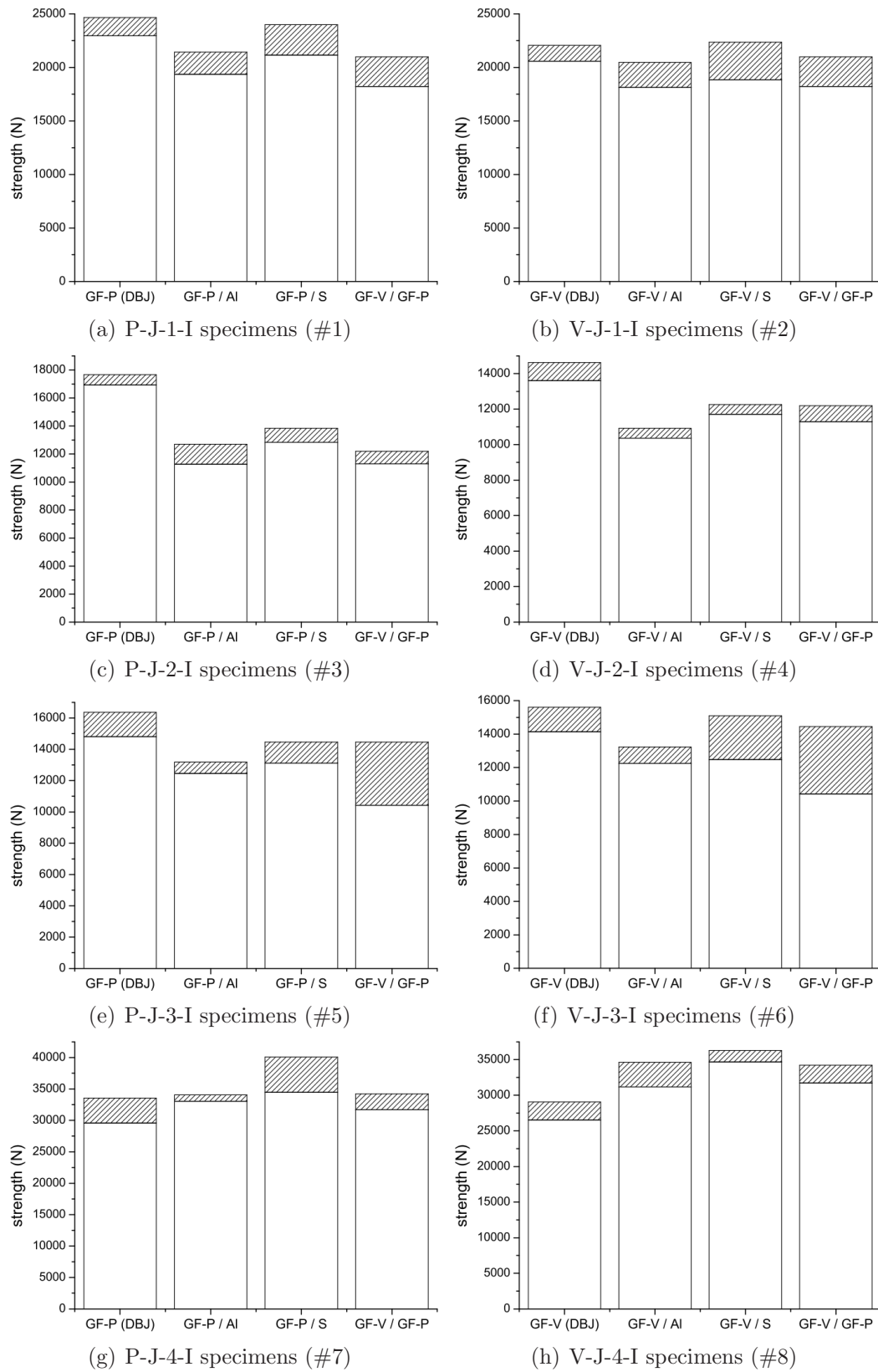


Figure 3.123: Strength for SBJ specimens

Figures 3.120 and 3.121 clarify this second effect. Figure 3.120 shows the load-displacement curve for the V-A-4-I specimen. After the linear region, in the point A of the curve, delamination occurs and it reduces the stiffness of the specimen. The point B is the peak of the curve where the bearing became predominant. Figure 3.121 shows the joint with the delamination. It should be noted the deformation of the specimen due to the bending moment. It may be noted also the bearing and the penetration of the washer into the material. This penetration is responsible for the increase of the load carried by the joint.

3.5.4.9 Design charts

In Section 3.5.4.8 a discussion on the relative performance of each material was presented. However, it is more useful summarize the results using design charts that can easily relate the strength of the joint to the geometric parameters d , w and e . The experimental points were fitted using a smoothing spline imposing that when $w/d \geq 5$ and $e/d \geq 4$ the strength is equal to the maximum the bearing strength. These fitting functions allow to generate for each material combination the contour plots of the P/dh as function of w/d and e/d . The variable P/dh is used as normalized load and has the same meaning of the bearing stress. It should be pointed out that the charts presented are affected by some limitations:

- the experimental points used, were generated for diameters of the bolts of 6mm and 10mm. The curves then, can be used for all the diameter between 6mm and 10mm, that are practically those used in industry. For diameter out of the range the estimation may not be sufficiently accurate.
- it is assumed that the flexural compliances of the two joined parts of a SBJ are comparable. If one of the two parts has a much higher compliance, the joints does not exhibit high displacements out-of-plane when subjected to external load; in this case, the DBJ chart should be used.
- as showed by Camanho *et al.* [126] the diameter influences the characteristic distance in compression and in tension. In the present charts this effect is not taken into account and it is considered negligible for the range of diameters under investigation (6mm and 10mm).

Figures 3.124-3.131 show the design charts for the following cases: DBJ Glass-Epoxy, DBJ Glass-Vinylester, DBJ Glass-Phenolic, SBJ Glass-Vinylester/Aluminum, SBJ Glass-Vinylester/Steel, SBJ Glass-Phenolic/Aluminum, SBJ Glass-Phenolic/Steel, SBJ Glass-Vinylester/Glass-Phenolic.

For all the materials (or material combinations), with the exception of the Glass-Epoxy, when w/d or e/d increase, the strength of the joint increases. Only for Glass-Epoxy joint when w/d decreases the strength increases. This is due to the fact that Glass-Epoxy were manufactured using prepregs and these exhibit a much higher strength if tension failure occurs. However the failure should be always the bearing because a net-tension failure produces an instable failure.

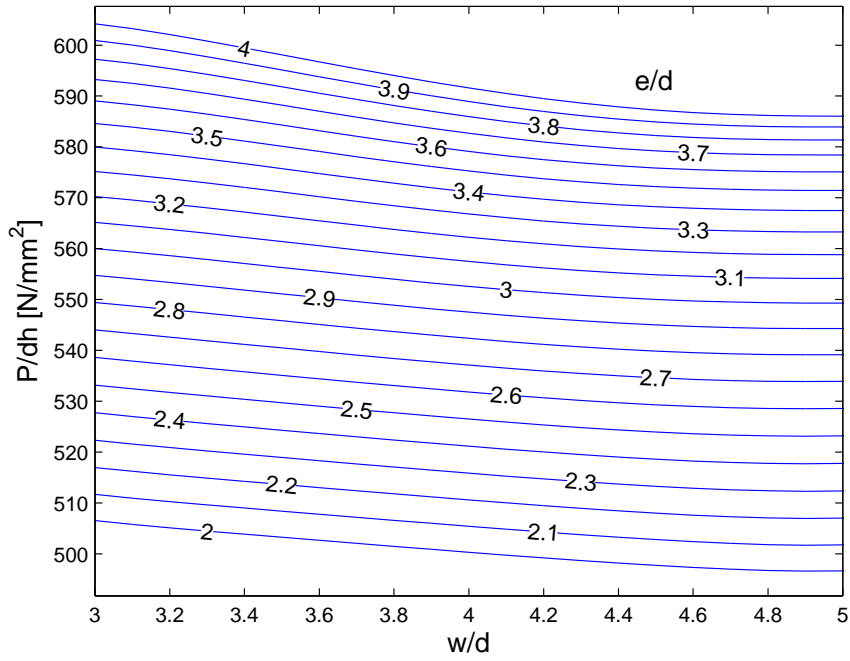


Figure 3.124: DBJ Glass-Epoxy design chart

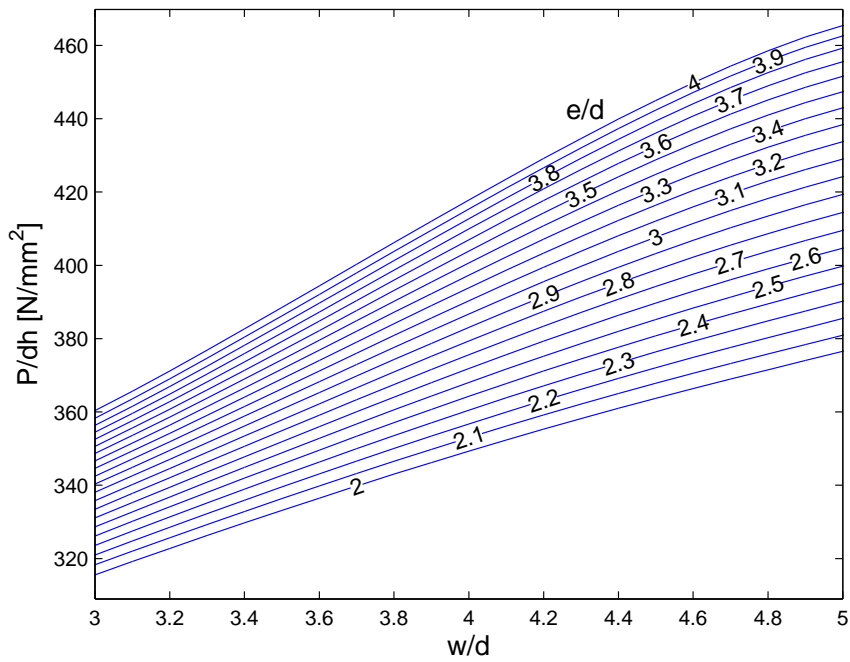


Figure 3.125: DBJ Glass-Vinylester design chart

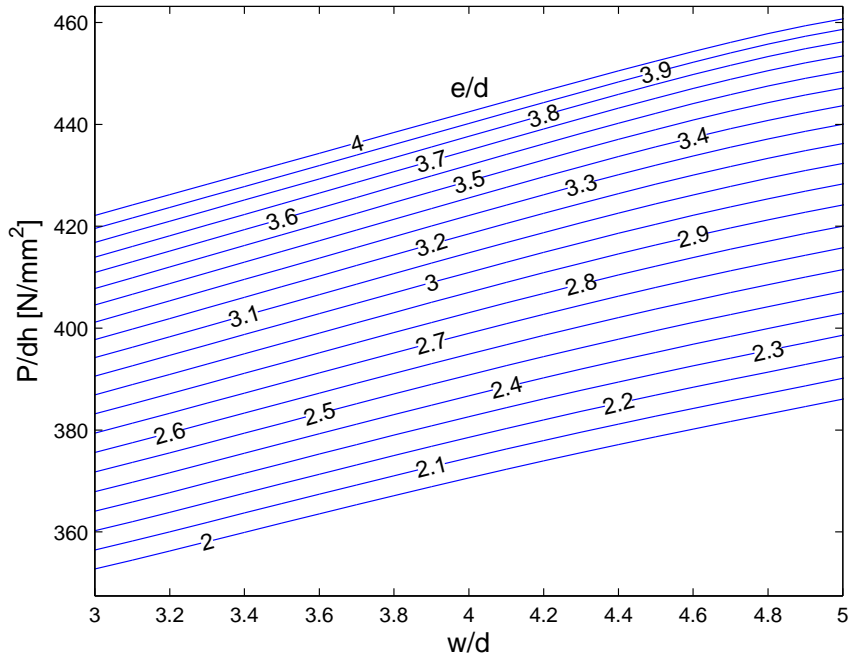


Figure 3.126: DBJ Glass-Phenolic design chart

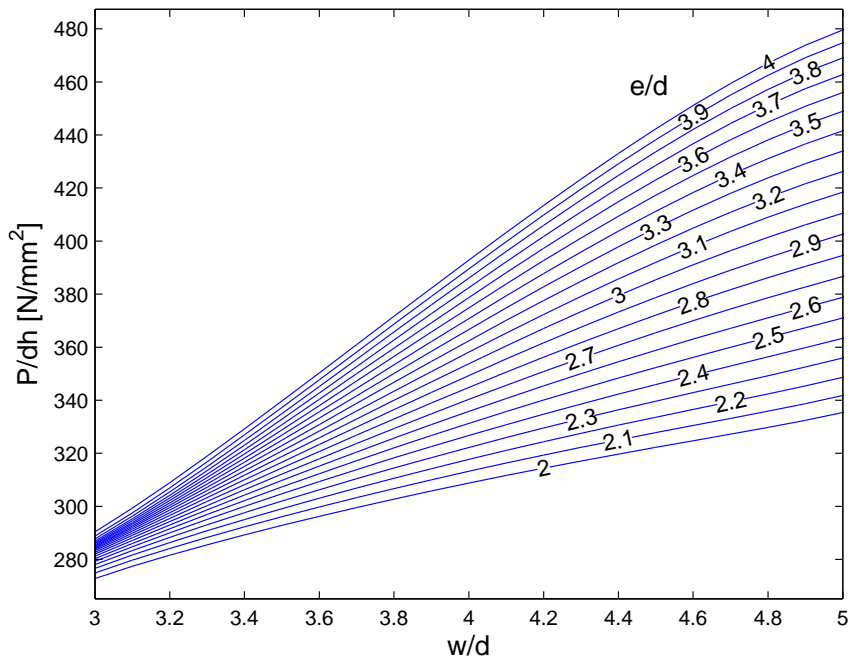


Figure 3.127: SBJ Glass-Vinylester/Aluminum design chart

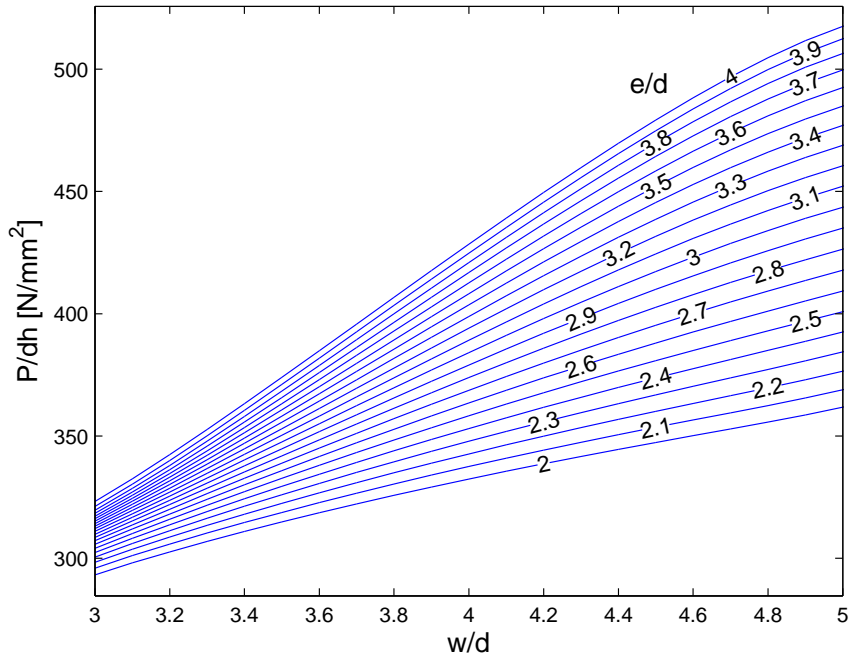


Figure 3.128: SBJ Glass-Vinylester/Steel design chart

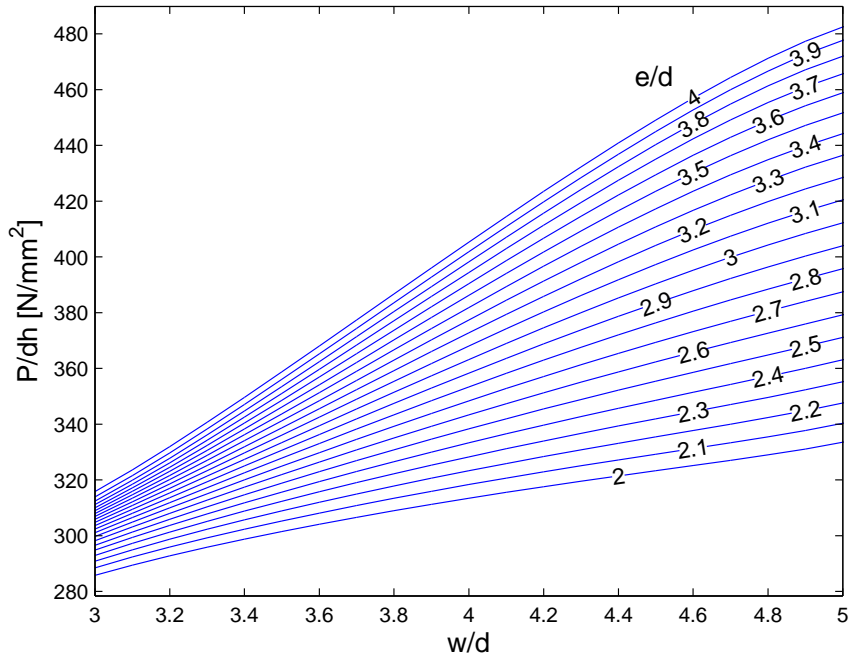


Figure 3.129: SBJ Glass-Phenolic/Aluminum design chart

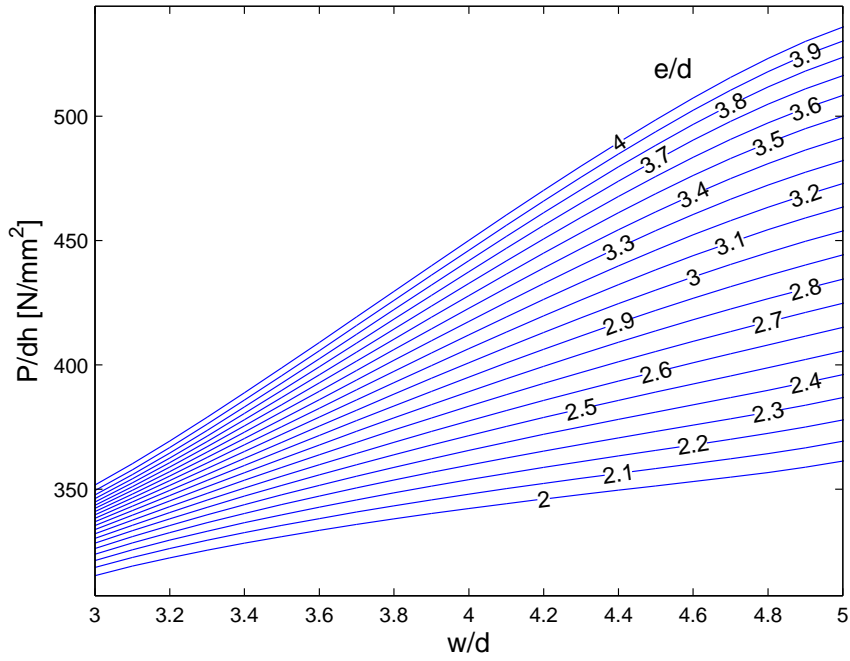


Figure 3.130: SBJ Glass-Phenolic/Steel design chart

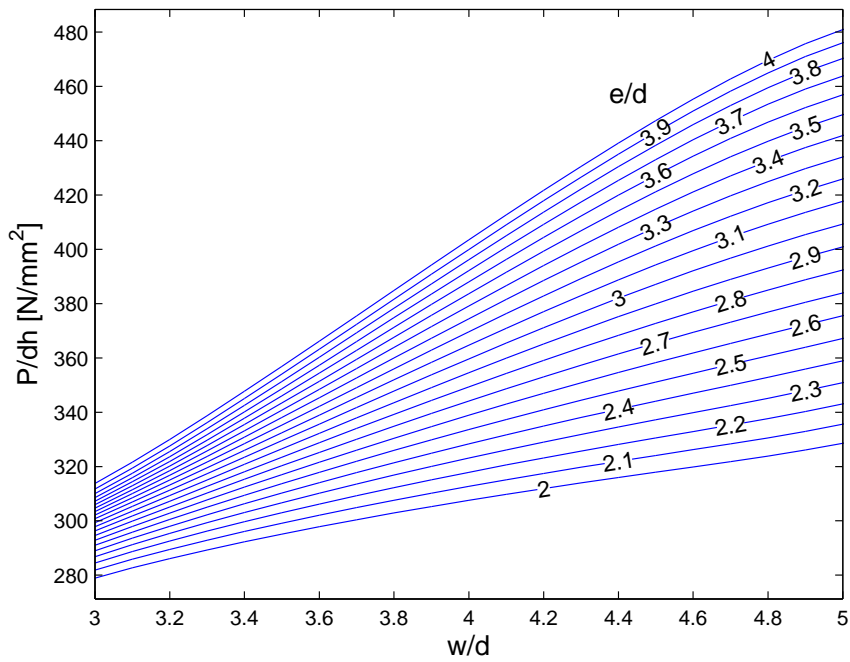


Figure 3.131: SBJ Glass-Vinylester/Glass-Phenolic design chart

3.5.5 Pull-Trough Test

3.5.5.1 Description of the test

The pull-through is performed following the norm *Standard Test Method for Measuring the Fastener Pull-Through Resistance of a Fiber-Reinforced Polymer Matrix Composite* [131].

This test method contains two procedures, *A* and *B*. Since procedure *A* is more complex and has inherent problems associated with the flexural stiffness of the specimen to test, the specimens procedure *B* is used.

The test was conducted using the INSTRON-4208 testing machine in the laboratories of INEGI. Figure 3.132 shows the experimental set-up used. The testing machine was equipped with a load cell of 100kN. The speed of the machine (displacement controlled test) is 2mm/min. The temperature of the room was 23°C and the relative humidity was 50% for all the duration of the tests.



Figure 3.132: Equipment set-up for PT test

After each test the damaged specimen was examined and the type of failure was identified.

The test results depend on Clearance Hole parameter (C_b). This is the diameter of the plate that it is used in procedure *B* of the test. In the tests performed $C_b = 30\text{mm}$. For each specimen are reported the dimensions, the ratio of the Clearance Hole Diameter C_b to Fastener Hole Diameter d , and the ratio of the Fastener Hole Diameter to the thickness of the specimen (h). Specimens are squares with a length of 120mm.

3.5.5.2 Derived properties

The curve of the load as a function of the displacement for a pull-through test is used to identify three important characteristics that are:

- the Initial Sub-Critical Failure Force: the force at the first sub-critical failure of the specimen;
- the Initial Sub-Critical Failure Displacement: the displacement at the first sub-critical failure of the specimen;
- the Failure Force: the maximum force attained in the test.

The specimen shows a first failure mode (generally delamination) at a low load. After delamination, the specimen is able to support increasing loads. This point is identified in the curve by a changing of the linearity or by a peak.

3.5.5.3 GF-epoxy specimens

Table 3.53 reports the dimensions of the specimens and the geometric parameters of the equipment used. Figure 3.133 shows the plots of the force/load curves for epoxy specimens. Plot 3.133(a) shows the curves for PT-E-6-I while plot 3.133(b) show the curves for PT-E-10-I. In Table 3.54-3.55 the derived properties for the specimen tested are reported.

It should be noted that some specimen exhibited a bolt failure⁸.

Table 3.53: GF-E specimens' dimensions

Specimen	Diameter (mm)	Cb/D	h (mm)	D/h
PT-E-6-1	6	5	6.45	0.930
PT-E-6-2	6	5	6.30	0.952
PT-E-6-3	6	5	6.40	0.938
PT-E-10-1	10	3	6.50	1.538
PT-E-10-2	10	3	6.50	1.538
PT-E-10-3	10	3	6.40	1.563

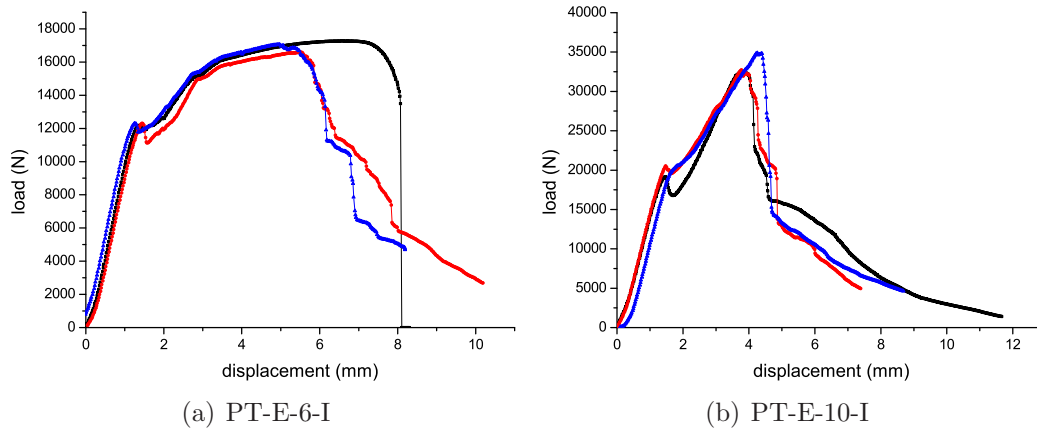
⁸The bolts used for these tests were not those described in 3.4.2 but general purpose bolts (D933 8.8)

Table 3.54: Pull-trough test, results for PT-E-6-I specimens

specimen	In. Sub-crit. failure load (N)	failure load (N)	In. Sub-crit. failure displ. (mm)
PT-E-6-1	12184	17272	1.344
PT-E-6-2	12004	16596	1.447
PT-E-6-3	12312	17068	1.258
Average	12167	16979	1.350
STDV	155	347	0.095
CV (%)	1	2	7
IC (95%)	384	861	0.236

Table 3.55: Pull-trough test, results for PT-E-10-I specimens

specimen	In. Sub-crit. failure load (N)	failure load (N)	In. Sub-crit. failure displ. (mm)
PT-E-10-1	19140	32460	1.462
PT-E-10-2	20532	32724	1.477
PT-E-10-3	20584	34888	1.829
Average	20085	33357	1.590
STDV	819	1332	0.208
CV (%)	4	4	13
IC (95%)	2035	3309	0.516

**Figure 3.133:** Pull-trough test; load vs. displacement for GF-epoxy specimens

3.5.5.4 GF-phenolic specimens

Table 3.56 reports the dimensions of the specimens and the geometric parameters of the equipment used. Figure 3.134 shows the plots of the force/load curves for epoxy specimens. Plot 3.134(a) shows the curves for PT-E-6-I while plot 3.134(b) show the curves for PT-E-10-I. In Table 3.57-3.58 the derived properties for the specimen tested are reported.

Table 3.56: GF-P specimens' dimensions

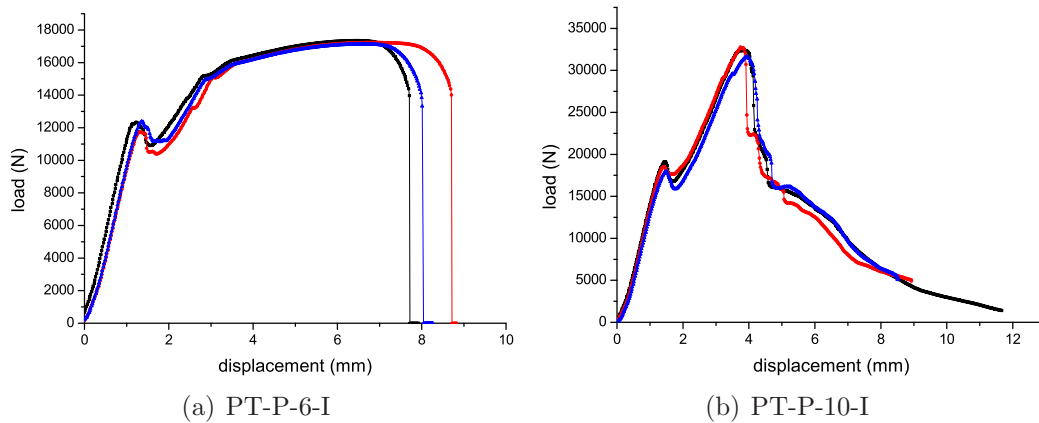
Specimen	Diameter (mm)	Cb/D	h (mm)	D/h
PT-P-6-1	6	5	6.80	0.882
PT-P-6-2	6	5	6.80	0.882
PT-P-6-3	6	5	6.80	0.882
PT-P-10-1	10	3	6.60	1.515
PT-P-10-2	10	3	6.80	1.471
PT-P-10-3	10	3	6.50	1.538

Table 3.57: Pull-trough test, results for PT-P-6-I specimens

specimen	In. Sub-crit. failure load (N)	failure load (N)	In. Sub-crit. failure displ. (mm)
PT-P-6-1	12340	17348	1.228
PT-P-6-2	11752	17236	1.301
PT-P-6-3	12384	17132	1.360
Average	12158	17238	1.296
STDV	352	108	0.066
CV (%)	3	1	5
IC (95%)	876	268	0.164

Table 3.58: Pull-trough test, results for PT-P-10-I specimens

specimen	In. Sub-crit. failure load (N)	failure load (N)	In. Sub-crit. failure displ. (mm)
PT-P-10-1	19140	32460	1.462
PT-P-10-2	18528	32780	1.403
PT-P-10-3	17976	31608	1.492
Average	18548	32282	1.452
STDV	582	605	0.045
CV (%)	3	2	3
IC (95%)	1446	1504	0.112

**Figure 3.134:** Pull-trough test; load vs. displacement for GF-phenolic specimens

3.5.5.5 GF-vinylester specimens

Table 3.59 reports the dimensions of the specimens and the geometric parameters of the equipment used. Figure 3.135 shows the plots of the force/load curves for epoxy specimens. Plot 3.135(a) shows the curves for PT-E-6-I while plot 3.135(b) show the curves for PT-E-10-I. In Table 3.60-3.61 the derived properties for the specimen tested are reported.

Table 3.59: GF-V specimens' dimensions

Specimen	Diameter (mm)	Cb/D	h (mm)	D/h
PT-V-6-1	6	5	7.00	0.857
PT-V-6-2	6	5	7.15	0.839
PT-V-6-3	6	5	6.80	0.882
PT-V-10-1	10	3	7.00	1.429
PT-V-10-2	10	3	6.70	1.493
PT-V-10-3	10	3	7.20	1.389

Table 3.60: Pull-trough test, results for PT-V-6-I specimens

specimen	In. Sub-crit. failure load (N)	failure load (N)	In. Sub-crit. failure displ. (mm)
PT-V-6-1	11200	17184	1.127
PT-V-6-2	11404	17624	1.315
PT-V-6-3	11340	17204	1.463
Average	11314	17337	1.302
STDV	104	248	0.168
CV (%)	1	1	13
IC (95%)	259	617.213	0.418

Table 3.61: Pull-trough test, results for PT-V-10-I specimens

specimen	In. Sub-crit. failure load (N)	failure load (N)	In. Sub-crit. failure displ. (mm)
PT-V-10-1	18448	34172	1.447
PT-V-10-2	18920	32864	1.440
PT-V-10-3	18876	39692	1.477
Average	18748	35576	1.455
STDV	260	3624	0.020
CV (%)	1	10	1
IC (95%)	647	9002	0.049

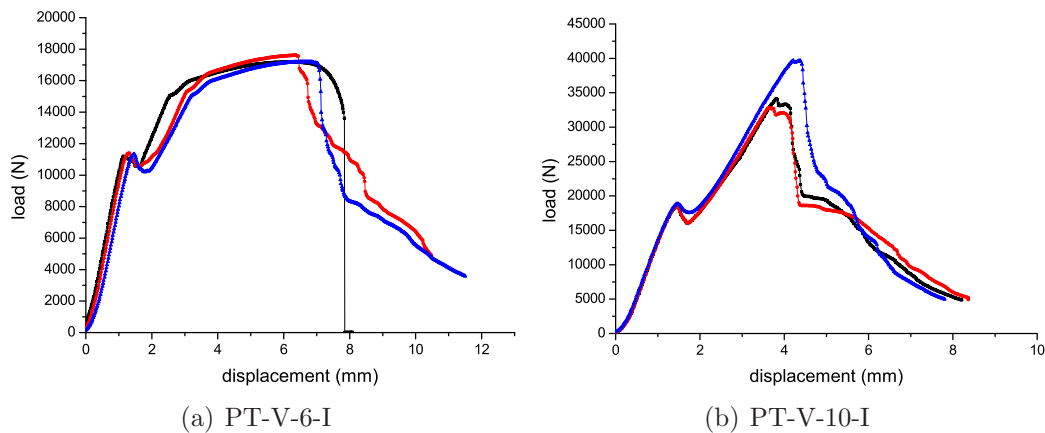


Figure 3.135: Pull-trough test; load vs. displacement for GF-vinylester specimens

3.5.5.6 Damaged zones

Figure 3.136 shows the photos of a specimen after being tested. Both sides of the specimen are visible. The bottom side, Figure 3.136(b), shows delamination near the hole. As explained before, delamination occurs at the begin of the test when the load is relatively low (initial sub-critical failure). If the load increases, the intralaminar fracture in the material starts and, at the end, the specimen is totally penetrated by the washer.

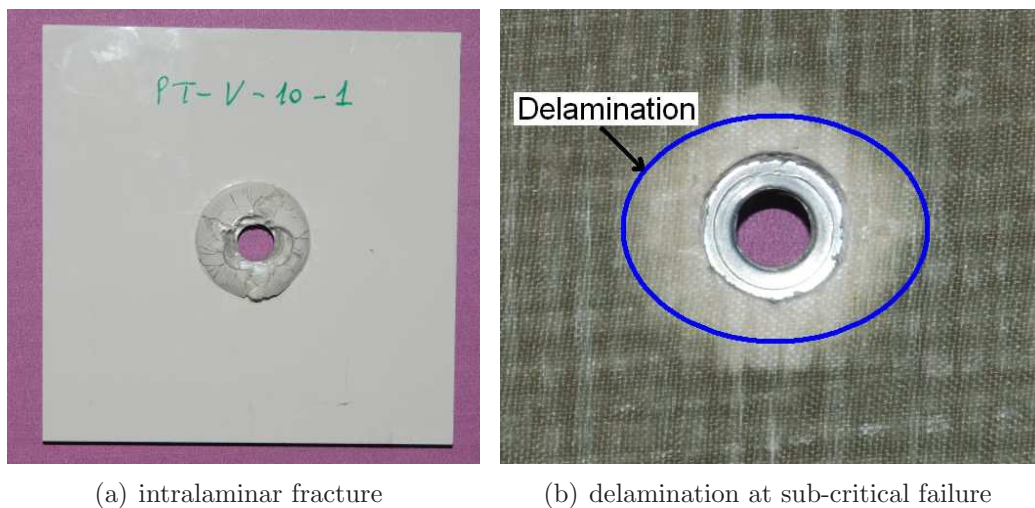


Figure 3.136: Pull-trough specimens after loading

3.5.5.7 Comparison of the PT test results

Figure 3.137 shows the failure loads of the specimens tested. As expected, increasing the diameter increases both the sub-initial critical failure load and the failure load

of the specimen. The results show that the material exhibit slight differences in the values of the two failure loads considered. This is in contrast with the previous tests on bolted joints where epoxy specimens had better performance. It should be also noted that increasing the diameter also increases the ratio between the initial sub-critical failure load to the ultimate failure load. This means that larger holes exhibit an initial sub-critical failure load that is relatively lower when compared to the ultimate failure load.

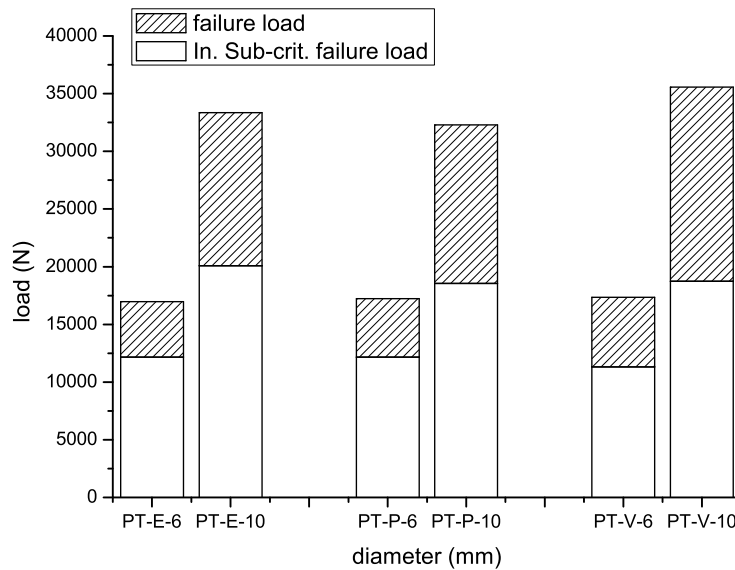


Figure 3.137: Comparison of PT tests failure loads

3.6 Conclusions

In this chapter a comprehensive experimental study on hybrid joints was presented. Two types of test were considered: in plane shear test and pull-through tests. All the tests were conducted considering specimens with different geometries and with different materials or material combinations. It was shown that the geometry affects the failure mode and that materials with the same geometries may show a different failure mode.

The main differences in the failure load of the in-plane shear test occur in the epoxy specimens that always show a value of the failure load higher than that of the other specimens. This was attributed to the fact that epoxy-specimens were manufactured using prepregs while the other specimens (phenolic and vinylester) were manufactured using resin infusion.

The results of the in-plane shear tests are presented as design charts that can be used during the conception of a hybrid structure (see section 3.5.4.9).

If pull-through is considered, the results are approximatively the same for the three materials, both in terms of the failure load and of the initial sub-critical failure load.

Chapter 4

CT-CC experimental tests

A simple empirical design methodology for multi-material bolted joints was presented in the previous chapter. However, a purely empirical design methodology require a high number of experimental tests in bolted joints. An improved design methodology, consists in performing a few experimental tests to characterize the basic material properties, and use these properties in analysis models. This chapter addresses the measurement of two properties that are required to simulate the fracture of composite bolted joints: the fracture toughness associated to fiber-dominated failure mechanism. For this purpose, the measurement of the crack resistance curve is essential. In fact, crack resistance curves not only characterize the fracture toughness of the material but it also allows to identify the parameters of softening laws used in the numerical simulation of failure in composite bolted joints [132–134]. These parameters are used in the numerical 3D model presented in Chapter 5.

The test is performed following the procedure described by Pinho *et al.* [135] and using the Digital Image Correlation (DIC) to compute in a fast way the crack resistance curve of the material. The proposed method is based on the identification of the crack tip location using Digital Image Correlation and the calculation of the J-integral directly from the test data using a simple expression derived for cross-ply composite laminates.

The material tested are carbon IM7/8552 and epoxy-glass fiber (presented in Chapter 3) respectively.

4.1 DIC technique

4.1.1 Introduction

The digital image correlation, developed by Sutton *et al.* [136,137] allows to compare digital images of the body at the undeformed state (reference state) and deformed state (state of the body at time t). Each image is described using a discrete function that represents the gray level at each pixel. At time t^* , this function can be expressed

as:

$$f^*(\mathbf{x}^*) = f(\mathbf{x} + \mathbf{d}(\mathbf{x})) \quad (4.1)$$

where f is the discrete function at the reference state, f^* is the function at the deformed state, \mathbf{x} and \mathbf{x}^* are the vector of the coordinate of the points at the reference state and at the deformed state, $\mathbf{d}(\mathbf{x})$ is the displacement of each point. The determination of the displacements, $\mathbf{d}(\mathbf{x})$, is obtained minimizing the coefficient of correlation C defined as:

$$C = 1 - \frac{\int_{\Delta M} f(\mathbf{x}) f(\mathbf{x} + \mathbf{d}(\mathbf{x})) d\mathbf{x}}{\sqrt{\int_{\Delta M} f^2(\mathbf{x}) d\mathbf{x} \int_{\Delta M} f^2(\mathbf{x} + \mathbf{d}(\mathbf{x})) d\mathbf{x}}} \quad (4.2)$$

where ΔM is the surface of the reference pattern. The displacements are expressed as:

$$\mathbf{d}(P) = \sum_j n_j(P) \mathbf{u}_j \quad (4.3)$$

where, u_j are the unknown displacements, P is a point of the pattern, and n_j are the functions chosen. $\mathbf{d}(P)$ is found minimizing equation (4.2).

Since the displacements u_j are unknown, equations (4.3) is written j times. In this case the problem admits a solution.

Finally, equation (4.3) can be written in a compact way as:

$$\mathbf{d} = [\mathbf{M}] \mathbf{u} \quad (4.4)$$

where \mathbf{d} is the vector of displacements that minimizes equation (4.2), $[\mathbf{M}]$ is the matrix of functions \mathbf{n}_j and \mathbf{u} is the vector of unknown displacements. The problem is solved merely inverting the matrix $[\mathbf{M}]$:

$$\mathbf{u} = [\mathbf{M}]^{-1} \mathbf{d} \quad (4.5)$$

The functions \mathbf{n}_j are generally bilinear ($\{n_j\} = \{x, y, xy, 1\}$) and a cubic-spline interpolation is used to find the displacement field [138].

The Figure 4.1 shows a pattern $ABCD$ centered in P and the deformed pattern $A^*B^*C^*D^*$ centered in P^* .

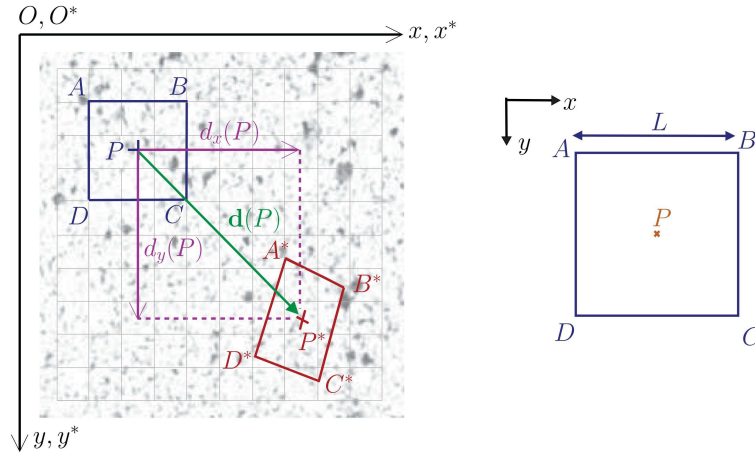


Figure 4.1: Initial and deformed pattern

The displacement of a point of the pattern can be written as:

$$d_x(x, y) = u_1\tilde{x} + u_2\tilde{y} + u_3\tilde{x}\tilde{y} + u_4 \quad (4.6)$$

$$d_y(x, y) = u_5\tilde{x} + u_6\tilde{y} + u_7\tilde{x}\tilde{y} + u_8 \quad (4.7)$$

where $\tilde{x} = \frac{x-x_A}{L}$ and $\tilde{y} = \frac{y-y_A}{L}$ are the homogenized coordinate on the pattern and L is the length of the side of the pattern.

In the equations (4.6) there are 8 displacements unknown, for this reason it is written for each point of the undeformed and deformed pattern ($ABCD, A^*B^*C^*D^*$). The matrix $[\mathbf{M}]$ in Equation 4.5 is then 8×8 .

It should be observed that the technique of digital image correlations uses continuous functions and for this reason it is complicated obtain good results in the case of a fracture in the material. For this reason a numerical algorithm [139] is used to evaluate the crack length in the case of discontinuous displacements.

4.1.2 Crack detection algorithm

The algorithm used should be able to detect a crack into the material. The following assumptions are made:

- M and N are two points in the reference image;
- $\mathbf{d}(\mathbf{x})$ is the displacement applied at the image;
- M^* and N^* are the two points in the deformed image and are separated by a geometric or material discontinuity (see Figure 4.2).

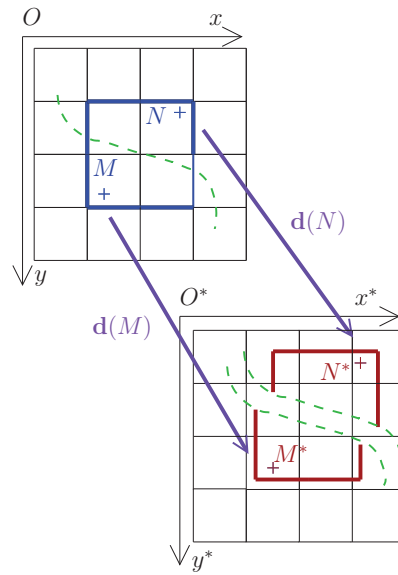


Figure 4.2: Points M and N before and after crack propagation

The measure of the variation of distance between these two points, $M \wr N$, in presence of a discontinuity can be expressed as:

$$M \wr N = \left\| \vec{M^*N^*} - \vec{MN} \right\| \quad (4.8)$$

Generally, $\forall (P, P^*), \vec{O^*P^*} = \vec{OP} + \mathbf{d}(P)$. Equation (4.8) can be re-written as:

$$M \wr N = \|\mathbf{d}(N) - \mathbf{d}(M)\| \quad (4.9)$$

If the discontinuity between two points is defined in this way a criterion that allows to detect a discontinuity into a pattern $ABCD$ should be written as (see Figure 4.3):

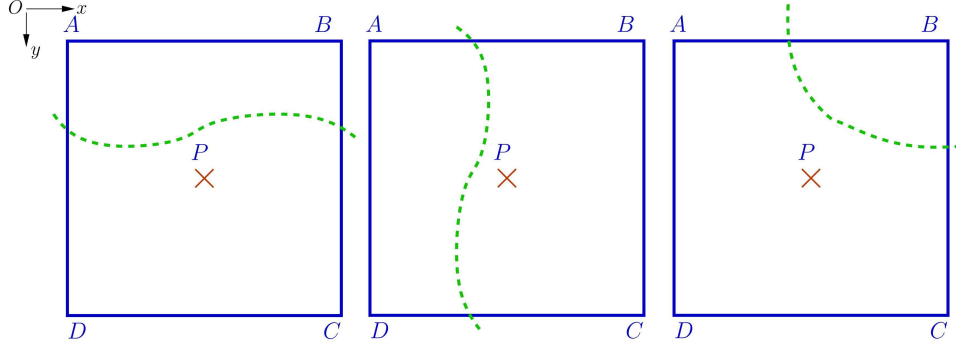


Figure 4.3: Different position of the discontinuity respect to the pattern

$$K(P) = \max(A \setminus C; B \setminus D) \max(\|\mathbf{d}(C) - \mathbf{d}(A)\|; \|\mathbf{d}(D) - \mathbf{d}(B)\|) \quad (4.10)$$

Figure 4.3 shows that this criterion is able to detect a crack into the material independently of the direction that assumes this crack into the pattern. It should be noticed that this criterion is able to detect the crack only in the case of brittle fracture.

Equation (4.10) provides a measure of the discontinuity inside the pattern. To discriminate if a pattern is damaged or undamaged a threshold should be applied to this function. If is assumed that the threshold applied is proportional to the arithmetic average of function $K(P)$ overall the image, the threshold function $K_T(P)$ can be defined as:

$$K(P) \geq \alpha \bar{K} \Rightarrow K_T(P) = 1 \quad (4.11)$$

$$K(P) < \alpha \bar{K} \Rightarrow K_T(P) = 0 \quad (4.12)$$

$$K(P) = \text{NaN} \Rightarrow K_T(P) = 0 \quad (4.13)$$

where \bar{K} is the average of $K(P)$ overall the image, α is a threshold value that can be chosen by the operator and NaN indicate that for that pattern the information is not available. In this work a low value of α , $\alpha = 2$, was chosen to do not lose the information in proximity of the crack tip. Figure 4.4 shows the relation between the crack length and time for different values of α .

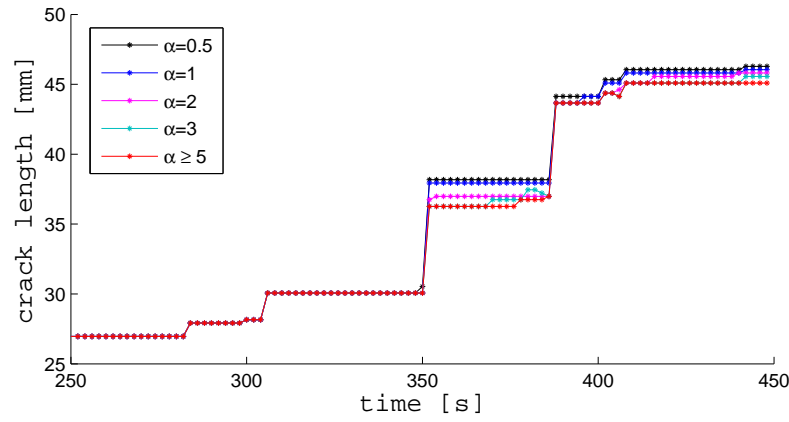


Figure 4.4: Relation between the crack length and time for different values of α

Using equations (4.11-4.13), the function $K_T(P)$ takes the values:

- $K_T(P) = 0$ in the patterns where the material is undamaged;
- $K_T(P) = -1$ if no information are available. Typically this happens in the pattern where the material is completely damaged and no information is possible obtain using the digital image correlation;
- $K_T(P) = 1$ in the patterns where a discontinuity is present but the material is not completely damaged. This happens at the crack tip.

Figure 4.5 shows the K_T function computed for a CT carbon specimen. It is noted that the function takes the value $K_T = 0$ where the material is undamaged, $K_T = -1$ where the material is completely fractured and $K_T = 1$ at the crack tip where damage occurs.

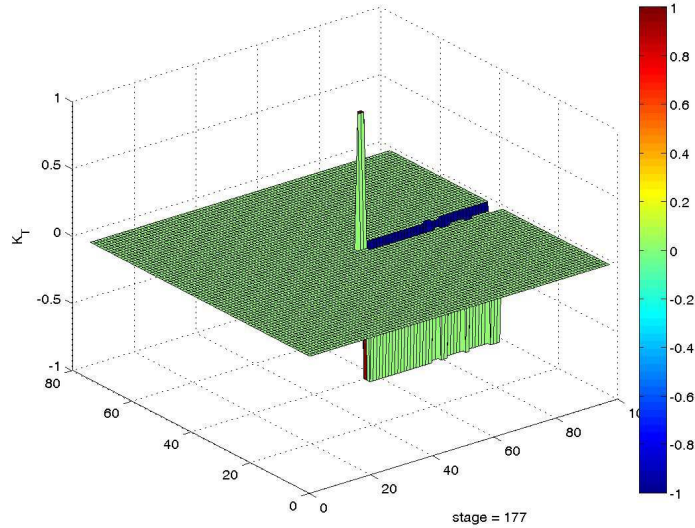


Figure 4.5: KT function

The information that has to be extracted from the DIC system is the crack length that is computed as the distance from the crack point in the deformed image and the crack tip in the undeformed image. Considering that patterns of 15×15 pixels² are used, spatial resolution of the method is ± 7 pixels. Considering that the conversion factor assumed the average value of $c_f \approx 0.016 \frac{\text{mm}}{\text{pixel}}$ the crack length was obtained with an approximation of ± 0.10 mm. The Matlab® code that implements this algorithm is shown in Appendix A.

4.1.3 J-Integral computation

4.1.3.1 J-Integral of a composite laminate

This section presents a procedure to calculate the J-integral for the CT and CC specimens using the Digital Image Correlation (DIC). Kang *et al.* [140] used a similar way to evaluate the J-Integral for cracks in metallic foils. The procedure is extended here for the case of a composite laminate.

Figure 4.6 shows the contour at the crack tip used for the calculation of the J-integral in 2D case.

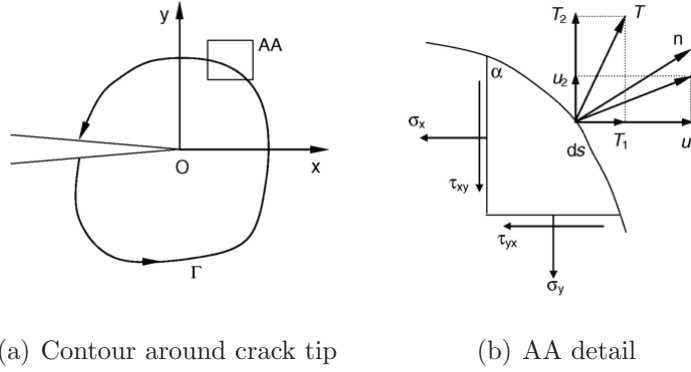


Figure 4.6: Contour for the calculation of the J-Integral in 2D case

The 2D J-Integral for an elastic material can be written as:

$$J = \int_{\Gamma} \left(W dy - T_i \frac{\partial u_i}{\partial x} ds \right) \quad (4.14)$$

where Γ is an anticlockwise contour around the crack tip, W is the strain energy density, T_i and u_i are, respectively, the components of the traction and displacement vectors on Γ . s is the curvilinear coordinate on Γ .

From the equilibrium of the triangular element $\widehat{dx dy ds}$ shown in Figure 4.6(b), the following relations are derived:

$$n_1 = \cos \alpha = \frac{dy}{ds} \quad (4.15)$$

$$n_2 = \sin \alpha = -\frac{dx}{ds} \quad (4.16)$$

$$(4.17)$$

and

$$\{T\} = [\sigma] \{n\} = \begin{bmatrix} \sigma_{xx} & \sigma_{xy} \\ \sigma_{xy} & \sigma_{yy} \end{bmatrix} \begin{Bmatrix} \cos \alpha \\ \sin \alpha \end{Bmatrix} = \begin{bmatrix} \sigma_{xx} \cos \alpha & \sigma_{xy} \sin \alpha \\ \sigma_{xy} \cos \alpha & \sigma_{yy} \sin \alpha \end{bmatrix} \quad (4.18)$$

where n_1 and n_2 are the directions cosines of the outer normal vector of the arc element ds as reported in Figure 4.6(b).

The strain energy density can be written as:

$$W = \int_0^{\varepsilon_{ij}} \sigma_{ij} d\varepsilon_{ij} = \frac{1}{2} \{\sigma\} \{\varepsilon\}^T = \frac{1}{2} (\sigma_{xx} \varepsilon_{xx} + \sigma_{yy} \varepsilon_{yy} + \sigma_{xy} \varepsilon_{xy}) \quad (4.19)$$

where $\{\sigma\} = \{\sigma_{xx} \ \sigma_{yy} \ \sigma_{xy}\}^T$ and $\{\varepsilon\} = \{\varepsilon_{xx} \ \varepsilon_{yy} \ \varepsilon_{xy}\}$.

Equation (4.14) allows to evaluate the value of the J-Integral in the 2D case. In the case of a laminate the equation (4.14) should be extended to the 3D case and the thickness of the laminate must be taken into account.

Figure 4.7 shows the contour for the calculation of the J-integral in the case of a body with thickness t .

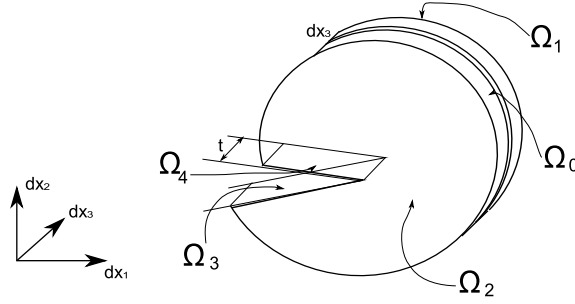


Figure 4.7: Contour for the calculation of J-integral in 3D case

The surface surround the crack is equal to $\Omega = \Omega_0 + \Omega_1 + \Omega_2$. As $n_1 = 0$ and $T_i = 0$ on Ω_1 and Ω_2 , the J-integral is written as:

$$J = \frac{1}{t} \int_0^t \int_{\Omega_0} \left(W dx_2 dx_3 - T_i \frac{\partial u_i}{\partial x_1} ds dx_3 \right) \quad (4.20)$$

If the laminate is a cross-ply only 0° and 90° laminae are present. If the thicknesses of 0° and 90° laminae are t^0 and t^{90} respectively, equation (4.20) can be re-expressed as:

$$J = \frac{1}{t} \int_{\Omega_0} \left(\int_0^{t^0} \left(W^0 dx_2 - T_i^0 \frac{\partial u_i}{\partial x_1} ds \right) dx_3 + \int_0^{t^{90}} \left(W^{90} dx_2 - T_i^{90} \frac{\partial u_i}{\partial x_1} ds \right) dx_3 \right) \quad (4.21)$$

Equation (4.21) implicitly assumes that strains (and displacements) through the thickness are constant. Moreover, assuming that no bending occurs (the laminate is balanced), substituting equations (4.18-4.19) in equation (4.21) results in:

$$\begin{aligned} J &= \frac{1}{t} \int_{\Omega_0} \left(\int_0^{t^0} W^0 n_1 dx_3 - \frac{\partial u_i}{\partial x_1} \int_0^{t^0} T_i^0 dx_3 + \int_0^{t^{90}} W^{90} n_1 dz - \frac{\partial u_i}{\partial x_1} \int_0^{t^{90}} T_i^{90} dx_3 \right) ds = \\ &= \frac{1}{t} \int_{\Omega_0} \left(\frac{1}{2} \left(\int_0^{t^0} \{\sigma^0\} dz + \int_0^{t^{90}} \{\sigma^{90}\} dx_3 \right) n_1 \{\varepsilon\}^T ds + \dots \right. \\ &\quad \left. \dots - \left(\int_0^{t^0} [\sigma^0] dz + \int_0^{t^{90}} [\sigma^{90}] dx_3 \right) \{n\} \left\{ \frac{\partial u}{\partial x_1} \right\}^T ds = \right. \\ &= \frac{1}{t} \int_{\Omega_0} \left(\frac{1}{2} (\{\sigma^0\} t_0 + \{\sigma^{90}\} t^{90}) n_1 \{\varepsilon\}^T - ([\sigma^0] t_0 + [\sigma^{90}] t_{90}) \{n\} \left\{ \frac{\partial u}{\partial x_1} \right\}^T \right) ds \end{aligned} \quad (4.22)$$

If the thickness $t^0 = t^{90} = t/2$ equation (4.22) can be simplified as:

$$\begin{aligned} J &= \int_{\Omega_0} \left(\frac{1}{2} \left(\frac{1}{2} \{\sigma^0\} + \frac{1}{2} \{\sigma^{90}\} \right) n_1 \{\varepsilon\}^T - \left(\frac{1}{2} [\sigma^0] + \frac{1}{2} [\sigma^{90}] \right) \{n\} \left\{ \frac{\partial u}{\partial x_1} \right\}^T \right) ds \\ &= \int_{\Omega_0} \left(\frac{1}{2} \{\bar{\sigma}\} n_1 \{\varepsilon\}^T - [\bar{\sigma}] \{n\} \left\{ \frac{\partial u}{\partial x_1} \right\}^T \right) ds \end{aligned} \quad (4.23)$$

where $\bar{\sigma}$ are the averaged values of the stresses ($\bar{\sigma} = \sigma^0 + \sigma^{90}$).

Therefore, the J-Integral for the laminate can be calculated using the averaged stress through the laminate in equation (4.14). Using the Digital Image Correlation, only the strains are obtained and the averaged value of the stress can be obtained averaging the values of the elastic matrix of the material ($\{\bar{\sigma}\} = [\bar{C}] \{\varepsilon\}$ where $[\bar{C}] = \frac{1}{2} ([C^0] + [C^{90}])$).

Details of the algorithm used to calculate the J-Integral are presented in Section 4.1.3.3.

4.1.3.2 J-Integral for quasi-brittle materials

Figure 4.8 shows the contour for the calculation of J-Integral in the presence of a cohesive zone. For the path-independence of the J-Integral the following conservation integral is defined:

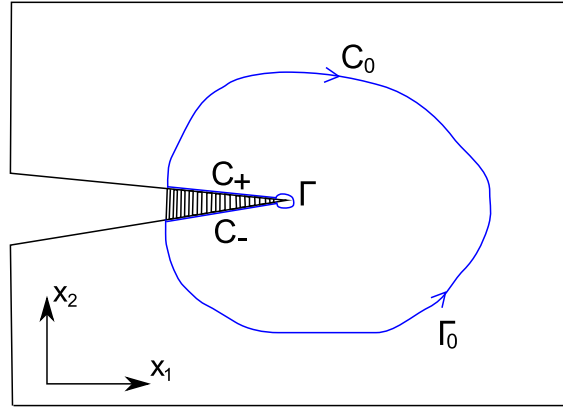


Figure 4.8: Contour in presence of a cohesive zone

$$I = \oint_{\Gamma+C_0+C_++C_-} \left(W n_1 - \frac{\partial u}{\partial x_1} \cdot \mathbf{t} \right) ds = 0 \quad (4.24)$$

I is equal to zero because the complete path is closed and the limited region is simply connected.

Equation (4.24) can be extended as:

$$\begin{aligned}
I = & \int_{\Gamma} \left(W n_1 - \frac{\partial \mathbf{u}}{\partial x_1} \cdot \mathbf{t} \right) ds + \int_{C_0} \left(W n_1 - \frac{\partial \mathbf{u}}{\partial x_1} \cdot \mathbf{t} \right) ds + \\
& + \int_{C_+} \left(-\frac{\partial \mathbf{u}^+}{\partial x_1} \cdot \mathbf{t}^+ \right) ds + \int_{C_-} \left(-\frac{\partial \mathbf{u}^-}{\partial x_1} \cdot \mathbf{t}^- \right) ds
\end{aligned} \quad (4.25)$$

since $n_1 = 0$ on C_+ and C_- . The two last integrals in equation 4.25 represent the contribution of the cohesive zone. Since $t^+ = -t^- = t$ from equilibrium considerations, and $dx = dx_1$:

$$I_{COH} = \int_{C_-} \left(\mathbf{t}^- \cdot \left(\frac{\partial \mathbf{u}^+}{\partial x_1} - \frac{\partial \mathbf{u}^-}{\partial x_1} \right) \right) dx_1 = - \int_C \left(\mathbf{t} \cdot \frac{\partial \|\mathbf{u}\|}{\partial x_1} \right) dx_1 \quad (4.26)$$

where $\|\mathbf{u}\|$ is the crack opening. From Rice [141]:

$$I_{COH} = - \int_C \frac{\partial}{\partial x_1} \left(\int_0^{\|\mathbf{u}\|} \mathbf{t} \cdot d\|\mathbf{u}\| \right) dx_1 = \int_0^{\|\mathbf{u}_T\|} \mathbf{t} \cdot d\|\mathbf{u}\| \quad (4.27)$$

where $\|\mathbf{u}_T\|$ is the crack opening at the beginning of the FPZ.

Therefore, equation (4.25) can be re-written as:

$$\int_{\Gamma} \left(W n_1 - \frac{\partial \mathbf{u}}{\partial x_1} \cdot \mathbf{t} \right) ds + \int_0^{\|\mathbf{u}_T\|} \mathbf{t} \cdot d\|\mathbf{u}\| - \int_{\Gamma} \left(W n_1 - \frac{\partial \mathbf{u}}{\partial x_1} \cdot \mathbf{t} \right) ds = 0 \quad (4.28)$$

$$\int_{\Gamma} \left(W n_1 - \frac{\partial \mathbf{u}}{\partial x_1} \cdot \mathbf{t} \right) ds + \int_0^{\|\mathbf{u}_T\|} \mathbf{t} \cdot d\|\mathbf{u}\| = \int_{\Gamma} \left(W n_1 - \frac{\partial \mathbf{u}}{\partial x_1} \cdot \mathbf{t} \right) ds \quad (4.29)$$

In equation (4.29) the first integral represents the J-Integral at the crack tip, J_{TIP} , the second, as explained before is the J-Integral at the cohesive zone, J_{COH} , while the third integral is the J-Integral calculated on the external path, J_{EXT} .

Equation (4.29) can be re-written as:

$$J_{EXT} = J_{COH} + J_{TIP} \quad (4.30)$$

During the development of the R-curve:

$$J_{TIP} + \int_0^{\|\mathbf{u}_T\|} \mathbf{t} \cdot d\|\mathbf{u}\| = J_{EXT} \quad (4.31)$$

During steady-state propagation:

$$J_{TIP} + \int_0^{\|\mathbf{u}_T^*\|} \mathbf{t} \cdot d\|\mathbf{u}\| = J_{EXT} \quad (4.32)$$

4.1.3.3 Algorithm implemented in Matlab

Using the digital Image correlation the following parameters can be obtained:

- the matrices of the displacements on the plane $[u_1], [u_2]$
- the matrices of the strains $[\varepsilon_{11}], [\varepsilon_{22}], [\varepsilon_{12}]$

This information will be used for the calculation of the J-integral and are stored as matrices $m \times n$ where m and n are the dimension, in pixels, of the processed part of the original image. Therefore, displacements and strain are $m \times n$ matrices.

Figure 4.9 shows the rectangular contour used and the boundary of the images. This contour contains a finite number of pixels at therefore only discrete quantities of the relevant parameters are determined along this pattern.

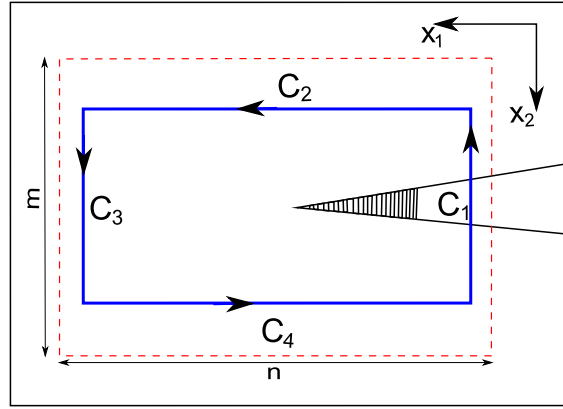


Figure 4.9: Contour used in Matlab algorithm

The calculation of the J integral follows the following steps:

- Average stresses, $\{\bar{\sigma}\}$. The average stresses are computed from the transformed stiffness matrices of the 0° and 90° plies, $[\bar{C}^0]$ and $[\bar{C}^{90}]$ respectively, as $\{\bar{\sigma}\} = \frac{1}{2} \left([\bar{C}^0] + [\bar{C}^{90}] \right) \{\varepsilon\}$.
- Differentials dx_1 , dx_2 and dS . The differentials dx_1 and dx_2 are taken as the differences between the centers of adjoining subsets, measured along the corresponding axes. The differential dS is the Euclidian norm of dx_1 and dx_2 .
- Vectors normal to the contour, $\{n\}$. These vectors are directly defined by the simple contour sub-divisions shown in Figure 4.9, taking the following forms: $\{1, 0, 0\}^T$ on C_3 , $\{0, 1, 0\}^T$ on C_4 , $\{-1, 0, 0\}^T$ on C_1 , and $\{0, -1, 0\}^T$ on C_2 .

- Derivative of the displacement field, $\left\{ \frac{\partial u}{\partial x_1} \right\}$. This vector is calculated using the central difference method applied in three adjoining subsets:

$$\left\{ \frac{\partial u}{\partial x_1} \right\} \approx \left\{ \frac{\Delta u}{\Delta x_1} \right\} = \left\{ \frac{u^{i+1} - u^{i-1}}{2\Delta x_1} \right\} \quad (4.33)$$

The algorithm to calculate the J-Integral of a composite laminate is implemented in Matlab code and is reported in Appendix B. The Algorithms for the calculation of the crack length and the J-Integral are used in a interactive Matlab code that allows an easy and fast calculation of the crack R-curve. Figure 4.10 shows the main window of the developed software.

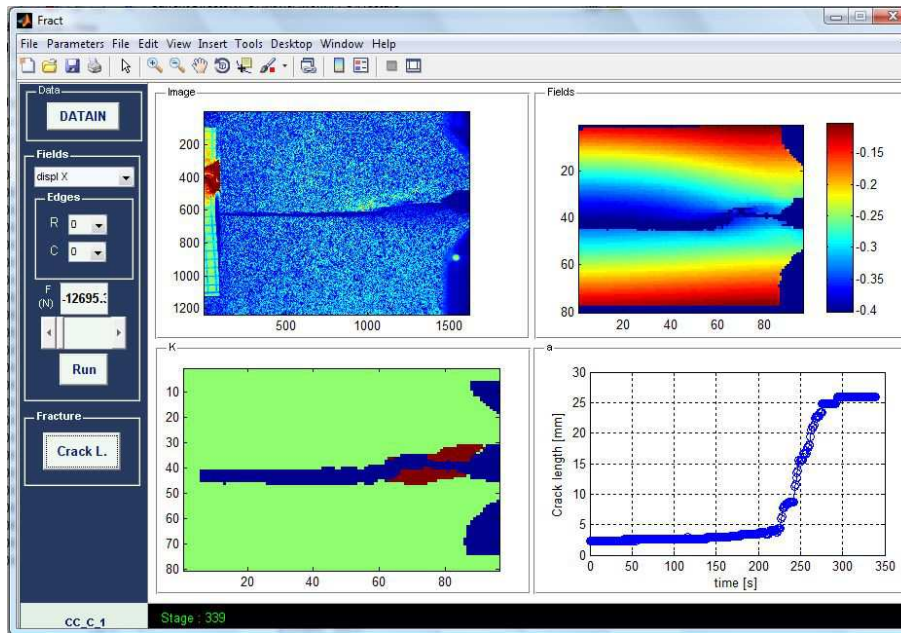


Figure 4.10: Main window of Matlab software developed

4.2 Experimental Work

4.2.1 Experimental Setup

4.2.1.1 Preparation of the specimens

The specimen were manufactured as described in Pinho *et al.* [135]. Figure 4.11 shows the geometry for CT and CC specimens.

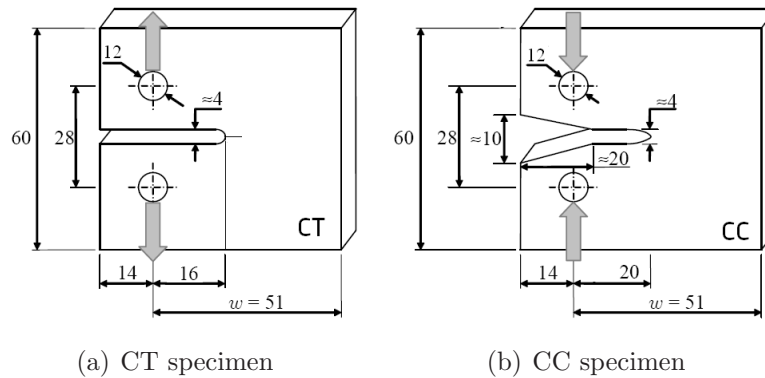


Figure 4.11: Geometry of CT-CC specimens

For the carbon specimens (IM78552) the lay-up was $[0^\circ/90^\circ]_{8s}$ for a total thickness of $h=4$ mm. For the glass-specimens the lay-up was $[0^\circ/90^\circ]_{2s}$ for a total thickness of $h=6$ mm.

To use the Digital Image Correlation, the specimens were painted with a speckle of the average dimension of 0.1 mm.

Pinho *et al.* [135] noticed that paint peeled in compression specimens and this effect did not allow to have data for the region near the crack tip. To avoid this effect the surface of the specimens was treated as in the case of strain gauges are used (see 3.2.2). The manual abrasion of the specimen surface and the degreasing using acetone and isopropanol permit a perfect adhesion between the paint and the specimen. Not peeling effects were observed in the vicinity of the crack tip during the tests.

4.2.1.2 Specimens nomenclature

The denomination adopted for the specimens is the following:

J-M-I

where J identifies the type of test (CT or CC) where M is the material used, and I is the index that identifies the number of the sample:

- J=CT, CC;
- M=C (carbon), G (glass);
- I=1,2,3.

4.2.1.3 Testing machine set-up

The test was conducted using the MTS 312.31 testing machine in FEUP's laboratories. The capacity of the testing machine is 250 kN. Tests were performed using

a load cell of 100 kN. The speed of the machine (displacement controlled test) was 2mm/min. Figure 4.12 shows the equipment set-up adopted during CT-CC tests.



Figure 4.12: Equipment set-up during CT-CC tests

4.2.1.4 Photomechanical set-up and measurement parameters

The digital image correlation ARAMIS software by GOM (<http://www.gom.com/>) was used in this work. This measurement system is equipped with an 8-bit Baumer Optronic FWX20 camera (resolution of 1624×1236 pixels, pixel size of $4.4 \mu\text{m}$ and sensor format of $1/1.8''$) coupled with a Schneider-Kreuznach Componar-S 50mm $f/2.8$ lenses. For mobility and adaptability, the support of the cameras was mounted on a Foba ALFAE tripod, which was positioned facing the testing machine.

In the set-up, the optical system was positioned with regard to the surface of the specimen, mounted into the testing machine. A laser pointer was used to guarantee a correct alignment. The working distance (defined between the specimen's surface and the support of the cameras) was set in the range of 200 mm. The lens was adjusted to be in focus with regard to the surface of interest, setting the lens aperture to $f/2.8$ in order to minimize the depth of field. The aperture of the lens was then slightly closed ($f/11$) in order to improve the depth of field during testing. The shutter time was set to 50 ms, according to the cross-head displacement rate during testing ($2 \text{ mm} \cdot \text{min}^{-1}$) and the size of the camera unit cells ($4.4 \mu\text{m}$). The light source was finally adjusted in order to guarantee an even illumination of the specimen's surface and to avoid over-exposition (i.e., the saturation of pixels over the field of view).

Table 4.1: Parameters used in the ARAMIS-GOM software

<i>Project parameter - Facet</i>	
Conversion factor	0.180 mm/pixel
Facet size	30 pixel
Step size	30 pixel
<i>Project parameter - Strain</i>	
Computation size	5 macro-pixel
Validity code	55%
Strain computation method	Total
<i>Image recording</i>	
Acquisition frequency	1 Hz

Table 4.1 reports the parameters used in ARAMIS-GOM software. For the region of interest was set about $20 \times 20 \text{ mm}^2$, defining a conversion factor of about $0.185 \text{ mm} \cdot \text{pixel}^{-1}$. In the digital image correlation method, the displacement field is measured by analysing the geometrical deformation of the images of the surface of interest, recorded before and after loading. For this purpose, the initial (undeformed) image is mapped by square facets (correlation windows), within which an independent measurement of the displacement is calculated. Therefore, the facet size, on the plane of the object, will characterise the displacement spatial resolution. The facet step (i.e., the distance between adjacent facets) can also be set either for controlling the total number of measuring points over the region of interest or for enhancing the spatial resolution by slightly overlapping adjacent facets. Typically, a great facet size will improve the precision of the measurements but also will degrade the spatial resolution [142]. Thus, a compromise must be found according to the application to be handled. In this work, a facet size of $30 \times 30 \text{ pixel}^2$ was chosen, attending to the size of the region of interest, the optical system (magnification) and the quality of the granulate (average speckle size) obtained by the spray paint. The facet step was also set to $30 \times 30 \text{ pixel}^2$ (Table 4.1), in order to avoid statistically correlated measurements. The in-plane displacements were then numerically differentiated in order to determine the strain field need for the material characterization problem.

4.2.2 Experimental results

To evaluate the fracture toughness of the fiber CT and CC specimens are used and two techniques are used to calculate the fracture toughness. The first technique [135] requires the use FEM to evaluate the J-integral. The J-integral is calculated for a FE model representing a specimen with unitary thickness. The fracture toughness of the specimen is obtained as:

$$G = J_{FEM} \left(\frac{P}{h} \right)^2 \quad (4.34)$$

where J_{FEM} is the J-integral calculated from the FEM, P is the load during the experimental test and h is the thickness of the composite.

The second technique, here proposed, consists in the calculation of the J-Integral using directly the data that come out from Aramis, as explained in Section 4.1.3.3.

4.2.2.1 Calculation of J-integral using FEM

To evaluate the J-integral directly from the FEM a parametric numerical model was defined using Abaqus 6.7 [106]. The Python [143] script of the parametric model is reported in Appendix C. This allows to automatically generate and run several CT-CC FE models for different crack lengths. The function J_{FEM} of equation (4.34) is calculated from the FE model and it can be used to compute the energy release rate G of the laminate when at a given value of the crack length. The energy release rate of the fiber is shown by Pinho *et al.* [135] to be equal to twice this value.

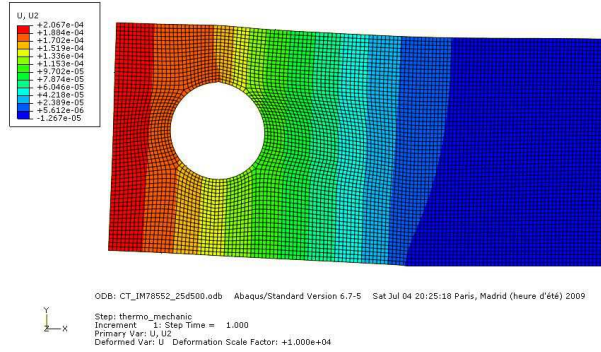


Figure 4.13: FEM model of CT/CC specimen

The J-Integral can be fitted by a function of the crack length a :

$$JI = (p_0 + p_1 a^{p_2}) \frac{p_3 + p_4 a}{p_5 - p_6 a} \quad (4.35)$$

where p_i are the best-fitting parameters. In Table 4.2 the parameters for the Glass Fiber and IM7/8552 tested are reported. It should be noted that these parameters are function of the geometry of the specimen.

Table 4.2: Parameters for the J-integral fitting (thickness $h = 4\text{mm}$)

Specimen	p_0	p_1	p_2	p_3	p_4	p_5	p_6
IM78552	-1.870e-6	-6.984e-21	9.044	-4.996	1.517	-4.269e+1	-8.874e-1
GF	-8.775e-7	-2.571e-21	9.145	-7.312	1.004	-4.584e+1	-9.556e-1

Figure 4.14 reports the fitting function and the numerical point from FEM. A good level of approximation is observed.

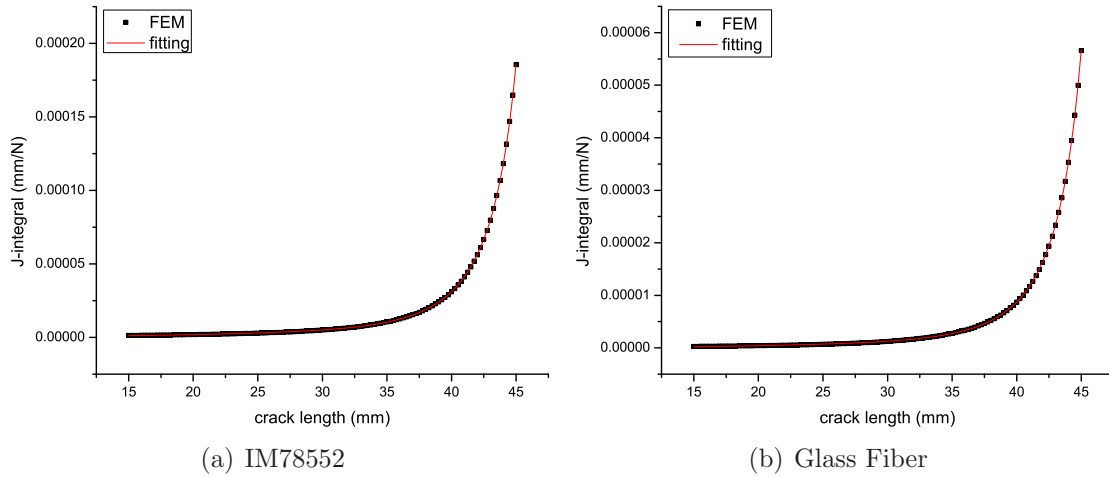


Figure 4.14: J-Integral for CT/CC specimens: numerical values and fitting functions.

4.2.2.2 CT-C-I specimens

A typical load-displacement relation obtained in the CT tests is shown in Figure 4.15.

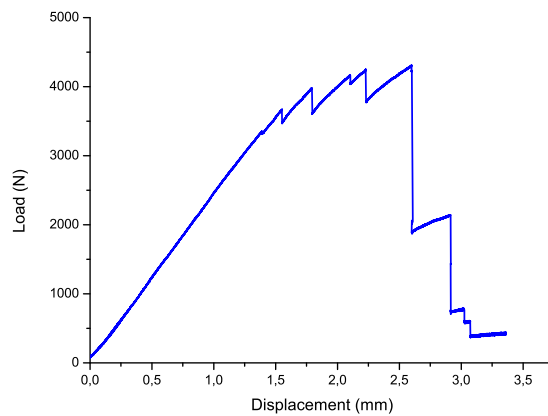


Figure 4.15: Load-displacement in a CT-C-I test specimen

The load was measured using the 100kN load cell, and the displacement was measured using the linear variable differential transformer (LVDT) connected to the hydraulic actuator of the test machine.

Figure 4.15 shows that the load-displacement relation is linear up to approximately 80% of the peak load, and that crack propagation occurs in discrete jumps.

Figure 4.16 shows the R-curve measured from the FEM post-processing of the test results method proposed by Pinho *et al.* [135] and that obtained by post-processing the displacement and strain fields measured by the DIC system.

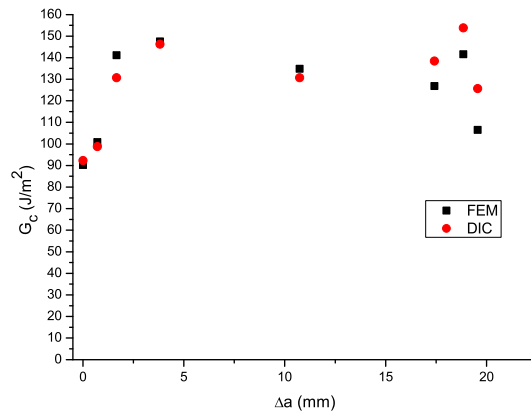


Figure 4.16: R-curves extracted from a CT-C-I specimen using FEM and DIC

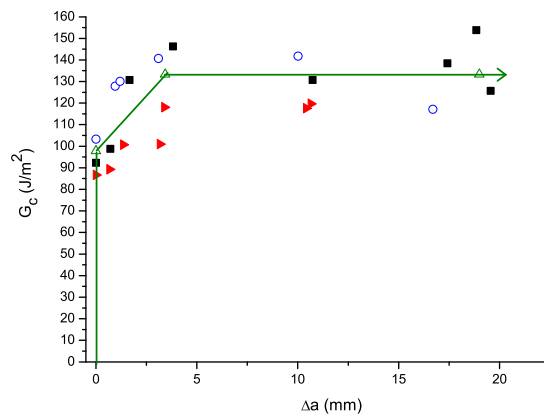


Figure 4.17: R-curves extracted from all CT-C specimens using DIC, and corresponding mean R-curve. Each symbol corresponds to one CT test

Figure 4.16 shows a good correlation between the FEM and DIC data reduction methods. This means that the fracture process zone that bridges the crack has a minor effect on the displacement and strain fields in the regions where the Finite Element model computes the J-integral.

Figure 4.17 shows the R-curves obtained from the three CT tests. Figure 4.17 also shows the mean value of the fracture process zone, 3.4mm, and the mean values

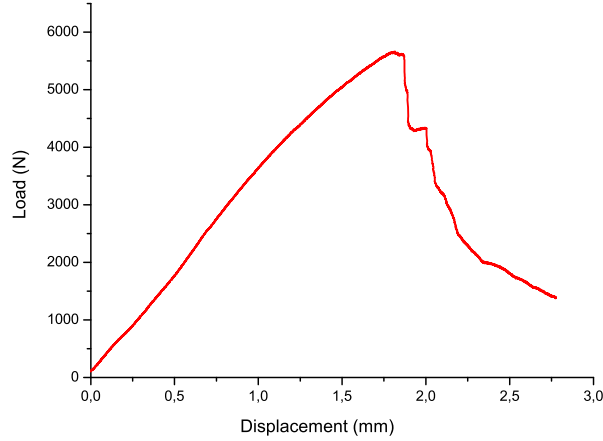


Figure 4.18: Load-displacement in a CC-C-I test specimen

of the initial fracture toughness and that corresponding to steady-state crack propagation, 97.8J/m^2 and 133.3J/m^2 respectively. These values are slightly lower than the mean values of the fracture toughness for initiation and steady-state propagation, 113.8J/m^2 and 146.7J/m^2 respectively, measured by Pinho [144] for the same material system.

4.2.2.3 CC-C-I specimens

A typical load-displacement relation obtained from a CC test is shown in Figure 4.18.

Figure 4.18 shows the R-curve measured from the FEM post-processing of the test results obtained by the method proposed by Pinho *et al.* and the R-curve obtained using the DIC data reduction procedure proposed here.

Figure 4.19 shows that the FEM-based solution yields unrealistically high values of the fracture toughness during the propagation of fiber kink bands. For 15mm of kink-band propagation the fracture toughness computed using the FEM is approximately twice that calculated using the DIC system. The reason for this fact is that the FEM-based calculation of the J-integral does not account for the contact and load transfer across the band of the kinked fibers. These effects clearly affect the displacement and strain fields along the contours of the J-integral computed using FEM. On the other hand, the DIC-based method uses the actual displacement and strain fields on the surface of the specimen, thus providing a more accurate R-curve. However, the contact stresses that are transferred along the kink band still pollute the data obtained using DIC because they introduce one additional term on the LHS of equation (4.29).

Delamination associated with the propagation of the kink band from the initial notch was also observed in the CC-C tests. The presence of delamination renders

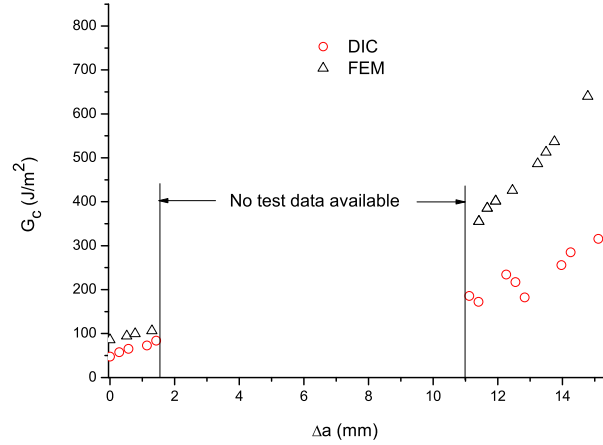


Figure 4.19: R-curves extracted from a CC specimen using FEM and DIC

this test method unsuitable to measure the R-curve in compression because there is another energy dissipating mechanism apart from those related to the kink band itself. In addition, the presence of delamination invalidates the assumptions of a two-dimensional crack, and of constant strain through the thickness of the laminate (assumption used in equation 4.29). Delamination was also the reason why the DIC-based method could not detect the tip of the kink band for $2\text{mm} \leq \Delta a \leq 11\text{mm}$. The out-of-plane displacement of the delaminated plies renders the experimental determination of the displacement and strain fields impossible with just one camera. The delamination propagation stopped after 11mm of kink-band propagation, and the identification of its extremity was again possible.

4.2.2.4 CT/CC-G-I specimens

Unfortunately, no results are available for the glass specimen tested. In fact, during the test several problems arose.

First of all, a straight crack propagation was not observed during the test. In fact, indentation in the proximity of the holes, large delaminations and crack propagation in the direction perpendicular to the main crack were observed.

All these phenomena do not allow the use of FEM or of DIC to calculate the R-curve. Figure 4.20 shows a CC-G-I specimen during the loading and the associated function K_T defined in equation (4.11).

It can be noticed that the use of DIC and the crack detection algorithm enable the identification of complicated crack paths. However, the J-Integral computed is wrong because using DIC the out-of-plane displacements are considered zero and obviously this is not the case. It means that the strains calculated by DIC are affected by this error. Moreover, the other failure mechanism that appears during the test (in addition at the propagation of the main crack) are not negligible.

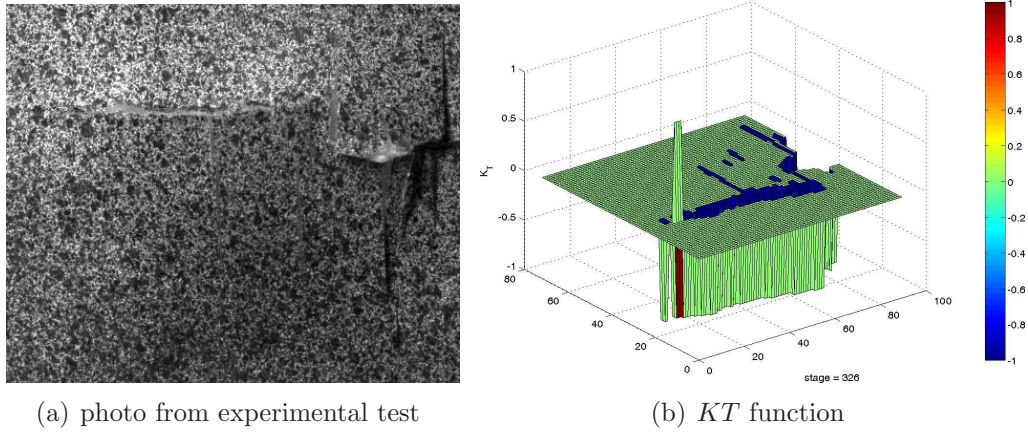


Figure 4.20: CC-G-I specimen during the loading

4.2.2.5 Conclusion on CT and CC tests

The comparison between the R-curves obtained in CT specimens using the FE-based post-processing and the DIC-based method indicates that the results are virtually the same and that the method proposed here is a valid alternative to measure R-curves associated with longitudinal tensile failure mechanisms in composite materials. The initial value of the fracture toughness associated with longitudinal tensile failure mechanisms in IM7/8552 is 98.7J/m^2 , and it raised up to 133.7J/m^2 for steady state propagation. The mean value of the associated cohesive zone is 3.4mm.

It is concluded that the FE-based data reduction method is inadequate for the measurement of R-curves in CC specimens because it severely overpredicts the fracture toughness. The DIC-based method is an improvement over FE-based data reduction methods because it is based on the actual displacement field on a pre-defined contour. However, the contribution of the contact tractions to the J-integral still needs to be quantified and used in the data reduction method to improve the accuracy of the data. The initial value of the fracture toughness associated with longitudinal compressive failure mechanisms in IM7-8552 measured using DIC was 47.5J/m^2 ; the measured fracture toughness increased up to 315J/m^2 for 15mm of propagation of a kink-band. However, the values computed for the fracture toughness using the CC specimen do not account for the energy dissipated by the delamination that accompanied the propagation of the kink-band. In addition, the delamination does not allow the accurate measurement of the tip of the kink-band. Therefore, it is concluded that these difficulties render the CC test method unsuitable to generate R-curves and that an alternative test method should be developed.

The same considerations apply for Glass fiber specimens. In addition, these specimens showed additional failure mechanisms that render the use of the CT/CC specimens unsuitable to measure the fracture toughness of fiber-dominated failure mechanism. In this case a new test method should be developed.

4.2.2.6 Determination of the parameters of the softening law

The CT and CC tests were performed to compute the parameters of the softening law of the progressive damage model. For each damage mode the softening laws are used to represent the evolution of the damage in terms of the dissipated energy (see Figure 4.21).

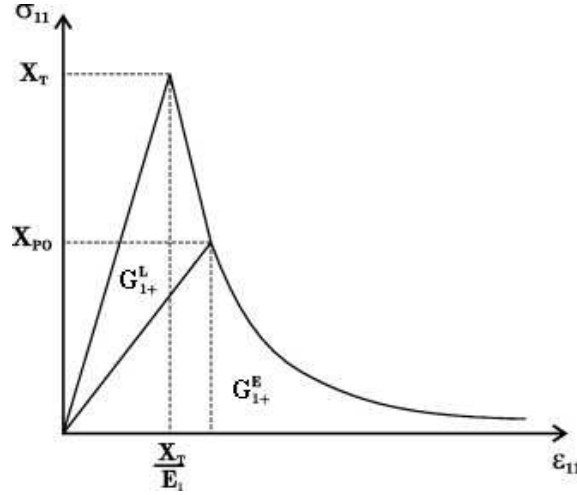


Figure 4.21: Softening law used in the progressive damage model.

Dávila *et al.* [132] proposed a methodology to compute the parameter of the exponential law proposed by Maimí *et al.* [133, 134]:

$$X_{PO} = (1 - n) X_c f(m, n) \quad (4.36)$$

$$G_c^L = G_c [1 - (1 - m) f(m, n)] \quad (4.37)$$

$$G_c^L = G_c (1 - m) f(m, n) \quad (4.38)$$

with:

$$f(m, n) = 1 - \frac{1 - n}{n} \frac{m}{1 - m} \quad (4.39)$$

$$m = G_1 / G_c \quad (4.40)$$

$$n = 1 - \frac{2}{3} \gamma \frac{1 - m}{l_p} \frac{E G_c}{X_c^2} \quad (4.41)$$

where X_c is the ultimate failure strength, X_{PO} is the pull-out or transition strength, $l_p z$ is the length of process zone (LPZ), γ is the parameter for the models for the LPZ ($\gamma = 0.884$ for Rice model), G_c , G_1 , G_c^L and G_c^E are respectively the energy release

rate, the initiation value of the energy release rate, the linear and the exponential partitions.

Using equations (4.36-4.41) and considering that for IM7/8552 carbon specimen the following values were measured: $G_c = 133.8$, $X_c = 2326.2$, $lp = 3.4$, $E = 90.65E3$, $G_1 = 98.7$, the parameters computed for the longitudinal cohesive law in tension are:

$$X_{PO}^+ = 161.0\text{MPa}, G_c^{L+} = 119.9\text{J/m}^2, G_c^{E+} = 23.8\text{J/m}^2.$$

For the longitudinal cohesive law in compression no parameters are available and an inverse identification technique was used; the parameters obtained were:

$$X_{PO}^- = 600\text{MPa}, G_c^{L-} = 72.6\text{J/m}^2, G_c^{E-} = 77.4\text{J/m}^2.$$

Chapter 5

3D Numerical Model

Having defined a new experimental technique to measure the fracture toughness associated to fibre-dominated failure mechanism, this chapter describes the 3D numerical model developed to predict the strength of composite bolted joints. As previously mentioned, the strength of a mechanically fastened joint depends on the pressure applied by the bolt. In fact, a pressure of 22MPa on the washer is suggested in the literature for carbon fiber joints to maximize the strength [6] while for glass this value increases up to 70MPa [19]. The application of a lateral pressure has a beneficial effect on the strength of the composite (obviously until the pressure is lower than a critical value). For this reason the failure criteria used in the numerical model has to consider 3D stress states.

The objective of this chapter is to develop a new 3D numerical model that is applicable to composite bolted joints.

5.1 Matrix Failure Criteria for 3D stress states

The failure criteria proposed in this chapter can be thought as an extension of the LARC03 criteria to 3D stress states [145]. It should be noticed that the effect of the lateral pressure σ_{33} has an influence mainly on the matrix-dominated failure modes (matrix failure and fiber kinking). The influence of σ_{33} on the fiber tensile failure mode was taken as negligible.

For a general stress state, the failure criteria is a function of the traction vector acting on the fracture plane as shown in Figure 5.1. Defining α as the angle between the fracture plane and the through-the-thickness direction, the failure index depends on the stresses acting on the fracture surface and therefore on α .

The stress tensor is denoted as T :

$$T = \begin{bmatrix} \sigma_{11} & \tau_{12} & \tau_{13} \\ \tau_{12} & \sigma_{22} & \tau_{23} \\ \tau_{13} & \tau_{23} & \sigma_{33} \end{bmatrix} \quad (5.1)$$

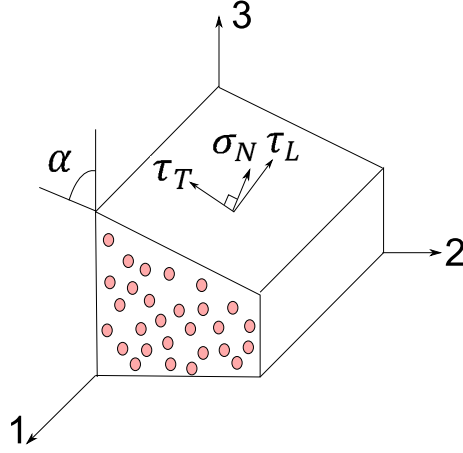


Figure 5.1: Components of traction on the fracture plane

and the unit normal vector to the fracture plane is $n = \{0 \quad \cos(\alpha) \quad \sin(\alpha)\}^T$ the vector of the traction stress t_n acting on the fracture plane is obtained as:

$$t_n = T \cdot n = \begin{Bmatrix} \cos(\alpha) \tau_{12} + \sin(\alpha) \tau_{13} \\ \cos(\alpha) \sigma_{22} + \sin(\alpha) \tau_{23} \\ \cos(\alpha) \tau_{23} + \sin(\alpha) \sigma_{33} \end{Bmatrix} \quad (5.2)$$

The orientation of the fracture plane is function of the components of the traction vector that maximizes a failure index for a particular value of α . These components are the normal stress and the two shear stresses (longitudinal and transverse) as shown in Figure 5.1.

The component in N direction is obtained as

$$\sigma_N = t_n \cdot \begin{Bmatrix} 0 \\ \cos(\alpha) \\ \sin(\alpha) \end{Bmatrix}^T = \cos(\alpha)^2 \sigma_{22} + 2 \cos(\alpha) \sin(\alpha) \tau_{23} + \sin(\alpha)^2 \sigma_{33} \quad (5.3)$$

while the component in T direction, τ_T , is given by

$$\begin{aligned} \tau_T &= t_n \cdot \begin{Bmatrix} 0 \\ -\sin(\alpha) \\ \cos(\alpha) \end{Bmatrix}^T = \\ &= -\sin(\alpha) \cos(\alpha) \sigma_{22} - \sin(\alpha)^2 \tau_{23} + \cos(\alpha)^2 \tau_{23} + \cos(\alpha) \sin(\alpha) \sigma_{33} \end{aligned} \quad (5.4)$$

Finally, the component in L direction, τ_L , is obtained as

$$\tau_L = t_n \cdot \begin{Bmatrix} 1 \\ 0 \\ 0 \end{Bmatrix}^T = \cos(\alpha) \tau_{12} + \sin(\alpha) \tau_{13} \quad (5.5)$$

The failure criteria developed here depend on the sign of the normal stress. There is a failure criterion for matrix compression if $\sigma_N > 0$, and failure criterion for matrix tension when $\sigma_N < 0$.

5.1.1 Failure criteria for matrix compression

5.1.1.1 Puck criterion

Puck *et al.* [146–149] performed matrix compression tests and noticed that a modified Mohr-Coulomb criterion can be used to predict the orientation of the fracture plane. For pure transverse compression loading ($\sigma_{22} \neq 0$ and $\sigma_{ij} = 0$) the maximum shear stress occurs for $\alpha = \pm\pi/4$. However, experimentally, it was observed that, generally, for fiber reinforced plastics the fracture angle is equal to $\alpha_0 = 53 \pm 2^\circ$. The difference between the two angles was associated to the presence of the compressive stress.

Puck and Shürmann's criterion [148] is expressed as:

$$FMC = \left(\frac{\tau_L}{S_L^{is} - \eta_L \sigma_N} \right)^2 + \left(\frac{\tau_T}{S_T^{is} - \eta_T \sigma_N} \right)^2 \quad (5.6)$$

where S_L^{is} is the longitudinal shear strength, S_T^{is} is the *in-situ* transversal shear strength, and η_L and η_T are the two slopes in the σ_N - τ diagram when $\sigma_N = 0$ and are defined as:

$$\eta_L = - \left. \frac{\partial \tau_L}{\partial \sigma_N} \right|_{\sigma_N=0} \quad \eta_T = - \left. \frac{\partial \tau_T}{\partial \sigma_N} \right|_{\sigma_N=0} \quad (5.7)$$

It should be noted that in all the formulation presented here the *in-situ* strengths are used. Equation (5.6) can be used to evaluate in a consistent way the different parameters that define the failure criteria.

5.1.1.1.1 Hypothesis 1: $\sigma_{22} = -Y_C^{is}$ If a only compression $\sigma_{22} = -Y_C^{is}$ is applied in the transverse direction (2) the material should fail with a fracture angle equal to $\alpha = \alpha_0$.

If the loading stress is used in equation (5.6) the failure index is expressed as:

$$FMC = \frac{\sin(\alpha)^2 \cos(\alpha)^2 Y_C^{is2}}{(S_T^{is} + \eta_T \cos(\alpha)^2 Y_C^{is})^2} \quad (5.8)$$

while the derivative of this function with respect to α yields:

$$\begin{aligned} \frac{\partial FMC}{\partial \alpha} = & 2 \frac{\sin(\alpha) \cos(\alpha)^3 Y_C^{is2}}{(S_T^{is} + \eta_T \cos(\alpha)^2 Y_C^{is})^2} - 2 \frac{\sin(\alpha)^3 \cos(\alpha) Y_C^{is2}}{(S_T^{is} + \eta_T \cos(\alpha)^2 Y_C^{is})^2} \\ & + 4 \frac{\sin(\alpha)^3 \cos(\alpha)^3 Y_C^{is3} \eta_T}{(S_T^{is} + \eta_T \cos(\alpha)^2 Y_C^{is})^3} \end{aligned} \quad (5.9)$$

The fracture should occur at the plane $\alpha = \alpha_0$ or $\alpha = \pi - \alpha_0$. For this value of the angle α it should be $FMC = 1$ and $\partial FMC / \partial \alpha = 0$. Substituting $\alpha = \alpha_0$ in equations (5.8) and (5.9), the transversal shear strength and the compressive transversal strength can be obtained solving this system of equations:

$$\begin{cases} FMC|_{\alpha=\alpha_0} = 1 \\ \frac{\partial FMC}{\partial \alpha}|_{\alpha=\alpha_0} = 0 \end{cases} \quad (5.10)$$

Assuming the following relationship for the friction coefficients [149]

$$\frac{\eta_L}{\eta_T} = \frac{S_L^{is}}{S_T^{is}} \quad (5.11)$$

and considering that the in-plane shear strength and the longitudinal friction coefficient are material parameters that can be measured, the system of equation (5.10) can be solved obtaining the following values for Y_C^{is} and S_T^{is} :

$$Y_C^{is} = -\frac{S_L^{is} (2 \cos(\alpha_0)^2 - 1)}{\eta_L \cos(\alpha_0)^2} \quad (5.12)$$

$$S_T^{is} = \frac{1}{2} \frac{(2 \sin(\alpha_0)^2 - 1) S_L^{is}}{\sqrt{1 - \sin(\alpha_0)^2} \sin(\alpha_0) \eta_L} \quad (5.13)$$

If these definitions are used the failure index is equal to 1, the first derivative is equal to zero and the second derivative reads:

$$\frac{\partial^2 FMC}{\partial \alpha^2} \Big|_{\alpha=\alpha_0} = \frac{2}{\cos(\alpha_0)^2 (\cos(\alpha_0)^2 - 1)} \quad (5.14)$$

which is negative as required. This assures that for $\alpha = \alpha_0$ the maximum of the function is found. If the conditions expressed by equations (5.12) and (5.13) are not satisfied the function will take the value 1 for $\alpha = \alpha_0$ but the maximum of the function will be somewhere else. This will result in errors if the failure angle is found maximizing numerically the equation (5.8).

For example, for carbon IM7/8552 ($S_L^{is} = 130.2$, $\eta_L = 0.5$) the failure index as a function of the angle α is shown in Figure 5.2. It should be noticed that the maximum is correctly calculated for $\alpha = \alpha_0$.

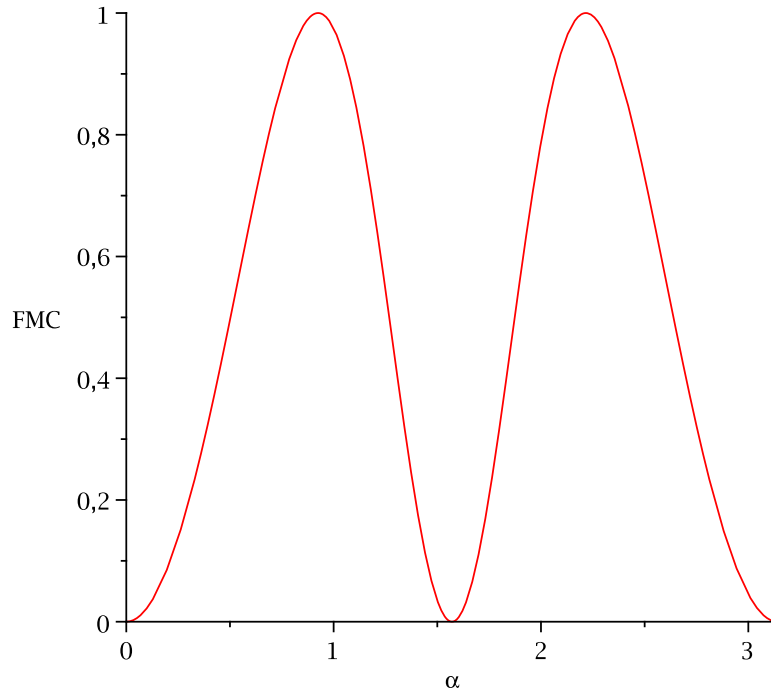


Figure 5.2: FMC as a function of α for IM-78552 ($\sigma_{22} = -Y_C^{is}$)

5.1.1.1.2 Hypothesis 2: $\tau_{12} = S_L^{is}$ If only the shear $\tau_{12} = S_L^{is}$ is applied the fracture plane must be defined by $\alpha = 0$.

In this case the failure index of equation (5.6) assumes simply the value

$$FMC = \cos(\alpha)^2 \quad (5.15)$$

while the derivative of this function assumes the value

$$\frac{\partial FMC}{\partial \alpha} = -2 \cos(\alpha) \sin(\alpha) \quad (5.16)$$

As expected, the failure index and the derivative assume the value of 1 and 0 respectively when $\alpha = 0$. The second derivative of this function takes a negative value ($\partial^2 FMC / \partial \alpha^2 = -2$) and this assures that the point found is a maximum for the failure index function. Figure 5.3 shows the failure index as a function of the angle α . The fracture angle is well predicted.

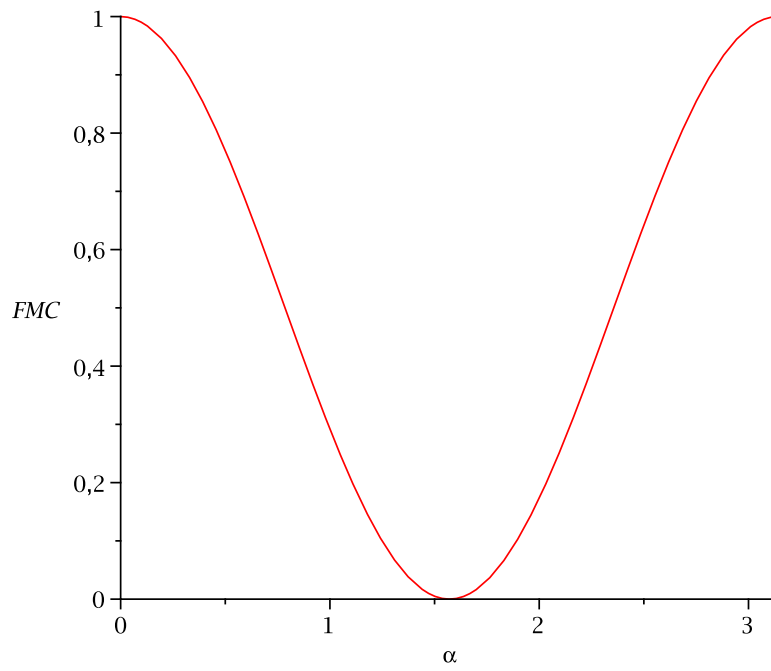


Figure 5.3: FMC as a function of α ($\tau_{12} = S_L^{is}$)

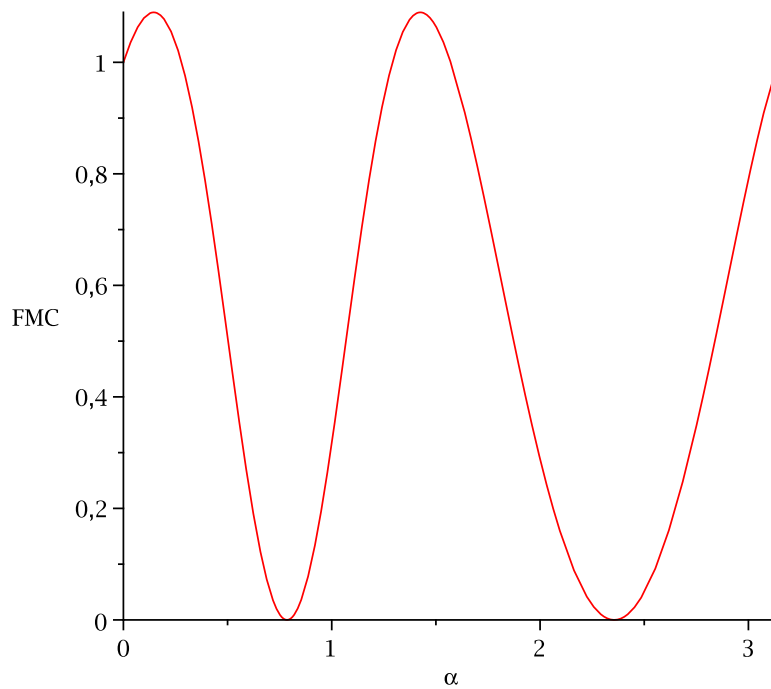


Figure 5.4: FMC as a function of α ($\tau_{23} = Y_T^{is}$)

5.1.1.1.3 Hypothesis 3: $\tau_{32} \neq 0$ Supposing that only $\tau_{23} \neq 0$ the failure index is:

$$FMC = \frac{(-\sin(\alpha)^2 \tau_{23} + \cos(\alpha)^2 \tau_{23})^2}{(S_T^{is} - 2\eta_T \cos(\alpha) \sin(\alpha) \tau_{23})^2} \quad (5.17)$$

If τ_{23} reaches its critical value ($\tau_{23} = Y_T^{is}$) the fracture plane occurs at an angle of $\alpha = 45^\circ$. However, in this case equation (5.17) does not take the value of 1 but 0 as shown in Figure 5.4. This means that this type of fracture cannot be computed using Puck's criterion for compression.

5.1.1.1.4 Conclusion Puck's failure criterion describe very well the fracture of the matrix if Y_C^{is} and S_T^{is} are defined according to equations (5.12) and (5.13). If only τ_{23} is different from zero the criterion cannot be used to predict the fracture angle. For this reason, Puck's criterion should be only used when $\sigma_N < 0$ and not when $\sigma_N = 0$.

5.1.2 Failure Criteria for Matrix Tension

5.1.2.1 Quadratic Interaction Criterion

The quadratic interaction criterion proposed by Pinho [150] assumes a quadratic relationship between the components of the stress on the fracture plane. The criterion is given by the following expression

$$FMT = \left(\frac{\sigma_N}{Y_T^{is}}\right)^2 + \left(\frac{\tau_L}{S_L^{is}}\right)^2 + \left(\frac{\tau_T}{S_T^{is}}\right)^2 \quad (5.18)$$

5.1.2.1.1 Hypothesis: $\sigma_{22} = Y_T^{is}$ Consider that a stress $\sigma_{22} = Y_T^{is}$ is applied to the material. The fracture plane should be $\alpha = 0^\circ$. Under these hypotheses the failure index assumes the value $FMT = 1$. However, if the fracture angle is not given, but rather searched by maximizing the failure index as a function α , as normally done, the failure index reads:

$$FMT = \cos(\alpha)^4 + \sin(\alpha)^2 \cos(\alpha)^2 k^2 \quad (5.19)$$

where $k = Y_T^{is}/S_T^{is}$.

Figure 5.5 shows the FMT function as a function of k .

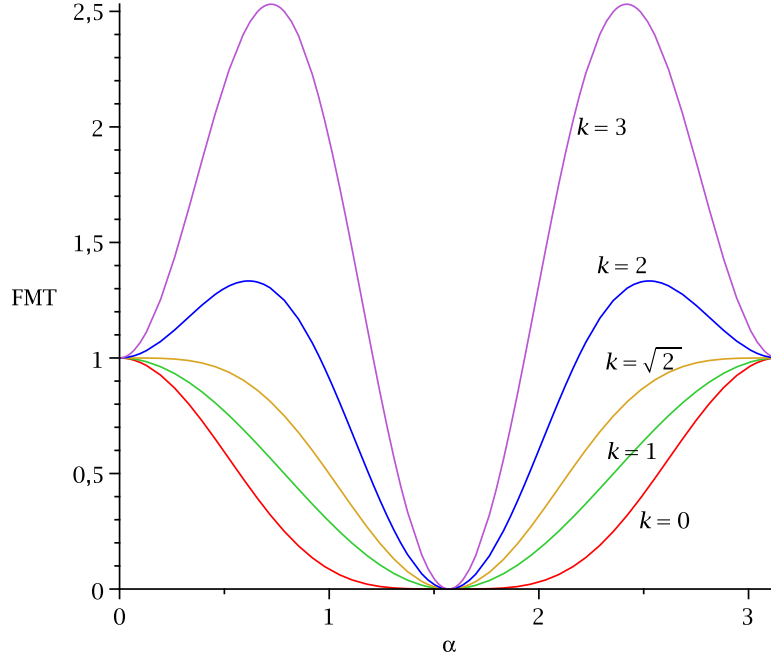


Figure 5.5: FMT as a function of α for different k ($\sigma_{22} = -Y_T^{is}$)

The derivative of equation (5.19) is:

$$\frac{\partial FMT}{\partial \alpha} = -4 \cos(\alpha)^3 \sin(\alpha) + 2 \sin(\alpha) \cos(\alpha)^3 k^2 - 2 \sin(\alpha)^3 \cos(\alpha) k^2 \quad (5.20)$$

while the second derivative reads:

$$\frac{\partial^2 FMT}{\partial \alpha^2} = -4 + 2k^2 \quad (5.21)$$

that should be negative for a maximum of the function given by equation (5.19). Consequently in the case of a unidirectional compression the criterion results in correct prediction only if:

$$k \leq \frac{\sqrt{2}}{2} \Rightarrow Y_T^{is} \leq \sqrt{2} S_T^{is} \quad (5.22)$$

For example, in the case of IM7/8552 carbon the k assumes the value $k_{IM78552} = \frac{Y_T^{is}}{S_T^{is}} = \frac{160.2}{74.7} = 2.1$. It should be noted that the value of S_T^{is} is calculated using equation (5.10). The failure index FMT for IM7/8552 is reported in Figure 5.6

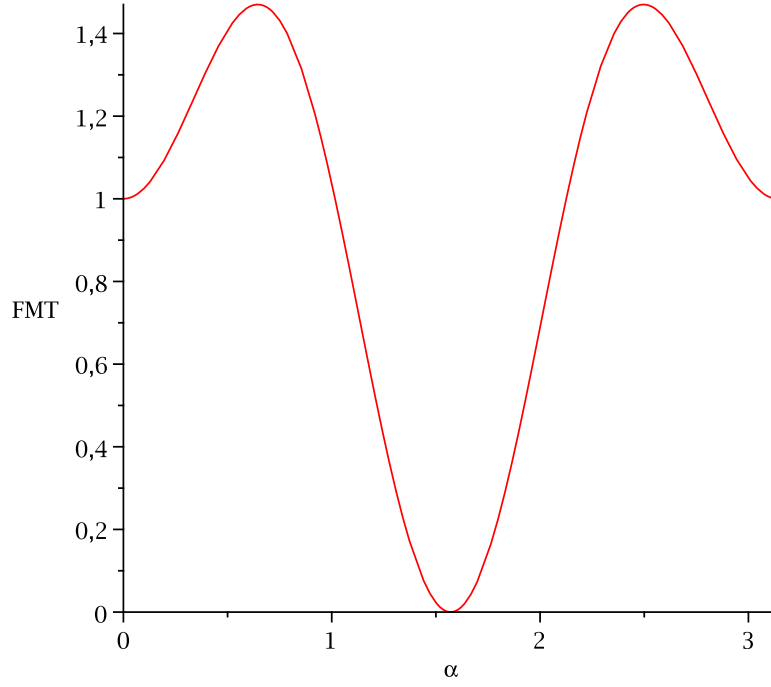


Figure 5.6: FMT as a function of α for IM7/8552 (quadratic criterion)

This means that under pure transverse tension, the failure criterion will predict that the failure occurs when $\sigma_{22} < Y_T^{is}$, and the corresponding fracture plane will be different than $\alpha = 0$. This is obviously wrong.

5.1.2.2 Puck criterion

Puck proposed an elliptical interaction criterion that can be written as [151]:

$$FMT = \left(\frac{\tau}{S^{is}}\right)^2 + c_1 \frac{\sigma_N}{Y_T^{is}} + c_2 \left(\frac{\sigma_N}{Y_T^{is}}\right)^2 \quad (5.23)$$

where τ is the shear on the fracture plane, σ_N is the normal stress and c_1 and c_2 are parameters that can be determined imposing appropriate boundary conditions. S^{is} is the shear strength on the fracture plane. The shear on the fracture plane is given as

$$\tau = \sqrt{\tau_L^2 + \tau_T^2} \quad (5.24)$$

and the angle ω between the shear stress τ_T and τ is equal to:

$$\omega = \arctan\left(\frac{\tau_L}{\tau_T}\right) \quad (5.25)$$

5.1.2.2.1 Determination of S^{is} If only τ_T and τ_L are present and σ_N is equal to zero the failure criteria for tension (equation (5.23)) and for compression (equation (5.6)) should give the same results. If not the two criteria are not consistent. Therefore, $FMC = FMT$ when $\sigma_N = 0$.

Under this hypothesis the following expression for S^{is} is derived:

$$S^{is} = \frac{1}{\sqrt{(\sin(\omega)/S_L^{is})^2 + (\cos(\omega)/S_T^{is})^2}} \quad (5.26)$$

Obviously, S^{is} depends on S_L^{is} , S_T^{is} and ω .

5.1.2.2.2 Determination of c_1 and c_2 To evaluate c_1 and c_2 , assume that a unidirectional tensile stress $\sigma_{22} = Y_T^{is}$ is applied in the transverse direction. The failure index is equal to 1 and the angle of fracture α is equal to 0. Imposing these conditions the following condition is obtained:

$$c_1 + c_2 = 1 \quad (5.27)$$

Taking the derivative of the failure index of equation (5.23)

$$\frac{\partial FMT}{\partial \sigma_N} = \frac{2\tau}{S^{is2}} \frac{\partial \tau}{\partial \sigma_N} + \frac{c_1}{Y_T^{is}} + \frac{2c_2 \sigma_N}{Y_T^{is2}} \quad (5.28)$$

and supposing that $\sigma_N = 0$ equation (5.28) results in:

$$\left. \frac{\partial FMT}{\partial \sigma_N} \right|_{\sigma_N=0} = -\frac{2\tau \eta}{S^{is2}} + \frac{c_1}{Y_T^{is}} \quad (5.29)$$

where $\eta = -\left. \frac{\partial \tau}{\partial \sigma_N} \right|_{\sigma_N=0}$.

The expression of η can be expressed in function of η_L and η_T . In fact, considering the following equation:

$$\tau^2 = \tau_L^2 + \tau_T^2 \quad (5.30)$$

and differentiating in $\frac{\partial}{\partial \sigma_N}$ it results in:

$$2\tau \frac{\partial \tau}{\partial \sigma_N} = 2\tau_L \frac{\partial \tau_L}{\partial \sigma_N} + 2\tau_T \frac{\partial \tau_T}{\partial \sigma_N} \quad (5.31)$$

then remembering the definition of the friction coefficients (equation (5.7)), under the hypothesis of $\sigma_N = 0$, equation (5.31) yields:

$$\eta = \eta_L \frac{\tau_L}{\tau} + \eta_T \frac{\tau_T}{\tau} \quad (5.32)$$

To calculate the coefficient c_1 , consider the following stress state: $\sigma_N = 0$, $\tau_T = 0$ and $\tau_L = S_L^{is}$. In this case the matrix should fail and the derivative of equation (5.29) should be equal to zero because the failure index is a maximum at that point. Under these hypotheses $\eta|_{\tau_T=0} = \eta_L$ and equation (5.29) can be re-written as:

$$\frac{\partial FMT}{\partial \sigma_N} = -\frac{2\eta_L}{S_L^{is}} + \frac{c_1}{Y_T^{is}} = 0 \quad \implies c_1 = \frac{2\eta_L Y_T^{is}}{S_L^{is}} \quad (5.33)$$

Substituting the c_1 in equation (5.27) c_2 is obtained

$$c_1 + c_2 = 1 \quad \implies c_2 = 1 - \frac{2\eta_L Y_T^{is}}{S_L^{is}} \quad (5.34)$$

The failure index of equation (5.23) assumes that the following expression:

$$FMT = \left(\frac{\tau}{S^{is}}\right)^2 + \frac{2\eta_L \sigma_N}{S_L^{is}} + \left(1 - \frac{2\eta_L Y_T^{is}}{S_L^{is}}\right) \left(\frac{\sigma_N}{Y_T^{is}}\right)^2 \quad (5.35)$$

5.1.2.2.3 Hypothesis: $\sigma_{22} = Y_T^{is}$ If $\sigma_{22} = Y_T^{is}$ with $\sigma_{ij} = 0$ the material should fail by transverse matrix cracking and the angle should $\alpha = 0$. The failure index under this hypothesis is $FMT = 1$ and the first derivative is equal to $\partial FMT / \partial \alpha = 0$.

However the second derivative reaches:

$$\left. \frac{\partial^2 FMT}{\partial \alpha^2} \right|_{\alpha=0} = \frac{2Y_T^{is^2}}{S_T^{is^2}} - \frac{4\eta_L Y_T^{is}}{S_L^{is}} - \frac{4(S_L^{is} - 2\eta_L Y_T^{is})}{S_L^{is}} \quad (5.36)$$

that should be negative if the fracture angle α corresponds to the maximum of the function FMT . The second derivative is negative when:

$$\frac{\left(-\eta_L S_T^{is} + \sqrt{\eta_L^2 S_T^{is^2} + 2S_L^{is^2}}\right) S_T^{is}}{S_L^{is}} < Y_T^{is} < \frac{\left(-\eta_L S_T^{is} - \sqrt{\eta_L^2 S_T^{is^2} + 2S_L^{is^2}}\right) S_T^{is}}{S_L^{is}} \quad (5.37)$$

For example, for carbon IM7/8552 equation (5.37) can be written as

$$-129 < Y_T^{is} < 86 \quad [\text{MPa}] \quad (5.38)$$

that is not respected. This means that in this case, the point for $\alpha = 0$ will not be a maximum for the function FMT , as clearly shown in the Figure 5.7 that represents FMT as a function of α .

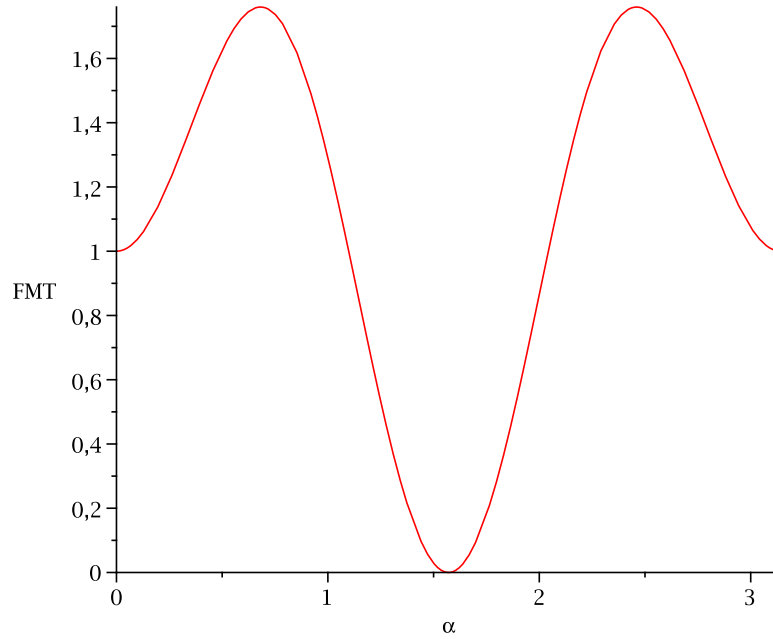


Figure 5.7: Puck criterion: FMT as a function of α for IM7/8552 ($\sigma_{22} = Y_T^{is}$)

5.1.2.3 Conclusion

The 3D interaction criteria previously proposed cannot be used to predict the failure of the matrix in general conditions. In fact, both the quadratic and the elliptical criteria, for the case of a simple transversal compression work if some condition are satisfied. These conditions are not realistic for most technical composites. It should be noted that the equations (5.22) and (5.37) assure the applicability of the failure criteria only in the case of pure transversal tension. Otherwise the applicability of the criterion used depends on the stress state applied.

5.1.2.4 Proposed Criterion

It was previously demonstrated that the quadratic interaction criteria of equations (5.18)-(5.23) cannot be used to predict the failure of the material under general stress states. Therefore, a new failure criterion is proposed in this chapter.

First of all it should be noticed that, experimentally, when a tensile stress is applied to a brittle material the fracture plane is always perpendicular to the maximum principal stress.

Puck noticed that the presence of the shear stresses reduces the strength of the matrix. However, the orientation of the fracture plane is defined by the maximum principle stress, and not by the shear stress [151].

A criterion that uses the maximum principal stress on the transverse plane (23) and considers that fracture occurs when the principal stress reaches the value of the transversal strength Y_T^{is} could be expressed as:

$$FMT = \left(\frac{\tau_L}{S_L^{is}} \right)^2 + \left(\frac{\sigma_I}{Y_T^{is}} \right)^2 \quad (5.39)$$

where σ_I is the maximum principal stress on the transversal plane (23) and τ_L is the shear in direction 1 that acts on the surface perpendicular to σ_I . Obviously $\sigma_I \geq 0$.

The principal stress σ_I is given as:

$$\sigma_I = \frac{\sigma_{22} + \sigma_{33}}{2} + \sqrt{\left(\frac{\sigma_{22} - \sigma_{33}}{2} \right)^2 + \tau_{23}^2} \quad (5.40)$$

The angle between the direction of the highest principal stress and the 22 axis is given by

$$\alpha_I = \frac{1}{2} \arctan \left(\frac{2\tau_{23}}{\sigma_{22} - \sigma_{33}} \right) \quad (5.41)$$

The shear stress τ_L that acts on the fracture plane is given as:

$$\tau_L = \cos(\alpha_I) \tau_{12} + \sin(\alpha_I) \tau_{13} \quad (5.42)$$

It should be noted that the criterion proposed yields accurate predictions for the several load cases that were previously considered. In fact:

- if $\sigma_{22} = Y_T^{is}$ and $\sigma_{ij} = 0$ the failure index takes the value $FMT = 1$ and the fracture plane is $\alpha_I = 0$;
- if $\sigma_{33} = Y_T^{is}$ and $\sigma_{ij} = 0$ the failure index takes the value $FMT = 1$ and the fracture plane is $\alpha_I = \pi/2$;
- if $\tau_{23} \neq 0$ and $\sigma_{ij} = 0$ the failure index takes the value $FMT = 1$ when $\tau_{23} = Y_T^{is}$ and the fracture plane is $\alpha_I = \pi/4$.

However, the criterion defined is only applicable if the principal stress is predominant with respect to the shear τ_L .

Consider for example the following stresses state: $\tau_{12} = S_L^{is}$, $0 < \sigma_{33} < Y_T^{is}$ and $\sigma_{ij} = 0$. Under this hypothesis the material should fail. However, if the criterion of equation (5.39) is used the fracture plane is given by $\alpha = \pi/2$. Using equation (5.5) results in $\tau_L = 0$ and consequently $FMT < 1$, that is obviously wrong.

Consequently the criterion proposed here is written as:

$$FMT = \left(\frac{\tau_L}{S_L^{is}} \right)^2 + \left(\frac{\sigma_N}{Y_T^{is}} \right)^2 \quad (5.43)$$

where σ_N and τ_L are defined in equations (5.3) and (5.5) respectively and are determined maximizing the failure index FMT respect to α .

If τ_L is not predominant the criteria of equations (5.43) and (5.39) give the same results. Different stresses states are considered in the following to show that the criterion proposed can be effectively used to predict failure of matrix when $\sigma_N \geq 0$.

5.1.2.4.1 Hypothesis 1: $\sigma_{22} = Y_T^{is}$ Consider that a stress $\sigma_{22} = Y_T^{is}$ is applied to the material. The function FMT assumes the value:

$$FMT = \cos(\alpha)^4 \quad (5.44)$$

Figure 5.8 shows the failure index FMT as a function of α . The predicted fracture plane is correctly computed as $\alpha = 0$ and the failure index takes correctly the value of $FMT = 1$.

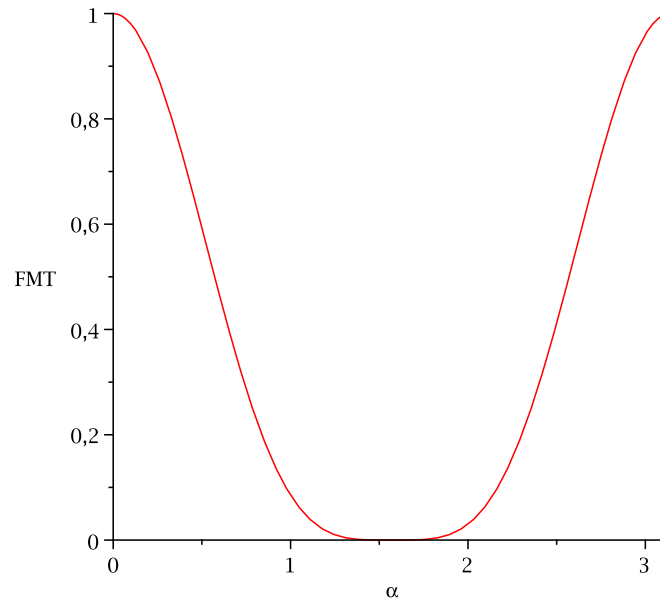


Figure 5.8: FMT as a function of α ($\sigma_{22} = Y_T^{is}$)

5.1.2.4.2 Hypothesis 2: $\sigma_{33} = Y_T^{is}$ Consider that a stress $\sigma_{33} = Y_T^{is}$ is applied to the material. The function FMT assumes the value:

$$FMT = \sin(\alpha)^4 \quad (5.45)$$

Figure 5.9 shows the failure index FMT as a function of α . The predicted fracture plane is correctly computed as $\alpha = \pi/2$. The failure index takes correctly the value $FMT = 1$ at the fracture plane.

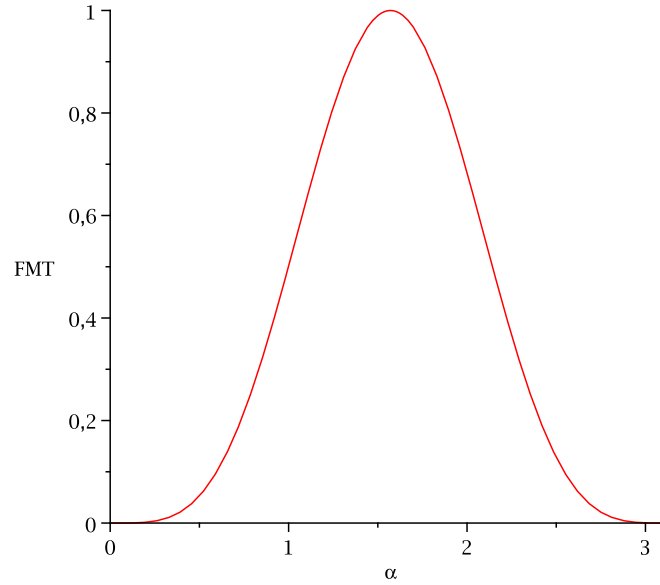


Figure 5.9: FMT as a function of α ($\sigma_{33} = Y_T^{is}$)

5.1.2.4.3 Hypothesis 3: $\tau_{23} = Y_T^{is}$ Consider that a stress $\tau_{23} = Y_T^{is}$ is applied to the material. The function FMT assumes the value:

$$FMT = 4\cos(\alpha)^2\sin(\alpha)^2 \quad (5.46)$$

Figure 5.10 shows the failure index FMT as a function of α . The predicted fracture plane is correctly computed as $\alpha = \pm\pi/4$ and the failure index takes correctly the value of $FMT = 1$.

5.1.2.4.4 Hypothesis 4: $\tau_{12} = S_L^{is}$ Consider that a stress $\tau_{12} = S_L^{is}$ is applied to the material. The function FMT assumes the value:

$$FMT = \cos(\alpha)^2 \quad (5.47)$$

Figure 5.11 shows the failure index FMT as a function of α . The predicted fracture plane is correctly computed as $\alpha = 0$ and the failure index takes correctly the value of $FMT = 1$.

5.1.2.4.5 Hypothesis 5: $\tau_{13} = S_L^{is}$ Consider that a stress $\tau_{13} = S_L^{is}$ is applied to the material. The function FMT assumes the value:

$$FMT = \sin(\alpha)^2 \quad (5.48)$$

Figure 5.12 shows the failure index FMT as a function of α . The predicted fracture plane is correctly computed as $\alpha = \pi/2$ and the failure index takes correctly the value of $FMT = 1$.

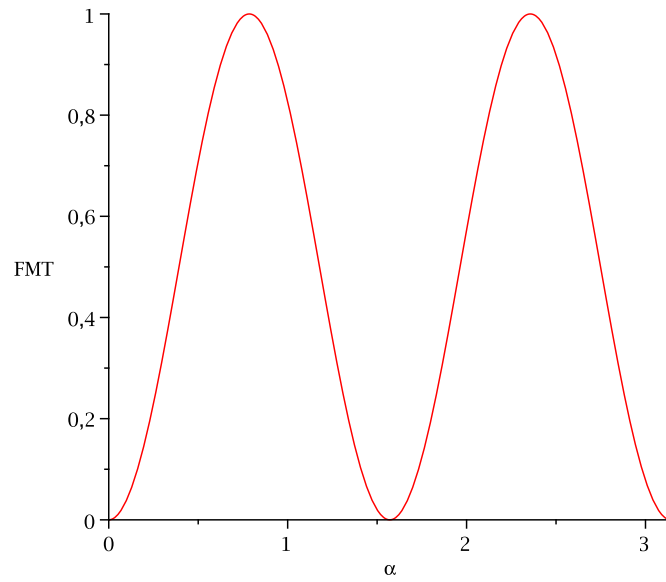


Figure 5.10: FMT as a function of α ($\tau_{23} = Y_T^{is}$)

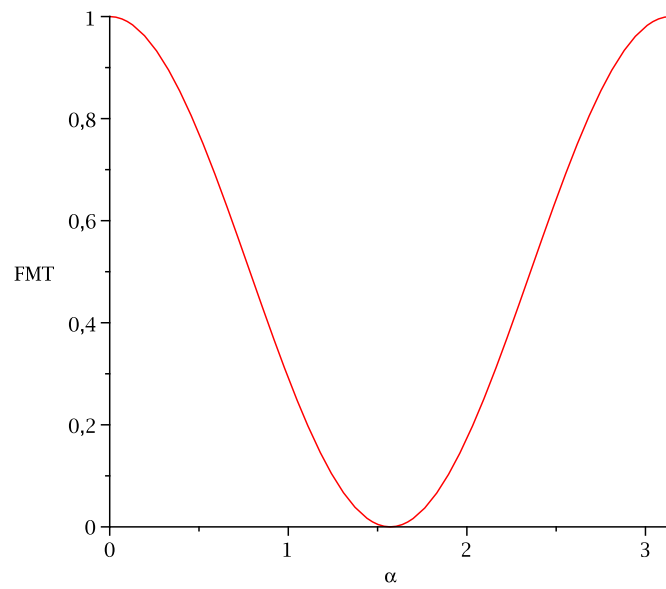


Figure 5.11: FMT as a function of α ($\tau_{12} = S_L^{is}$)

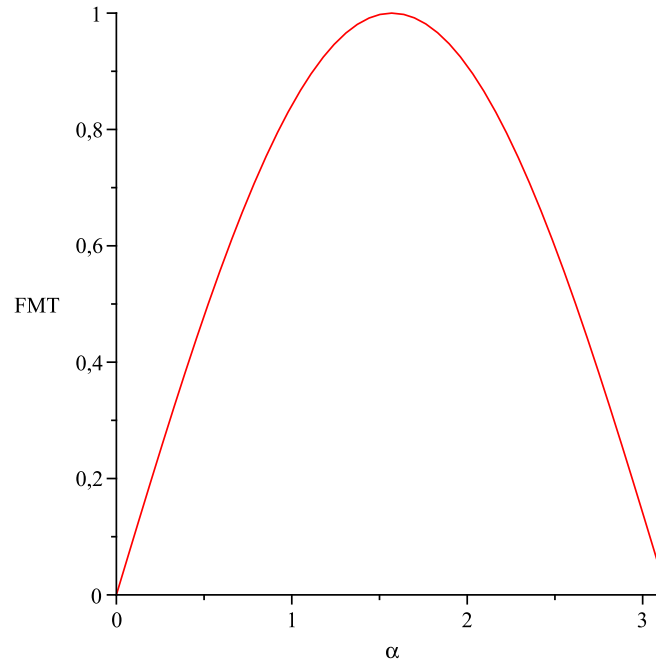


Figure 5.12: FMT as a function of α ($\tau_{13} = S_L^{is}$)

5.1.2.4.6 Summary The criterion defined provides accurate predictions for the different load cases analyses. In fact:

- if $\sigma_{22} = Y_T^{is}$ and $\sigma_{ij} = 0$ the failure index takes the value $FMT = 1$ and the fracture plane is $\alpha = 0$;
- if $\sigma_{33} = Y_T^{is}$ and $\sigma_{ij} = 0$ the failure index takes the value $FMT = 1$ and the fracture plane is $\alpha = \pi/2$;
- if $\tau_{23} \neq 0$ and $\sigma_{ij} = 0$ the failure index takes the value $FMT = 1$ when $\tau_{23} = Y_T^{is}$ and the fracture plane is $\alpha_I = \pi/4$;
- if $\tau_{12} = S_L^{is}$ and $\sigma_{ij} = 0$ the failure index takes the value $FMT = 1$ and the fracture plane is $\alpha = 0$;
- if $\tau_{13} = S_L^{is}$ and $\sigma_{ij} = 0$ the failure index takes the value $FMT = 1$ and the fracture plane is $\alpha = \pi/2$.

In the case that only τ_{23} is different from zero, Puck's criterion for compression cannot predict the fracture angle (see Section 5.1.1.1.3). However experimental evidence shows that if the only τ_{23} is present, the fracture plane is oriented at 45° . This criterion can detect the right fracture plane and so it should be used when $\sigma_N \geq 0$, while the Puck's criterion for compression should be used only in the case of $\sigma_N < 0$.

5.1.2.5 Failure envelopes for matrix failure

Figures 5.13-5.17 show the failure envelopes for matrix failure when Puck's criterion is used for compression, $\sigma_N < 0$, and the proposed criterion is used for tension $\sigma_N \geq 0$, for an IM7/8552 carbon laminate. The parameter used to the definition of the material are reported in Table 5.1¹

Table 5.1: Mechanical properties of IM7/8552

X_T (MPa)	X_C (MPa)	Y_T^{is} (MPa)	Y_C^{is} (MPa)	S_L^{is} (MPa)	η_L	α_0 (°)	G_{12} (MPa)
2323.5	1200.1	160.2	198	130.2	0.5	53	5290.0

Figure 5.13(a) shows the shear τ_{12} as a function of σ_{22} . As a 2D case is considered the two criteria takes simply the form of the Puck criterion for 2D, when $\sigma_{22} < 0$, and Hashin criterion, when $\sigma_{22} \geq 0$. As expected, when σ_{22} becomes compressive the apparent shear strength increases.

Figure 5.13(b) shows the shear τ_{13} as a function of σ_{22} . As τ_{13} and σ_{22} act on different planes no interaction between them is noticed and the value of τ_{13} remains always lower than S_L^{is} .

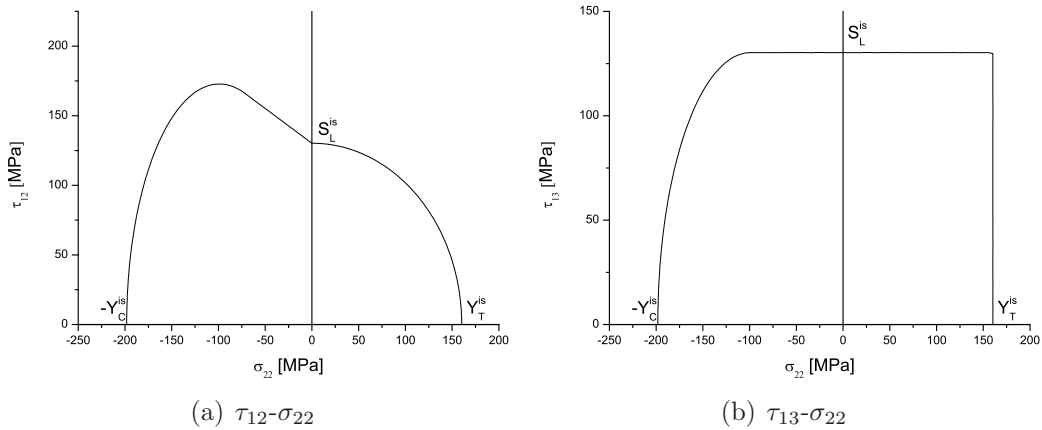


Figure 5.13: Shear stresses as a function of σ_{22}

¹It should be noted that *in-situ* strength are used; therefore, an embedded lamina is considered.

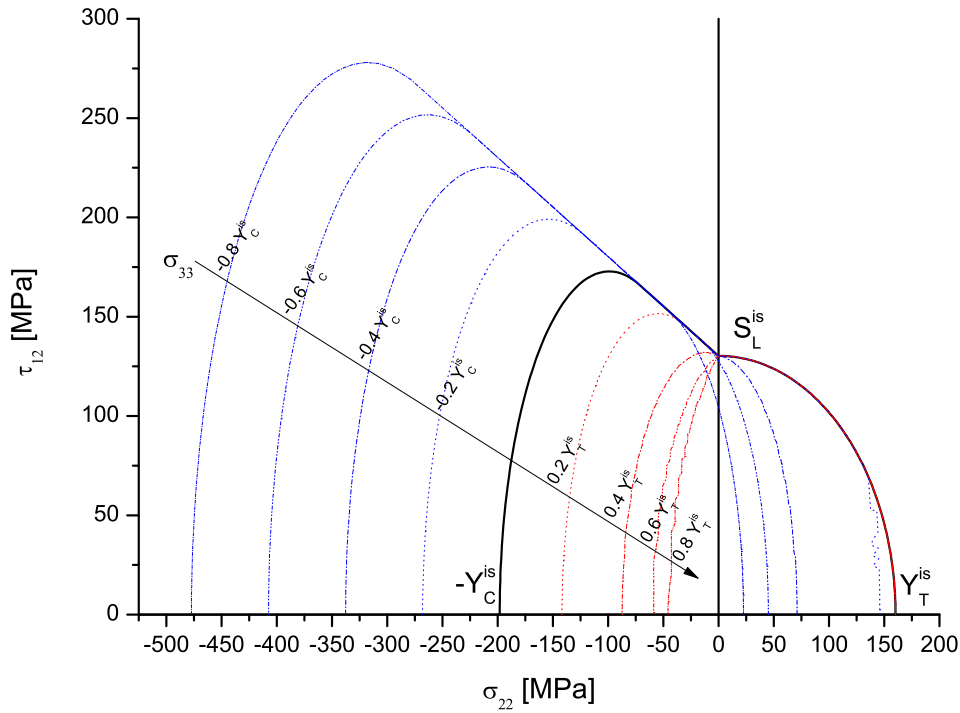


Figure 5.14: τ_{12} as a function of σ_{22} for several value of the transverse stress σ_{33}

Figure 5.14 shows the shear τ_{12} as a function of σ_{22} when a transverse stress, σ_{33} , is applied. The red envelopes are obtained when σ_{33} is positive and the blue ones when it is negative. If $\sigma_{33} > 0$ the envelope remain constant when $\sigma_{22} > 0$. This can be explained with the fact that there is no interaction between σ_{22} and σ_{33} when both are positive. In this case the fracture plane is calculated using the principal stress on the transverse plane (23). If $\sigma_{22} < 0$, an application of a positive σ_{33} decreases the strength. In the case that a compressive σ_{33} is applied the reduction of strength is noticed in tension ($\sigma_{22} > 0$) although in compression ($\sigma_{22} < 0$) the compressive σ_{33} is beneficial.

Figures 5.15-5.17 show the failures envelopes of σ_{33} as a function of σ_{22} when the shear stresses (respectively τ_{12} , τ_{13} , τ_{23}) vary.

As expected, when the shear stresses (τ_{12} , τ_{13} , τ_{23}) are equal to zero the failure envelope intercept the two axis in the points $(Y_T, 0)$, $(0, Y_T)$, $(-Y_C, 0)$ and $(0, -Y_C)$. Moreover, it should pointed out that when σ_{22} and σ_{33} are both positive the failure envelope remains correctly inside the region defined by $\sigma_{22} \leq 0$ and $\sigma_{33} \leq 0$. Finally, it should be observed that the failure envelopes are open in the region characterized by hydrostatic pressure ($\sigma_{22} = \sigma_{33} = -p$).

In Figures 5.15-5.16 the shear stresses (τ_{12} , τ_{13}) vary between 0 and S_L^s while in Figure 5.17 τ_{23} varies between 0 and S_T^{is} . This for the reason that outside these values the material should fail. However, it should be noticed the maximum value of τ_{23} for $\sigma_N \geq 0$ is Y_T^{is} . This is not represented in Figure 5.17 because in the case of compression it does not make any sense.

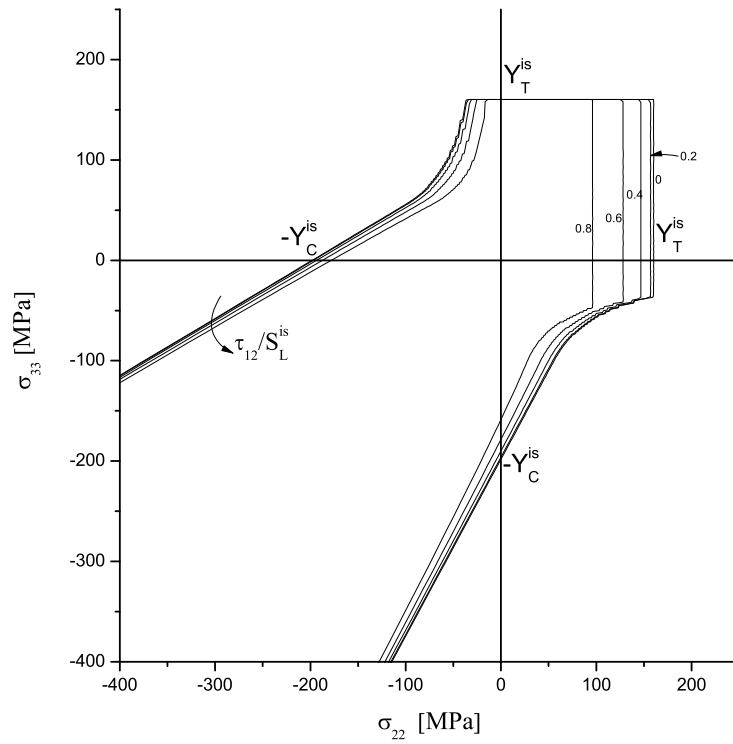


Figure 5.15: σ_{33} as a function of σ_{22} for different values of τ_{12}

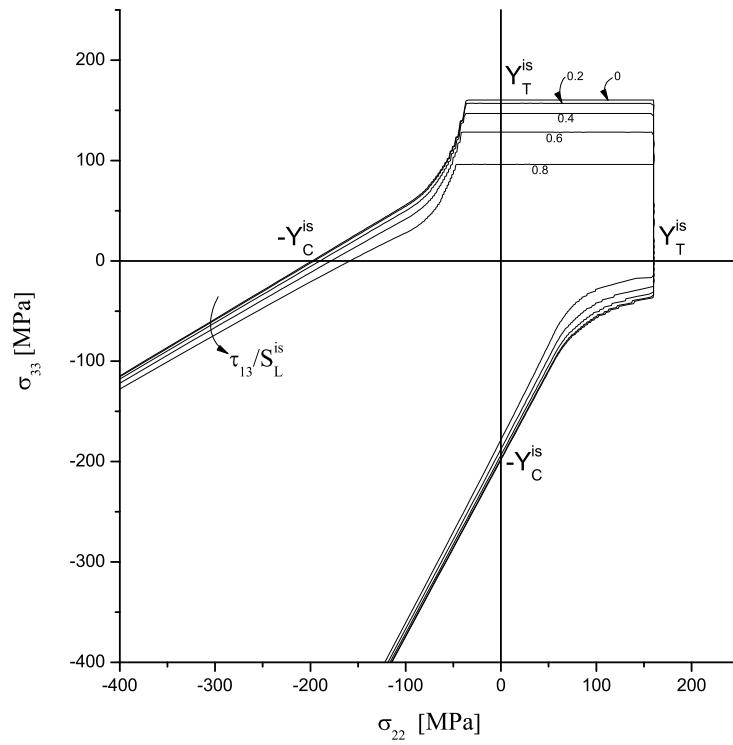


Figure 5.16: σ_{33} as a function of σ_{22} for different values of τ_{13}

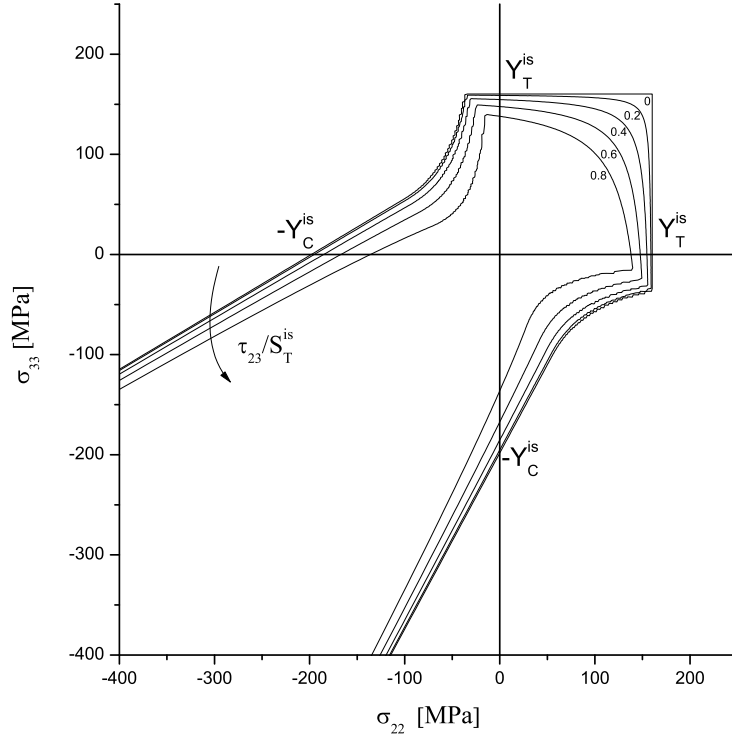


Figure 5.17: σ_{33} as a function of σ_{22} for different values of τ_{23}

5.2 Fiber Failure Criteria for 3D stress states

5.2.1 Fiber tension failure ($\sigma_{11} > 0$)

The failure index for failure in compression as suggested by Dávila *et al.* [145] can be calculated simply as:

$$FI_F = \frac{\varepsilon_{11}}{\varepsilon_1^T} \quad (5.49)$$

In this case it is simply assumed that transversal stress has a negligible influence on the longitudinal strength of the fibers.

5.2.2 Fiber kinking failure ($\sigma_{11} \leq 0$)

The 3D stress state has a relevant influence on on fiber kinking. Two hypotheses are normally made:

- the first hypothesis, from Rosen, considers that kink band are the final result of micro-buckling of the fibers [152];
- the second hypothesis, from Argon, assumes that kink bands are triggered by localized matrix failure in the vicinity of misaligned fibers [153].

Schultheisz and Waas [154] concluded that in technical composites kinking is originated by local micro-structural defects that could trigger the kinking phenomenon.

The model presented here is based on Argon's approach [153] and on the subsequent developments by Dávila *et al.* [145] and Pinho *et al.* [150].

Figure 5.18 shows the different coordinate systems and planes that are used in this model. The coordinate system 123 is aligned with the material axes of the composite: 1 represents the fiber direction, 2 and 3 the transverse directions.

In Figure 5.18(a) the kinking plane is highlighted. The coordinate system relative to the kinking plane is $1^{(\theta)}2^{(\theta)}3^{(\theta)}$ and it is obtained by 123 rotating itself around the axis 1 of an angle θ .

Figure 5.18(b) show the fibers on the kinking plane. The kinking-angle is φ and the respective coordinate system is $1^{(\varphi)}2^{(\varphi)}3^{(\varphi)}$ that can be obtained by $1^{(\theta)}2^{(\theta)}3^{(\theta)}$ after a rotation of an angle φ around the axis $3^{(\theta)}$. Then it is possible use the failure criteria of equations (5.6) and (5.43) in the misalignment coordinate system $1^{(\varphi)}2^{(\varphi)}3^{(\varphi)}$ to check for failure.

Figure 5.18(c) shows the fracture angle with respect to the misalignment frame, and identified by the angle α .

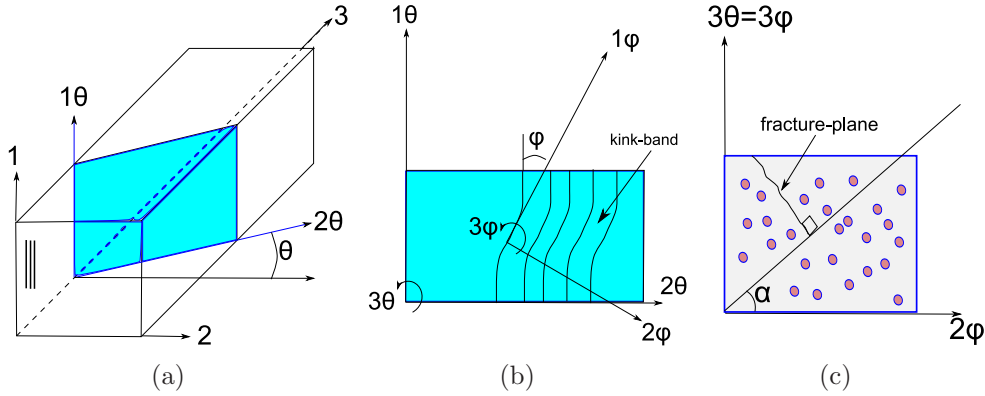


Figure 5.18: Fiber kinking, coordinate systems

Kinking failure can then be predicted using the matrix failure index in the misalignment frame. This require a double rotation of the stress tensor.

First of all the angle θ should be calculated. Generally, the kinking plane is triggered by the defects in the composite and so it means that θ is function of the local defects of the material. However, if we make the hypothesis that the influence of the defects can be neglected the angle θ can be taken as a function of the stresses and it can be calculated by the maximum principal stress that acts on the transverse plane 23. In fact, if $\tau_{23}^{(\theta)} \neq 0$ this will result in a movement perpendicular to the kinking-plane contradicting the evidence that fibers kink on this plane. For this reason, using the Mohr's circle theory the angle θ can be obtained as:

$$\tan(2\theta) = \frac{2\tau_{23}}{\sigma_{22} - \sigma_{33}} \quad (5.50)$$

Using the stress tensor defined in equation (5.1), if a rotation of θ (counterclockwise) is applied the stress tensor in the new coordinate system results:

$$T^{(\theta)} = R(\theta) \cdot T \cdot R(\theta)^T \quad (5.51)$$

where $R(\theta)$ is the rotation matrix defined as:

$$R(\theta) = \begin{bmatrix} 1 & 0 & 0 \\ 0 & \cos(\theta) & \sin(\theta) \\ 0 & -\sin(\theta) & \cos(\theta) \end{bmatrix} \quad (5.52)$$

In the θ coordinate system stresses assume the values:

$$\sigma_{11}^{(\theta)} = \sigma_{11} \quad (5.53)$$

$$\sigma_{22}^{(\theta)} = \cos^2(\theta) \sigma_{22} + 2 \cos(\theta) \sin(\theta) \tau_{23} + \sigma_{33} \sin^2(\theta) \quad (5.54)$$

$$\sigma_{33}^{(\theta)} = \sin^2(\theta) \sigma_{22} - 2 \cos(\theta) \sin(\theta) \tau_{23} + \sigma_{33} \cos^2(\theta) \quad (5.55)$$

$$\tau_{12}^{(\theta)} = \cos(\theta) \tau_{12} + \sin(\theta) \tau_{13} \quad (5.56)$$

$$\tau_{23}^{(\theta)} = -\sin(\theta) \cos(\theta) \sigma_{22} + \cos(\theta) \sin(\theta) \sigma_{33} + (\cos^2(\theta) - \sin^2(\theta)) \tau_{23} \quad (5.57)$$

$$\tau_{13}^{(\theta)} = -\sin(\theta) \tau_{12} + \cos(\theta) \tau_{13} \quad (5.58)$$

Having found the fiber-kinking plane, the stresses should be rotated in the misalignment frame. The stresses on this coordinate system can be written as:

$$T^{(\varphi)} = R(\varphi) \cdot T^{(\theta)} \cdot R(\varphi)^T \quad (5.59)$$

where $R(\varphi)$ is the rotation matrix defined as:

$$R(\varphi) = \begin{bmatrix} \cos(\varphi) & \sin(\varphi) & 0 \\ -\sin(\varphi) & \cos(\varphi) & 0 \\ 0 & 0 & 1 \end{bmatrix} \quad (5.60)$$

Finally the stresses in the misalignment frame can be expressed as:

$$\sigma_{11}^{(\varphi)} = \cos^2(\varphi) \sigma_{11}^{(\theta)} + 2 \cos(\varphi) \sin(\varphi) \tau_{12}^{(\theta)} + \sigma_{22}^{(\theta)} \sin^2(\varphi) \quad (5.61)$$

$$\sigma_{22}^{(\varphi)} = \sin^2(\varphi) \sigma_{11}^{(\theta)} - 2 \cos(\varphi) \sin(\varphi) \tau_{12}^{(\theta)} + \sigma_{22}^{(\theta)} \cos^2(\varphi) \quad (5.62)$$

$$\sigma_{33}^{(\varphi)} = \sigma_{33}^{(\theta)} \quad (5.63)$$

$$\tau_{12}^{(\varphi)} = -\sin(\varphi) \cos(\varphi) (\sigma_{11}^{(\theta)} - \sigma_{22}^{(\theta)}) + (\cos^2(\varphi) - \sin^2(\varphi)) \tau_{12}^{(\theta)} \quad (5.64)$$

$$\tau_{23}^{(\varphi)} = -\sin(\varphi) \tau_{13}^{(\theta)} + \cos(\varphi) \tau_{23}^{(\theta)} \quad (5.65)$$

$$\tau_{13}^{(\varphi)} = \cos(\varphi) \tau_{13}^{(\theta)} + \sin(\varphi) \tau_{23}^{(\theta)} \quad (5.66)$$

Then, matrix failure can be predicted using equations (5.6,5.43). The components of the traction on the fracture plane can be expressed as:

$$\sigma_N^{(\varphi)} = \cos(\alpha)^2 \sigma_{22}^{(\varphi)} + 2 \cos(\alpha) \sin(\alpha) \tau_{23}^{(\varphi)} + \sin(\alpha)^2 \sigma_{33}^{(\varphi)} \quad (5.67)$$

$$\tau_T^{(\varphi)} = -\sin(\alpha) \cos(\alpha) (\sigma_{22}^{(\varphi)} - \sigma_{33}^{(\varphi)}) + (\cos(\alpha)^2 - \sin(\alpha)^2) \tau_{23}^{(\varphi)} \quad (5.68)$$

$$\tau_L^{(\varphi)} = \cos(\alpha) \tau_{12}^{(\varphi)} + \sin(\alpha) \tau_{13}^{(\varphi)} \quad (5.69)$$

If $\sigma_N^{(\varphi)} < 0$ the failure index becomes:

$$FK_{MC} = \left(\frac{\tau_L^{(\varphi)}}{S_L^{is} - \eta_L \sigma_N^{(\varphi)}} \right)^2 + \left(\frac{\tau_T^{(\varphi)}}{S_T^{is} - \eta_T \sigma_N^{(\varphi)}} \right)^2 \quad (5.70)$$

while if $\sigma_N^{(\varphi)} \geq 0$ the failure index reads:

$$FK_{MT} = \left(\frac{\tau_L^{(\varphi)}}{S_L^{is}} \right)^2 + \left(\frac{\sigma_N^{(\varphi)}}{Y_T^{is}} \right)^2 \quad (5.71)$$

The failure index for fiber kinking will assume the value

$$FK = \max \{ \max \{ FK_{MC} \}, \max \{ FK_{MT} \} \} \quad (5.72)$$

where $\max \{ FK_{MC} \}$ and $\max \{ FK_{MT} \}$ are the maximum values of equations (5.70) and (5.71) with respect to α .

5.2.2.1 Determination of the angle φ

Dávila *et al.* [145] used a combination of Argon's approach and LaRC02/03 failure criterion to calculate the angle φ in the 2D case. The stresses in the misalignment coordinate frame of Figure 5.19 are:

$$\sigma_{11}^{(m)} = \cos(\varphi)^2 \sigma_{11} + \sin(\varphi)^2 \sigma_{22} + 2 \sin(\varphi) \cos(\varphi) |\tau_{12}| \quad (5.73)$$

$$\sigma_{22}^{(m)} = \sin(\varphi)^2 \sigma_{11} + \cos(\varphi)^2 \sigma_{22} - 2 \sin(\varphi) \cos(\varphi) |\tau_{12}| \quad (5.74)$$

$$\tau_{12}^{(m)} = -\sin(\varphi) \cos(\varphi) \sigma_{11} + \sin(\varphi) \cos(\varphi) \sigma_{22} + (\cos(\varphi)^2 - \sin(\varphi)^2) |\tau_{12}| \quad (5.75)$$

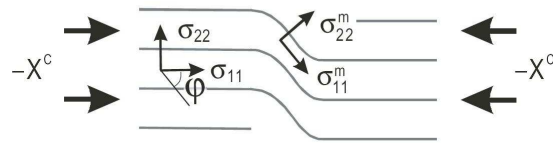


Figure 5.19: Stresses in the misalignment frame (2D)

Supposing that the material fails under axial compression the stresses take the values $\sigma_{11} = -X_C$, $\sigma_{22} = \tau_{12} = 0$. Substituting these values, equations (5.73) can be rewritten

$$\sigma_{11}^{(m)} = -\cos(\varphi_C)^2 X_C \quad (5.76)$$

$$\sigma_{22}^{(m)} = -\sin(\varphi_C)^2 X_C \quad (5.77)$$

$$\tau_{12}^{(m)} = \sin(\varphi_C) \cos(\varphi_C) X_C \quad (5.78)$$

where φ_C is the angle at the failure when a pure axial compression is applied.

Substituting these stress in the LaRC02/03 failure criterion it becomes:

$$S_L^{is} = X_C (\sin(\varphi_C) \cos(\varphi_C) - \eta_L \sin(\varphi_C)^2) \quad (5.79)$$

Equation (5.79) can be solved for φ_C obtaining

$$\varphi_C = \arctan \left(\frac{1 - \sqrt{1 - 4 \left(\frac{S_L^{is}}{X_C} + \eta_L \right) \frac{S_L^{is}}{X_C}}}{2 \left(\frac{S_L^{is}}{X_C} + \eta_L \right)} \right) \quad (5.80)$$

The total misalignment φ can be thought as the sum of an initial constant misalignment angle φ_0 (that represents the manufacture defects and imperfections in the materials) and a γ_m angle that is originated by the shear loading applied and depends on the shear constitutive law $\tau = f(\gamma_m)$.

At failure under axial compression the additional angle γ_m becomes:

$$\gamma_{mC} = f^{-1}(\tau_{12}^{(m)}) = f^{-1}(\sin(\varphi_C) \cos(\varphi_C) X_C) \quad (5.81)$$

For a material that exhibits linear behavior in shear, $\tau_{12}^{(m)} = G_{12}\gamma_m$ equation (5.81) can be solved in close form obtaining

$$\gamma_{mC} = \frac{\sin(2\varphi_C) X_C}{2G_{12}} \approx \frac{\varphi_C X_C}{G_{12}} \quad (5.82)$$

considering small angle approximation.

The initial misalignment angle can then obtained as

$$\varphi_0 = \varphi_C - \gamma_{mC} \quad (5.83)$$

For a generic loading the strain γ_m is obtained solving the equation $f(\gamma_m) = \tau_{12}^{(m)}$ that can be written as:

$$f(\gamma_m) = -\sin(\varphi) \cos(\varphi) (\sigma_{11} - \sigma_{22}) + 2 (\cos(\varphi)^2 - \sin(\varphi)^2) |\tau_{12}| \quad (5.84)$$

Solving equation (5.84) for γ_m the angle φ becomes:

$$\varphi = \text{sgn} \{ \tau_{12} \} (\varphi_0 + \gamma_m) \quad (5.85)$$

Assuming small angle approximation equation (5.84) results

$$f(\gamma_m) = (\varphi_0 + \gamma_m)(-\sigma_{11} + \sigma_{22}) + |\tau_{12}| \quad (5.86)$$

that for a material that exhibits linear behavior can be solved as:

$$\gamma_m = \frac{\varphi_0 G_{12} + |\tau_{12}|}{G_{12} + \sigma_{11} - \sigma_{22}} - \varphi_0 \quad (5.87)$$

Pinho *et al.* [150] suggested to apply the the equations (5.84- 5.87) considering the stresses that acts on the kinking plane. Equation (5.84) becomes:

$$f(\gamma_m) = -\sin(\varphi) \cos(\varphi) \left(\sigma_{11}^{(\theta)} - \sigma_{22}^{(\theta)} \right) + 2 \left(\cos(\varphi)^2 - \sin(\varphi)^2 \right) \left| \tau_{12}^{(\theta)} \right| \quad (5.88)$$

Finally for linear shear behavior equation (5.88) results:

$$\gamma_m = \frac{\varphi_0 G_{12} + \left| \tau_{12}^{(\theta)} \right|}{G_{12} + \sigma_{11}^{(\theta)} - \sigma_{22}^{(\theta)}} - \varphi_0 \quad (5.89)$$

5.2.2.2 Failure envelopes for fiber failure

Figures 5.20-5.23 show the failure envelopes for an IM7/8552 carbon laminate. The parameter used to the definition of the material are reported in Table 5.1.

Figure 5.20 shows the σ_{11} - σ_{22} failure envelope where are highlighted the regions interested by different failure phenomena.

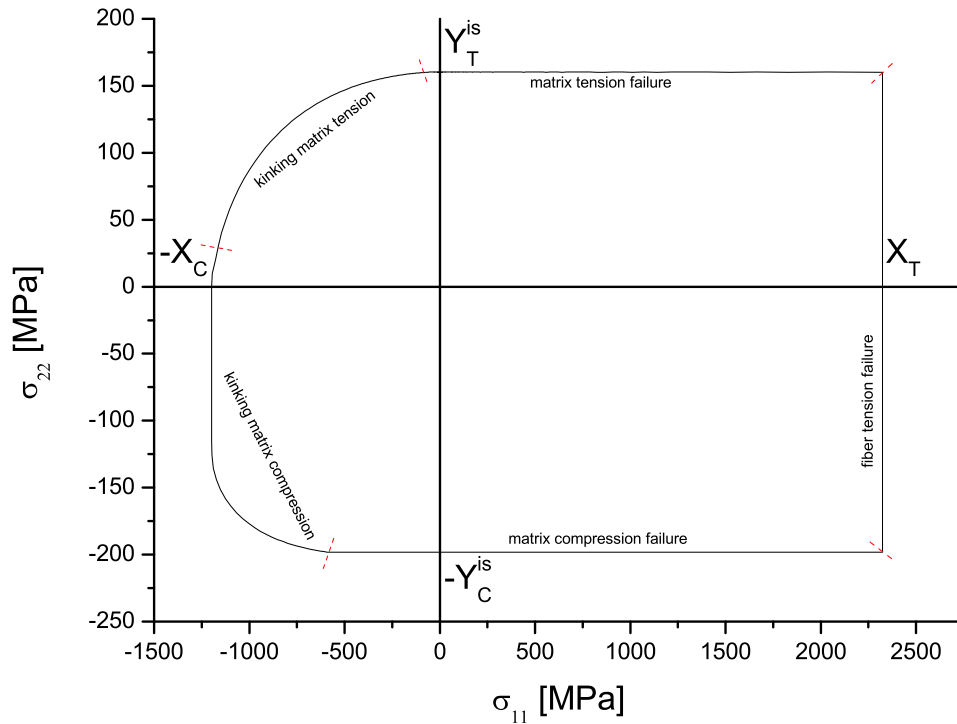


Figure 5.20: σ_{11} - σ_{22} failure envelope for IM7/8552 carbon

In the region characterized by kinking for matrix compression, the LaRC03 failure criterion predicts an increase of the axial compressive strength and this is confirmed by experimental results [155]. The criterion proposed here shows an increase of the compressive strength only in a small region of the envelope² but there is not an increasing of the compressive strength if a biaxial compression is applied. This seems to contradict the experimental evidence but it is not the case. First of all, it should be highlighted that the fact that the compressive stress does not increase can be explained remembering the definition of the angle θ that identify the kink band plane. When σ_{22} becomes smaller than zero ($\sigma_{33} = 0$), the angle of the principal stress changes from 0° to 90° . If a compression in 2 direction is applied this will not influence the fiber kinking because the fiber will kink in the perpendicular plane. It is consistent with the model defined having a constant value of the compressive strength when $\sigma_{22} < 0$. However, if the loading condition or the manufacture of the material can justify a predisposition of the material to kink with an angle $\theta = 0$ (in 2 direction) the proposed failure criteria can detect the increasing of compressive strength in the biaxial compression region.

Figure 5.21 shows the σ_{11} - σ_{22} failure envelope when a transverse stress is applied.

²Near the point that identifies the switching of failure from kinking for matrix tension to kinking for matrix compression

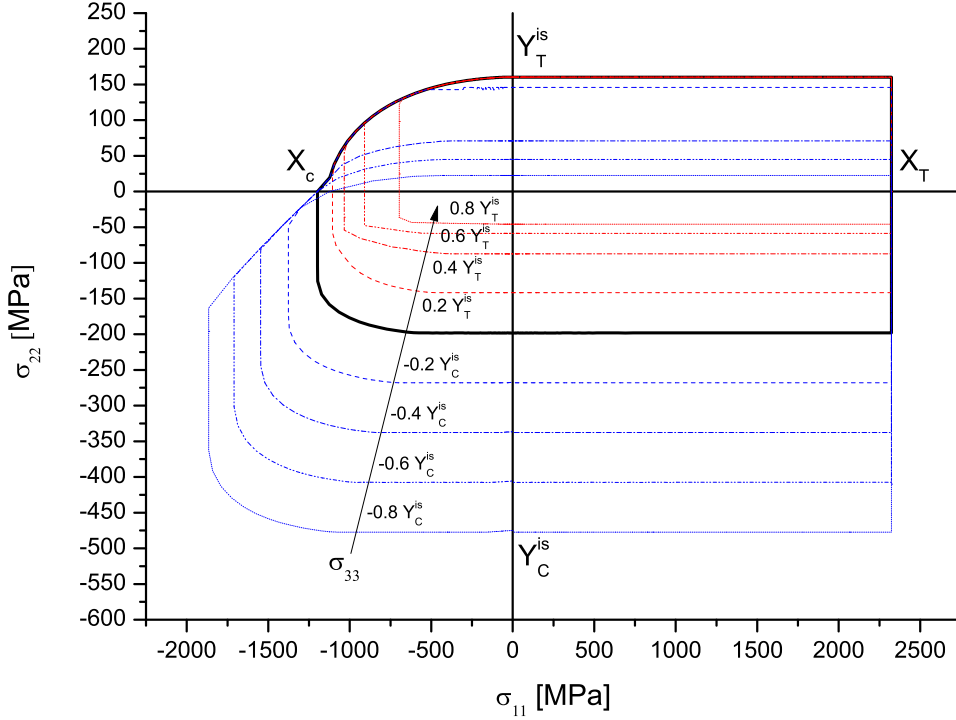


Figure 5.21: σ_{11} - σ_{22} failure envelope for different values of transverse stress σ_{33} for IM7/8552 carbon

In this case, as both σ_{22} and σ_{33} are compressive the increase of the strength in the biaxial compression region is shown. It should be noticed that when a transverse compression is applied ($\sigma_{33} < 0$) the strength of the material decreases in tension ($\sigma_{22} > 0$) and increases in compression ($\sigma_{22} < 0$). When a transverse tension is applied the compressive strength decreases ($\sigma_{22} < 0$) but no effects can be noticed in the tensile strength ($\sigma_{22} > 0$) and this is due to the fact that in tension ($\sigma_N > 0, \tau_L = 0$) the failure index is function of the principal stress on the transversal plane (23), it means that there is not interaction between σ_{22} and σ_{33} because the failure depends only on the maximum value of σ_{22} or σ_{33} . In this case in fact $\sigma_N = \max\{\sigma_{22}, \sigma_{33}\}$.

Figure 5.22 shows the σ_{11} - τ_{12} failure envelope. For the symmetry the envelopes σ_{11} - τ_{12} and σ_{11} - τ_{13} should be the same. It should be noticed that when only σ_{11} and τ_{12} (or τ_{13}) are applied, the principal stresses on the transverse plane are zero and for these reason θ assume infinite values. Under these conditions, the kinking-plane is triggered by the defects of the material and theoretically infinite solutions are possible because θ can take all the values between 0 and π . Figure 5.22 shows the two envelopes for $\theta = 0$ and $\theta = \pi/2$ that represent the boundaries of the relevant region. As the envelope for $\theta = 0$ gives the most conservatives results this should be used.

Figure 5.21 shows the σ_{11} - τ_{12} failure envelope when a transverse stress σ_{33} is applied. When $\sigma_{33} < 0$ the kinking plane is calculated by $\theta = 0$ while is $\sigma_{33} > 0$,

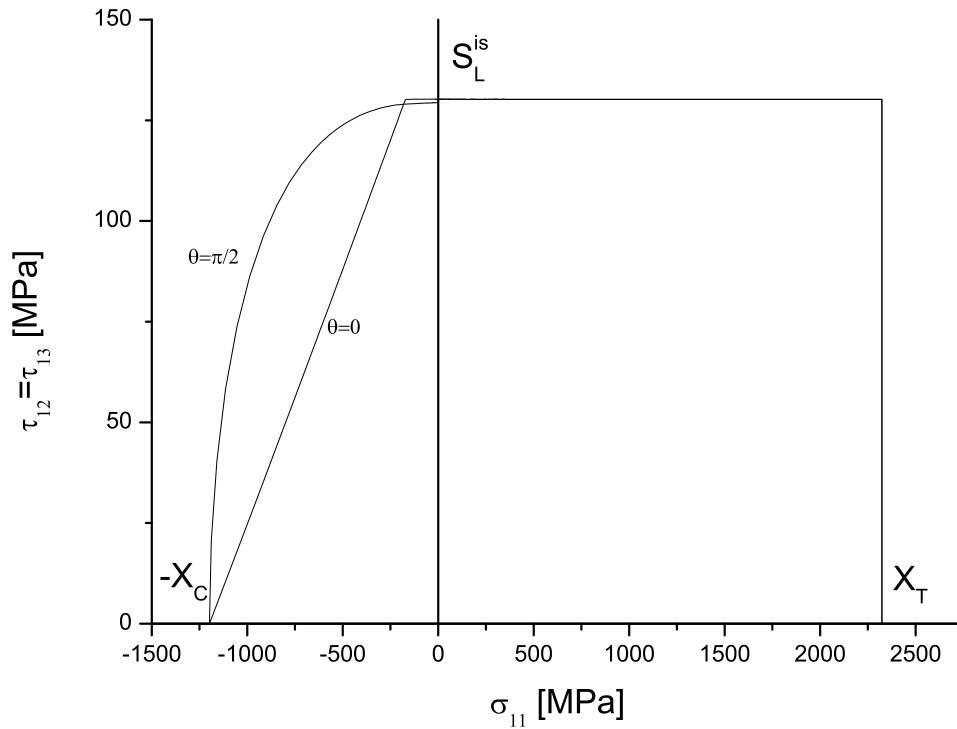


Figure 5.22: σ_{11} - τ_{12} failure envelope for IM7/8552 carbon

$\theta = \pi$. An increasing in transverse compression or tension results in a reduction of the strength of the material.

5.3 Verification Problems

5.3.1 Example 1: Relationship between Y_C^{is} , η_L and S_L^{is}

In Section 5.1.1.1 the following relationship between Y_C^{is} , η_L and S_L^{is} was found:

$$Y_C^{is} = -\frac{S_L^{is} (2 \cos(\alpha_0)^2 - 1)}{\eta_L \cos(\alpha_0)^2} \quad (5.90)$$

This relationship is written for the *in-situ* properties but has to be respected also in the case of a unidirectional lamina.

It is shown here that equation (5.90) is respected for the technical composites commonly used. Table 5.2 reports the material parameters of AS4/55A, E-Glass/LY556/HT907/DY063 and T800/3900-2 unidirectional laminae.

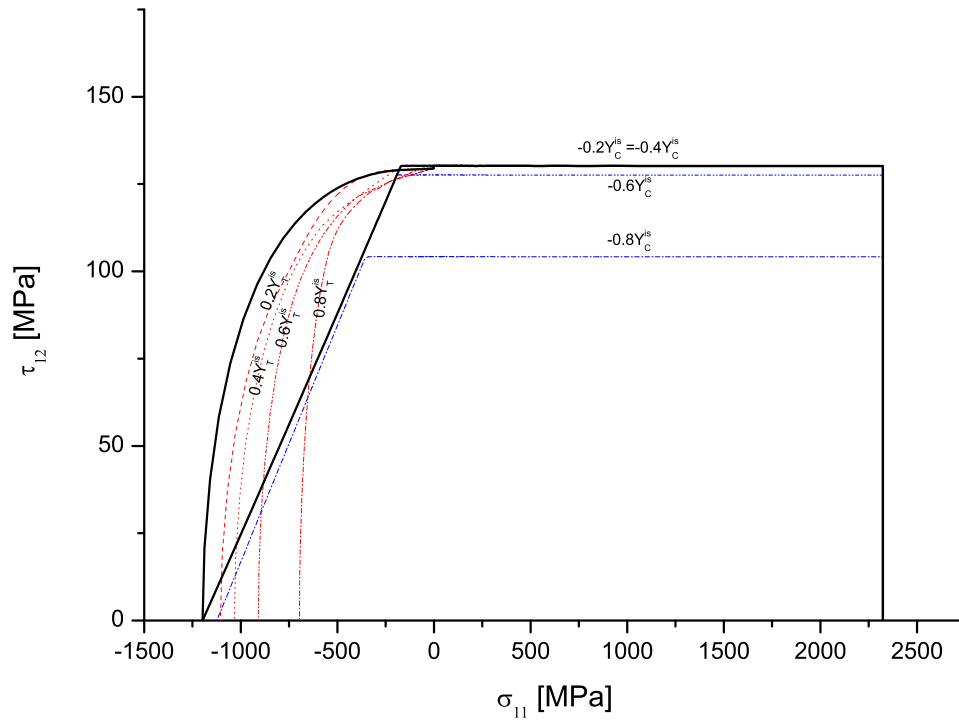


Figure 5.23: σ_{11} - τ_{12} failure envelope for different values of transverse stress σ_{33} for IM7/8552 carbon

Table 5.2: Material properties of investigated composites

material	AS4/55A	E-Glass/LY556/HT907/DY063	T800/3900-2
reference			
X_T (MPa)	–	1140	–
X_C (MPa)	–	570	–
Y_T (MPa)	27.0	35	48.8
Y_C (MPa)	91.8	130	201.7
S_L (MPa)	66.0	72	100.9
G_{12} (MPa)	6600	5830	5500
α_0 (°)	53	53	53

Figure 5.24 shows the τ_{12} as a function of σ_{22} for the materials of Table 5.2. For each curve the tangent is calculated for $\sigma_N \rightarrow 0$ and remember the definition of η_L (equation (5.7)) is possible to calculate its value for each material as the angular coefficient of the tangent.

Table 5.3 reports for each material the measured S_L , Y_C , η_L and the value of Y_C that can be calculated using equation (5.90). The predicted values of Y_C are in good agreement with the experimental results.

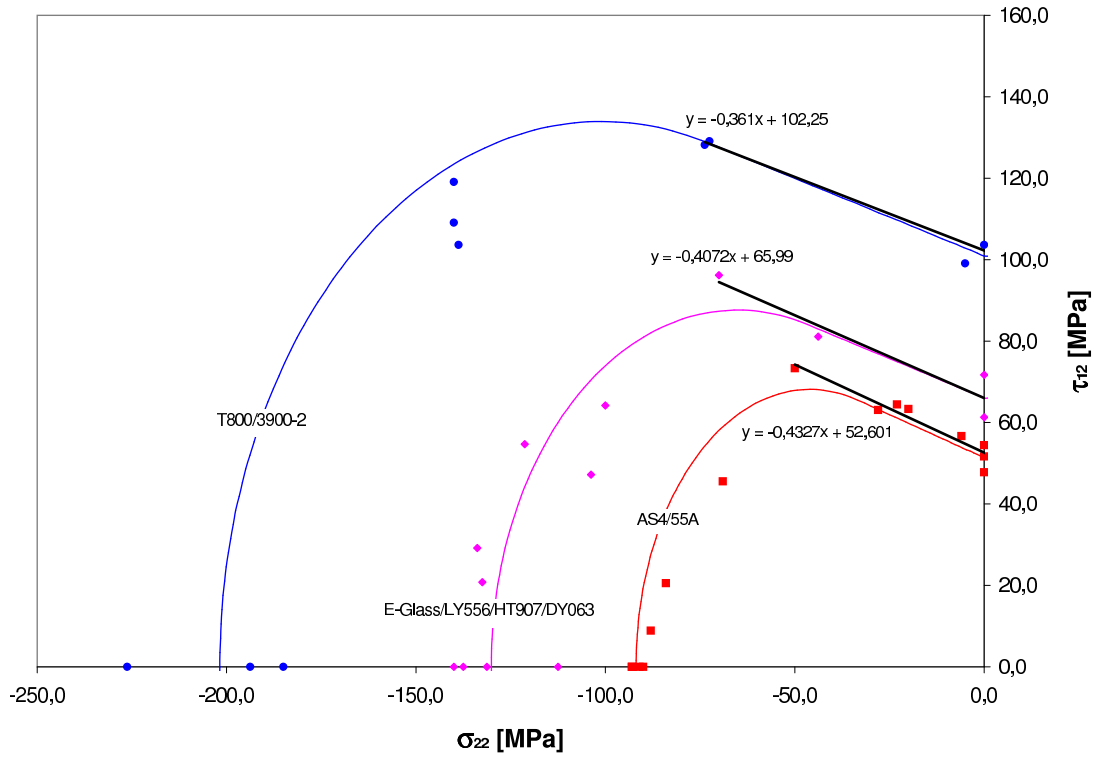


Figure 5.24: τ_{12} as a function of σ_{22} for different materials and correspondent values of Y_C^{is} , η_L and S_L^{is}

Table 5.3: Material properties of investigated composites

material	S_L	η_L	measured Y_C	calculated Y_C
AS4/55A	51.3	0.43	91.8	90.2
E-Glass/LY556/HT907/DY063	66.0	0.41	130.0	123.0
T800/3900-2	100.9	0.36	201.7	212.0

5.3.2 Example 2: σ_{22} - τ_{12} failure envelopes

Figure 5.25 show the σ_{22} - τ_{12} failure envelopes for four different materials: AS4/55A, E-Glass/LY556/HT907/DY063, T800/3900-2 and IM7/8552. The mechanical parameters are reported in Tables 5.2 and 5.4. For carbon IM7/8552 static and dynamic results are reported. It can be noticed that the proposed model fits well the experimental results for static and dynamic case.

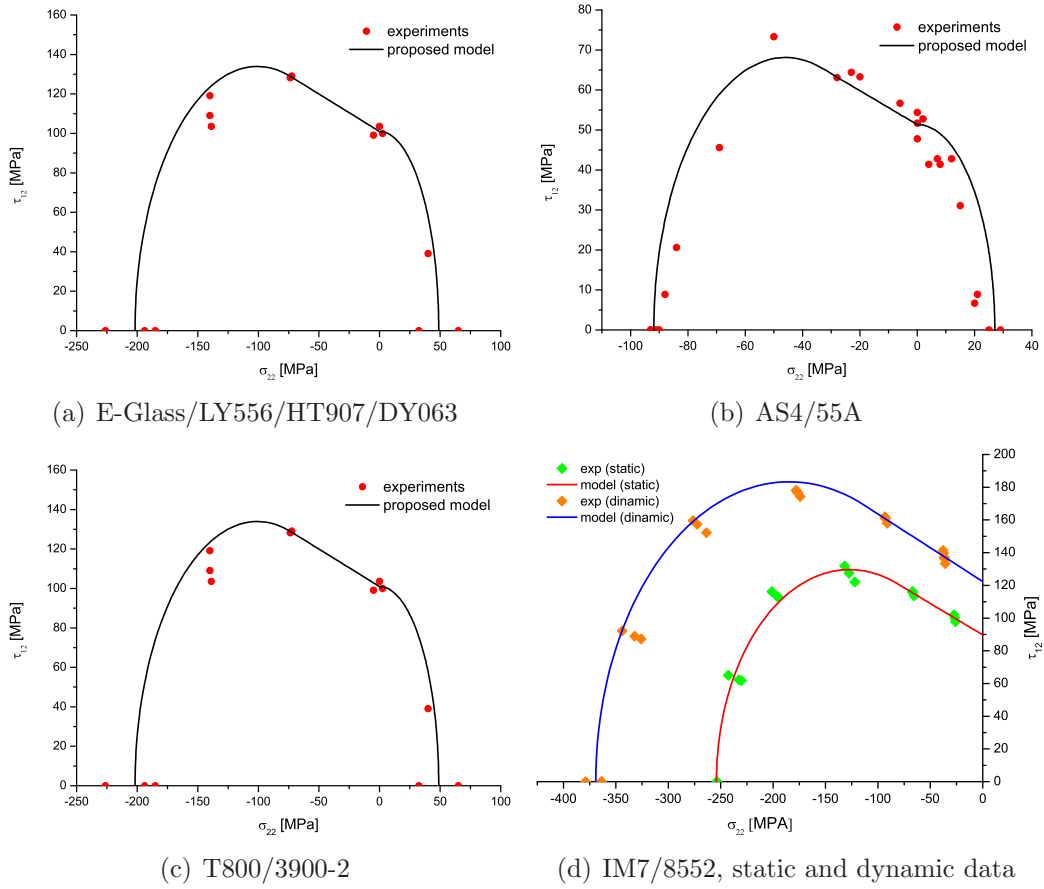


Figure 5.25: σ_{22} - τ_{12} failure envelopes for different material

Table 5.4: Material properties of IM78552

test type	static	dynamic
X_T (MPa)	2323.5	–
X_C (MPa)	1017.5	1428.0
Y_T (MPa)	160.2	–
S_L (MPa)	89.6	122.3
η_L	0.38	0.41
G_{12} (MPa)	5290	5290
α_0 (°)	55.3	56.3

5.3.3 Example 3: Compression of thick lamina

Koerber *et al.* [156] presented compression test based on ASTM Standard D 695 of end-loaded thick specimens. The specimens are manufactured using IM7/8552 carbon-epoxy. The material parameters are shown in Table 5.4.

Two types of test are performed:

- transverse compression;
- off-axis compression at 0° , 15° , 30° , 45° , 60° , 75° .

The test are conducted statically and dynamically. Experimental data and numerical results are reported in Figure 5.26. Good agreement between experimental results and the proposed model is observed.

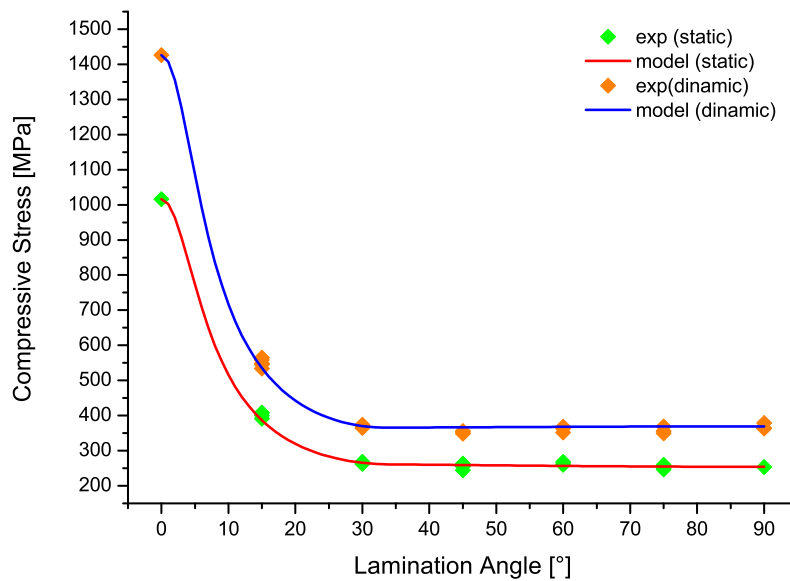


Figure 5.26: Off-axis compression test of IM7/8552 carbon lamina

5.3.4 Example 4: σ_{11} - σ_{22} failure envelopes

Hinton *et al.* [157] report biaxial test of E-Glass/MY750 epoxy lamina. Table 5.5 shows the material properties of E-Glass/MY750 epoxy.

Table 5.5: Material properties of E-Glass/MY750 epoxy

X_T (MPa)	X_C (MPa)	Y_T (MPa)	Y_C (MPa)	S_L (MPa)	G_{12} (MPa)	α_0 (°)
1280	800	40	145	73	5830	53

The experimental data and the numerical results are shown in Figure 5.27. It should be noted that some data are not taken into accounts to validate the numerical model because they are affected by experimental errors due to the presence of buckling. These points are highlighted in Figure 5.27. For the other points good agreement between experiments and the proposed model is observed.

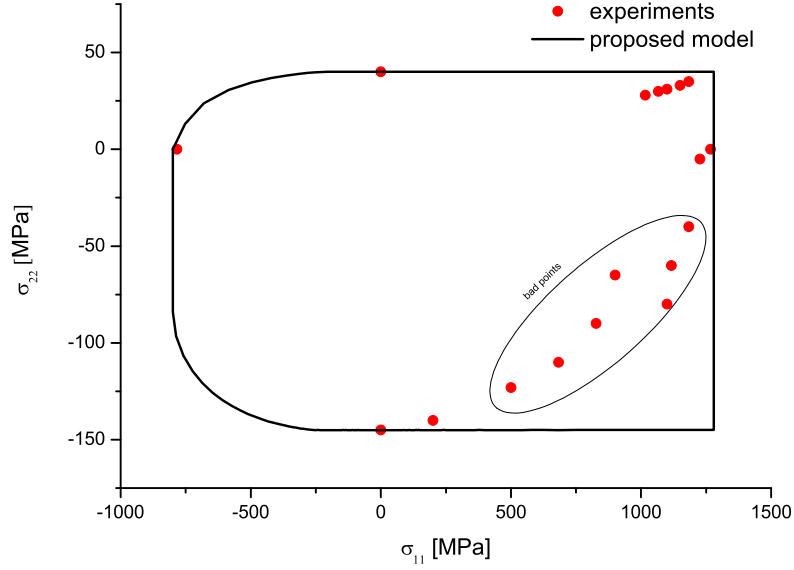


Figure 5.27: σ_{11} - σ_{22} failure envelope for E-Glass/MY750 epoxy lamina

5.3.5 Example 5: σ_{11} - τ_{12} failure envelopes

Hinton *et al.* [157] present experimental test of T300/914C. The mechanical parameter of the material are shown in Table 5.6.

Figure 5.28 show the failure envelope generated by the proposed failure criteria and the experimental data.

The model reports the two extreme solutions for $\theta = 0$ and $\theta = \pi$. The dispersion presented by the data could be an effect of the different angles of the kinking plane. The data present a high dispersion and some of them are clearly affected by experimental error (as those that present a shear strength higher than S_L^{is}). For this reason, it could be concluded that the comparison between experiments and the proposed model is acceptable.

Table 5.6: Material properties of T300/914C

X_T (MPa)	X_C (MPa)	Y_T (MPa)	Y_C (MPa)	S_L (MPa)	G_{12} (MPa)	α_0 ($^\circ$)
1500	900	27	200	80	5500	53

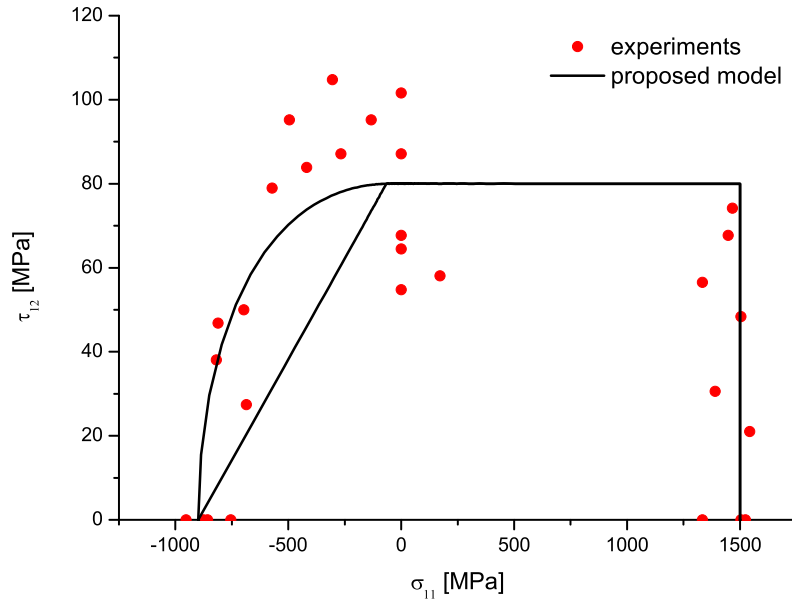


Figure 5.28: σ_{11} - τ_{12} failure envelope for T300/914C lamina

5.3.6 Example 6: Influence of hydrostatic pressure

As discussed previously, the proposed model predicts higher value of the strength when a hydrostatic pressure is applied to the composite.

However, to predict the correct value of the strength under high hydrostatic pressure is a formidable task. In fact, hydrostatic pressure [155] has a very important influence on the mechanical parameter of the composites. If a hydrostatic pressure is applied:

- the elastic and shear moduli increase. Depending on the resin used the elastic and shear moduli are linear or bilinear functions of the hydrostatic pressure. The bilinear behavior is considered an effect of the hydrostatic pressure that shifts the sub-zero secondary glass transition temperature;
- some resins exhibit yielding when the applied pressure is greater than 200 MPa. As the yielding phenomenon is pressure-dependent a pressure-dependent yield criterion should be used to predict this behavior. Pae [155] proposed for the resin a criterion that consider the second invariant of the deviatoric stress tensor, J_2 , a material constant α_m , and the first invariant of the stress tensor I_1 . Successively, this theory was extended to the anisotropic materials;
- the composites exhibit a plastic behavior.

Hine *et al.* [158] presented experimental results of a E-glass/MY750 lamina tested in compression and in shear under hydrostatic confinement. The mechanical properties of the material are shown in Table 5.5.

Figures 5.29-5.30 show the compressive strength and the shear strength as a function of the superimposed hydrostatic pressure of thick lamina tested under hydrostatic pressure.

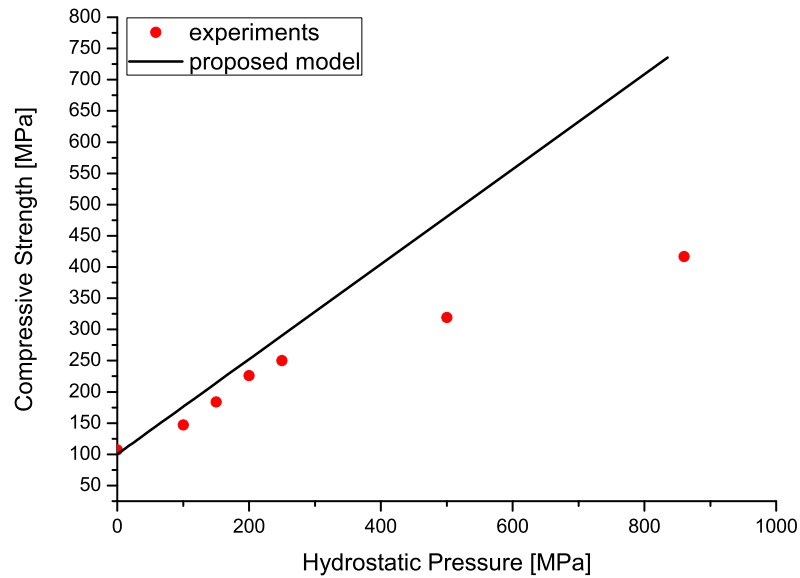


Figure 5.29: Compressive strength as function of the hydrostatic pressure

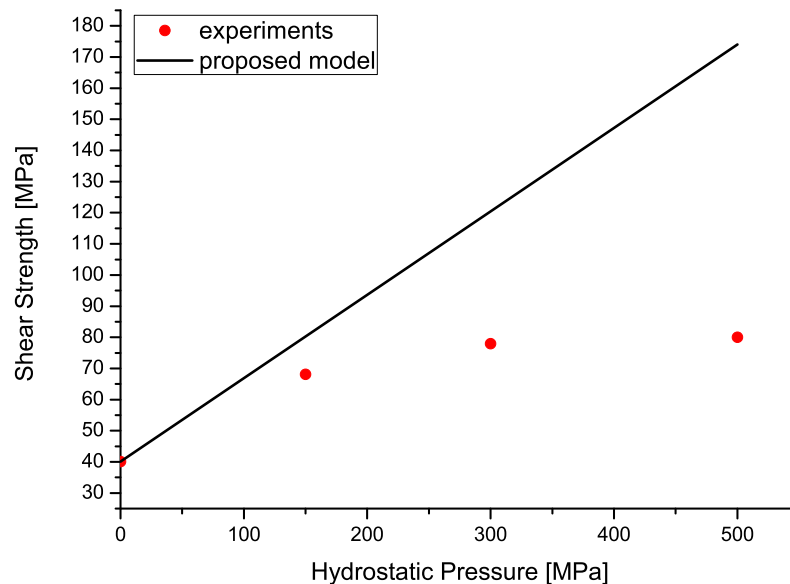


Figure 5.30: Shear strength as function of the hydrostatic pressure

It can be concluded that the proposed criterion can tackle the increase in the strength of the composites under high values of the hydrostatic pressure. However the correlation between predictions and experimental data appears to be acceptable up

to a pressure of 200 MPa. This pressure should represent the pressure that shifts the sub-zero secondary glass temperature at the room temperature at which the test are conducted. After this pressure, some material parameters change for the reasons explained before, and as these effects are not taken into account in the proposed failure criteria, the experimental data and the predicted model are different for hydrostatic pressure higher than 200MPa.

5.3.7 Conclusions

The proposed failure criteria are able to consider the effect of a three-axial stress state on a composites. The model is completely defined when these parameters are known: X_T , X_C , α_0 , Y_T^{is} , η_L , S_L^{is} and G_{12} . It was shown that Y_C^{is} is function of α_0 , S_L^{is} and η_L . As experimentally the value of Y_C^{is} is very difficult to measure, equation (5.90) gives a very easy method to calculate Y_C^{is} .

The model can predict the experimental results in different load conditions and a good agreement is shown. If high value of hydrostatic pressure are applied the elastic properties of the material change and this is not taken into account.

The introduction of the non-linear behavior and the hydrostatic pressure effect should be subjects of further developments.

5.4 Damage Model

Maimí *et al.* [133,134] proposed a constitutive damage model for laminated composites that has its foundation in irreversible thermodynamics, and that uses the LaRC04 criteria as damage activation functions.

In this work the same damage model is used but with different damage activation functions. Changes made concern the introduction of the softening law for fiber compression and the extension to the 3D stress state. The details will be explained in the following points.

5.4.1 Complementary free energy and damage operators

The scalar function proposed for the complementary free energy density [133] is:

$$\begin{aligned}
 G = & \frac{\sigma_{11}^2}{2(1-d_1)E_1} + \frac{1}{2E_2} \left(\frac{\sigma_{22}^2}{(1-d_2)} + \frac{\sigma_{33}^2}{(1-d_3)} \right) - \frac{\nu_{12}}{E_1} \sigma_{11} (\sigma_{22} + \sigma_{33}) + \\
 & - \frac{\nu_{23}}{E_2} \sigma_{22} \sigma_{33} + \frac{\sigma_{12}^2 + \sigma_{13}^2}{2(1-d_6)G_{12}} + (\alpha_{11}\sigma_{11} + \alpha_{22}(\sigma_{22} + \sigma_{33})) \Delta T + \\
 & + (\beta_{11}\sigma_{11} + \beta_{22}(\sigma_{22} + \sigma_{33})) \Delta M
 \end{aligned} \tag{5.91}$$

where:

- E_1, E_2, ν_{12} and G_{12} are the in-plane elastic orthotropic properties of the uni-directional lamina
- d_1, d_2 and d_6 are the damage variable. The damage variable d_1 is associated with longitudinal (fiber) failure, whereas d_2 is the damage variable associated with transverse matrix cracking and d_6 is a damage variable influenced by longitudinal and transverse cracks
- α_{11} and α_{22} are the coefficients of thermal expansion in the longitudinal and transverse directions
- β_{11} and β_{22} are the coefficients of hygroscopic expansion in the longitudinal and transverse directions
- ΔT and ΔM are the differences of temperature and moisture content with respect to the corresponding reference values.

Using this definition of the free energy it can be shown that the strain tensor is equal to the derivative of the complementary free energy density with respect to the stress tensor:

$$\varepsilon = \frac{\partial G}{\partial \sigma} = \mathbf{H} : \sigma + \alpha \Delta T + \beta \Delta M \quad (5.92)$$

where the compliance tensor \mathbf{H} can be written as:

$$\mathbf{H} = \begin{bmatrix} \frac{1}{(1-d_1)E_1} & -\frac{\nu_{12}}{E_1} & -\frac{\nu_{12}}{E_1} & 0 & 0 \\ -\frac{\nu_{12}}{E_1} & \frac{1}{(1-d_2)E_2} & -\frac{\nu_{23}}{E_2} & 0 & 0 \\ -\frac{\nu_{12}}{E_1} & -\frac{\nu_{23}}{E_2} & \frac{1}{(1-d_3)E_2} & 0 & 0 \\ 0 & 0 & 0 & \frac{1}{(1-d_6)G_{12}} & 0 \\ 0 & 0 & 0 & 0 & \frac{1}{(1-d_6)G_{12}} \end{bmatrix} \quad (5.93)$$

To determine the active damage variables, it is necessary to define the longitudinal and transverse damage modes as follows:

$$\begin{aligned} d_1 &= d_{1+} \frac{\langle \sigma_{11} \rangle}{|\sigma_{11}|} + d_{1-} \frac{\langle -\sigma_{11} \rangle}{|\sigma_{11}|} \\ d_2 &= d_{2+} \frac{\langle \sigma_{22} \rangle}{|\sigma_{22}|} + d_{2-} \frac{\langle -\sigma_{22} \rangle}{|\sigma_{22}|} \\ d_3 &= d_{2+} \frac{\langle \sigma_{33} \rangle}{|\sigma_{33}|} + d_{2-} \frac{\langle -\sigma_{33} \rangle}{|\sigma_{33}|} \end{aligned} \quad (5.94)$$

where $\langle x \rangle$ is the McCauley operator defined as $\langle x \rangle := (x + |x|)/2$.

5.4.2 Damage activation functions

The four damage activation functions, F_N , associated with damage in the longitudinal ($N = 1+, 1-$) and transverse ($N = 2+, 2-$) directions, are defined as:

$$\begin{aligned} F_{1+} &= \phi_{1+} - r_{1+} \leq 0 \quad ; \quad F_{1-} = \phi_{1-} - r_{1-} \leq 0 \\ F_{2+} &= \phi_{2+} - r_{2+} \leq 0 \quad ; \quad F_{2-} = \phi_{2-} - r_{2-} \leq 0 \end{aligned} \quad (5.95)$$

where the loading functions ϕ_N ($N = 1+, 1-, 2+, 2-$) depend on the strain tensor and material constants (elastic and strength properties). The elastic domain thresholds r_N ($N = 1+, 1-, 2+, 2-$) take an initial value of 1 when the material is undamaged, and they increase with damage. The elastic domain thresholds are internal variables of the constitutive model, and are related to the damage variables d_M ($M = 1+, 1-, 2+, 2-, 6$) by the damage evolution laws.

The criterion for fiber tension failure (see equation 5.49) is:

$$\phi_{1+} = FI_F = \frac{E_1}{X_T} \varepsilon_{11} \quad (5.96)$$

where the effective stress tensor $\tilde{\sigma}$ is computed as $\tilde{\sigma} = \mathbf{H}_0^{-1} : \varepsilon$. \mathbf{H}_0 is the undamaged compliance tensor obtained from equation (5.93) using $d_1 = d_2 = d_6 = 0$.

The damage activation function used to predict damage under longitudinal compression ($\tilde{\sigma}_{11} < 0$) is established to be equal to

$$\phi_{1-} = \sqrt{FK} \quad (5.97)$$

where FK is defined in equation (5.72).

The damage activation function used to predict damage under transversal tension ($\sigma_N > 0$) is (see equation (5.43)):

$$\phi_{2+} = \sqrt{FMT} = \sqrt{\left(\frac{\tau_L}{S_L^{is}}\right)^2 + \left(\frac{\sigma_N}{Y_T^{is}}\right)^2} \quad (5.98)$$

The damage activation function used to predict damage under transversal compression ($\sigma_N \leq 0$) is (see equation (5.6)):

$$\phi_{2-} = \sqrt{FMC} = \sqrt{\left(\frac{\tau_T}{S_T^{is} - \eta_T \sigma_N}\right)^2 + \left(\frac{\tau_L}{S_L^{is} - \eta_L \sigma_N}\right)^2} \quad (5.99)$$

5.4.3 Damage evolution

The evolution of the threshold values r_N is mathematically expressed by the *Kuhn-Tucker conditions*:

$$\dot{r}_N \geq 0 \quad ; \quad F_N \leq 0 \quad ; \quad \dot{r}_N F_N = 0 \quad (5.100)$$

The damage activation functions, equations (5.95), must always be non-positive and if the gradient is positive, there is damage evolution; the consistency condition to satisfy is:

$$\dot{F}_N = \dot{\phi}_N - \dot{r}_N = 0 \quad (5.101)$$

The evolution of the elastic domain can be represented by the following equations [133]:

- *transverse loading*:

$$\text{Tension loading:} \quad \dot{r}_{2+} = \dot{\phi}_{2+} \quad \text{and} \quad \dot{r}_{2-} = 0$$

$$\text{Compression loading:} \quad \dot{r}_{2-} = \dot{\phi}_{2-} \quad \text{and} \quad \dot{r}_{2+} = \begin{cases} \dot{\phi}_{2-} & \text{if } r_{2+} \leq r_{2-} \\ 0 & \text{if } r_{2+} > r_{2-} \end{cases}$$

The integration of the previous expressions results in:

$$\begin{aligned} r_{2+} &= \max \left\{ 1, \max_{s=0,t} \{ \phi_{2-}^s \}, \max_{s=0,t} \{ \phi_{2+}^s \} \right\} \\ r_{2-} &= \max \left\{ 1, \max_{s=0,t} \{ \phi_{2-}^s \} \right\} \end{aligned} \quad (5.102)$$

- *longitudinal loading*

$$\text{Tension loading:} \quad \dot{r}_{1+} = \dot{\phi}_{1+} \quad \text{and} \quad \dot{r}_{1-} = 0$$

$$\text{Compression loading:} \quad \dot{r}_{1-} = \dot{\phi}_{1-} \quad \text{and} \quad \dot{r}_{1+} = \begin{cases} \dot{\phi}_{1-} & \text{if } r_{1+} \leq r_{1-} \\ 0 & \text{if } r_{1+} > r_{1-} \end{cases} \quad (5.103)$$

The integration of the previous expressions results in:

$$\begin{aligned} r_{1+} &= \max \left\{ 1, \max_{s=0,t} \{ \phi_{1+}^s \}, \max_{s=0,t} \{ \phi_{1-}^s \} \right\} \\ r_{1-} &= \max \left\{ 1, \max_{s=0,t} \{ \phi_{1-}^s \} \right\} \end{aligned} \quad (5.104)$$

5.4.4 Dissipation

The rate of energy dissipation per unit volume resulting from the evolution of damage is given by:

$$\Xi = \frac{\partial G}{\partial d_1} \dot{d}_1 + \frac{\partial G}{\partial d_2} \dot{d}_2 + \frac{\partial G}{\partial d_6} \dot{d}_6 = Y_1 \dot{d}_1 + Y_2 \dot{d}_2 + Y_6 \dot{d}_6 \geq 0 \quad (5.105)$$

The form of the complementary free energy assures that the thermodynamic forces (Y_M) conjugated to their respective damage variables (d_M) are always positive:

$$\begin{aligned} Y_1 &= \frac{\partial G}{\partial d_1} = \frac{\sigma_{11}^2}{2(1-d_1)^2 E_1} \geq 0 \\ Y_2 &= \frac{\partial G}{\partial d_2} = \frac{\sigma_{22}^2}{2(1-d_2)^2 E_2} \geq 0 \\ Y_6 &= \frac{\partial G}{\partial d_6} = \frac{\sigma_{12}^2}{2(1-d_6)^2 G_{12}} \geq 0 \end{aligned} \quad (5.106)$$

Therefore, the condition of positive evolution of damage variables ($\dot{d}_M \geq 0$) is a sufficient condition for the fulfillment of the second law of thermodynamics.

5.4.5 Damage evolution laws

To define the constitutive model, the damage variables d_N must be related to the internal variables r_N . In particular, when material is undamaged the internal variables r_N take the initial value of 1, and $d_N(r_N = 1) = 0$.

5.4.6 Computational Model

Using Bažant's crack band model [159], the damage evolution laws for each damage variable take the values [134]:

Bažant's crack band model [159] assures the correct response of the finite element model regularizing the dissipated energy:

$$g_M = \frac{G_M}{l^*}, \quad M = 1+, 1-, 2+, 2-, 6 \quad (5.107)$$

where G_M is the fracture toughness, g_M is the energy dissipated per unit volume, and l^* is the characteristic length of the finite element.

$$\begin{aligned} d_{1+} &= 1 - \frac{1}{r_{1+}} \exp [A_{1+} (1 - r_{1+})] \\ d_{1-} &= 1 - \frac{1}{r_{1-}} \exp [A_{1-} (1 - r_{1-})] \\ d_{2+} &= 1 - \frac{1}{r_{2+}} \exp [A_{2+} (1 - r_{2+})] \\ d_{2-} &= 1 - \frac{1}{r_{2-}} \exp [A_{2-} (1 - r_{2-})] \\ d_6(r_{2+}) &= 1 - \frac{1}{r_{2+}} \exp [A_6 (1 - r_{2+})] \end{aligned} \quad (5.108)$$

The energy dissipated per unit volume for uniaxial stress conditions is obtained by integrating the rate of dissipation, equation (5.105):

$$g_M = \int_0^\infty Y_M \dot{d}_M dt = \int_1^\infty \frac{\partial G}{\partial d_M} \frac{\partial d_M}{\partial r_M} dr_M, \quad M = 1+, 1-, 2+, 2-, 6 \quad (5.109)$$

Applying the crack band model, equation (5.107):

$$\int_1^\infty \frac{\partial G}{\partial d_M} \frac{\partial d_M}{\partial r_M} dr_M = \frac{G_M}{l^*}, \quad M = 1+, 1-, 2+, 2-, 6 \quad (5.110)$$

Using equations (5.107) and (5.109) and substituting in (5.110), it is possible to calculate the damage law parameters A_M that assure that the dissipated energy computed by the numerical model is independent of mesh refinement. It is possible to obtain the following analytical closed form solutions:

$$A_{1+} = \frac{2l^* X_T^2}{2E_1 G_{1+} - l^* X_T^2} \quad (5.111)$$

$$A_{1-} = \frac{2l^* X_C^2}{2E_1 G_{1-} - l^* X_C^2} \quad (5.112)$$

$$A_{2+} = \frac{2l^* Y_T^2}{2E_2 G_{2+} - l^* Y_T^2} \quad (5.113)$$

$$A_{2-} = \frac{2l^* Y_C^2}{2E_2 G_{2-} - l^* Y_C^2} \quad (5.114)$$

$$A_6 = \frac{2l^* S_L^2}{2G_{12} G_6 - l^* S_L^2} \quad (5.115)$$

Chapter 6

Numerical Results

A 3D numerical model was presented in Chapter 5, while in Chapter 4 a methodology to measure the resistance curves in the longitudinal failure of composites was proposed. The R-curves allow the calculation of the parameters of the softening laws used in the progressive damage model, and describe the damage in function of the dissipated energy for each failure mode. The softening law parameters are calculated from empirical data in Section 4.2.2.6 for IM7/8552 carbon in tension and are computed using an inverse technique method for compression.

In this chapter, the numerical results will be compared with experimental data on IM7/8552 double shear bolted joints presented by Camanho *et al.* [160].

The tests were performed on double shear bolted joints having three different geometries that results in different failure modes: bearing, shear-out and tension failure modes. The geometries of the specimens are presented in Table 6.1.

Table 6.1: Nominal dimensions of the bolted joints tested.

specimen	d mm	w mm	w/d	e mm	e/d	d_w ⁴ mm	h ⁵ mm
DBJB ¹	7	42	6	21	3	12.5	3
DBJT ²	6	12	2	24	4	12	3
DBJS ³	6	36	6	9	1.5	12	3

¹ Double Shear Bolted Joint Bearing

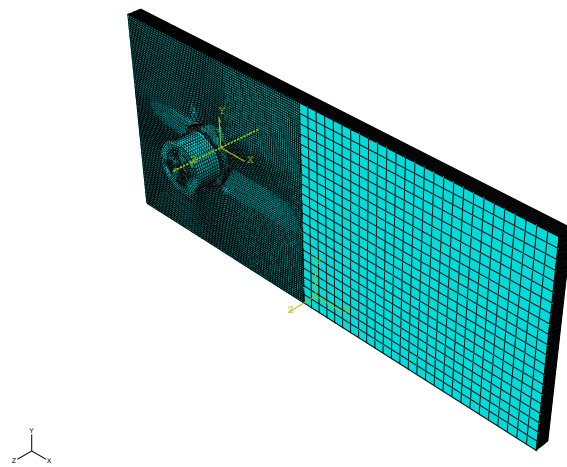
² Double Shear Bolted Joint Tension

³ Double Shear Bolted Joint Shear-Out

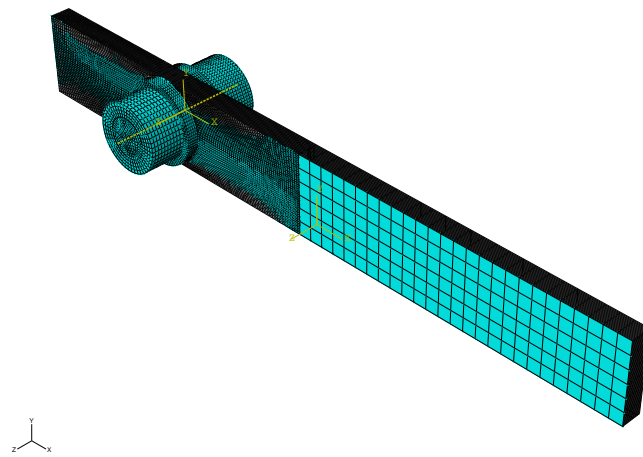
⁴ diameter of the washer

⁵ thickness

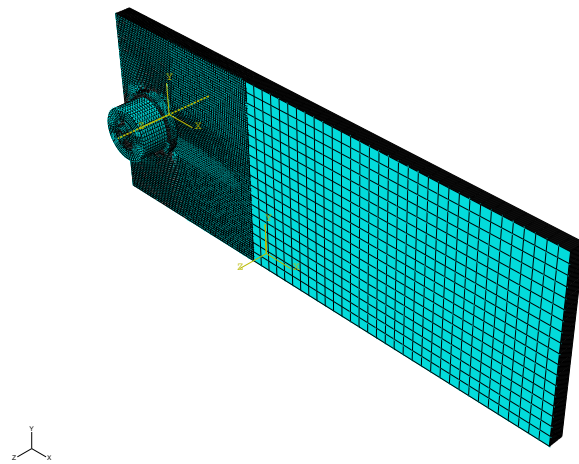
Three different Finite Element models of the double shear bolted joints, shown in Figure 6.1, were created using a Python parametric model. The numerical results are compared with experimental data in terms of both the stresses and the damaged zones.



(a) bearing



(b) tension



(c) shear

Figure 6.1: FE models

6.1 FE model

6.1.1 Python scripts

Using Python script, a parametric model of the double bolted joint was developed.

The scripts that generate the models, written in Python, enable the generation of several FEM models simply running these script in the Abaqus CAE utility. It should be noticed that the following parameters can be easily changed:

1. The materials of the joint. The materials are managed using Python dictionaries [143]. The user can introduce other materials just adding other dictionaries.
2. The geometry of the joint. The following parameters can be set:
 - (a) The diameter of the bolt d_b
 - (b) The clearance c between the diameter of the bolt d_b and the diameter of the hole d
 - (c) The width of the joint w
 - (d) The end-distance e
 - (e) The length of the joint L
 - (f) The type and the geometry of the bolt (screw, nut and washer)
 - (g) The thickness of each ply and the thickness of the cohesive elements (if cohesive elements are requested)
 - (h) The orientation of the fiber for each lamina
3. The loads applied during the steps (and in particular the thermal load during the thermo-mechanic step, the pressure on the washer, and the displacement applied to the joint)
4. Other numerical parameters that influence the analysis (time step, time increment, mass scaling, etc...)

6.1.2 Details of the models

6.1.2.1 Geometry of the model

Figure 6.2 shows the isometric view of the DBJM. As explained before, all the geometric parameters can be set in a input file and are generated automatically in Abaqus CAE. It can be observed that different parts are modeled: the bolt (screw, nut and washers) and the composite laminate.

First of all, it is possible to observe that the laminate it is not modeled taking advantage of the symmetry. Even if the plane xy is a symmetry plane the joint was entirely modeled. This for two reasons: first, if a damage model is used, damage can

occur in one side of the joint and the symmetry is lost; second, if a plane of symmetry is used, on the symmetry plane the cohesive elements have to have a thickness that is half of that of the other cohesive elements. In an explicit analysis this means that the critical time increment is reduced and so, CPU time increases. With cohesive elements the use of a plane of symmetry can result in an higher computational cost.

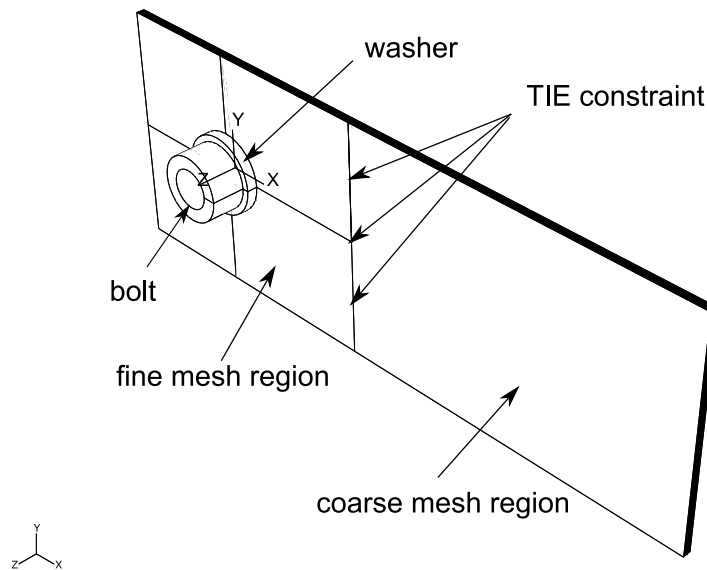


Figure 6.2: Isometric view of DBJ model

6.1.2.2 TIE constraints

The use of cohesive elements and a damage material model results in high computational times. To mitigate this problem, it is possible to use the damage model only in the parts of the joint where damage occurs. In the other regions, not affected by damage propagation, the composite is simulated as a linear elastic material. For this reason, the composite laminate consists of two different regions that can be easily identified in Figure 6.4. The region around the hole is modeled using cohesive elements and damage model for bricks. In the second region only elastic elements are present.

The dimensions of the elements in these two region are quite different. As explained before in Section 5.4.6, in order to guarantee that the numerical solution is independent of the discretization, the elements must have a size lower than a critical value [159]. Obviously this is not necessary for the elastic elements. For these reasons the two regions are modeled with different elements sizes that are shown in Figure 6.4.

To connect these two region TIE constraints are used on the two surfaces with non-conforming meshes. If a TIE constraint is applied nodes are tied only where

the surfaces are close to one another and this connection is kept during the entire analysis. Generally one surface in the constraint is designated to be the slave surface; the other surface is the master surface. Figure 6.3 shows a magnified view of the connection between this two region. The red surface is that one where TIE constraint are applied.

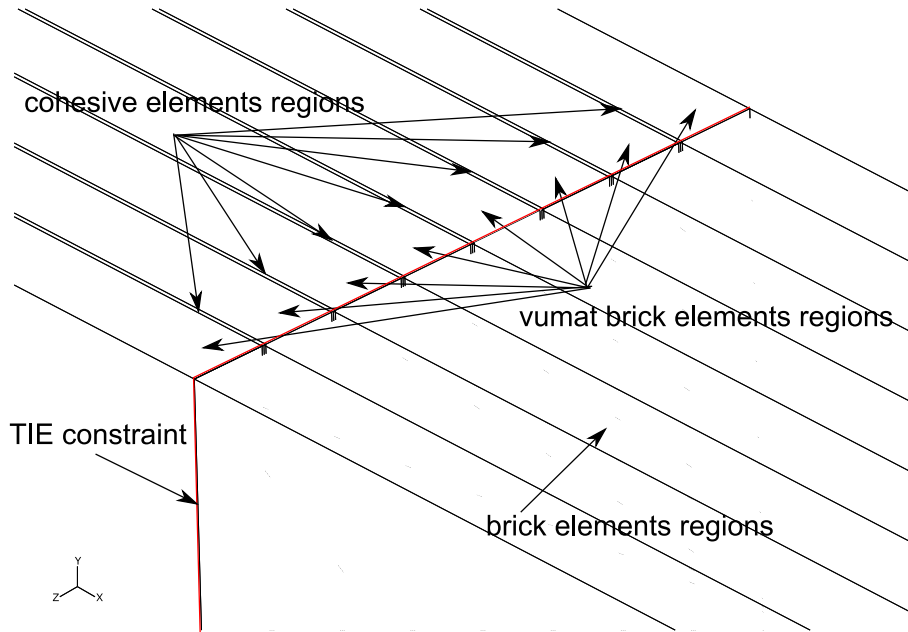


Figure 6.3: Isometric view of DBJ model, detail

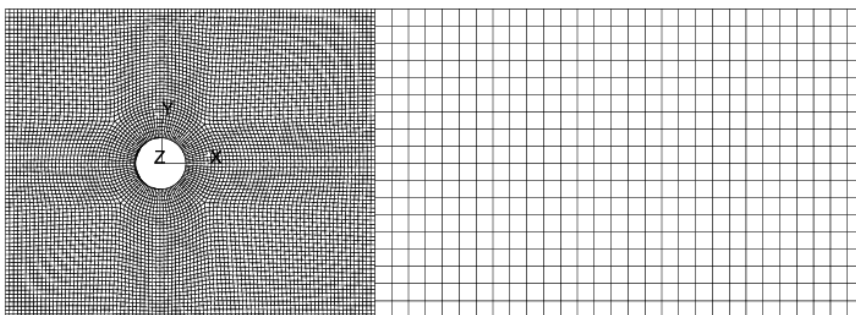


Figure 6.4: DBJ model, mesh

6.1.2.3 Loading

To reproduce the experimental tests for a Double Bolted Joint the simulation is divided in three load steps:

1. first step: thermo-mechanical step. In this step a thermal load, $\Delta T < 0$ is applied to the composite laminate. This correspond to the thermal load occurring during the curing process. This thermal load generates residual stresses that have influence on the damage of the composite.
2. second step: bolt pre-loading. The pre-load is generated applying two opposite forces to the screw and the nut. This two forces are designated with P in Figure 6.5(a). During this load step the surface of contact between the bolt and the nut is characterized by:
 - (a) frictionless tangential behavior. The friction on the surface highlighted in Figure 6.5(b) is equal to $f = 0$.
 - (b) hard contact normal behavior, that avoids interpenetration between the screw and the nut.
 - (c) the separation after contact is allowed.
3. third step: loading of the joint. In this step the u displacements are applied to the joint. During this step the contact surface is defined as:
 - (a) rough tangential behavior. The friction on the surface between screw and nut is equal to $f = \infty$.
 - (b) hard contact normal behavior, that avoids interpenetration between the screw and the nut.
 - (c) the separation after contact is not allowed.

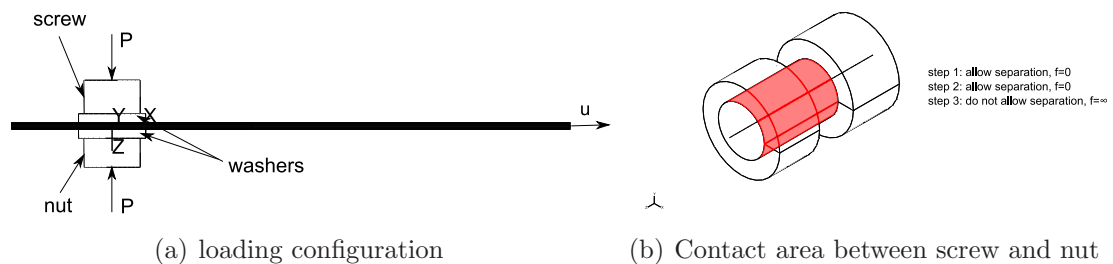


Figure 6.5: DBJ model, loading configuration

It should be noted that using this technique the behavior of the bolt is simulated in a very efficient way. Many authors simulate the presence of a bolt simply introducing a pressure on the area of contact between washers and laminate. However, the simple use of a pressure is not suitable to study bolted joint for different reasons. First of all, if a progressive damage model is used, as the damage occurs in the

proximity of the hole the pressure on the contact area has to decrease because if the material is damaged the stiffness of the bolted joint reduces and also the bolt load is reduced. Therefore, the use of a constant pressure on the washers is not correct. In the same way, in the case of single bolted joint, the application of the load generally causes a deformation of the joint in the direction normal to the laminate. In this conditions the heads of the bolt contribute with the bottom surface to the load carried by the joint. Therefore the pressure applied on the washers has to increase.

6.1.2.4 Elements used and typical size

Three different type of elements are used:

- 8-node brick elements, with elastic material;
- 8-node brick elements, with VUMAT constitutive model;
- 8-node brick elements, with VUMAT constitutive model for cohesive elements. The explicit formulation for cohesive elements is described in the work of González *et al.* [161]

6.1.2.5 Contacts

In 6.1.2.3 the different contact definitions will be explained for the contact pair nut/screw. For all other surfaces the general explicit contact has be used. The general contact algorithm has to be chosen because it allows to consider the contact of a body with itself and the failure of the elements. The friction is set to be equal to $f = 0.3$.

6.2 Comparison between FEM and experiments

6.2.1 Bearing

Figure 6.6 shows the relation between the bearing stress and the corrected displacement for the FE model and for the experimental tests. The bearing stress (see Section 2.1.1) is defined as:

$$\sigma^b = \frac{P}{dh} \quad (6.1)$$

where P is the load, d is the diameter of the hole, h is the thickness of the specimen. The displacement is corrected to take into account the compliance of the testing machine. If δ_{meas} is the measured displacement and C is the compliance of the machine, the corrected displacement δ can be computed as:

$$\delta = \delta_{meas} - CP \quad (6.2)$$

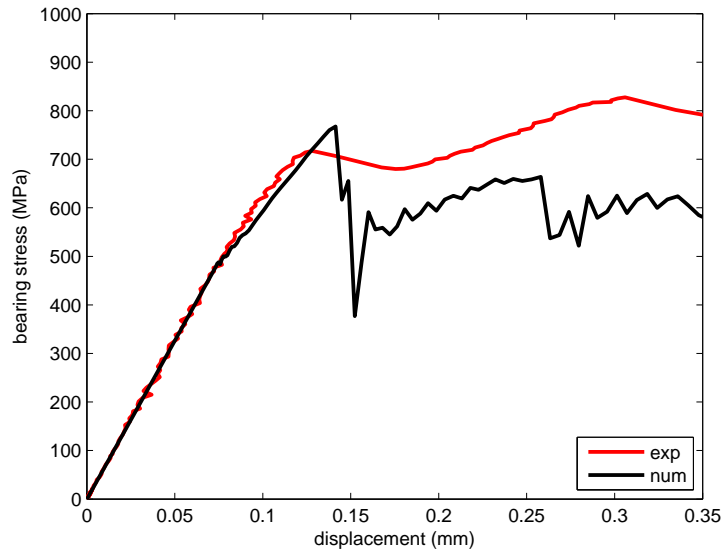


Figure 6.6: Bearing stress as function of the corrected displacement

It should be noted that the first-peak load is predicted accurately but after that damage occurs the experimental and the numerical curves show a difference that is attributable mainly to two reasons:

- the proposed failure criteria are fully 3D while the damage model used is quasi-3D. This means that the failure onset is accurately predicted but not the evolution of the damage in conditions where the 3D stress states prevail;
- the damage evolution in bearing failure mode depends primarily to the softening law for fiber in compression. This was not found experimentally but using an inverse identification technique. The parameters used may differ from the real parameters.

Figure 6.7 shows the contour plot of the damage index of the fiber, d_1 , in function of the bearing stress σ^b . The damaged zones correspond to those observed experimentally (see Figure 6.8) and are located uniformly in the neighborhood of the hole.

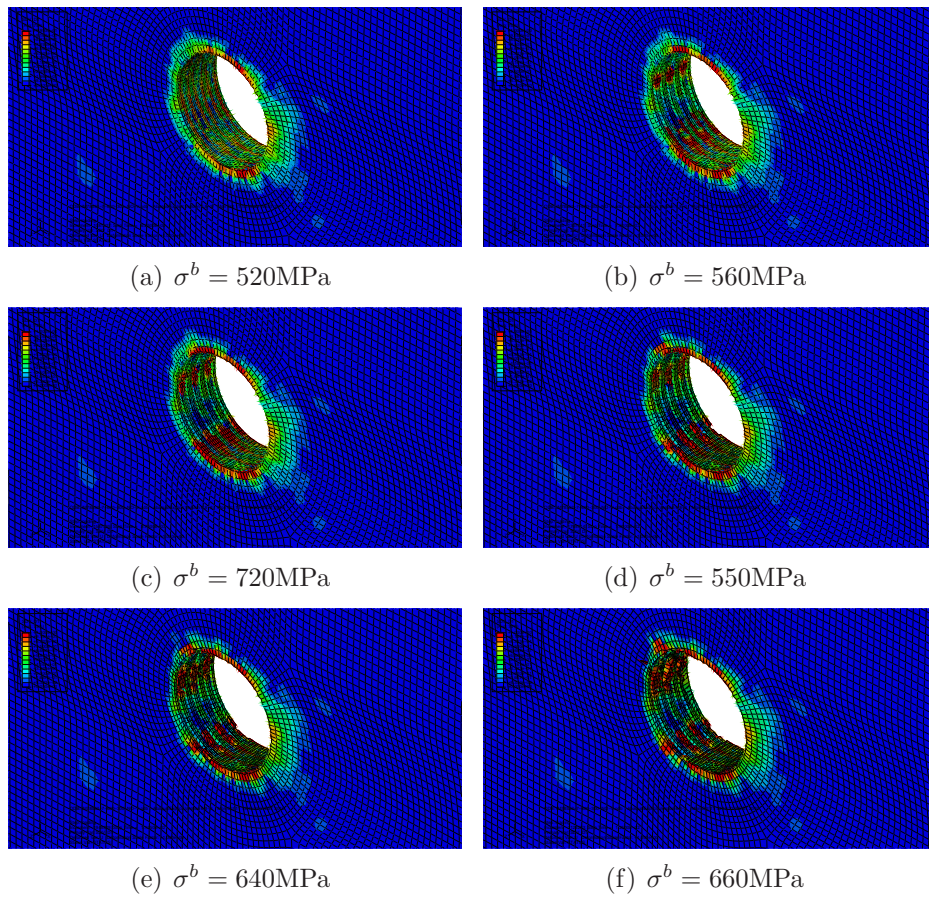


Figure 6.7: Contour plots of the damage index of the fiber in function of the bearing stress for the bearing specimen

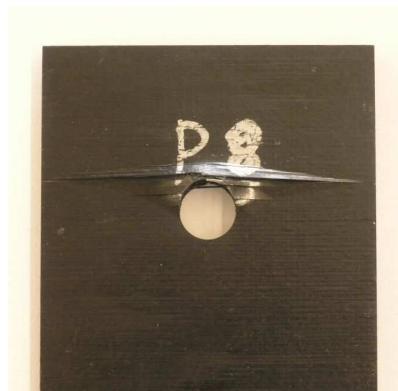


Figure 6.8: Bearing specimen after loading

6.2.2 Net-Tension

Figure 6.9 shows the relation between the bearing stress and the corrected displacement for the FE model and for the experimental tests of the tension specimen.

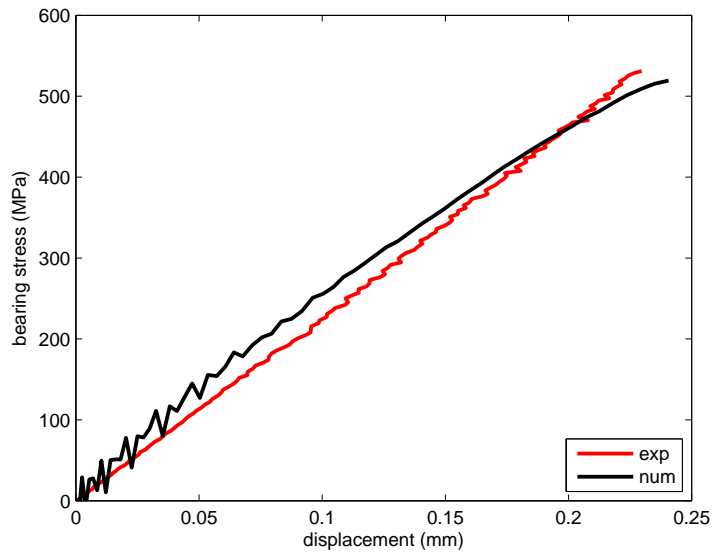


Figure 6.9: Tensile stress as function of the corrected displacement

Figure 6.11 shows the contour plot of the damage index of the fiber, d_1 , in function of the bearing stress σ^b . As expected for tension failure (see Figure 6.10), the main damaged zones are located along the net-section plane of the specimen.

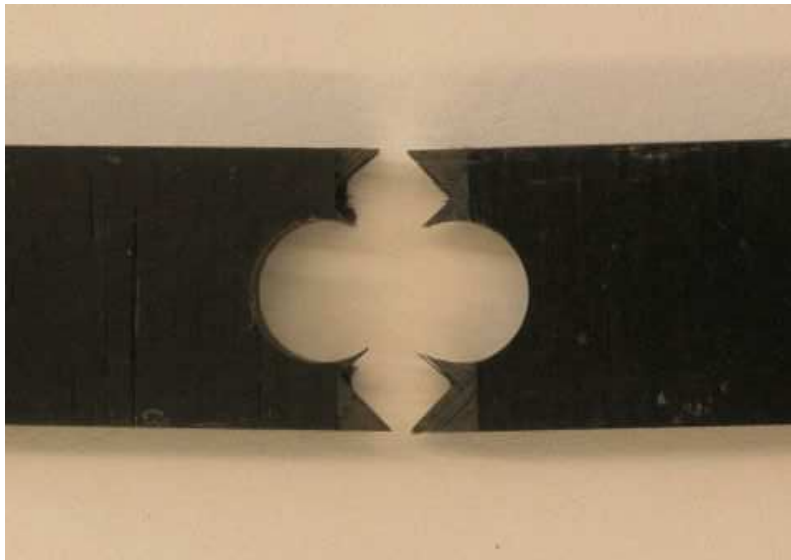


Figure 6.10: Tension specimen after loading

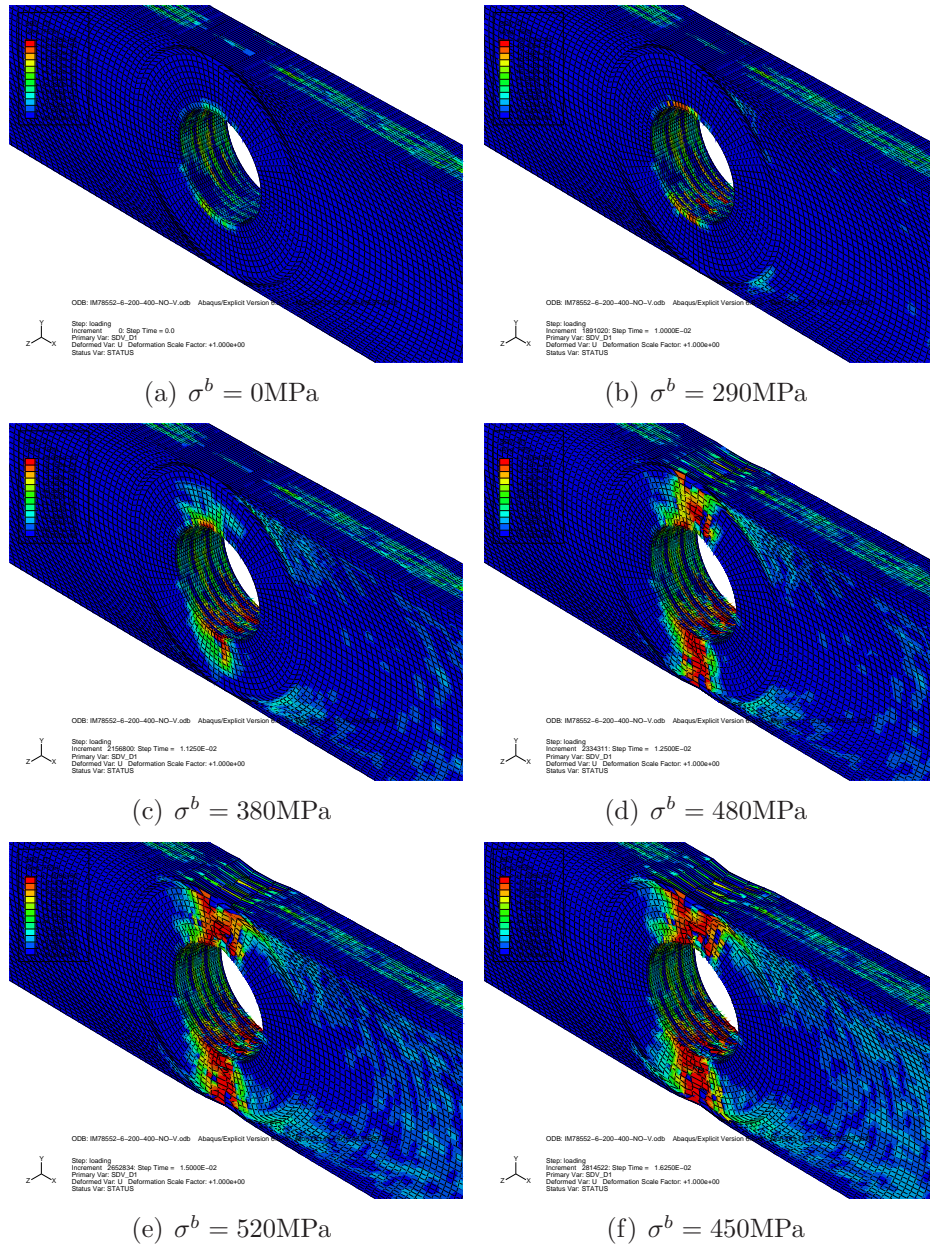


Figure 6.11: Contour plots of the damage index of the fiber in function of the bearing stress for the tension specimen

6.2.3 Shear-Out

Figure 6.12 shows the relation between the bearing stress and the corrected displacement for the FE model and for the experimental tests of the shear specimen.

Figure 6.14 shows the contour plot of the damage index of the fiber, d_1 , in function of the bearing stress σ^b . It should be noted that when damage is developed, the fracture is located on the shear plane (see Figure 6.14(h)).

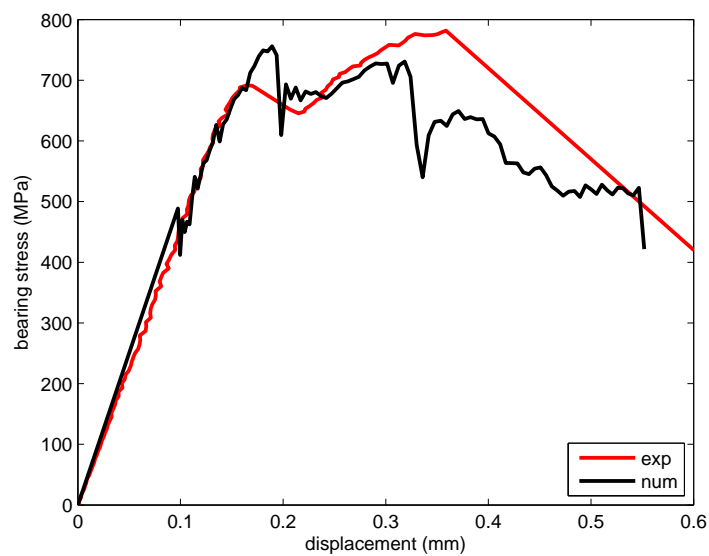


Figure 6.12: Shear stress as function of the corrected displacement



Figure 6.13: Shear specimen after loading

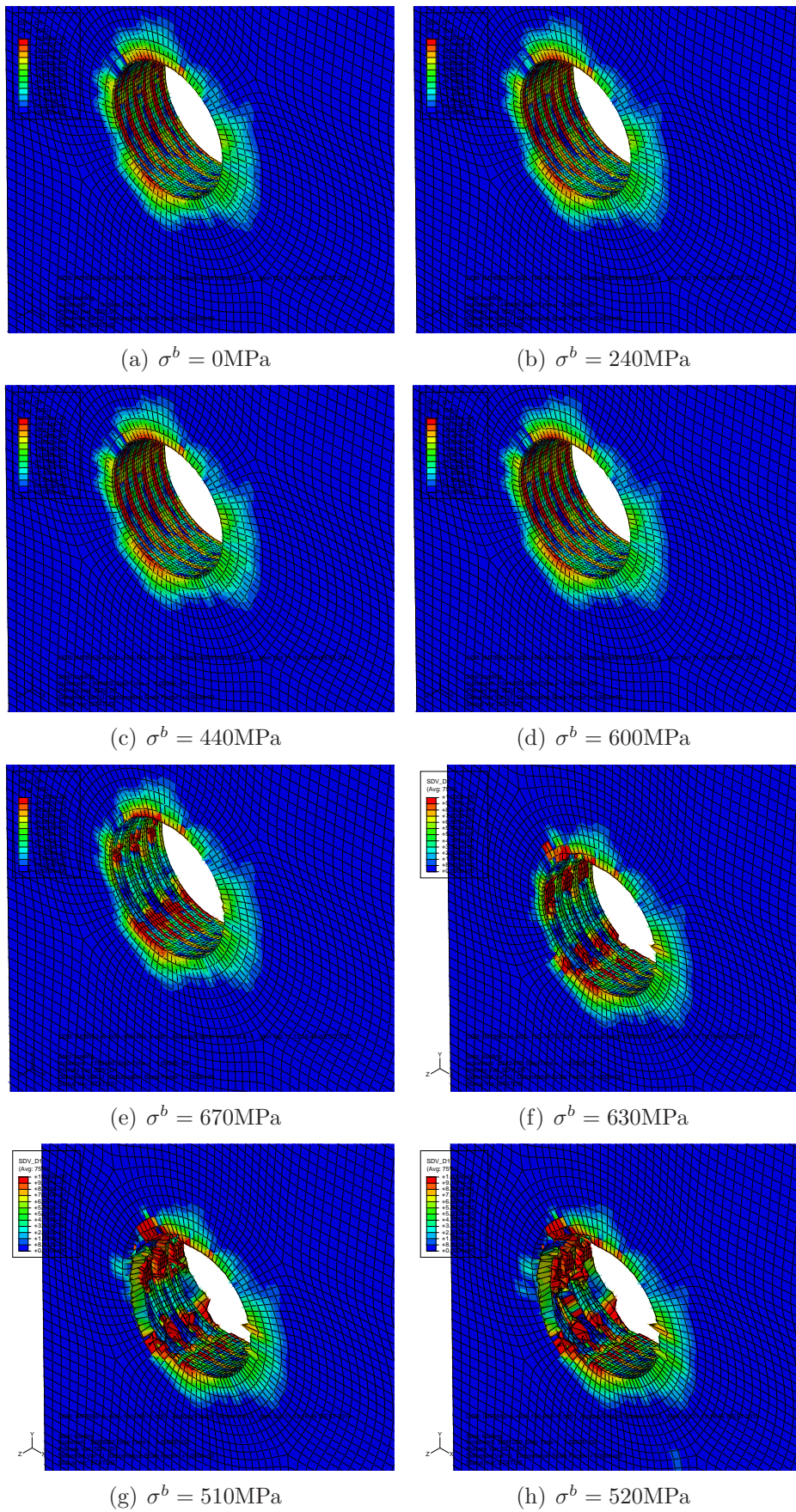


Figure 6.14: Contour plots of the damage index of the fiber in function of the bearing stress for the shear specimen

6.3 Conclusions

The first-peak load for each specimen is reported in Table 6.2, and the mean value is compared with the numerical predictions. Good agreement is found in the prediction of the first peak load.

Table 6.2: First-peak load (N)

Specimen Ref.	1	2	3	4	5	mean	numerical	error (%)
DBB	15060	15950	16080	16300	16120	15902	16120	1.4
DTB	10136	9356	9428	9344	9560	9564.8	9348	2.3
DSB	12450	13140	12780	12180	13180	12746	13610	6.3

It can be concluded that 3D numerical simulations can predict with accuracy the value of the first peak load. However the computational cost is not suitable for industrial applications because each model takes about 3 days to run using a cluster of 32 cpus. Therefore a simplified two-dimensional method will be presented in the following chapter.

Chapter 7

2D Numerical Model

7.1 Introduction

3D failure models provide a good prediction for the behavior of a composite bolted joints, from damage onset to failure of the joint. However, the use of such type of analysis is not applicable in an industrial environment where results should be obtained quickly. For this reason, a two-dimensional (2D) model is proposed here to provide fast predictions of the strength of composite bolted joints. Experimental tests of a subcomponent are performed, and the results are used to verify the accuracy of the model.

In Section 2.5 the connections that can be manufactured using a combination of different materials (metals and composites) in train structures were identified.

Here, one of these connection (connection C in Figure 2.16) is analyzed. An industrial design method is proposed and experimental test are performed. Numerical simulations are compared with experimental results. A quick-design method is discussed in the last part of the chapter and a methodology to predict the joint strength in a fast way is proposed.

7.2 Experimental Analysis

7.2.1 Subcomponent Design

The design of the industrial sub-component is shown in Figure 7.1. It represents the connection between the side of the carbody shell (in steel, 1 in Figure 7.1) and the omega beam of the roof (in glass-fiber, 2 in Figure 7.1).

The lay-up of the laminate is $[(0/\pm 45)_6/0]_s$ where 0° corresponds to the longitudinal direction of the omega beam. The nominal thickness of the composite beams, in the neighboring of the holes is equal to 11.8mm. The mechanical properties of the unidirectional lamina are shown in Table 7.1.

The connection is made using the 5mm UNBRAKO bolts (3 in Figure 7.1)

already used in experimental test described in Chapter 3. Section 3.4.2 provides the mechanical parameters of these bolts. It should be highlighted that, as explained before, the torque used to install the bolts is very low and therefore bolts work in shear and not in traction. This means that for this kind of application the use of bolts or rivets is indifferent.

Table 7.1: UD mechanical properties

E_1 (MPa)	37500
$E_2 = E_3$ (MPa)	3000
ν_{12}	0.35
$\nu_{13} = \nu_{23}$	0.3
G_{12} (MPa)	2715
$G_{13} = G_{23}$ (MPa)	2715
X_T (MPa)	617
$Y_T = Z_T$ (MPa)	20
X_C (MPa)	300
$Y_C = Z_C$ (MPa)	30
S_T (MPa)	19
S_L (MPa)	20

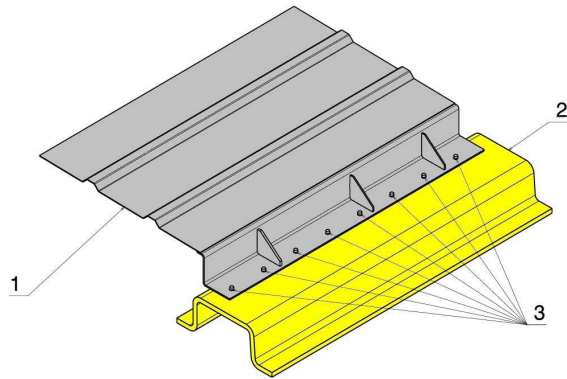


Figure 7.1: Design of the sub-component

7.2.2 Experimental Setup

To study the behavior of the joint, when a bearing failure mode is present, the sub-component is tested as shown in Figure 7.2. As the steel panel is very flexible, the load has to be applied using a hinge in order to guarantee a predominant shear stress field on the plane of the bolts.

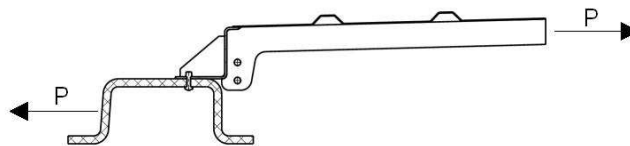


Figure 7.2: Loading configuration

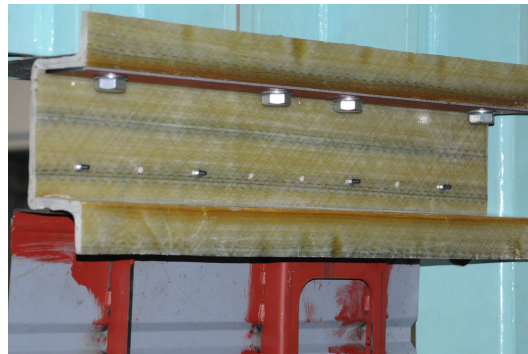
Figure 7.3 shows the experimental setup of the Instron machine used to test the sub-component.

Figure 7.4 shows the solution used to connect the component to the test fixture. On the top, the component is connected to the main structure of the machine as shown in Figure 7.4(a). Bolts are used in conjunction with a drilled steel-plate to prevent damage of the composite during loading.

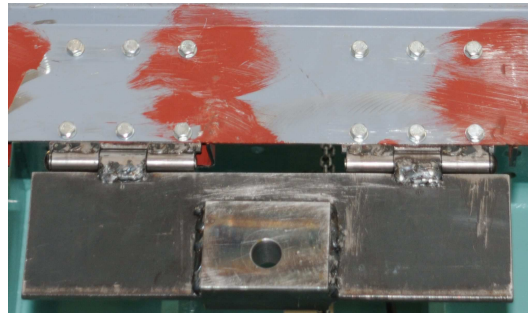
Figure 7.4(b) shows the connection on the bottom of the sub-component. An hinge was designed to connect the component to the cylinder of the servo-hydraulic machine. The hinge allows testing the sub-component in the presence of misalignment of the load rig.



Figure 7.3: Equipment setup



(a) top connection



(b) bottom connection

Figure 7.4: V-P-4-1 specimen after loading

7.2.3 Experimental Results

To reduce the value of the peak-load during the test, only a few bolts were used to connect the two parts of the sub-component. For safety reasons, it was decided to use only 2 bolts during the tests. The tests were performed in displacement control and a speed of 1mm/min was used.

Figure 7.5 shows a representative load-displacement curve obtained during the experimental test.

Figure 7.5 compare the load-displacement curve with the elastic load-displacement curve (tangent to the curve). The first non-linearity point is for $P_{nl} \approx 15000\text{N}$ and the peak-load is $P_{max} \approx 25800\text{N}$.

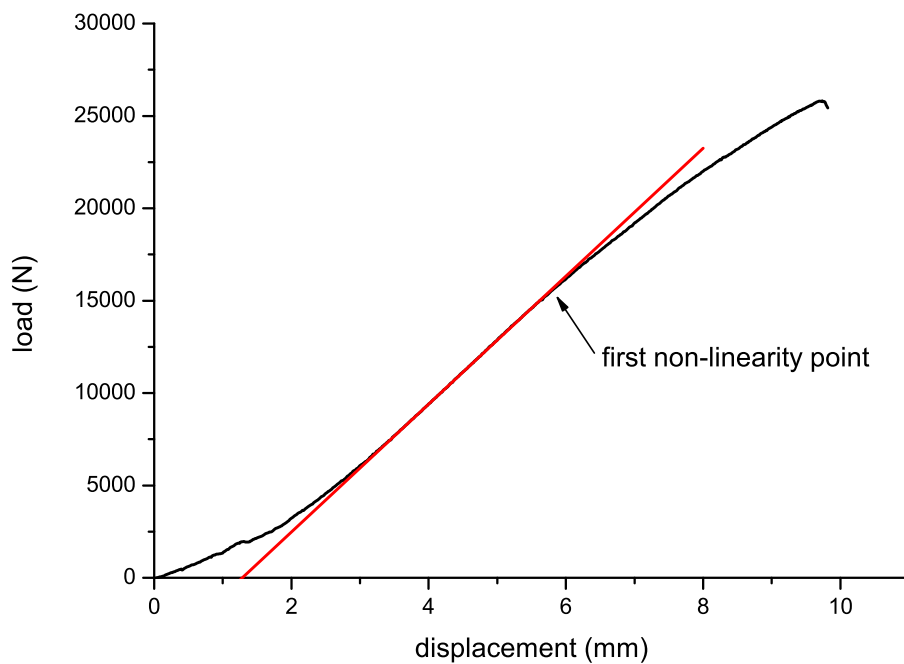


Figure 7.5: Load - displacement curve

When the load P reach the critical value P_{nl} the composite start to fail (elastic limit). The failure mode is bearing as shown in Figure 7.6(a). At the same load, also the steel panel exhibits bearing failure in proximity of the bolts as reported in Figure 7.6(b). Finally, when the load reach the peak-load P_{max} the bolts fail (see Figure 7.6(c)) because of the combination of shear and traction applied.

Generally, in design, the elastic limit is considered as the limit condition and not the ultimate failure of the bolt. The methodology described in the following will enable the prediction of the load at which the composite start to fail (i.e. the value of P_{nl}).



(a) bearing in the composite

(b) bearing steel

(c) fracture of the bolt

Figure 7.6: Failure modes of the multi-material sub-component

7.3 Quick Design Tool and Analysis Results

7.3.1 Generalities

Camanho and Lambert [126] proposed a methodology that enables the prediction of the elastic limit and of the ultimate joint failure load in a short amount of time. This methodology uses the Complex Variable Theory of Elasticity (CVTE) to obtain analytical solutions for the stress distribution around the hole avoiding the use of the Finite Element Method. Using the Classical Lamination Theory the stress distribution is calculated for each ply.

The prediction of the elastic limit is based on the LaRC03 failure criteria while the prediction of the joint failure is based on the use of a characteristic curve [162], applying the failure criteria on the characteristic curve, using local and averaged stresses. Obviously, the characteristic distances in compression and in tension should be measured.

The stress distribution around the hole, considering plane stress, is based on the use of the Airy stress function F :

$$\sigma_{xx} = \frac{\partial^2 F}{\partial y^2} \quad (7.1)$$

$$\sigma_{yy} = \frac{\partial^2 F}{\partial x^2} \quad (7.2)$$

$$\sigma_{xy} = -\frac{\partial^2 F}{\partial x \partial y} \quad (7.3)$$

The general expression for the function F depends upon the root of the characteristic equation and is defined as:

$$F = 2\Re \{F_1(Z_1) + F_2(Z_2)\} \quad (7.4)$$

where $F_1(Z_1)$ and $F_2(Z_2)$ are analytical functions of the complex variables $Z_1 = x + R_1y$ and $Z_2 = x + R_2y$ respectively.

The methodology used to define the function $F_i(Z_i)$ is based on the work done by Garbo and Ogonowski [163]. The stress distribution is considered as obtained by the superposition of the in-plane bearing and by-pass loads as shown in Figure 7.7.

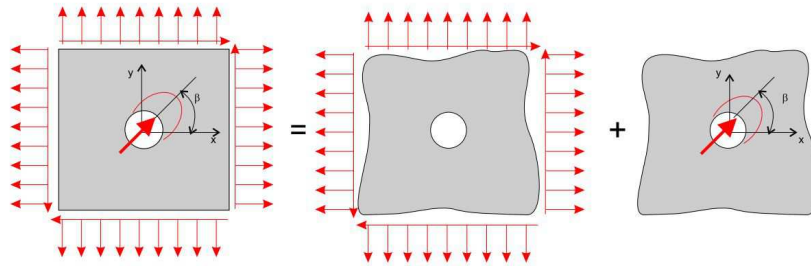


Figure 7.7: Superposition of load cases

Therefore, the stress distribution of a laminate with a loaded hole is obtained by superimposing two stress distributions: that of a cosinusoidal distribution of pressure on the contact zone of the hole (in-plane bearing) and the stress distribution of a laminate with an open hole remotely loaded.

The resulting stress distribution is a good approximation of the real stress state when the ratio $w/d \geq 4$ and $e/d \geq 3$, i.e. when bearing failure mode is present. It should be noted that the stress distribution is calculated under the hypothesis that no bending is present in the mid-plane of the laminate and when the pressure can be assumed cosinusoidal (this happens when the laminate is quasi-isotropic and the clearance is small).

However, some problems arise in industrial application. For example, in some parts the geometrical conditions $w/d \geq 4$ and $e/d \geq 3$ are not respected and in this case the stress distribution around the hole could not be sufficiently approximated. The 2D method proposed here tries to solve this problem and presents several advantages that are fundamental in an industrial environment, namely:

- the method is fast;
- the method is sufficiently realistic;
- different failure criteria can be implemented (for composite parts, metal parts, bolts and rivets);
- the method uses automatically the results of the FE analysis and this simplifies the work of the engineers.

A bolt is simply represented by a kinematic constraint of different nodes that are as many as the parts connected together. For example, for a simple connection of two panels, two nodes will be part of the same kinematic constraint.

For each node it is possible to consider a path of nodes that lie around the coupled node. Figure 7.8 shows the coupled node (in red) and the nodes (in blue) that lie in a path around the coupled node (contour nodes). After the analysis has been performed, it is possible to postprocess the data and obtain the nodal loads applied to each node. In particular F_x^{bolt} , F_y^{bolt} and F_x^i , F_y^i are obtained for the coupled

node and the contour nodes respectively. x and y lie on the plane identified by the contour nodes, z is parallel to the axis of the bolt.

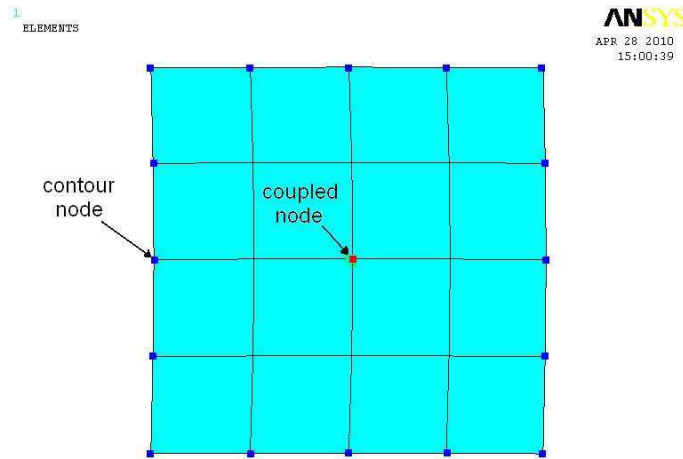


Figure 7.8: Coupled node and contour nodes considered for the submodelling.

For each coupled node, a submodel can be defined and solved to obtain a good approximation of the stress distribution around the hole. Figure 7.9 shows the submodel generated by the algorithm for each coupled node. At each of the contour nodes of Figure 7.8 corresponds a node on the contour. At this node the nodal loads F_x^i and F_y^i are applied. At the edge of the hole an equivalent cosinusoidal pressure is applied.

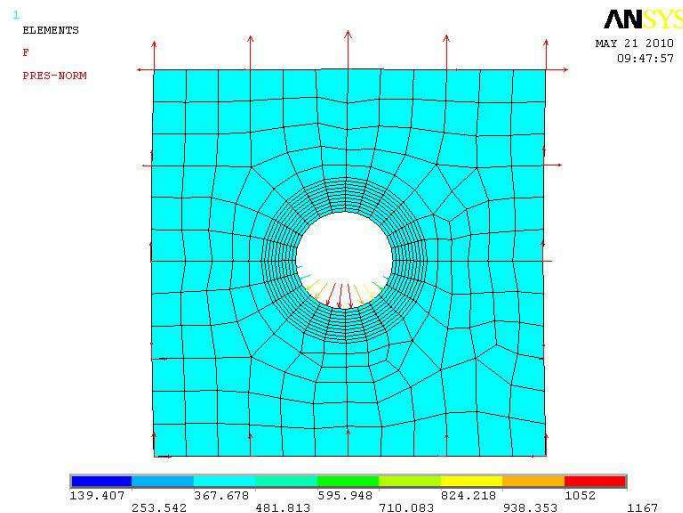


Figure 7.9: Loads and pressure applied to the sub-model

Solving this model the real stress distribution is found and the Failure Indexes of the materials and of the bolts can be evaluated. In the case of a composite the

Failure Index is computed using the set of failure criteria presented in Chapter 5 but limited at the 2D case while for metals the failure criterion is simply $FI = \sigma_{eq}/\sigma_y$ where σ_{eq} is the von-Mises stress. The Failure Indexes for the connected parts are then locally calculated for each element. Failure Indexes for bolts (shear, traction, combined shear/traction) are defined following NF EN 1993-1-8 norm [164]. The failure index for shear, FI_s , is:

$$FI_s = P_s/P_s^R \quad (7.5)$$

with

$$P_s^R = \frac{\alpha_v f_{ub} A_b}{\gamma_{M2}} \quad (7.6)$$

where P_s is the shear load acting on the bolt, P_s^R is the shear load at rupture, A_b is the gross section area of the bolt, α_v is a parameter that depends on the class of the bolt and f_{ub} is the ultimate tensile strength of the bolt. For tension the failure index FI_t is calculated as:

$$FI_t = P_t/P_t^R \quad (7.7)$$

with

$$P_t^R = \frac{k_2 f_{ub} A_s}{\gamma_{M2}} \quad (7.8)$$

where P_t is the tensile load acting on the bolt, P_t^R is the tensile load at rupture, A_s is the tensile stress area of the bolt and k_2 is a parameter that is equal to 0.63 for countersunk bolts and 0.9 for the others. The failure index for the combining presence of shear and traction, FI_{st} , is calculated as:

$$FI_{st} = FI_s + \frac{FI_t}{1.4} \quad (7.9)$$

7.3.2 Industrial application

The methodology explained in 7.3.1 is applied to a real industrial case and in particular at the prototype designed and tested as discussed in 7.2.

The commercial software ANSYSv10 is used to define the FE model of the prototype. Figure 7.10 shows the FE model of the prototype where the loads and displacement applied and the coupled nodes are shown. As only two components are linked together the each kinematic constraint consist of only 2 nodes: 4334-20708 and 4329-20711 are the two couples of nodes that represent the bolts. Between the two components contact elements are used to avoid element interpenetration.

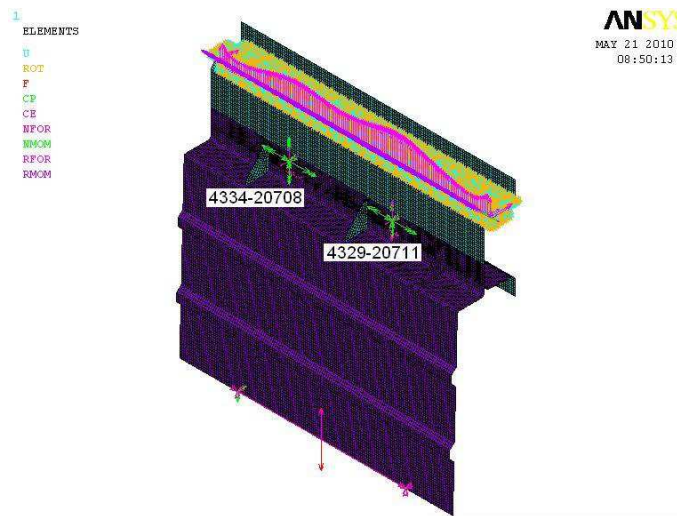


Figure 7.10: FE model of the prototype

A non-linear static analysis is conducted and for each step the algorithm is run. For each coupled node the algorithm is run and the distribution of the Failure Index in the material is obtained.

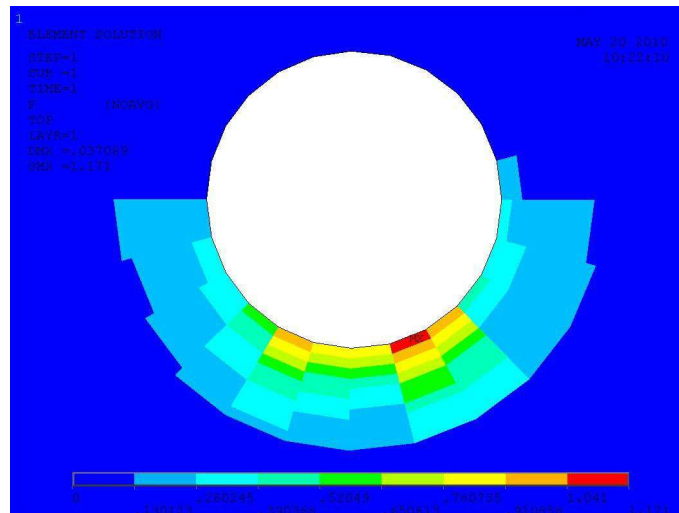


Figure 7.11: Contour plot of the Failure Index around the hole for the submodel

Figure 7.12 shows the Failure Indexes at the critical element as function of the applied load. The material starts to fail in proximity of the bolt 4329-20711. Steel and composite have approximately the same failure index and the load at which failure begins is equal to 15000 N. This finding is in agreement with the experimental results.

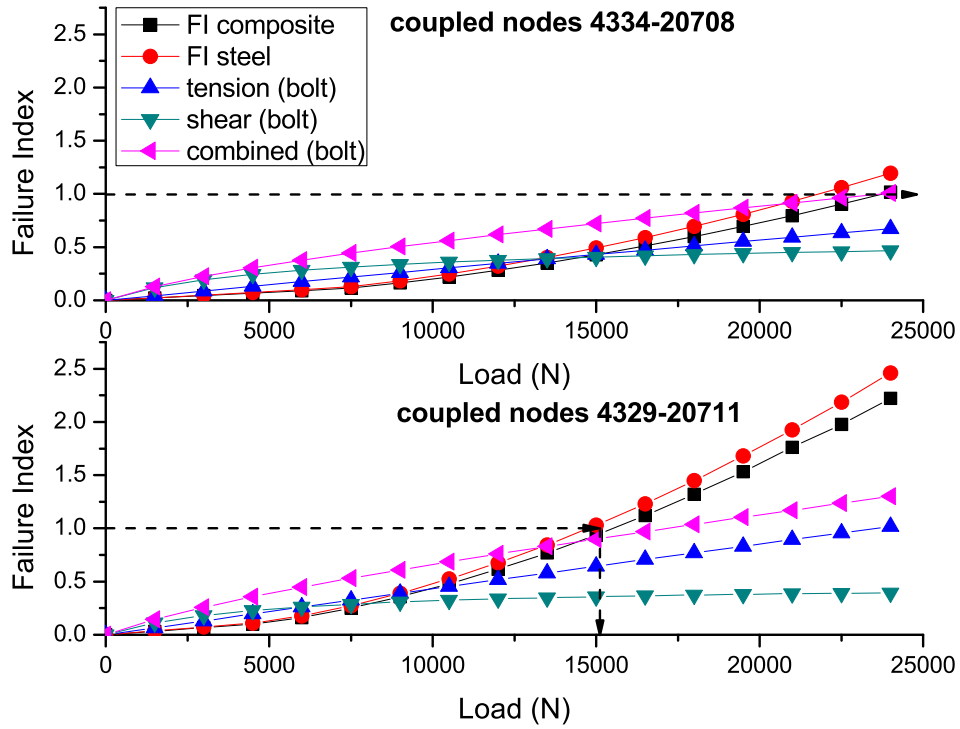


Figure 7.12: Failure Indexes as function of the applied load

Chapter 8

Conclusions and future work

8.1 Conclusions

In this thesis, an investigation of composite bolted joints was presented at different levels of detail.

A preliminary experimental campaign was performed to investigate the influence of the geometric parameters on single-shear or double-shear bolted joints with different materials or material combinations. The results were used to present design charts that can be used by engineers during the preliminary design of a composite joint. Two types of test were considered: in plane shear test and pull-through tests. All the tests were conducted considering specimens with different geometries and with different materials or material combinations. It was shown that the geometry affects the failure mode, and that materials with the same geometries may show a different failure mode.

The main differences in the failure load of the in plane shear test concerns with the epoxy specimens that show always a value of the failure load that is higher than that shown by other specimens. This is due to the fact that epoxy-specimens were manufactured using prepregs while the other specimens(phenolic and vinylester) were manufactured using resin infusion.

If pull-through is considered the results are almost the same for the three materials, considering both the failure load and the initial sub-critical failure load. As expected, it was found that increasing the diameter, increases both the sub-initial critical failure load and the failure load of the specimen. This means that larger holes exhibit an initial sub-critical failure load that is relatively lower if compared to the ultimate failure load. The values of the sub-critical load and of the failure load are virtually the same for the different material tested.

After this preliminary study a 3D set of failure criteria to take into account the clamping pressure applied to the bolt was developed.

It was shown that, for matrix compression, Puck's failure criterion can be used

for the unidirectional laminate and for the embedded lamina, but only if the *in-situ* parameters are correctly computed. If not, the model does not work properly. In particular it was shown that Y_C and S_T are *in-situ* parameters that can be calculated knowing η_L , α_0 and S_L^{is} .

For matrix-tension, it was shown that Puck's elliptical failure criterion and Pinho's quadratic criterion cannot be used for composite materials. The new failure criterion proposed for matrix-tension allows to obtain a consistent definition of the failure index for a general 3D stress state. It was also shown that the failure criterion proposed is applicable for $\sigma_n \geq 0$, and that it can be used consistently together with Puck criterion for compression. As the matrix failure has a critical influence on the fiber kinking, the failure criteria for fiber kinking were also modified.

The predictions of the fully 3D failure criteria were compared with experimental results and good agreement is generally observed. It was shown also that if a hydrostatic compression is present, up to a critical value, the difference between the experimental data and the predicted values is acceptable.

The failure criteria proposed were used in a progressive damage model. Even if the failure criteria is fully 3D the progressive damage model is only quasi-3D.

The progressive damage model uses softening laws that define the evolution of the damage in terms of the dissipated energy. To compute the parameters of the softening laws, an experimental campaign was performed using CT and CC specimen for both IM7/8552 and glass fiber.

Using the digital image correlation (DIC) a new methodology was proposed to compute the J-integral around the crack tip and to measure the crack length.

The comparison between the R-curves obtained in CT specimens using the FE-based post-processing and the DIC-based method indicates that the results are virtually the same and that the proposed method is a valid alternative to measure R-curves associated with longitudinal tensile failure mechanisms in composite materials. The initial value of the fracture toughness associated with longitudinal tensile failure mechanisms in IM7/8552 is 98.7J/m^2 , and it raised up to 133.7J/m^2 for steady state propagation. The mean value of the associated cohesive zone is 3.4mm.

It is concluded that the FE-based data reduction method is inadequate for the measurement of R-curves in CC specimens because it severely overpredicts the fracture toughness. The DIC-based method is an improvement over FE-based data reduction methods because it is based on the actual displacement field on a pre-defined contour. However, the contribution of the contact tractions to the J-integral still needs to be quantified and used in the data reduction method to improve the accuracy of the data. The initial value of the fracture toughness associated with longitudinal compressive failure mechanisms in IM7/8552 measured using DIC was 47.5J/m^2 ; the measured fracture toughness increased up to 315J/m^2 for 15mm of propagation of a kink-band. However, the values computed for the fracture toughness using the CC specimen do not account for the energy dissipated by the de-

lamination that accompanied the propagation of the kink-band. In addition, the delamination does not allow the accurate measurement of the tip of the kink-band. Therefore, it is concluded that these difficulties render the CC test method unsuitable to generate R-curves and that an alternative test method or test procedure should be developed.

The same considerations apply for Glass fiber specimens. In addition, these specimens showed additional failure mechanism that render the use of the CT/CC specimens unsuitable to measure the fracture toughness of fiber-dominated failure mechanisms. In this case, a new test method should be proposed.

Having defined the relevant parameters for the cohesive laws, a progressive damage model was used to simulate failure in IM7/8552 double-shear bolted joints.

Using a parametric Python script, three FE models were defined: bearing, tension, and shear models. It was concluded that the 3D numerical simulations can predict with accuracy both the value of the first peak load and the damage zones.

However, the computational cost of a 3D numerical simulation is not suitable for industrial applications because each model takes about 3 days to run using a cluster of 32 cpus. Therefore, a simplified two-dimensional method was developed.

The two-dimensional numerical model computes the damage of the composite using a two-dimensional version of the previously proposed failure criteria. Since this FE model is generally applied to the entire structure, or to a sub-assembly, the model also considers the onset of the damage in the other connected parts, or in the bolts. If the connected parts are metallic, the failure index is simply calculated using the von-Mises stress. The failure indexes for the bolts (shear, traction, combined shear/traction) are defined following the NF EN 1993-1-8 norm. To validate the model, a mock-up of a real train connection was manufactured and the experimental data was compared with experimental results. It was concluded that the two-dimensional model proposed can accurately predict the onset of the damage in the connected parts of the sub-assembly.

8.2 Future work

The following topics will be the subject of further studies:

- a fully three-dimensional progressive damage model will be defined to be consistent with the three-dimensional failure criteria already proposed;
- a methodology to evaluate the R-curve in compression will be developed as no methodologies to evaluate the energy release rate in compression currently available;
- a methodology to homogenize the cohesive laws on the laminate thickness will be proposed. This will allow the use of one brick/shell element for the entire

thickness of the laminate and will enable the use of the progressive damage model at the laminate level, thus reducing the computational cost.

Bibliography

- [1] Comparaison entre caisses à technologie différent. Technical report, Alstom Transport, 2008.
- [2] P.P. Camanho and F.L. Matthews. Stress analysis and strength prediction in frp: a review. *Composites - Part A*, 28:529–47, 1997.
- [3] *ASTM D5961 / D5961M - 08 Standard Test Method for Bearing Response of Polymer Matrix Composite Laminates*.
- [4] L. J. Hart-Smith. Mechanically-fastened joints for advanced composites-phenomenological considerations and simple analysis. *Douglas Paper*, 6748:1–32, 1978. McDonnell Douglas Corporation.
- [5] G. Kretsis and F. L. Matthews. The strength of bolted joints in glass fibre/epoxy laminates. *Composites*, 16:92–105, 1985.
- [6] T. A. Collings. The strength of bolted joints in multi-directional cfrp laminates. *Composites*, 8:43–54, 1977.
- [7] L. J. Hart-Smith. Design and analysis of bolted and riveted joints in fibrous composite structures. *Douglas Paper*, pages 1–15, 1986. McDonnell Douglas Corporation.
- [8] F. L. Matthews, P. F. Kilty, and E. W. Godwin. Load-carrying joints in fibre reinforced plastics. *Plastic and Rubber Process and Applications*, 2:19–25, 1982.
- [9] J. M. Hodgkinson, D. L. de Beer, and F. L. Matthews. The strength of bolted joints in kevlar rp. *ESA SP-243*, pages 53–61, 1986. ESA, European Space Agency.
- [10] T. A. Collings. On the bearing strengths of cfrp laminates. Technical Report 82033, RAE, Royal Aircraft Establishment, 1982. 1-23.
- [11] W. J. Quinn and F. L. Matthews. The effect of stacking sequence on the pin-bearing strength in gfrp. *Journal of Composite Materials*, 11:139–145, 1987.

- [12] T. A. Collings. Experimentally determined strength of mechanically fastened joints. *Joining Fibre-Reinforced Plastics*, 11:139–145, 1987.
- [13] R. T. Cole, E. J. Bateh, and J. Potter. Fasteners for composite structures. *Composites*, 13:233–240, 1982.
- [14] P. Herrera-Franco and G. L. Cloud. Strain-relief inserts for composite fasteners- an experimental study. *Journal of Composite Materials*, 26:751–768, 1992.
- [15] S. Nilsson. Increasing strength of graphite/epoxy bolted joints by introducing an adhesively bonded metallic insert. *Journal of Composite Materials*, 23:643–650, 1989.
- [16] L. Mirabella and S. C. Galea. An experimental investigation into the use of inserts to enhance the static performance of thin composite bolted lap joints. volume 6, pages 148–157. ICCM-11 Conference Proceedings, Woodhead Publishing Ltd., 1997.
- [17] A. C. Rufin. Fastener hole reinforcement in composites using cold-expanded inserts. *Journal of Composites Technology and Research*, 17:145–151, 1995.
- [18] Matthews. F. L., A. A. Roshan, and L. N. Phillips. The bolt-bearing strength of glass/carbon hybrid composites. *Composites*, 13:255–227, 1982.
- [19] J. H. Oh, Y. G. Kim, and D. G. Lee. Optimum bolted joints for hybrid composite materials. *Composite Structures*, 38:329–341, 1997.
- [20] E. W. Godwin, F. L. Matthews, and P. F. Kilty. Strength of multi-bolt joints in grp. *Composites*, 13:268–272, 1982.
- [21] M. W. Hyer and D. Liu. Stresses in pin-loaded orthotropic plates: Photoelastic results. *Journal of Composite Materials*, 19:138–153, 1985.
- [22] R. Prabhakaran. Photoelastic investigation of bolted joints in composites. *Composites*, 13:253–256, 1982.
- [23] J. H. Crews. Bolt-bearing fatigue of a graphite/epoxy laminate. in *Joining of Composite Materials*, pages 131–144, 1981. Kedward, ed., ASTM STP 749.
- [24] P. A. Smith and K. J. Pascoe. Fatigue of bolted joints in (0/90) cfrp laminates. *Composites Science and Technology*, 29:45–69, 1987.
- [25] P. D. Herrington and M. Sabbaghian. Fatigue failure of composite bolted joints. *Journal of Composite Materials*, 27:491–512, 1993.
- [26] T. de Jong. Stresses around pin-loaded holes in elastically orthotropic or isotropic plates. *Journal of Composite Materials*, 11:313–331, 1977.

- [27] N. I. Muskhelishvili. *Some Basic Problems of the Mathematical Theory of Elasticity*. Noordhoff International Publishing, Leyden, The Netherlands, 1977.
- [28] S. G. Lekhnitskii. *Theory of Elasticity of an Anisotropic Body*. Mir Publishers, Moscow, USSR, 1981.
- [29] K. D. Zhang and C. E. S. Ueng. Stresses around a pin-loaded hole in orthotropic plates. *Journal of Composite Materials*, 18:432–446, 1987.
- [30] P. Conti. Influence of geometric parameters on the stress distribution around a pin-loaded hole in a composite laminate. *Composites Science and Technology*, 25:1–19, 1986.
- [31] R. A. Naik and J. H. Crews. Stress analysis method for a clearance-fit bolt under bearing conditions. *AIAA Journal*, 24:1348–1353, 1985.
- [32] T. S. Ramamurthy. New studies on the effect of bearing loads in lugs with clearance fit pins. *Composite Structures*, 11:135–150, 1989.
- [33] T. S. Ramamurthy. Recent studies on the behaviour of interference fit pins in composite plates. *Composite Structures*, 13:81–99, 1989.
- [34] J. H. Crews, C. S. Hong, and I. S. Raju. Stress-concentration factors for finite orthotropic laminates with a pin-loaded hole. Technical Report NASA TP 1862, National Aeronautics and Space Administration, 1981.
- [35] T. L. Wilkinson, R. E. Rowlands, and R. D. Cook. An incremental finite-element determination of stresses around loaded holes in wood plates. *Computers and Structures*, 14:123–128, 1981.
- [36] R. E. Rowlands, M. U. Rahman, T. L. Wilkinson, and Y. I. Chiang. Single and multiple-bolted joints in orthotropic materials. *Composites*, 13:273–279, 1982.
- [37] L. I. Eriksson. Contact stresses in bolted joints of composite laminates. *Composite Structures*, 6:57–75, 1986.
- [38] U. Graham, M. R. Wisnom, and J. P. H. Webber. A novel finite element investigation of the effects of washer friction in composite plates with bolt-filled holes. *Composite Structures*, 29:329–339, 1994.
- [39] R. M. Jones. *Mechanics of Composite Materials*. Taylor and Francis, USA, 1975.
- [40] F. L. Matthews, C. M. Wong, and S. Chryssafitis. Stress distribution around a single bolt in fibre-reinforced plastic. *Composites*, 13:316–322, 1982.

- [41] W. H. Chen, S. S. Lee, and J. T. Yeh. Three-dimensional contact stress analysis of a composite laminate with bolted joint. *Composite Structures*, 30:287–297, 1995.
- [42] P. A. Smith, K. J. Pascoe, C. Polak, and D. O. Stroud. The behaviour of single-lap bolted joints in cfrp laminates. *Composite Structures*, 6:41–55, 1986.
- [43] I. H. Marshall, W. S. Arnold, and J. Wood. Observations on bolted connections in composite structures. *Composite Structures*, 13:133–151, 1989.
- [44] S. M. Sarabian. An experimental and finite element investigation into the nonlinear material behaviour of pin-loaded composite laminates. Technical Report Report TR 91-2, MTL, 1991. 1-265.
- [45] R. Barboni, P. Gandenzi, and S. Carlini. A three-dimensional analysis of edge effects in composite laminates with circular holes. *Composite Structures*, 15:115–136, 1990.
- [46] E. Iarve. Spline variational three-dimensional stress analysis of laminated composite plates with open holes. *International Journal of Solids and Structures*, 33:2095–2118, 1996.
- [47] E. Iarve. Stress analysis in laminated composites with fastener holes. In *Proceedings of the American Society for Composites 10th Technical Conference*, pages 408–419, Lancaster, PA, 1995. Technomic Publishing Co.
- [48] S. J. Kim and J. H. Kim. Finite element analysis of laminated composites with contact constraint by extended interior penalty methods. *International Journal for Numerical Methods in Engineering*, 36:3421–3439, 1993.
- [49] S. Wang and Y. Han. Finite element analysis for load distribution of multi-fastener joints. *Journal of Composite Materials*, 22:124–135, 1988.
- [50] O. H. Griffin, M. W. Hyer, D. Cohen, M. J. Shuart, S. R. Yalamanchili, and C. B. Prasad. Analysis of multifastener composite joints. *Journal of Spacecraft and Rockets*, 31:278–284, 1994.
- [51] R. A. Naik and J. R. Crews. Stress analysis method for clearance-fit joints with bearing-by-pass load. *AIAA Journal*, 29:89–95, 1991.
- [52] E. W. Godwin and F. L. Matthews. A review of the strength of joints in frp part 1: Mechanically fastened joints. *Composites*, 11:155–160, 1982.
- [53] M. Johnson and F. L. Matthews. Determination of safety factors for use when designing bolted joints in grp. *Composites*, 10:73–76, 1979.

- [54] J. P. Waszczak and T. A. Cruse. Failure mode and strength prediction of anisotropic bolt bearing specimens. *Journal of Composite Materials*, 5:421–425, 1979.
- [55] S. Tang. Failure of composite joints under combined tension and bolt loads. *Journal of Composite Materials*, 15:329–335, 1981.
- [56] R. A. Naik and J. H. Crews. Ply-level failure analysis of a graphite/epoxy laminate under bearing-bypass loading. Technical Report NASA TM 100578, National Aeronautics and Space Administration, 1988. 1-35.
- [57] J. H. Crews and R. A. Naik. Combined bearing-bypass loading on a graphite/epoxy laminate. *Composite Structures*, 6:21–40, 1986.
- [58] J. H. Crews. A survey of strength analysis methods for laminates with holes. *Journal of the Aeronautical Society of India*, 36:287–303, 1984.
- [59] J. M. Whitney and R. J. Nuismer. Stress fracture criteria for laminated composites containing stress concentrations. *Journal of Composite Materials*, 8:253–265, 1974.
- [60] B. L. Agarwal. Static strength prediction of bolted joint in composite materials. *AIAA Journal*, 18:1371–1375, 1980.
- [61] D. W. Wilson and R. B. Pipes. Analysis of the shearout failure mode in composite laminates. In *1st International Conference on Composite Structures*, pages 34–49, 1981.
- [62] F. K. Chang, R. A. Scott, and G. S. Springer. Strength of mechanically fastened composite joints. *Journal of Composite Materials*, 16:470–494, 1982.
- [63] A. V. Murthy, B. Dattaguru, H. L. Narayana, and A. K. Rao. Stress and strength analysis of pin joints in laminated anisotropic plates. *Composite Structures*, 19:299–312, 1991.
- [64] L. I. Eriksson. An analysis method for bolted joints in primary composite. In *AGARD Conference Proceedings 427*, pages 6.1–6.19, Madrid, Spain, 1987. Advisory Group for Aerospace Research and Development.
- [65] Lin C. C. and C. H. Lin. Stress and strength analysis of composite joints using direct boundary element method. *Composite Structures*, 25:209–215, 1993.
- [66] W. S. Arnold, I. H. Marshall, and J. Wood. Optimum design considerations for mechanically fastened composite joints. *Composite Structures*, 16:85–101, 1990.

- [67] F. K. Chang, R. A. Scott, and G. S. Springer. Failure strength of nonlinearly elastic composite laminates containing a pin loaded hole. *Journal of Composite Materials*, 18:464–477, 1984.
- [68] S. E. Yamada and C. T. Sun. Analysis of laminate strength and its distribution. *Journal of Composite Materials*, 12:275–284, 1978.
- [69] H. T. Hahn and S. W. Tsai. Nonlinear elastic behaviour of unidirectional composite laminate. *Journal of Composite Materials*, 7:102–110, 1973.
- [70] F. K. Chang and K .Y. Chang. A progressive damage model for laminated composites containing stress concentrations. *Journal of Composite Materials*, 21:834–855, 1987.
- [71] F. K. Chang and K .Y. Chang. Post-failure analysis of bolted composite joints in tension or shear-out mode failure. *Journal of Composite Materials*, 21:809–833, 1987.
- [72] F. K. Chang and L. B. Lessard. Damage tolerance of laminated composites containing an open hole and subjected to compressive loadings: Part i analysis. *Journal of Composite Materials*, 25:2–43, 1991.
- [73] K. Y. Chang, S. Liu, and F. K. Chang. Damage tolerance of laminated composites containing an open hole and subjected to tensile loadings. *Journal of Composite Materials*, 25:274–301, 1991.
- [74] I. S. Shahid and F. K. Chang. An accumulative damage model for tensile and shear failures of laminated composite plates. *Journal of Composite Materials*, 29:926–981, 1995.
- [75] C. L. Hung and F. K. Chang. Bearing failure of bolted composite joints: Part ii: Model and verification. *Journal of Composite Materials*, 30:1359–1400, 1996.
- [76] H. S. Wang, C. L. Hung, and F. K. Chang. Bearing failure of bolted composites joints part i: Experimental characterization. *Journal of Composite Materials*, 30:1284–1313, 1996.
- [77] H. T. Sun. *Strengths of Composite-to-Metal Double-Lap Bolted Joints*. Ph.d. thesis, Department of Mechanical Engineering Stanford University, California, U.S.A., 1997.
- [78] S. C. Tan. A progressive failure model for composite laminates containing openings. *Journal of Composite Materials*, 25:556–577, 1991.
- [79] S. C. Tan and J. Perez. Progressive failure of laminated composites with a hole under compressive loading. *Journal of Reinforced Plastics and Composites*, 12:1043–1057, 1993.

- [80] R. J. Nuismer and S. C. Tan. Constitutive relations of a cracked composite lamina. *Journal of Composite Materials*, 22:306–321, 1988.
- [81] S. C. Tan and R. J. Nuismer. A theory for progressive matrix cracking in composite laminates. *Journal of Composite Materials*, 23:1029–1047, 1989.
- [82] W. H. Chen and Y. J. Lee. Failure process and pin-bearing strength of laminated composites at elevated temperatures. *Journal of Reinforced Plastics and Composites*, 11:743–771, 1992.
- [83] Y. Tsujimoto and D. Wilson. Elasto-plastic failure analysis of composite bolted joints. *Journal of Composite Materials*, 20:236–252, 1986.
- [84] L. B. Lessard and M. M. Shokrieh. Two-dimensional modeling of composite pinned-joint failure. *Journal of Composite Materials*, 29:671–697, 1995.
- [85] S. J. Kim, J. S. Hwang, and H. K. Kim. Progressive failure analysis of pin-loaded laminated composites using penalty finite element method. *AIAA Journal*, 36:75–80, 1998.
- [86] C. C. Chamis, S. N. Singhal, and L. Minnetyan. Probabilistic simulation of progressive fracture in bolted-joint composite laminates. Technical Report NASA TM 107107, National Aeronautics and Space Administration, 1994.
- [87] C. C. Chamis and L. Minnetyan. Probabilistic evaluation of bolted joints in polymer matrix composites. In *AGARD Conference Proceedings 590*, pages 25.1–25.11, Florence, Italy. Advisory Group for Aerospace Research and Development.
- [88] W. H. Chen and S. S. Lee. Numerical and experimental failure analysis of composite laminates with bolted joints under bending loads. *Journal of Composite Materials*, 29:15–36, 1995.
- [89] K. Gamble, M. Pilling, and A. Wilson. An automated finite element analysis of the initiation and growth of damage in carbon-fibre composite materials. *Composite Structures*, 32:265–274, 1995.
- [90] Z. Hashin. Failure criteria for unidirectional fiber composites. *Journal of Applied Mechanics*, 47:329–334, 1980.
- [91] S. W. Tsai and H. T. Hahn. *Introduction to Composite Materials*. Technomic Publishing Company, Westport, USA, 1980.
- [92] L. Ye. Role of matrix resin in delamination onset and growth in composite laminates. *Composites Science and Technology*, 33:257–277, 1988.
- [93] B. L. Agarwal. Behaviour of multifastener bolted joints in composite materials. *AIAA Journal*, 80-0307:1–7, 1980.

- [94] F. K. Chang, R. A. Scott, and G. S. Springer. Failure of composite laminates containing pin loaded holes-method of solution. *Journal of Composite Materials*, 18:255–278, 1984.
- [95] M. W. Hyer and P. A. Chastain. Effect of bolt load proportioning on the capacity of multiple-bolt composite joints. *Journal of Aircraft*, 25:184–189, 1987.
- [96] K. N. Shivakumar and J. H. Crews. Bolt clamp-up relaxation in a graphite/epoxy laminate. Technical Report NASA TM 83268, National Aeronautics and Space Administration, 1982.
- [97] K. N. Shivakumar and J. H. Crews. An equation for bolt clampup relaxation in transient environments. Technical Report NASA TM 84480, National Aeronautics and Space Administration, 1982.
- [98] R.R. Schmitt and W. J. Horn. Viscoelastic relaxation in bolted thermoplastic composite joints. In *35th International SAMPE Symposium and Exhibition*, page 133647.
- [99] W. J. Horn and R. R. Schmitt. Influence of clamp-up force on the strength of bolted composite joints. *AIAA Journal*, 32:665–667, 1994.
- [100] S. D. Thoppul, R.F. Gibson, and R. A. Ibrahim. Phenomenological modeling and numerical simulation of relaxation in bolted composite joints. *Journal of Composite Materials*, 42(17), 2008.
- [101] S. D. Thoppul, R.F. Gibson, and R. A. Ibrahim. Analytical and experimental characterization of the effects of vibration on relaxation in composite bolted joints. In *American Society for Composites 21st Technical Conference 192*, volume 42, Dearborn, MI,USA, 2006.
- [102] K.G. Kibler and H. G. Carter. Viscoelastic parameters of epoxy resin from thermomechanical and electrical conductivity measurements. In *Composite Materials: testing and design 5th conf.*, page 282288. ASTM STP 674, American Society Testing Material, 1979.
- [103] S. W. Beckwith. Viscoelastic creep behavior of filament-wound case materials. *Journal of Spacecraft Rockets*, 21(6):54652, 1984.
- [104] R. A. Schapery. Inelastic behavior of composite materials. In Herakovich CT, editor, *ASME applied mechanics symposia series 192*, volume 13, pages 127–155, Uston, TX,USA, 1975.
- [105] R. F. Gibson. *Principles of composite material mechanics*. Taylor and Francis Group, Boca Raton, Florida, 2th edition, 2007.

- [106] *Abaqus Version 6.7 Documentation*, 2007.
- [107] B. K. Parida, R. V. Prakash, P. D. Mangalgiri, and K. Vijayaraju. Influence of environmental and geometric parameters on the behavior of fastener joints in advanced composites. composite materials: fatigue and fracture. *ASTM STP 1285*, E.A. Armanios. *Am Soc Test Mater*, 6:42351, 1997.
- [108] H. S. Wang, C. L. Hung, and F. K. Chang. Bearing failure of bolted composite joints, part i: experimental characterization. *J Comp Mat*, 12:1284313, 1999.
- [109] W. A. Counts and W. S. Johnson. Temperature effects on ultimate bearing strength of polymeric composite joints. *J Comp Tech Res*, 24(1):17–23, 2002.
- [110] N. Hirano, Y. Takato, and W. X. Wang. Effects of temperature on the bearing strength of cf/epoxy pinned joints. *J Comp Mat*, 41(3):335–51, 2007.
- [111] W. A. Counts and W. S. Johnson. Bolt bearing fatigue behavior of polymer-matrix composites at elevated temperature. *Int J Fatigue*, 24(2-4):197–204, 2002.
- [112] A. R. Kallmeyer and R. I. Stephens. Creep elongation of bolt holes subjected to bearing loads in a polymermatrix composite laminate. *Comp. Mat.: Fatigue and Fracture*, *ASTM STP 1285*, Armanois EA editor, American Society for Testing and Materials, 6:452–67, 1997.
- [113] H. Ahmad, W.S. Johnson, and W.A. Counts. Evaluation of bolt bearing behavior of highly loaded composite joints at elevated temperature. *J Comp Mat*, 23 (6):559–571, 2003.
- [114] G.J. Turvey and P. Wang. Failure of pultruded grp single-bolt tension joints under hot-wet conditions. *Compos Struct*, 77 (4):514–520, 2007.
- [115] S. Hurd and R. Yuan. Hydrothermal effects on the bearing strength of gfrp composite joint, 1996.
- [116] S. Walker. Thermal effects on the pin-bearing behavior of im7/peti-5 composite joints. *J Comp Mat*, 36 (23):26232651, 2002.
- [117] S. Goswami. A finite element investigation on progressive failure analysis of composite bolted joints under thermal environment. *J Reinforced Plastics Compos*, 24 (2):161171, 2005.
- [118] H.-S. Chen and Y.-J. Lee. Failure process and pin-bearing strength of laminated composite at elevated temperature. *J Reinforced Plastics Compos*, 11 (7):743771, 1992.
- [119] M. M. Shokrieh, L. B. Lessard, and C. Poon. Three-dimensional progressive failure analysis of pin/bolt loaded composite laminates, 1996.

- [120] T. Yilmaz and T. Sinmazcelik. Geometric parameters and chemical corrosion effects on bearing strength of polyphenylenesulphide (pps) composites source. *Mater Design*, 28 (5):1695–1698, 2007.
- [121] *French Norm NF F 16-101:1988. All vehicles - the burning behavior - materials to choose*, DOctober 1988.
- [122] *European Norm EN 10149-2:1995. Hot-rolled flat products made of high yield strength steels for cold forming Part 2 : Delivery conditions for thermomechanically rolled steels*, December 1995.
- [123] *European Norm NF EN 485-2:2007. Aluminium and aluminium alloys Sheet, strip and plate Part 2: Mechanical properties*, Juin 2007.
- [124] A. Mkaddem. *Expérimentation et simulation du pliage de tôles H.L.E. Prévission du comportement en service des pièces pliées*. PhD thesis, Thèse de doctorat, ENSAM Angers, 2003.
- [125] *French Norm NF T 57-107:1986. Glass-fibre-reinforced plastics - Measurement of the change of characteristics during hot water treatment*, Decembre 1986.
- [126] P. P. Camanho and M. Lambert. A design methodology for mechanically fastened joints in laminated composite materials. *Composites Science and Tecnology*, 66:3004–3020, 2006.
- [127] G. Taguchi and S. Konishi. *Taguchi methods: orthogonal arrays and linear graphs*. ASI Press, Allen Park, Michigan, USA, 5th edition, 1987.
- [128] R. L. Mason, R. F. Gunst, and Hess J. L. *Statistical Design and Analysis of Experiments*. John Wiley & Sons, Inc., 2nd edition, 2003. Wiley series in probability and statistics.
- [129] D. C. Montgomery. *Design and Analysis of Experiments*. John Wiley & Sons, Inc., 5th edition, 2003.
- [130] *ASTM D790 - 07e1 Standard Test Methods for Flexural Properties of Unreinforced and Reinforced Plastics and Electrical Insulating Materials*.
- [131] *ASTM D7332 / D7332M - 09 Standard Test Method for Measuring the Fastener Pull-Through Resistance of a Fiber-Reinforced Polymer Matrix Composite*.
- [132] C. G. Dávila, C. A. Rose, and P. P. Camanho. A procedure for superposing linear cohesive laws to represent multiple damage mechanism in the fracture of composites. *International Journal of Fracture*, 2009.

- [133] P. Maimí, P. P. Camanho, J. A. Mayugo, and C. G. Dávila. A continuum damage model for composite laminates: Part i constitutive model. *Mechanics of Materials*, 39(10):897–908, 10 2007.
- [134] P. Maimí, P. P. Camanho, J. A. Mayugo, and C. G. Dávila. A continuum damage model for composite laminates: Part ii computational implementation and validation. *Mechanics of Materials*, 39(10):909–919, 10 2007.
- [135] S.T. Pinho, P. Robinson, and L. Iannucci. Fracture toughness of the tensile and compressive fibre failure modes in laminated composites. *Composites Science and Technology*, 66:2069–79, 2006.
- [136] M. A. Sutton, W. J. Wolters, W. H. Peters, W. F. Ranson, and S. R. McNeill. Determination of displacement using an improved digital correlation method. *Image and Vision Computing*, 1:133–39, 1983.
- [137] M. A. Sutton, M. Cheng, W. H. Peters, Y. J. Chao, and S. R. McNeill. Application of a optimized digital correlation method to planar deformations analysis. *Image and Vision Computing*, 4:143–50, 1986.
- [138] S. Touchal-Mguil. *Une technique de corrélation d’images numériques : application la détermination de courbes limites de formages et proposition d’un critère de striction*. PhD thesis, Ph.D. thesis, INSA-LYON, 1997.
- [139] Grégoire D. *Initiation, propagation, arrêt et redémarrage de fissures sous impact*. PhD thesis, Thèse de doctorat, Institute national des sciences appliquées de Lyon, 2008.
- [140] Y.-L. Kang, Z.-F. Zhang, H.-W. Wang, and Qin Q.-H. Experimental investigation of the effect of thickness on fracture toughness of metallic foils. *materials Science and Engineering*, A 394:312–19, 2005.
- [141] J.R. Rice. A path independent integral and the approximate analysis of strain concentration by notches and cracks. *J Appl Mech*, 31:379–86, 1968.
- [142] Lecompte D., Smits A., Bossuyt S., Sol H., Vantomme J., Van Hemelrijck D., and Habraken A.M. Quality assessment of speckle patterns for digital image correlation. *Optics and Lasers in Engineering*, 44(11):1132–45, 2006.
- [143] Mark Lutz and Asher David. *Learning Python*. O’Reilly & Associates, 2nd edition, 2003.
- [144] S. T. Pinho. Private communication, 2009.
- [145] C. G. Dávila, P. P. Camanho, and C. A. Rose. Failure criteria for frp laminates. *Journal of Composite Materials*, 39(4):323–345, 2005. Cited By (since 1996): 23.

- [146] Puck A. Calculating the strength of glass fibre/plastic laminates under combined load. *Kunstst German Plast*, 55:18–19, 1969. original in German.
- [147] Puck A. and Schneider W. On failure mechanism and failure criteria of filamentwound glass-fibre/resin composites. *Plast Polym*, pages 33–44, 1969. original in German.
- [148] Puck A. and H. Schürmann. Failure analysis of frp laminates by means of physically based phenomenological models. *Composites Science and Technology*, 58:1045–67, 1998.
- [149] Puck A. and H. Schürmann. Failure analysis of frp laminates by means of physically based phenomenological models. *Composites Science and Technology*, 62:1633–62, 2002.
- [150] Pinho S.T., Iannucci L., and Robinson P. Physically-based failure models and criteria for laminated fibre-reinforced composites with emphasis on fibre kinking: Part i: Development. *Composites Part A*, 37:63–73, 2006.
- [151] M. Knops. *Analysis of Failure in Fiber Polymer Laminates, The Theory of Alfred Puck*. Springer, first edition, 2008.
- [152] V.W. Rosen. Mechanics of composite strengthening. *Metals Park OH: Fiber Composite Materials American Society of Metals*, pages 37–75, 1965.
- [153] A.S. Argon. *Fracture of Composites in: treatise on material science and technology*. New york: Academic Press, 1972.
- [154] C.R. Schultheisz and A.M. Waas. Compressive failure of composites. part i. testing and micromechanical theories. *Progress in Aerospace Sciences*, 32:1–42, 1996.
- [155] K.D. Pae. Influence of hydrostatic pressure on the mechanical behavior and properties of unidirectional, laminated, graphite-fiber/epoxy-matrix thick composites. *Composites: Part B*, 27B:599–611, 1996.
- [156] H. Koerber and P.P. Camanho. High strain rate characterisation of unidirectional carbon-epoxy im7-8552 in transverse compression and in-plane shear using digital image correlation. *Mechanics of Materials*, 2010. doi:10.1016/j.mechmat.2010.09.003.
- [157] M.J. Hinton, A.S. Kaddour, and Soden P.D. A comparison of the predictive capabilities of current failure theories for composite laminates, judged against experimental evidence. *Composites Science and Technology*, 62:1725–97, 2002.
- [158] P.J. Hine. The effect of hydrostatic pressure on the mechanical properties of glass fiber/epoxy unidirectional composites. *Composites: Part A*, 36:279–89, 2005.

- [159] Z.P. Bažant and B.H. Oh. Crack band theory for fracture of concrete. *Materials and structures*, 16:155–177, 1983.
- [160] C. M. L. Camanho, P. P. and Tavares, J. B. Almeida, P. M. Bandeira, and P. M. Portela. Test plan and test procedures. Technical report, INEGI, 2003. Technical Note 2, Project ESA-ESTEC 16813.
- [161] E. V. González, P. Maimí, A. Turon, P.P. Camanho, and J. Renart. Simulation of delamination by means of cohesive elements using an explicit finite element code. *Computers, Materials and Continua*, 9:51–92, 2009.
- [162] C. L. Hung and F. K. Chang. Strength envelope of bolted composite joints under bypass loads. *Journal of Composite Materials*, 30:1402–1435, 1996.
- [163] S. P. Garbo and J. M. Ogonowski. Effects of variances and manufacturing tolerances on the design strength and life of mechanically fastened composite joints. Technical Report AFWAL-TR-81-3041, U. S. Air Force Wright Aeronautical Laboratories, 1981.
- [164] *European Norm EN 1993-1-8. Calculation of structures in steel*, December 2005.

Appendix A

Crack detection algorithm

```
1 % Algorithm to find crack length
2 % G. Catalanotti, 2009

3 clear all

4 % name of the project
5 specimen='CC_G_2';
6 % name of the directory
7 dir='F:\PhD\CT-CC\Fracture';

8 % load the data
9 string_path=strcat(dir,'\ ',specimen,'\rawdata.mat');
10 eval(['load -mat' ' ' string_path ]);
11 string_path=strcat(dir,'\ ',specimen,'\misc.mat');
12 eval(['load -mat' ' ' string_path ]);
13 string_path=strcat(dir,'\ ',specimen,'\matdata.mat');
14 eval(['load -mat' ' ' string_path ]);

15 dir_res=[dir '\ ' 'Mat_Res' '\ ' specimen '\ ' specimen];

16 % displacement of the image
17 stages = length(aramis2D.displ);

18 % find size of image
19 Size=size(aramis2D.displ(1,1).X);
20 m=Size(1,1);
21 n=Size(1,2);

22 % preallocated variables
23 K_all= struct;
24 length_windows=zeros(stages,1);
25 length_J_windows=0;

26 % for loop for all stages of the test
27 for J = 1:stages

28 % load displacement along x for stage J
29 displ_x = aramis2D.displ(1,J).X;
30 % load displacement along y for stage J
31 displ_y = aramis2D.displ(1,J).Y;

32 % find the dimensions of the matrix
33 Size=size(aramis2D.displ(1,J).X);
34 m=Size(1,1);
35 n=Size(1,2);
```

```

36 %
37 % find the matrix of the displacements
38 displ= (displ_x.^2+displ_y.^2).^0.5;

39 % zeros
40 n_zeros=zeros(m,1);
41 m_zeros=zeros(1,n+1);

42 % the algorithm is implemented here
43 % this variable are defined concatenated the displacement
44 % values with a empty row and a empty colon
45 % if displacement matrix has dimension m*n these
46 % matrices have dimensions (m+1)*(n+1)
47 displ_A= vertcat(horzcat(displ,n_zeros),m_zeros)./4;
48 displ_B= vertcat(horzcat(n_zeros,displ),m_zeros)./4;
49 displ_C= vertcat(m_zeros,horzcat(displ,n_zeros))./4;
50 displ_D= vertcat(m_zeros,horzcat(n_zeros,displ))./4;

51 matr_transf=ones(m+1,n+1);
52 matr_transf(1:m+1, 1)=2;
53 matr_transf(1:m+1, n+1)=2;
54 matr_transf(1, 1:n+1)=2;
55 matr_transf(m+1, 1:n+1)=2;

56 matr_transf(1, 1)=4;
57 matr_transf(1, n+1)=4;
58 matr_transf(m+1, 1)=4;
59 matr_transf(m+1, n+1)=4;

60 % grid_values is the matrix that contains the values
61 % of the displacements for the vertex of the patterns
62 grid_values=(displ_A+displ_B+displ_C+displ_D).*matr_transf;

63 displ_A=grid_values(1:m, 1:n);
64 displ_B=grid_values(1:m, 2:n+1);
65 displ_C=grid_values(2:m+1, 1:n);
66 displ_D=grid_values(2:m+1, 2:n+1);

67 % modulus of displacement for vertex of the patterns
68 displ_CA=abs((displ_C-displ_A));
69 displ_DB=abs((displ_D-displ_B));

70 % compute matrix K (criterion)
71 K=max(displ_CA,displ_DB);

72 % treshold
73 alpha=2.0;

74 K_=K;
75 % apply criterion
76 % K_T = -1 if value of K for the pattern is NaN
77 % in this case the material is completed damaged
78 K_NaN=isnan(K);
79 K(isnan(K))=-1;
80 % K_T equal to zero if the value of K is less
81 % the the average for the image. in this case the
82 % material is undamaged
83 K_(isnan(K_))=0;
84 avg_K=sum(sum(K_))/sum(sum(K_NaN));
85 K((K<alpha*avg_K)&(K>0)) = 0;
86 % K_T = 1 for the crack tip
87 K(K>=alpha*avg_K) = 1;

88 % delete solutions for the edge of the image
89 edge=5;

```

```

90 K(1:edge,:)=0;
91 K(m-edge:m,:)=0;
92 K(:,1:edge)=0;

93 surf(K)
94 set(gca, 'CLim', [-1.0, 1.0]);
95 colorbar
96 zlim([-1 +1])
97 xlabel(['stage = ',num2str(J)])
98 ylabel('K_T')
99 % eval( ['print -dpng' ' ' dir_res '-' num2str(J,'%03.4g')] )
100 M(J) = getframe;

101 [row,col] = find(K~=0);

102 if isempty(col);
103     length_J_windows=0;
104 else
105     length_J_windows=n-col(1);
106 end
107 K_all(1,J).K= K ;
108 % compute the crack length (unity of measure is in this
109 % case the length of the size of the pattern= 15mm)
110 length_windows(J)= length_J_windows;

111     if length_J_windows>0.95*n
112         break
113     end
114 end

115 photo_number=(1:1:J)';
116 crack=zeros(J,1);

117 % apply conversion factor to obtain the crack length in mm
118 pixel_window=15;
119 for I = 1:J
120     crack(I,1)=(length_windows(I)-...
121         length_windows(1))*pixel_window*...
122         converfactor+a0;
123 end

124 filename_movie=[specimen '.avi'];
125 % movie2avi(M, filename_movie)

126 % find time of the stages.
127 % this is useful for the correlation
128 % of the data from the MTS to find the
129 % function load=load(crack)
130 time_photo=photo_number.*deltaT;

131 plot(time_photo,crack,'-o');
132 xlabel('time [s]');
133 ylabel('crack length [mm]');

134 % save data
135 string_path=strcat(dir,'\ ',specimen,'\Aramis.mat');
136 save(string_path, 'time_photo', 'crack')

```


Appendix B

J-Integral algorithm

```
1 % J-integral calculation algorithm
2 %G. Catalanotti, 2009
3
4 clear all
5
6 Ex=90650;
7 Ey=90650;
8 v_xy=0.32;
9 Gxy=5290;
10
11 % name of the project
12 specimens=['CT_C_1'; 'CT_C_2'; 'CT_C_3'];
13 % name of the directory
14 dir='F:\PhD\CT-CC\Fracture';
15
16 for JJ=1:3,
17 specimen=specimens(JJ,:);
18 % load the data
19 string_path=strcat(dir,'\ ',specimen,'\rawdata.mat');
20 eval(['load -mat' ' ' string_path ]);
21 string_path=strcat(dir,'\ ',specimen,'\misc.mat');
22 eval(['load -mat' ' ' string_path ]);
23 string_path=strcat(dir,'\ ',specimen,'\matdata.mat');
24 eval(['load -mat' ' ' string_path ]);
25 string_path=strcat(dir,'\ ',specimen,'\Aramis.mat');
26 eval(['load -mat' ' ' string_path ]);
27
28 % displacement of the image
29 stages = length(aramis2D.displ);
30 % find size of image
31 Size=size(aramis2D.displ(1,1).X);
32 m=Size(1,1);
33 n=Size(1,2);
34 %contour for J integral
35 ji_vect=zeros(stages,1);
36 % homogeneize matrix
37 SIZES=zeros(stages,2);
38
39 for J = 1:stages
40     SIZES(J,:)=size(aramis2D.displ(1,J).X);
41 end
42 M=min(SIZES(:,1)) ; N=min(SIZES(:,2)) ;
43
44 % foor loop for all stages of the test
45 for J = 2:stages
46
```

```

47 | % load displacement along x for stage J
48 | displ_x = aramis2D.displ(1,J).X;
49 | % load displacement along y for stage J
50 | displ_y = aramis2D.displ(1,J).Y;
51 |
52 | % find the dimensions of the matrix
53 | Size=size(aramis2D.displ(1,J).X);
54 | m=Size(1,1);
55 | n=Size(1,2);
56 |
57 | %
58 | % find the matrix of the displacements
59 | displ= (displ_x.^2+displ_y.^2).^0.5;
60 |
61 | % zeros
62 | n_zeros=zeros(m,1);
63 | m_zeros=zeros(1,n+1);
64 |
65 | % compute the J integral directly from ARAMIS
66 |
67 | delt=2;
68 | N_=N-delt;
69 | M_=M-delt;
70 |
71 | % coordinate of top-left vertex of the image
72 | vm=int8((m-M_)/2);
73 | vn=int8((n-N_)/2);
74 |
75 | % contour is the matrix that has the value 1
76 | % in the points of the contours
77 | % used for the calculation of the J integral
78 | top=zeros(m,n);
79 | top(vm,vn+1:vn+N_)=ones(1,N_);
80 | top_left=zeros(m,n);
81 | top_left(vm,vn)=1;
82 | top_right=zeros(m,n);
83 | top_right(vm,vn+N_+1)=1;
84 | %
85 | bot=zeros(m,n);
86 | bot(vm+M_,vn+1:vn+N_)=ones(1,N_);
87 | bot_left=zeros(m,n);
88 | bot_left(vm+M_,vn)=1;
89 | bot_right=zeros(m,n);
90 | bot_right(vm+M_,vn+N_+1)=1;
91 |
92 | right=zeros(m,n);
93 | right(vm+1:M_-1+vm,vn)=ones(M_-1,1);
94 | left=zeros(m,n);
95 | left(vm+1:M_-1+vm,vn+N_+1)=ones(M_-1,1);
96 |
97 | contour=top+bot+bot_left+bot_right+...
98 |     top_left+top_right+right+left;
99 | %
100 | Dx=top-bot-1/2*bot_left-1/2*bot_right+...
101 |     +1/2*top_left+1/2*top_right;
102 | Dx=Dx*converfactor;
103 |
104 | Dy=left-right+1/2*bot_left-1/2*bot_right+...
105 |     +1/2*top_left-1/2*top_right;
106 | Dy=Dy*converfactor;
107 | %
108 | eps_x = aramis2D.strain(1,J).X;
109 | eps_y = aramis2D.strain(1,J).Y;
110 | eps_xy = aramis2D.strain(1,J).S*100;
111 | %

```



```

112 sigma_x=eps_x.*Ex-v_xy*Ey.*eps_y;
113 sigma_y=eps_y.*Ey-v_xy*Ey.*eps_x;
114 tau_xy=Gxy*eps_xy;
115 %
116 Wxy=1/2*(sigma_x.*eps_x+sigma_y.*eps_y+...
117     tau_xy.*eps_xy);
118
119 Wdy=Wxy.*Dy;
120 Wdy(isnan(Wdy))=0;
121
122 % compute derivatives
123 [d_displ_x,FY] = gradient(displ_x);
124 [d_displ_y,FY] = gradient(displ_y);
125
126
127 Dx(Dx==0)=Inf;
128 d_displ_x_dx = -d_displ_x/converfactor;
129 d_displ_y_dx = d_displ_y/converfactor;
130
131 % compute Ds
132 Ds=(Dx.^2 + Dy.^2).^0.5;
133
134 % compute directions cosines
135 n1=Dy./Ds;
136 n2=-Dx./Ds;
137
138 % compute tractions
139 T1=sigma_x.*n1+tau_xy.*n2;
140 T2=tau_xy.*n1+sigma_y.*n2;
141
142 t_du_dx_ds=T1.*d_displ_x_dx.*Ds+...
143     T2.*d_displ_y_dx.*Ds;
144 t_du_dx_ds(isnan(t_du_dx_ds))=0;
145 ji=Wdy-t_du_dx_ds;
146 ji=ji.*contour;
147
148 ji=(sum(sum(ji_)));
149
150 ji_vect(J,1)=ji;
151
152 end
153
154 % ji_vect refers to the laminate as the thickness of zero degree laminae is
155 % half of the total thickness, to find the ji-integral for zero-degree laminae
156 % this value has to be multiply by 2
157 ji_zero=ji_vect*2.0;
158
159 incr_crack=crack-ones(size(crack))*crack(1,1);
160
161 eval(['crack_' specimen '=crack'])
162 eval(['G_' specimen '=ji_zero'])
163 eval(['incr_crack_' specimen '=incr_crack'])
164 end
165
166 plot(incr_crack_CT_C_1,G_CT_C_1,'--ro',...
167     incr_crack_CT_C_2,G_CT_C_2,'--b*',...
168     incr_crack_CT_C_3,G_CT_C_3,'--^k')
169

```


220 APPENDIX C. PARAMETRIC MODEL FOR J-INTEGRAL CALCULATION

```

11 #           H           |           |
12 #           |           |           |
13 #           |           d2         |
14 #           |           |           |
15 #           |           |           |
16 #           |           |           |
17 #           |           |           |
18 #           |           |           |
19 #           |           |           |
20 H=30.0
21 L=65.0
22 #a=40.0
23 D=12.5
24 d1=7.5+12.5/2.0
25 d2=10.0+12.5/2.0
26
27 string_material='IM78552'
28
29 thickness_plies=32*[0.125]
30 angle_plies=8*[0, 90, 90, 0]
31
32 size_el=0.5
33
34 # type 'CT' or 'CC'
35 type_specimen='CC'
36 #-----#
37
38 a=a_eff+d1
39 from abaqus import *
40 from abaqusConstants import *
41 from caeModules import *
42 from driverUtils import executeOnCaeStartup
43 executeOnCaeStartup()
44
45 mdb.Model(name='Model-A')
46
47 s = mdb.models['Model-A'].ConstrainedSketch(name='__profile__',
48     sheetSize=200.0)
49 g, v, d, c = s.geometry, s.vertices, s.dimensions, s.constraints
50 s.setPrimaryObject(option=STANDALONE)
51 s.Line(point1=(0.0, 0.0), point2=(L-a, 0.0))
52 s.Line(point1=(L-a, 0.0), point2=(L-a, H))
53 s.Line(point1=(L-a,H), point2=(0.0, H))
54 s.Line(point1=(0.0,H), point2=(-a, H))
55 s.Line(point1=(-a,H), point2=(-a, 0.0))
56 s.Line(point1=(-a, 0.0), point2=(0.0, 0.0))
57 s.CircleByCenterPerimeter(center=(-(a-d1), d2), point1=(-(a-d1), d2+D/2.0))
58
59 p = mdb.models['Model-A'].Part(name='Part-1', dimensionality=THREE_D,
60     type=DEFORMABLE_BODY)
61 p = mdb.models['Model-A'].parts['Part-1']
62 p.BaseShell(sketch=s)
63 s.unsetPrimaryObject()
64 p = mdb.models['Model-A'].parts['Part-1']
65
66 del mdb.models['Model-A'].sketches['__profile__']
67
68 # finish geometry
69
70 #materials
71 execfile('library_materials.py')
72 mdb.models['Model-A'].Material(name=string_material, description='')
73 exec('MatId='+string_material)
74
75 mdb.models['Model-A'].materials[string_material].Elastic(type=ENGINEERING_CONSTANTS,

```

```

76         table=((MatId['E1'], MatId['E2'],MatId['E2'], MatId['v12'], MatId['v12'], MatId['v23'],
77             MatId['G12'], MatId['G23'], MatId['G23']), ))
78
79 mdb.models['Model-A'].materials[string_material].Density(table=((MatId['density'], ), ))
80 mdb.models['Model-A'].materials[string_material].Conductivity(table=((1.0, ), ))
81 mdb.models['Model-A'].materials[string_material].SpecificHeat(table=((1.0, ), ))
82 mdb.models['Model-A'].materials[string_material].Expansion(type=ORTHOTROPIC, table=((MatId['alpha1'],
83     MatId['alpha2'], MatId['alpha2']), ))
84
85
86 # definition of section
87 Layup=[]
88
89 for i in range(1,len(thickness_plies)+1):
90     exec("sectionLayer"+str(i)+"=section.SectionLayer(material='"+string_material+"',
91         thickness="+str(thickness_plies[i-1])+           ", orientAngle="+str(angle_plies[i-1])+",
92         numIntPts=3, plyName='ply_'+str(i)+" ' ) " )
93     exec("Layup.append(sectionLayer"+str(i)+" " )
94
95
96 mdb.models['Model-A'].CompositeShellSection(name='Section-1', preIntegrate=OFF,
97     poissonDefinition=DEFAULT, thicknessModulus=None, temperature=GRADIENT,
98     useDensity=OFF, nodalThicknessField='', integrationRule=SIMPSON, layup=tuple(Layup))
99
100 # assign sections
101 p = mdb.models['Model-A'].parts['Part-1']
102 f = p.faces
103
104 region = regionToolset.Region(faces=f)
105 p.SectionAssignment(region=region, sectionName='Section-1', offset=0.0)
106
107 # mesh
108 p.seedPart(size=size_el, deviationFactor=0.1)
109 p = mdb.models['Model-A'].parts['Part-1']
110 f = p.faces
111 pickedRegions = f
112 p.setMeshControls(regions=pickedRegions, elemShape=QUAD, algorithm=MEDIAL_AXIS)
113 p = mdb.models['Model-A'].parts['Part-1']
114
115 elemType1 = mesh.ElemType(elemCode=S8R, elemLibrary=STANDARD)
116 elemType2 = mesh.ElemType(elemCode=STRI65, elemLibrary=STANDARD)
117
118 p = mdb.models['Model-A'].parts['Part-1']
119 f = p.faces
120 faces = f
121 pickedRegions =(faces, )
122 p.setElementType(regions=pickedRegions, elemTypes=(elemType1, elemType2))
123
124 p.generateMesh()
125
126 # assembly
127 a = mdb.models['Model-A'].rootAssembly
128 a.DatumCsysByDefault(CARTESIAN)
129 p = mdb.models['Model-A'].parts['Part-1']
130 a.Instance(name='Part-1-1', part=p, dependent=ON)
131
132 # steps
133 mdb.models['Model-A'].StaticStep(name='thermo_mechanic', previous='Initial')
134
135 # symmetry
136 a = mdb.models['Model-A'].rootAssembly
137 e1 = a.instances['Part-1-1'].edges
138 edges1 = e1.getSequenceFromMask(mask=('[#4 ]', ), )
139 region = regionToolset.Region(edges=edges1)
140 mdb.models['Model-A'].YsymmBC(name='BC-1', createStepName='thermo_mechanic',

```

222 APPENDIX C. PARAMETRIC MODEL FOR J-INTEGRAL CALCULATION

```

141     region=region)
142
143 # constrain displacement on x
144 a1 = mdb.models['Model-A'].rootAssembly
145 v1 = a1.instances['Part-1-1'].vertices
146 verts1 = v1.getSequenceFromMask(mask=('[#1 ]', ), )
147 region = regionToolset.Region(vertices=verts1)
148 mdb.models['Model-A'].DisplacementBC(name='BC-3', createStepName='thermo_mechanic',
149     region=region, u1=0.0, u2=UNSET, u3=UNSET, ur1=UNSET, ur2=UNSET, ur3=UNSET,
150     amplitude=UNSET, fixed=OFF, distributionType=UNIFORM, fieldName='',
151     localCsys=None)
152
153 # static
154 if type_specimen=='CT':
155     fact=1.0
156 else:
157     fact=-1.0
158
159 a1 = mdb.models['Model-A'].rootAssembly
160 v1 = a1.instances['Part-1-1'].vertices
161 verts1 = v1.getSequenceFromMask(mask=('[#1 ]', ), )
162 region = regionToolset.Region(vertices=verts1)
163 mdb.models['Model-A'].ConcentratedForce(name='Load-1',
164     createStepName='thermo_mechanic', region=region, cf2=fact, localCsys=None)
165
166 a = mdb.models['Model-A'].rootAssembly
167
168 v1 = a.instances['Part-1-1'].vertices
169 verts1 = v1.getSequenceFromMask(mask=('[#4 ]', ), )
170 crackFront = regionToolset.Region(vertices=verts1)
171 a = mdb.models['Model-A'].rootAssembly
172 v1 = a.instances['Part-1-1'].vertices
173 verts1 = v1.getSequenceFromMask(mask=('[#4 ]', ), )
174 crackTip = regionToolset.Region(vertices=verts1)
175 v1 = a.instances['Part-1-1'].vertices
176 v11 = a.instances['Part-1-1'].vertices
177 a.engineeringFeatures.ContourIntegral(name='Crack', symmetric=ON,
178     crackFront=crackFront, crackTip=crackTip,
179     extensionDirectionMethod=Q_VECTORS, qVectors=((v1[1], v11[2]), ),
180     midNodePosition=0.5, collapsedElementAtTip=NONE)
181
182 mdb.models['Model-A'].fieldOutputRequests['F-Output-1'].setValues(variables=(
183     'S', 'E', 'U', 'JK' ))
184
185 mdb.models['Model-A'].historyOutputRequests['H-Output-1'].setValues(variables=(
186     'ALLAE', 'ALLCD', 'ALLDMD', 'ALLEE', 'ALLFD', 'ALLIE', 'ALLJD', 'ALLKE',
187     'ALLKL', 'ALLPD', 'ALLQB', 'ALLSE', 'ALLSD', 'ALLVD', 'ALLWK', 'ETOTAL',
188     'DBS', 'DBT', 'DBSF'))
189
190 mdb.models['Model-A'].HistoryOutputRequest(name='H-Output-2',
191     createStepName='thermo_mechanic', contourIntegral='Crack',
192     sectionPoints=DEFAULT, rebar=EXCLUDE, numberOfContours=25)
193
194 a_eff_s=str(a_eff)
195 ind=a_eff_s.index('.')
196 a_eff_s_1=a_eff_s[0:ind]
197 a_eff_s_2=a_eff_s[ind+1::]
198 a_eff_s_2=str()
199 for i in range(0,3):
200     try:
201         a_eff_s_2[i]
202         a_eff_s_2=a_eff_s_2+a_eff_s_2[i]
203     except IndexError:
204         a_eff_s_2=a_eff_s_2+'0'
205

```

```

206 | a_eff_s=a_eff_s_1+'d'+a_eff_s_2_
207 |
208 | string_name=type_specimen+'_'+string_material+'_'+a_eff_s
209 |
210 | mdb.models.changeKey(fromName='Model-A', toName=string_name)
211 |
212 | #--> go to odb

```

Filename: *library_materials.py*

```

1 | IM78552={'type':'composite',
2 |         'density':1.59e-9,
3 |         'E1':171420.,
4 |         'E2': 9080.,
5 |         'G12':5290,
6 |         'v12':0.32,
7 |         'alpha1':-5.5E-6,
8 |         'alpha2': 25.8E-6,
9 |         'XT': 2323.5,
10 |        'XPO':232.3,
11 |        'XC':1201,
12 |        'YT':160.2,
13 |        'YC':199.8,
14 |        'ALPHAO':0.925,
15 |        'SL': 130.2,
16 |        'SLud': 92.3,
17 |        'GIC_F1': 31.5,
18 |        'GIC_FE': 50.0,
19 |        'GIC_M':0.2774,
20 |        'GIIC_M': 0.7879,
21 |        'GIC_FC': 106.3,
22 |        'GIIC_M-': 1.3092,
23 |        'beta1':0.000,
24 |        'beta2':0.005,
25 |        'DM': 0.0,
26 |        'Eta_viscous':0.001,
27 |        'v23':0.52,
28 |        'G23':42000,      # check it
29 |        'GIC':0.969,
30 |        'GIIC':1.719,
31 |        'S3_o': 120.0,
32 |        'S1_o':120.0,
33 |        'ETA': 1.2,
34 |        'Em':120000.0,
35 |        'POISm': 0.3,
36 |        'del_ele':0.9,
37 |        'Em':9000,
38 |        'vm':0.3,
39 |        'density_m':1.59e-9,
40 |        'alpha_m':25.8E-6}

```

Filename: *read_odb.py*

```

1 | import os
2 | dir_path=os.getcwd()
3 |
4 | odb = session.openOdb(name=dir_path+'\\'+string_name+'.odb')
5 |
6 | assembly = odb.rootAssembly
7 | step=odb.steps
8 | skey=step.keys()[0]
9 | J_integral_contours=step[skey].historyRegions['ElementSet_PIBATCH'].historyOutputs
10 | J_integral_keys=J_integral_contours.keys()

```

224 APPENDIX C. PARAMETRIC MODEL FOR J-INTEGRAL CALCULATION

```
11 |
12 | J_integral=[]
13 |
14 | for key__ in J_integral_keys:
15 |     J_integral.append(J_integral_contours[key__].data[0][1])
16 |
17 | import cPickle
18 | FILE = open(string_name+'.JI', 'w')
19 | cPickle.dump(J_integral, FILE)
20 |
21 | FILE.close()
```

Filename: *analyze_data.py*

```
1 | import numpy as n
2 | import matplotlib.pyplot as plt
3 | import cPickle
4 | import os
5 | dir_path=os.getcwd()
6 |
7 | files_dir=os.listdir(dir_path)
8 |
9 | files_JI=[]
10 |
11 | for file_name_ in files_dir:
12 |     if file_name_[-3:]=='JI':
13 |         files_JI.append(file_name_)
14 |
15 | print files_JI
16 |
17 | CLO=[] #
18 | JI0=[] #
19 | JI_all0=[]
20 |
21 | for file_name_ in files_JI:
22 |     FILE = open(file_name_, 'r')
23 |     JI_ = cPickle.load(FILE)
24 |     JI_all0.append(JI_)
25 |
26 |     ind1=file_name_[::-1].find('.')
27 |     ind2=file_name_[::-1].find('_')
28 |     str_crack=file_name_[::-1][ind1+1:ind2][::-1]
29 |     ind_d=str_crack.find('d')
30 |     crack=float(str_crack[:ind_d]+'.'+str_crack[1+ind_d:])
31 |
32 |     CLO.append(crack)
33 |
34 |     JI_orig=[]
35 |     JI_orig.extend(JI_)
36 |
37 |
38 |     while JI_[-1]<0.0:
39 |         JI_.remove(JI_[-1])
40 |
41 |
42 |     JI0.append(JI_[-1])
43 |
44 |     print '-----'
45 |     print 'crack length='
46 |     print crack
47 |     print 'J-integral value='
48 |     print JI_[-1]
49 |     print 'contours JI'
50 |     print JI_orig
```



```
51 |     print 'modified contours JI'
52 |     print JI_
53 |
54 |     FILE.close()
55 |
56 | # graphs
57 | plt.plot(CLO,JIO,'-o')
58 | plt.ylabel('Energy Release')
59 | plt.show()
60 |
61 | #
62 | data_=[]
63 | data_.append(CLO)
64 | data_.append(JIO)
65 |
66 | data=n.array(data_)
67 | data=n.transpose(data)
68 | n.savetxt('JI_data.txt', data, fmt="%12.6G")
69 | #
70 | import cPickle
71 | FILE = open('CL_JI', 'w')
72 | cPickle.dump(CLO, FILE)
73 | cPickle.dump(JIO, FILE)
74 | FILE.close()
```


Appendix D

2D Model for Industrial Application

```
1  !* 2D failure model for industrial application
2  !* G. Catalanotti 2010
3
4  /NOPR
5
6  /OUT,output,txt
7  /COM,----- ANALYSIS RESULTS -----
8  /COM,
9  /COM, | node | F_Index | Shear | Tension | Combined | L Pres |
10 /COM,
11 /OUT
12
13 /UIS, MSGPOP,3
14 !/UIS,ABORT,OFF
15
16 *SET,ALL
17 PARSAV,ALL,'savedparameter','txt',' !initialize parameters file
18 /CLEAR !clear database
19 RESUME ! resume original job
20 ALLSEL,ALL
21
22 /INPUT,'zinput','txt',,, 0 ! import input data
23
24 ! find all the coupled nodes
25 *GET, MAX_coupled_number, CP, ,MAX
26 NSEL,S,CP,,1,MAX_coupled_number,1
27 *GET,highest_node,NODE,,NUM,MAX, , , ,
28 *DIM,all_nodes,ARRAY,highest_node,, , ,
29 *VGET,all_nodes,NODE, ,NSEL,, , ,2
30
31 ! number of selected nodes
32 *GET,n_number,NODE,,COUNT, , , ,
33 *DIM,coupled_nodes,ARRAY,n_number,, , ,
34
35 ff=0
36 *DO, I, 1, highest_node,1
37   *IF,all_nodes(I,1,1),EQ,1,THEN
38     ff=ff+1
39     coupled_nodes(ff,1,1)=I
40   *ENDIF
41 *ENDDO
42
43 *DIM,EL_NUMBER,ARRAY,n_number,, , ,
```

```

44 *DIM,TYPE_NUMBER,ARRAY,n_number,,, , ,
45 *DIM,CS_NUMBER,ARRAY,n_number,,, , ,
46 *DIM,REALC_NUMBER,ARRAY,n_number,,, , ,
47 *DIM,MAT_NUMBER,ARRAY,n_number,,, , ,
48 *DIM,SEC_NUMBER,ARRAY,n_number,,, , ,
49 !
50 *DO,I,1,n_number
51 NSEL,S, , , coupled_nodes(I,1,1)
52 ESLN,S
53 ESEL,R,ENAME,,element_used
54 *GET,highest_elem,ELEM,,NUM,MAX, , , ,
55 ALLSEL,ALL
56 !*
57 *GET,TN,ELEM,highest_elem,ATTR,TYPE
58 *GET,CSN,ELEM,highest_elem,ATTR,ESYS
59 *GET,RN,ELEM,highest_elem,ATTR,REAL
60 *GET,MN,ELEM,highest_elem,ATTR,MAT
61 !*
62 EL_NUMBER(I,1,1)=highest_elem
63 TYPE_NUMBER(I,1,1)=TN
64 CS_NUMBER(I,1,1)=CSN
65 REALC_NUMBER(I,1,1)=RN
66 MAT_NUMBER(I,1,1)=MN
67 !*
68 *ENDDO
69
70 !* get highest defined section in the model
71 *GET,highest_section, SECP, NUM, MAX
72
73 *DO, I, 1, n_number
74   *DO, J, 1,highest_section
75     ESEL,S, , , EL_NUMBER(I,1,1)
76     ESEL,U,SEC,,J
77     *GET,highest_elem,ELEM,,NUM,MAX, , , ,
78     *IF,highest_elem,EQ,0,THEN
79       SEC_NUMBER(I,1,1)=J
80     *EXIT
81   *ENDIF
82 *ENDDO
83 *ENDDO
84 !*
85 PI = 3.14159
86 *DIM,DIAMETERS,TABLE,n_number,1,1, , ,
87 *TREAD,DIAMETERS,'input_diameter','txt',' ',1,
88
89 *DIM,FURS,TABLE,n_number,1,1, , ,
90 *TREAD,FURS,'input_fur','txt',' ',1,
91
92 ! get jobname
93 *GET,jobname,ACTIVE, ,JOBNAM ! get current jobname
94
95 *DO, coupled_nodeI, 1, n_number, 1
96
97 PARSAV,ALL,'savedparameter','txt','
98 coupled_node=coupled_nodes(coupled_nodeI,1,1)
99
100 diameter=DIAMETERS(coupled_node)
101 fur=FURS(coupled_node)
102
103 ALLSEL,ALL
104 CSYS,0
105
106 allsel,all
107 *GET,highest_node,NODE,,NUM,MAX, , , ,
108 *DIM,all_nodes,ARRAY,highest_node,,, , ,

```

```

109
110 *GET,highest_elem,ELEM,,NUM,MAX, , , ,
111 *DIM,all_elem,ARRAY,highest_elem,, , ,
112 *DIM,all_elem2,ARRAY,highest_elem,, , ,
113 *DIM,all_elem3,ARRAY,highest_elem,, , ,
114
115 *DIM,before_nodes,ARRAY,highest_node,, , ,
116 *DIM,after_nodes,ARRAY,highest_node,, , ,
117
118 ! select coupled node
119 NSEL,S, , , coupled_node ! select coupled node
120
121 *GET,high_elem_4,ELEM,,NUM,MAX, , , ,
122 *GET,elem_area,ELEM,high_elem_4,AREA
123
124 side_elem=sqrt(elem_area)
125
126 half_side=NINT(2*diameter/side_elem)
127
128 *IF,half_side,EQ,0,then
129     half_side=1
130 *ENDIF
131
132 ! select coupled node
133 NSEL,S, , , coupled_node ! select coupled node
134
135 *DO, I, 1, half_side, 1
136     ! selected node in array
137     *VGET,before_nodes,NODE, ,NSEL,, , ,2
138     ! select elements attached to coupled node
139     ESLN,S
140     ! select nodes attached to elements
141     NSLE,S
142     *VGET,after_nodes,NODE, ,NSEL,, , ,2
143 *ENDDO
144
145 *DIM,contour,ARRAY,highest_node,, , ,
146 *VOPER,contour,after_nodes,SUB,before_nodes, , ,
147
148 *VSCFUN,contour_n,SUM,contour
149 contour_n=contour_n/2
150
151 *DIM,contour_nodes,ARRAY,contour_n,, , ,
152
153 NSEL,NONE
154
155 K=0
156 *DO, I, 1, highest_node, 1
157     *IF,contour(I,1,1),EQ,2,THEN
158         NSEL,A, , , I
159         K=K+1
160         ! array with the number of nodes on the contour
161         contour_nodes(K,1,1)=I
162     *ENDIF
163 *ENDDO
164
165 *DIM,contour_x,ARRAY,contour_n,, , ,
166 *DIM,contour_y,ARRAY,contour_n,, , ,
167 *DIM,contour_z,ARRAY,contour_n,, , ,
168
169 *DO, I, 1, contour_n, 1
170     *GET,xcoord,NODE,contour_nodes(I,1,1),LOC,X
171     *GET,ycoord,NODE,contour_nodes(I,1,1),LOC,Y
172     *GET,zcoord,NODE,contour_nodes(I,1,1),LOC,Z
173     !

```

```

174     contour_x(I,1,1)=xcoord
175     contour_y(I,1,1)=ycoord
176     contour_z(I,1,1)=zcoord
177     !
178     *SET,xcoord
179     *SET,ycoord
180     *SET,zcoord
181 *ENDDO
182
183 !!!!! sort nodes
184
185 NSEL,S, , ,   coupled_node !select copled node
186 ESLN,S      !select attached node
187 ESEL,R,ENAME,,element_used
188
189 *GET,elem_sys_n,ELEM,,NUM,MAX, , , ,
190
191 *GET,elem_sys,ELEM,elem_sys_n,ATTR,ESYS    ! get element coordinate system
192
193 *GET,max_coord_sys,CDSY, , NUM,MAX
194
195 *IF,max_coord_sys,LT,10,THEN
196     max_coord_sys=10
197 *ENDIF
198
199 max_coord_sys=max_coord_sys+1
200 ! define coordinate system concord to the nodes
201 CSYS,0,
202 DSYS,0,
203
204 *GET,center_x,NODE,coupled_node,LOC,X
205 *GET,center_y,NODE,coupled_node,LOC,Y
206 *GET,center_z,NODE,coupled_node,LOC,Z
207
208 CSYS,0,
209 DSYS,0,
210 CLOCAL, max_coord_sys,0, center_x,center_y, center_z
211
212 CSYS,0,
213 DSYS,0,
214 CLOCAL, max_coord_sys+1,1, center_x,center_y, center_z
215 !*
216 CSYS,max_coord_sys+1,
217 DSYS,max_coord_sys+1 ,
218
219 *DIM,contour_angle,ARRAY,contour_n,,, , ,
220
221 *DO, I, 1, contour_n, 1
222     *GET,angle_coord,NODE,contour_nodes(I,1,1),LOC,Y
223     *IF,angle_coord,LT,0,THEN
224         contour_angle(I,1,1)=angle_coord+360
225     *ELSE
226         contour_angle(I,1,1)=angle_coord
227     *ENDIF
228     *SET,angle_coord
229 *ENDDO
230
231 !sort_nodes
232 *DIM,key_points,ARRAY,contour_n,,, , ,
233 *DIM,key_points_x,ARRAY,contour_n,,, , ,
234 *DIM,key_points_y,ARRAY,contour_n,,, , ,
235 *DIM,key_points_z,ARRAY,contour_n,,, , ,
236
237 *VSCFUN,index_min_angle,LMIN,contour_angle
238 *VSCFUN,index_max_angle,LMAX,contour_angle

```

```

239
240 *IF,(360-contour_angle(index_max_angle,1,1)),LT,contour_angle(index_min_angle,1,1),THEN
241     contour_angle(index_max_angle,1,1)=contour_angle(index_max_angle,1,1)-360
242 *ENDIF
243
244 *DO, I, 1, contour_n, 1
245     *VSCFUN,index_min_angle,LMIN,contour_angle
246     key_points(I,1,1)=index_min_angle !contour_nodes(index_min_angle,1,1)
247     key_points_x(I,1,1)=contour_x(index_min_angle,1,1)
248     key_points_y(I,1,1)=contour_y(index_min_angle,1,1)
249     key_points_z(I,1,1)=contour_z(index_min_angle,1,1)
250     contour_angle(index_min_angle,1,1)=361
251 *ENDDO
252
253 CSYS,0
254 !
255 *GET,center_x,NODE,coupled_node,LOC,X
256 *GET,center_y,NODE,coupled_node,LOC,Y
257 *GET,center_z,NODE,coupled_node,LOC,Z
258
259 DSYS,0
260 section=SEC_number(coupled_nodeI,1,1)
261
262 *IF,section,NE,0,THEN
263     FLAG='C'
264     ! numero layer
265     *GET, num_layer, SHEL, section, PROP, NLAY
266     ! thickness
267     *GET, tot_thick, SHEL, section, PROP, TTHK
268     !
269     *DIM,thick_layer,ARRAY,num_layer,, , ,
270     *DIM,ori_layer,ARRAY,num_layer,, , ,
271     *DIM,mat_layer,ARRAY,num_layer,, , ,
272
273     *DO, I,1,num_layer,1
274         *GET, thick_layer_i, SHEL, section,LAYD, I, THIC
275         *GET, mat_layer_i, SHEL, section,LAYD, I, MAT
276         *GET, ori_layer_i, SHEL, section,LAYD, I, ANGL
277         thick_layer(I,1,1)=thick_layer_i
278         ori_layer(I,1,1)=ori_layer_i
279         mat_layer(I,1,1)=mat_layer_i
280     *ENDDO
281 *ELSE
282     FLAG='H'
283 *ENDIF
284 !
285 /POST1
286 INRES,ALL
287 FILE,, 'rst', '.'
288 SET,LIST,999
289 SET,,, , , , setnumb
290 ALLSEL,ALL
291 !*
292 NSEL,S, , , coupled_node
293 !*
294 RSYS, max_coord_sys
295 FSUM,RSYS,ALL
296 !*
297 *GET,FX,FSUM,,ITEM,FX
298 *GET,FY,FSUM,,ITEM,FY
299 *GET,FZ,FSUM,,ITEM,FZ
300 !*
301 *GET,uz_node,NODE,coupled_node,U,Z
302 FINISH
303 ALLSEL,ALL

```



```

369 CSKP,11,0,1000,key_points(1,1,1),key_points(2,1,1),1,1,
370 ! cylindrical
371 CSKP,12,1,1000,key_points(1,1,1),key_points(2,1,1),1,1,
372
373 DSYS,12
374 CSYS,12
375
376 *GET,k_y1,KP,key_points(1,1,1),LOC,Y
377 *GET,k_y2,KP,key_points(1+contour_n/4,1,1),LOC,Y
378 *GET,k_y3,KP,key_points(1+2*contour_n/4,1,1),LOC,Y
379 *GET,k_y4,KP,key_points(1+3*contour_n/4,1,1),LOC,Y
380
381 K,1001,rad,k_y1,0
382 K,1002,rad,k_y2,0
383 K,1003,rad,k_y3,0
384 K,1004,rad,k_y4,0
385
386 *GET,k_y1a,KP,key_points(1+contour_n/8,1,1),LOC,Y
387 *GET,k_y2a,KP,key_points(1+contour_n/4+contour_n/8,1,1),LOC,Y
388 *GET,k_y3a,KP,key_points(1+2*contour_n/4+contour_n/8,1,1),LOC,Y
389 *GET,k_y4a,KP,key_points(1+3*contour_n/4+contour_n/8,1,1),LOC,Y
390
391 K,1005,rad,k_y1a,0
392 K,1006,rad,k_y2a,0
393 K,1007,rad,k_y3a,0
394 K,1008,rad,k_y4a,0
395
396 LARC, 1001, 1002, 1005
397 LARC, 1002, 1003, 1006
398 LARC, 1003, 1004, 1007
399 LARC, 1004, 1001, 1008
400
401 K,2001,rad_bolt,k_y1,0
402 K,2002,rad_bolt,k_y2,0
403 K,2003,rad_bolt,k_y3,0
404 K,2004,rad_bolt,k_y4,0
405
406 K,2005,rad_bolt,k_y1a,0
407 K,2006,rad_bolt,k_y2a,0
408 K,2007,rad_bolt,k_y3a,0
409 K,2008,rad_bolt,k_y4a,0
410
411 LARC, 2001, 2002, 2005
412 LARC, 2002, 2003, 2006
413 LARC, 2003, 2004, 2007
414 LARC, 2004, 2001, 2008
415
416 DSYS,0
417 CSYS,0
418
419 LSTR, 2001, key_points(1,1,1)
420 LSTR, 2002, key_points(1+contour_n/4,1,1)
421 LSTR, 2003, key_points(1+contour_n/2,1,1)
422 LSTR, 2004, key_points(1+3*contour_n/4,1,1)
423
424 LSTR, 1001, 2001
425 LSTR, 1002, 2002
426 LSTR, 1003, 2003
427 LSTR, 1004, 2004
428
429 LCCAT,1,2
430 LCCAT,3,4
431 LCCAT,5,6
432 LCCAT,7,8
433

```

```

434 AL,1,2,18,13,17
435 AL,18,3,4,19,14
436 AL,19,5,6,20,15
437 AL,20,7,8,17,16
438
439 AL,22,14,23,10
440 AL,23,15,24,11
441 AL,24,16,21,12
442 AL,21,13,22,9
443
444 ratio=5
445
446 LESIZE,21,meshsize, , ,ratio, , , ,1
447 LESIZE,22,meshsize, , ,ratio, , , ,1
448 LESIZE,23,meshsize, , ,ratio, , , ,1
449 LESIZE,24,meshsize, , ,ratio, , , ,1
450
451 ALLSEL,ALL
452
453 Fboltz=FX
454 Fbolty=FY
455 Fboltz=abs(FZ)
456 Fboltxy=sqrt(Fboltz**2+Fbolty**2)
457 pres_max=Fboltxy/2/rad
458 beta=atan2(Fbolty,Fboltz)/PI*180
459
460 CDREAD,DB,, 'cdb' , , , , ,
461
462 TYPE, TYPE_NUMBER(coupled_nodeI,1,1)
463 MAT, MAT_NUMBER(coupled_nodeI,1,1)
464 REAL, REALC_NUMBER(coupled_nodeI,1,1)
465 *IF,SEC_NUMBER(coupled_nodeI,1,1),NE,0,THEN
466 SECNUM, SEC_NUMBER(coupled_nodeI,1,1)
467 *ELSE
468 SECNUM, ,
469 *ENDIF
470
471 ESYS, max_coord_sys
472
473 CSYS,max_coord_sys+1,
474 K,1200,rad*2,beta,,
475 !*
476 CSKP,max_coord_sys+2,1,1000,1200,1003,1,1,
477
478 ! store results for all layer
479 KEYOPT,TYPE_NUMBER(coupled_nodeI,1,1),8,1
480
481 LCCAT,1,2
482 LCCAT,3,4
483 LCCAT,5,6
484 LCCAT,7,8
485
486 ndiv0=10
487 LESIZE,9, , ,ndiv0, , , , ,1
488 LESIZE,10, , ,ndiv0, , , , ,1
489 LESIZE,11, , ,ndiv0, , , , ,1
490 LESIZE,12, , ,ndiv0, , , , ,1
491 LESIZE,13, , ,ndiv0, , , , ,1
492 LESIZE,14, , ,ndiv0, , , , ,1
493 LESIZE,15, , ,ndiv0, , , , ,1
494 LESIZE,16, , ,ndiv0, , , , ,1
495
496 siz1=2*PI*rad/4/10*2
497 LESIZE,17,siz1, , , , , , ,1
498 LESIZE,18,siz1, , , , , , ,1

```

```

499 LESIZE,19,siz1, , , , , ,1
500 LESIZE,20,siz1, , , , , ,1
501
502 MSHKEY,1
503 AMESH,ALL
504
505 CSYS,max_coord_sys+2,
506 NSEL,S,LOC,X,rad
507 NSEL,R,LOC,Y,-90,+90
508
509 ! pressure on hole's edge
510 *DEL,_FNCNAME
511 *DEL,_FNCMTID
512 *DEL,_FNC_C1
513 *DEL,_FNCCSYS
514 *SET,_FNCNAME,'COSIN'
515 *DIM,_FNC_C1,,1
516 *SET,_FNC_C1(1),pres_max
517 *SET,_FNCCSYS,max_coord_sys+2
518 *DIM,%_FNCNAME%,TABLE,6,3,1,,,_%FNCCSYS%
519 !
520 ! Begin of equation: pres_max*cos({Y})
521 *SET,%_FNCNAME%(0,0,1), 0.0, -999
522 *SET,%_FNCNAME%(2,0,1), 0.0
523 *SET,%_FNCNAME%(3,0,1), %_FNC_C1(1)%
524 *SET,%_FNCNAME%(4,0,1), 0.0
525 *SET,%_FNCNAME%(5,0,1), 0.0
526 *SET,%_FNCNAME%(6,0,1), 0.0
527 *SET,%_FNCNAME%(0,1,1), 1.0, -1, 10, 1, 3, 0, 0
528 *SET,%_FNCNAME%(0,2,1), 0.0, -2, 0, 1, 17, 3, -1
529 *SET,%_FNCNAME%(0,3,1), 1, 99, 0, 1, -2, 0, 0
530 ! End of equation: pres_max*cos({Y})
531
532 SF,ALL,PRES, %COSIN%
533
534 ALLSEL,ALL
535
536 FINISH
537 /SOL
538 !*
539 ANTYPE,0
540 DELTIM,1,1,1
541 OUTRES,ERASE
542 OUTRES,NSOL,LAST
543 OUTRES,RSOL,LAST
544 OUTRES,NLOA,LAST
545 OUTRES,STRS,LAST
546
547 submodelname=strcat('node_',CHRVAL(coupled_node))
548 !*
549 !***** submodel
550 !* select exterior lines
551 FLST,5,8,4,ORDE,2
552 FITEM,5,1
553 FITEM,5,-8
554 LSEL,S, , ,P51X
555 !* select attached nodes
556 NSLL,S,1
557 /PREP7
558 !* write NODE file
559 NWRITE, submodelname,'NODE'
560 allsel,all
561 FINISH
562
563 SAVE,submodelname,'db',

```

```

564 PARSAV,ALL,'savedparameter','txt','
565
566 !*
567 /CLEAR,START
568 /INPUT,'savedparameter','txt',,,0
569 RESUME,jobname,'db'
570 ALLSEL,ALL
571
572 /INPUT,'savedparameter','txt',,,0
573 /POST1
574 INRES,ALL
575 FILE,jobname,'rst','.'
576 SET,LAST
577 CBDOF,submodelname,'NODE',' ',submodelname,'CBDO',' ',0, ,0
578 PARSAV,ALL,'savedparameter','txt','
579 !*
580 FINISH
581 /CLEAR
582
583 /INPUT,'savedparameter','txt',,, 0
584 RESUME,submodelname,'db',,0,0
585
586 /INPUT,'savedparameter','txt',,, 0
587 /SOL
588 /INPUT,submodelname,'CBDO',,, 0
589 DCUM,ADD
590 !*
591 FINISH
592 command=strcat('/FILENAME','submodelname)
593 SAVE,submodelname,'db',
594 PARSAV,ALL,'savedparameter','txt','
595 /clear
596 /INPUT,'savedparameter','txt',,, 0
597 /FILENAME,submodelname,0
598 RESUME,submodelname,'db',,0,0
599 /SOLU
600 !*
601 SOLVE
602 !*
603 FINISH
604 !
605 /POST1
606 SET,LAST
607 !*
608 ! SEC_number(coupled_nodeI,1,1)
609 ! FLAG='C'
610 ! num_layer
611 ! tot_thick
612 ! thick_layer
613 ! ori_layer
614 ! mat_layer
615 ! thick_layer_i
616 ! mat_layer_i
617 ! ori_layer_i
618 ! thick_layer(I,1,1)
619 ! ori_layer(I,1,1)
620 ! mat_layer(I,1,1)
621 !*
622 ! FLAG='H'
623 !*
624 *GET,High_elem_sub,ELEM,,NUM,MAX, , , ,
625 !*
626 *DIM,F_MATRIX,ARRAY,High_elem_sub,1,1, , ,
627 *DIM,F_FIBER,ARRAY,High_elem_sub,1,1, , ,
628

```

```

629 | ! select areas near the bolts
630 |
631 | FLST,5,4,5,ORDE,2
632 | FITEM,5,5
633 | FITEM,5,-8
634 | ASEL,S, , ,P51X
635 | ESLA,S
636 |
637 | *DIM,dam_elem,ARRAY,High_elem_sub,1,1, , ,
638 | *VGET,dam_elem,ELEM, ,ESEL, , ,2
639 |
640 | *DIM,dam_elem2,ARRAY,High_elem_sub,1,1, , ,
641 | *VGET,dam_elem2,ELEM, ,ESEL, , ,2
642 |
643 | ALLSEL,ALL
644 |
645 | *VFUN,dam_elem2,PWR,dam_elem2,2, , ,
646 |
647 | *VOPER,dam_elem,dam_elem,EQ,dam_elem2, , ,
648 |
649 | ! define F ETABLE (full of zeros)
650 | ETABLE,F,U,X
651 | *VPUT,F_FIBER,ELEM, ,ETAB,F, , ,2
652 | !*
653 | *DIM,Mises_vect,ARRAY,High_elem_sub,1,1, , ,
654 | !*
655 | *IF,SEC_number(coupled_nodeI,1,1),EQ,0,THEN
656 | num_layer_ALL=1
657 | *ENDIF
658 |
659 | *DO,LAYER_Imo,1,num_layer_ALL,1
660 |
661 | *IF,SEC_number(coupled_nodeI,1,1),NE,0,THEN
662 |
663 | RSYS,SOLU !RSYS, max_coord_sys
664 | LAYER,LAYER_Imo
665 | !*
666 | ETABLE,S11,S,X
667 | ETABLE,S22,S,Y
668 | ETABLE,S12,S,XY
669 | !*
670 | mat_string=strcat('material_',CHRVAL(mat_layer(LAYER_Imo,1,1)))
671 |
672 | /INPUT,mat_string,'txt',,, 0 ! import material parameters
673 | !*
674 | ST_is=0.5*(2.0*sin(alpha0)**2-1.0)*SL_is/(sqrt(1.d0-sin(alpha0)**2)*sin(alpha0)*eta_L)
675 | YC_is=-SL_is*(2.0*cos(alpha0)**2-1.0)/(ETA_L*cos(alpha0)**2)
676 | eta_T=eta_L*ST_is/SL_is
677 |
678 | *DIM,S11vect,ARRAY,High_elem_sub,1,1, , ,
679 | *DIM,S22vect,ARRAY,High_elem_sub,1,1, , ,
680 | *DIM,S12vect,ARRAY,High_elem_sub,1,1, , ,
681 | *VGET,S11vect,ELEM, ,ETAB,S11, ,2
682 | *VGET,S22vect,ELEM, ,ETAB,S22, ,2
683 | *VGET,S12vect,ELEM, ,ETAB,S12, ,2
684 |
685 | *DO,I,1,High_elem_sub,1
686 |
687 | s11=S11vect(I,1,1)
688 | s22=S22vect(I,1,1)
689 | s12=S12vect(I,1,1)
690 |
691 | FMC=0
692 | FMT=0
693 |

```

```

694 *DO,alpha_deg,0 ,180,30
695
696 alpha=alpha_deg*PI/180.0
697
698 sigma_N=s22/2.0+s22/2.0*cos(2.0*alpha)
699 tau_T=-sin(alpha)*cos(alpha)*s22
700 tau_L=s12*cos(alpha)
701
702 *IF,sigma_N,LT,0,THEN
703     FM_C=(tau_T/(ST_is-eta_T*sigma_N))**2+(tau_L/(SL_is-eta_L*sigma_N))**2
704     *IF,FM_C,GT,FMC,THEN
705         FMC= FM_C
706     *ENDIF
707 *ENDIF
708
709     *IF,sigma_N,GE,0,THEN
710         FM_T=(sigma_N/YT_is)**2+ (tau_L/SL_is)**2
711         *IF,FM_T,GT,FMT,THEN
712             FMT=FM_T
713         *ENDIF
714     *ENDIF
715 *ENDDO
716
717 F_MATRIX(I,1,1)=max(FMT,FMC)
718     FIfT=0
719     FK_C=0
720     FKT=0
721     FK_MAX=0
722     FF_MAX=0
723     FK=0
724
725 *IF,S11,GE,0,THEN
726     FIfT = S11/XT
727 *ELSE
728
729 THETA=PI/2
730 cc = ABS(SL_is/XC)
731 aa = cc+ETA_L
732     *IF,1.0-4.0*aa*cc,LE,0, THEN
733         FMcCAULEY = 0.0
734     *ELSE
735         FMcCAULEY = 1.0-4.0*aa*cc
736     *ENDIF
737 sqr = sqrt(FMcCAULEY)
738 phiC = atan((1.0-sqr)/(2.0*aa))
739 ! calculation of gamma_mc
740 gamma_mc=sin(2.0*phiC)*XC/2.0/G12
741 ! calculation of phi_0
742 phi_0=phiC-gamma_mc
743
744 s11THETA=s11
745 s22THETA=s22*cos(THETA)**2
746 s33THETA =s22*sin(THETA)**2
747 s12THETA= cos(THETA)*s12
748 s23THETA=-sin(THETA)*cos(THETA)*s22
749 s13THETA= - sin(THETA)*s12
750
751 ! calculation of phi_0
752 phi_0_theta=PHI_0
753
754 gamma_m=(phi_0_theta*G12+abs(s12THETA))/(G12+s11THETA-s22THETA)-phi_0_theta
755
756 *if,s12THETA,GT,0,then
757     PHI=PHI_0_theta+gamma_m
758 *else

```

```

759     PHI=-(PHI_0_theta+gamma_m)
760 *endif
761
762 s11PHI=cos(PHI)**2*s11THETA+2.0*cos(PHI)*sin(PHI)*s12THETA+s22THETA*sin(PHI)**2
763 s22PHI=-2.0*cos(PHI)*sin(PHI)*s12THETA+s22THETA*cos(PHI)**2+sin(PHI)**2*s11THETA
764 !*
765 s12PHI=-sin(PHI)*cos(PHI)*s11THETA
766 s12PHI=s12PHI+cos(PHI)*sin(PHI)*s22THETA
767 s12PHI=s12PHI+2.0*cos(PHI)**2*s12THETA-s12THETA
768 !*
769 s23PHI=-sin(PHI)*s13THETA+cos(PHI)*s23THETA
770 s13PHI= cos(PHI)*s13THETA+sin(PHI)*s23THETA
771 s33PHI=s33THETA
772
773 FMCi=0
774 FMTi=0
775
776 *DO,alpha_deg,0 ,180,30
777
778 alpha=alpha_deg*PI/180.0
779
780 sigma_N=(s22PHI+s33PHI)/2.0+(s22PHI-s33PHI)/2.0*cos(2.0*alpha)+s23PHI*sin(2.0*alpha)
781 tau_T=-sin(alpha)*cos(alpha)*s22PHI-sin(alpha)**2.0*s23PHI+cos(alpha)**2.0*s23PHI
782 tau_T=tau_T+cos(alpha)*sin(alpha)*s33PHI
783 tau_L=s12PHI*cos(alpha)+s13PHI*sin(alpha)
784
785 *IF,sigma_N,LT,0,THEN
786     FM_C=(tau_T/(ST_is-eta_T*sigma_N))**2+(tau_L/(SL_is-eta_L*sigma_N))**2
787     *IF,FM_C,GT,FMC,THEN
788         FMCi= FM_C
789     *ENDIF
790 *ENDIF
791
792 *IF,sigma_N,GE,0,THEN
793 FM_T=(sigma_N/YT_is)**2+ (tau_L/SL_is)**2
794     *IF,FM_T,GT,FMT,THEN
795         FMTi=FM_T
796     *ENDIF
797 *ENDIF
798
799 *ENDDO
800
801 FK_MAX=max(FMCi,FMTi)
802
803 *ENDIF
804
805 *IF,FIfT,GE,FK_MAX,then
806 FF_MAX=FIfT
807 *else
808 FF_MAX=FK_MAX
809 *ENDIF
810
811 F_FIBER(I,1,1)=FF_MAX
812
813 *ENDDO
814
815 *VSCFUN,F_MATRIX_MAX,MAX,F_MATRIX
816 *VSCFUN,F_FIBER_MAX,MAX,F_FIBER
817
818 ETABLE,F_MATRIX,U,X
819 ETABLE,F_FIBER,U,X
820 *VPUT,F_MATRIX,ELEM, ,ETAB,F_MATRIX, , ,2
821 *VPUT,F_FIBER,ELEM, ,ETAB,F_FIBER, , ,2
822
823 SMAX,Fnew,F_MATRIX,F_FIBER,1,1,

```

```

824
825 *ELSE
826
827 mat_string=strcat('material_',CHRVAL(MAT_NUMBER(coupled_nodeI,1,1)))
828
829 /INPUT,mat_string,'txt',,, 0 ! import material parameters
830
831 ETABLE,Mises,S,EQV
832
833 SMULT,Fnew,MISES, ,1/yield_stress,1,
834
835 *ENDIF
836
837 SMAX,F,Fnew,F,1,1,
838
839 *ENDDO
840
841 *DIM,F,ARRAY,High_elem_sub,1,1, , ,
842 *VGET,F,ELEM, ,ETAB,F, ,2
843 *VOPER,F,F,MULT,dam_elem, , ,
844 *VSCFUN,F_MAX,MAX,F
845 *VPUT,F,ELEM, ,ETAB,F, , ,2
846
847 FINISH
848 !*
849
850 Fshear=Fboltxy/0.6/fur/PI/diameter**2*4*1.25
851 Ftension=Fboltz/0.6/fur/PI/diameter**2*4*1.25
852 Fcomb=Fshear+Ftension/1.4
853
854 alph=1
855 Flpres=Fboltxy/2.5/fur/alph/diameter/tot_thick*1.25
856 !
857
858 /OUT,output,txt,,APPEND
859 *VWRITE,coupled_node, F_MAX, Fshear, Ftension, Fcomb, Flpres
860 (F11.0,' ',F11.6, ' ',F11.6, ' ',F11.6, ' ',F11.6, ' ',F11.6, ' ',F11.6 )
861 /OUT
862 !
863 PARSAV,ALL,'savedparameter','txt','
864
865 /clear
866 /INPUT,'savedparameter','txt',,, 0
867 /FILENAME,jobname,0
868 RESUME
869 /INPUT,'savedparameter','txt',,, 0
870 *ENDDO
871
872 /GOPR

```